METAL-METAL OXIDE NANOCOMPOSITES: SYNTHESIS, CHARACTERIZATION AND ANTIMICROBIAL ACTIVITIES

Dissertation submitted in partial fulfillment of the requirements for the degree of

Doctor of Philosophy

In

MATERIALS ENGINEERING

Ву

MONICA PANDEY

(15ETPM03)

Under the guidance of

Dr. PRADIP PAIK and Prof. M. GHANASHYAM KRISHNA



SCHOOL OF ENGINEERING SCIENCES AND TECHNOLOGY
UNIVERSITY OF HYDERABAD
HYDERABAD-500046
INDIA

JANUARY, 2022

Dedicated To

Aaama

and

Buba



Certificate

This is to certify that the thesis entitled "Metal-Metal Oxide Nanocomposites: Synthesis, Characterization and Antimicrobial Activities" submitted by Monica Pandey bearing Reg. No. 15ETPM03 in fulfillment of the requirements for the award of Doctor of Philosophy in Materials Engineering is a bonafide work carried out by her under our supervision and guidance.

This thesis is free from plagiarism and has not been submitted previously in part or in full to this or any other university or institution for the award of any degree or diploma.

Parts of this dissertation have been filed for patents or published in peer-reviewed journals with the following references:

A. Patent Applications Filed:

- 1. A mesoporous anti-microbial nanocomposite and a method of preparation thereof. Pradip Paik;, Monica Pandey, Sukanya Patra, Monika Singh, Kirti Wasnik, Premshankar Gupta. (Indian Patent Application No. 202011031802, 2020)
- 2. A nanomaterial based antimicrobial composition and a method of preparation thereof. Pradip Paik, Monica Pandey, Ragini Tilak, Monika Singh (Indian Patent Application no.: 202011017968, 2020)

B. Publications in journal:

- 3. M. Pandey, M. Singh, K. Wasnik, S. Gupta, S. Patra, P.S. Gupta, D. Pareek, N.S.N. Chaitanya, S. Maity, A.B.M Reddy, R. Tilak, P. Paik, ACS Omega, 2021 6 (47), 31615-31631 (DOI: 10.1021/acsomega.1c04139)
- M. Pandey, K. Wasnik, S. Gupta, M. Singh, S. Patra, P.S. Gupta, D. Pareek, S. Maity, R. Tilak, P. Paik. RSC Advances, 2022 12, 1105-1120 (DOI https://doi.org/10.1039/D1RA07594B)

C. Presentation in conferences:

- 5. Monica Pandey, Presented (Poster) in "NanoSciTech", November 8-10, 2017, Chandigarh, India.
- Monica Pandey, Presented (Poster) in "ICN-2019", April 12-14, 2019, 6. Kottayam, India. (Best Poster Award)
- 7. Monica Pandey, Presented (Poster) in "ICAFNM- 2020", Kharagpur, India.
- 8. Monica Pandey, Presented (Pos er) in "(lcbr-2020)", February 27-29, 2020, Varanasi, India.

Further, the student has passed the following courses towards the fulfillment of the coursework required for the Ph.D.

Course	Name	Credits	Pass/Fail
Code			
MT-453	Materials Characterization	4	Pass
MT-452	Materials Modelling	4	Pass
MT-454	Materials Processing and Characterization	4	Pass
	Laboratory	•	1 400
MT-455	Seminar	2	Pass
MT-451	Diffusion and Phase Kinetics and Phase	4	Pass
WH 1-451	Transformations	•	1 433
MT-474	Surface Engineering	4	Pass
MT-460	Nano Biotechnology	4	Pass
MT-601	Research Methodology	4	Pass

Supervisors:

Dr. Pradin Paik,

Associate Professor,

Prof. Dibaker Das.

Prof. Centre for Advanced Studies in

School of Engineering Electronics Science & Technology Sciences and Technology,

School of Physics, University of Hyderabad HYDERABAD-500 046. Telangana, India.

Prof. Dibakar Das

School of Engineering Sciences and Technology University of Hyderabad, Hyderabad 500 046.

Declaration

I, Monica Pandey hereby declare that the work reported in this Ph.D. dissertation entitled: "METAL-METAL OXIDE NANOCOMPOSITES: SYNTHESIS, CHARACTERIZATION AND ANTIMICROBIAL ACTIVITIES" submitted to University of Hyderabad for the award of Doctor of Philosophy in Materials Engineering is original and has been carried out by me during my tenure as a Ph.D. scholar under the supervision of Dr. Pradip Paik, Associate Professor presently at IIT-BHU and Prof. M. Ghanashyam Krishna, Professor at the University of Hyderabad, INDIA. This dissertation has not been submitted in any form for the award of any degree, diploma, membership, or similar title of any University or Institution. Finally, the plagiarism of this dissertation has been checked and satisfied the requirements.

MONICA PANDEY

15ETPM03

University of Hyderabad,

Hyderabad-500046,

INDIA

Plagiarism-free statement

This is to certify that the thesis titled Metal-Metal Oxide Nanocomposites: Synthesis, Characterization and Antimicrobial Activities" has been screened by the Turnitin software at the Indira Gandhi Memorial Library of the University of Hyderabad. The software shows a 43% similarity index, out of which 39% came from the candidate's own research articles related to this thesis, which are already published and available online. Thus, the effective similarity index excluding her research articles is 43%-39%= 4%, which is lower than the 10% stipulated by the university guidelines. Therefore, this thesis is free from plagiarism.

M Manashyam . Prof. M.G. Krishna,

Prof. M. GHANASHYAM KRISHNA Supervisor

Electron.

School of Physics, University of myes adad HYDERABAD-500 046. Telangana, India.

ACKNOWLEDGEMENT

This is going to be long. Sit back and enjoy your tea as you read this. It has been a long journey- but it was worth it. I am grateful for everyone who has continuously supported, assisted and encouraged me throughout this time. There were instances when I wondered whether I would even see this day but the amount of support I received made me hopeful every time I doubted myself.

First and foremost, I am thankful to my research supervisors, Dr. Pradip Paik and Prof. Ghanashyam Krishna. Dr. Pradip Paik motivated me to improve at each instances and one of the biggest lesson that I've learnt from him is that whatever happens we will reach at a point where we started and never below it. So each time something failed, these words kept me going forward. I am grateful that Prof. M. Ghanashyam Krishna was there to always give some assurances, feedback, and motivation when I needed it the most.

I am also thankful to the Dean of the School (SEST), Prof. Dibaker Das who gave that much needed push during many instances and extended his support throughout. I am thankful to my doctoral review committee member Dr. Swati G. Acharyya (SEST) and all the faculties of SEST especially Prof. Srikanth and Prof. Koteswara Rao who have been very supportive over the last several years and have extended their constant motivation on several occasions.

I am fortunate enough to have had the opportunity to collaborate my research work with Dr. Bindu M. Reddy, faculty from the School of Life Science and Dr. Ragini Tilak, Medical Practitioner at Institute of Medical Science, B.H.U, Varanasi, U.P. I would take this occasion to also thank Dr. Monika Singh, Ms. Kirti Wasnik, Ms. Shubhra Gupta, Ms. Sukanya Patra and all the other scholars from the school of Biomedical Engineering, IIT-BHU who have helped me to execute the collaborative work during my research.

I would like to thank Dr. R.K Rana (Scientist IICT, Hyderabad) who extended support for XPS facility and Dr. Reena Goyal (RA, IIT-Roorkee) for her encouragement from time to time.

I would also like to thank the technicians and non-teaching staff of SEST, Centre for Nanotechnology and Central Instrument Laboratory and Technical staff at CNF, CIL and SEST- Mr. Pankaj for TEM imaging, Mr. Sathish for TGA and others who helped to collect data directly or indirectly.

I am also grateful to Ms. Neha Chalottra, Dr. Koushi, Dr. Naveen and Ms. Rutuparna (SLS) for their technical inputs at various instances. I am also grateful to my seniors, lab mates, and friends for their constant encouragement, cooperation, and support during my Ph.D.

I would like to thank my parents- Sh. Eak Nath Pandey and Smt. Tika Devi Pandey, Younita, my sibling and my friends Dipendra and Neha for their constant support, belief and especially for being with me during my lowest phases. My sisters: Suprabha, Neelam, Anjali, and Seema who are also my cheerleaders. Friends- Anusha, Divya, Debasrita, Himadri, Naveen, Ranjeeta, Somedutta and others including M.Tech. (2015 Batch) who helped me stand up twice.

I am grateful to my school friends, family, cousin Vikash and few others for constantly checking on me and listening.

I am also thankful to the funding agencies-UGC non net and CSIR for the financial support.

And lastly I will forever be grateful for all the blessing from the Almighty.

Thanks to all

Monica Pandey

LIST OF PATENT APPLICATIONS FILED/ PUBLICATIONS/ CONFERENCES

Patent Filed:

- [1] A mesoporous anti-microbial nanocomposite and a method of preparation thereof.

 Indian Patent Application No.: 202011031802, dated: July 24, 2020
- [2] A nanomaterial based antimicrobial composition and a method of preparation thereof Indian Patent Application no.: 202011017968, dated: April 27, 2020

Publications:

- [3] Targeted and Enhanced Antimicrobial Inhibition of Mesoporous ZnO-Ag₂O/Ag, ZnO-CuO, and ZnO-SnO₂ Composite Nanoparticles, **Monica Pandey**, Monika Singh, Kirti Wasnik, et. al, *ACS Omega* 2021 *6* (47), 31615-31631 **DOI:** 10.1021/acsomega.1c04139
- [4] Target specific inhibition of bacterial and Candida species by mesoporous Ag/Sn-SnO₂ composite nanoparticles: in silico and in vitro investigation, Monica Pandey, Kirti Wasnik, Shubhra Gupta, et. al, RSC Advances 2022,12, 1105-1120 DOI: 10.1039/D1RA07594B
- [5] Monica Pandey, Pradip Paik "Finding an alternative to Ag Nanocomposite by comparative antimicrobial activity with CuO-Ag and CuO-SnO₂" (Manuscript for submission)
- [6] Monica Pandey, Pradip Paik "Surfactant free synthesis of tri-metal NPs and their effective antimicrobial activities". (*Manuscript for preparation*)
- [7] Monica Pandey, Pradip Paik "An attempt to synthesize quaternary composite Nanomaterials for its antimicrobial activities" (*Manuscript for submission*)

Presentation and Conferences

- [8] Monica Pandey, "Mixed Metal Oxide Nanoparticles for Antibacterial Studies" Presented (Poster) in NanoSciTech, November 9-10, 2017, Panjab University, Chandigarh, Punjab, India.
- [9] Monica Pandey and Dr. Pradip Paik entitled "Surfactant free synthesis of Novel Zinc oxide and Copper Oxide Nanoparticles and the relative antibacterial activities".

 Presented (Poster) in Fourth International Conference on Nanomaterials:

 Synthesis, Characterization and Applications (ICN 2019), April 12-14, 2019, MG

 University, Kerala, India. (BEST POSTER)
- [10] Monica Pandey and Dr. Pradip Paik, "CuO-ZnO Nanoparticles: an antibiotic free system to arrest bacteria pathogen".
 Presented (Poster) in International Conference on Functional Nanomaterials (ICAFNM- 2020), January, 6-8, 2020, IIT Kharagpur, WB, India.
- [11] Monica Pandey and Dr. Pradip Paik, "Inorganic Metal Oxide Nanoparticles of Copper Oxide and Zinc Oxide for antibacterial activity in E. coli".

 Presented (Poster) in Indo-Us Conference on Bioengineering & Regenerative Medicine (Icbr-2020), February 27-29, 2020, IIT-BHU, Varanasi, India.

Abstract

Nanomaterials have been explored for various biological uses due to their immense potential one of which is their use as an antimicrobial component. There has been constant research to find suitable antibiotic drugs. Metal and metal oxide such as Cu and Ag are in use for a long time due to their antibacterial properties. Currently, nanoparticles based on polymer, metal, metal oxide, etc. are gaining momentum for use in this field. NPs like ZnO (zinc oxide), Graphene oxide, CuO (copper oxide), chitosan, SnO₂ (tin oxide), TiO₂ (Titanium oxide), Ag₂O (silver oxide), etc. have been reported and used for their antimicrobial properties. However, out of all these metallic/metal oxides NPs have unique properties and have been seen to interact with the thiol group of enzymes which inactivates the cellular activities of the proteins. It is also seen that the oxide nanoparticles felicitates the generation of reactive oxygen species which is said to be the reason behind their mechanism of action against the microbes. These NPs however mostly are synthesized by using a capping agent/surfactant for stability which sometimes hinders their efficiency, increases cost and synthesis time. Thus, developing colloidal stable NPs without using surfactant is also important and challengeable.

Moreover, India and many developing countries in the world are facing an acute crisis due to the growing concern over antimicrobial resistance (AMR). India is also one of the highest consumers of antibiotics in the world and has one of the highest Tuberculosis patients in the world. Thus, finding solutions to this problem is even more important for a country like India.

This dissertation focuses on the synthesis of metal and metal oxide nano-composite materials without the use of surfactant/capping agent by chemical reduction method, studies its properties by various characterization techniques, and finally understands their antimicrobial activity. It also tries to understand the mechanism behind the microbial activity via docking technique in some parts.

The dissertation starts with the introduction section which clearly defines the background, motivation, significance, and objective behind the work. This is followed by the materials and methods chapter which outlines the precursors used, microbial strains used, synthesis procedure, and the description of the microbial tests adopted. The third chapter describes the results and discussions which are divided into five parts. The final chapter summarizes the major findings and finally concludes by giving a few suggestions on the future scope of this work.

Since ZnO nanoparticles are popularly used in various applications, the first part of the result and discussion focuses on the synthesis of bi-metallic oxide nanocomposite of ZnO-CuO, ZnO-Ag₂O/Ag, and ZnO-SnO₂ which is then compared to single ZnO for their antimicrobial activities. All the nanocomposite materials had an average particle size below 10 nm. Further, a docking technique was used to find the binding energy of the nanocomposite in different proteins. This showed that ZnO-Ag₂O/Ag had the lowest binding energy efficiency and the in-vitro results coincided with the docking results. The mechanism of action studied showed that the even lower band gap energy favors the antibacterial efficiency.

Similarly, SnO₂ NPs are gaining momentum as an antimicrobial agent so in this section of results and discussions; the Ag-SnO₂/Sn nanocomposite was synthesized. The TEM image showed the average particle size is around 8 nm. The docking technique showed the same binding energy of the nanocomposite for all the strains. However, the in-vitro disk diffusion technique showed that the zone of inhibition was better for *C. albicans*. To further understand this difference, a different protein (Hsp90) was used in the docking tool and the mechanism has been discussed elaborately.

Since Ag is one of the most widely used NPs for antimicrobial activity; its overuse has again become a concern. Few reports of bacteria gaining resistance to Ag nanoparticles are also seen. To address this issue, CuO-SnO₂/Sn nanocomposite was synthesized as an alternative to Ag nanoparticles and the CuO-Ag/AgO was also synthesized to understand the comparative study in different strains. From the in-vitro studies in gram positive strains, we could see similar results for CuO-Ag/AgO and CuO-SnO₂/Sn. Further in the LB broth technique, we saw some resistance after a certain time. These results motivate making Sn/SnO₂ an alternative to Ag if it is further studied upon.

Since bi-metallic nanocomposites showed great results and improved MIC values compared to many existing results, tri-metallic composites were synthesized and their properties were studied. The specific surface area, pore width, etc. improved. We could also see from the TEM the average particles size had increased except for CuO-SnO₂-ZnO nanocomposite. Further, the antimicrobial results showed similar results to the bi-metallic nanocomposites.

In the final part of the third chapter, quaternary nanocomposite was synthesized and the TEM results, showed the average particle size was around 10 nm which is similar to bi-metal oxide nanocomposite and lower than the tri-metal oxide composite. The specific surface area however had increased and this might be due to the synergistic effect of the metal oxide complex that formed. Further, the antimicrobial efficiency had also improved and in fact, for *A. baumannii* which is under critical priority risk it showed the highest zone of inhibition and this result does give some hope for the future of antibiotic materials.

Contents

Acknowledgementv	
Abstractix	
List of Figuresxviii	
List of Tablesxxvii	
CHAPTER 1: Introduction and Literature Review	1
1.1 Introduction	
1.1.1 Basic concept of Nanotechnology and Nanomaterials	
1.1.2 Different types of Nanomaterials	
1.1.3 Different Synthesis approaches of NMs	
1.1.4 Basic concept of Antimicrobial Resistant (AMR) and its importance 4	
1.1.5 Antimicrobial Materials	
1.1.6 Importance of nanomaterial as an antimicrobial agent	
1.1.7 Types of antimicrobial Materials and their basic importances in the field of	
study	
1.2 Literature Review	
1.2.1 Various metals NPs as antimicrobial Agents	
1.3 The choice of the Synthesis Route:	
1.4 Choice of reducing agent:	
1.5 Different Antimicrobial Mechanisms and their justification	

1.6 The motivation behind the work:	
1.7 Objectives of this work:	
CHAPTER 2: Materials, Methods of synthesis and Characterization Techniques	31
2.1 Materials	
2.2 Methods of preparation	
2.2.1 Synthesis procedure	
2.2.2 Preparation of Phosphate Buffer Solution (PB) and Phosphate Buffer Saline	
(PBS)33	
2.3 Antibacterial evaluation techniques	
2.3.1 Disk Diffusion method	
2.3.2 Calculation of Minimum inhibitory concentration:	
2.3.3 Luria Bertani (LB) Broth Dilution Method:	
2.4 Physiochemical Characterizations Techniques	
2.4.1 X-Ray Diffraction	
2.4.2 UV-Vis absorption spectroscopy	
2.4.3 Transmission Electron Microscopy (TEM)	
2.4.4 Dynamic Light Scattering (DLS) and Zeta Potential	
2.4.5 Brunauer-Emmett-Teller (BET) Specific Surface Area	
2.4.6 Thermogravimetric analysis (TGA) and Differential Scanning Calorimetry	
(DSC)40	

2.4.7 X-ray Photoelectron Spectroscopy (XPS)	41
2.4.8 Fourier Transform Infra-red Spectroscopy (FT-IR)	42
2.5 Time scale dissolution and stability Studies	42
2.5.1 Time scale Zeta study	42
2.5.2 Time scale dissolution study through DLS:	43
CHAPTER 3: Results and Discussions	44
3.1 Targeted and Enhanced Antimicrobial Inhibition of mesoporous ZnO-Ag ₂ O/A	ng,
ZnO-CuO and ZnO-SnO ₂ composite nanoparticles	45
3.1.1 Abstract	45
3.1.2 Introduction	46
3.1.3 Experimental	50
3.1.4 Results and Discussions	53
3.1.5 Conclusions for this part	84
3.2 Target specific inhibition of bacterial and Candida species by mesoporous Ag/S	h-
SnO ₂ composite nanoparticles: in silico and in vitro investigation	86
3.2.1 Abstract:	86
3.2.2 Introduction:	87
3.2.3 Methodology	91
3.2.4 Results and Discussions:	93
3.2.5 Conclusions for this part:	19

3.3 Preparation of CuO-Sn/SnO ₂ and CuO-Ag/AgO nanocomposites and	d their
comparative Antimicrobial activity	121
3.3.1 Abstract	121
3.3.2 Introduction:	121
3.3.3 Methodology:	124
3.3.4 Results and Discussions	124
3.3.5 Conclusions for this part:	139
3.4 Synthesis and characterization of ternary metal oxide nanoparticles and the	neir in-
vitro antimicrobial studies	140
3.4.1 Abstract	140
3.4.2 Introduction	140
3.4.3 Methodology	141
3.4.4 Results and Discussions	143
3.4.5 Conclusions for this part:	160
3.5 PART V: An attempt to synthesize quaternary metal oxide nanocompos	ite and
study its antibacterial activity	161
3.5.1 Abstract	161
3.5.2 Introduction	161
3.5.3 Methods	163
3.5.4 Results and Discussions	164

3.5.5	5 Conclusions for this part:	176
CHAPTI	ER 4: Summary and Conclusions	177
4.1 Su	mmary	177
4.1.1	1 Chapter 1	177
4.1.2	2 Chapter 2	177
4.1.3	3 Chapter 3	178
4.2 Co	onclusions and future aspects of this work	182
5.	Appendix	184
6.	Bibliography	195

List of Figures:

Figure 1.1 Different uses of Nanomaterials
Figure 1.2: Classification of Nanomaterials
Figure 1.3: Classification of functional Nanomaterials
Figure 1.4: Different synthesis routes of Nanoparticles
Figure 1.5: WHO reported Antimicrobial priority list
Figure 1.6: Figure shows the year wise novel antimicrobial drugs approved by FDA 7
Figure 1.7: Different possible mechanisms in which nanomaterials can affect the various
micro-organism
Figure 1.8: Different types of metal-based nanoparticles
Figure 1.9: Representation of steps of contact killing mechanism of Cu proposed by
Grass et. al
Figure 1.10: Potential risk sites of NAg/Ag in the human body. This is mainly due to the
bioavailablity of Ag. The Ag species from Ag NPs products release, absorb, accumulate
Ag which increases the Ag bioavailability
Figure 1.11: Various mechanisms of antibacterials activity using metal-based
nanoparticles. 27
Figure 2.1: Schematic representation of Synthesis Procedure
Figure 3.1: HRTEM micrographs for (a) ZnO, (b) ZnO-CuO, (c) ZnO-Ag ₂ O/Ag, and (d)
ZnO-SnO ₂ : SAED pattern for (e) ZnO: (f) ZnO-CuO, (g) ZnO-Ag ₂ O/Ag, and (h) ZnO-

SnO_2 ; and d- spacing for (i) ZnO , (j) ZnO -CuO, (k) ZnO -Ag $_2O$ /Ag, and (l) ZnO - SnO_2 .
53
Figure 3.2: UV-Vis spectra of composite NPs: (a) ZnO NPs, (b) ZnO-CuO NPs, (c) ZnO-
SnO ₂ NPs and (d) ZnO-Ag ₂ O/Ag NPs
Figure 3.3: EDS spectrum of: (a) ZnO, (b) ZnO-CuO, (c) ZnO-SnO ₂ and (d) ZnO-
Ag/Ag ₂ O
Figure 3.4: Calculation of band gap (Eg) for different samples, of (a) ZnO (Z); (b)
$ZnO\text{-}CuO(CZ)\text{; }(c)ZnO\text{-}Ag/Ag_2O(AZ)and(d)ZnO\text{-}SnO_2(SZ)\text{.} \dots \\ \hspace{1.5cm} 57$
Figure 3.5: Shows the FTIR spectra for the materials
Figure 3.6: XRD patterns of (a) ZnO (b) ZnO-CuO (c) ZnO-SnO $_2$ (d) ZnO-Ag $_2$ O/Ag
NPs
Figure 3.7. BET surface area analysis results: N ₂ adsorption-desorption isotherm plots of
(a) ZnO (Z); (b) ZnO-SnO $_2$ (SZ); (c) ZnO-CuO (CZ); and (d) ZnO-Ag $_2$ O/Ag (AZ). Inset
represents the pore size distribution results calculated from the BJH desorption pore
volume data for the respective sample
Figure 3.8: Shows TGA results for Z (ZnO), CZ (ZnO-CuO), SZ (ZnO-SnO $_2$), and AZ
(ZnO-Ag ₂ O/Ag. Experiments performed in N ₂ gas environment
Figure 3.9:DSC of (a) ZnO; (b) ZnO-CuO; (c) ZnO-SnO $_2$; and (d) ZnO-Ag/Ag $_2$ O
Nanoparticle system. 64
Figure 3.10: XPS spectra of (a) full range for ZnO-CuO; (b) Zn $2p_{3/2}$ of ZnO-CuO; (c) Cu
$2p_{3/2}$ of ZnO-CuO. Fig.(d),the full range spectra for ZnO-SnO ₂ ; (e) Zn $2p_{3/2}$ of ZnO-
SnO_2 ; and (f) Sn 3d of ZnO - SnO_2 . Fig. (g) shows the full range spectra for ZnO -
$Ag_2O/Ag; (h)\ Zn\ 2p_{3/2}\ of\ ZnO-\ Ag_2O/Ag\ and\ (i)Ag\ 3d\ of\ ZnO-Ag_2O/Ag\$

Figure 3.11: Show molecular interactions of bacterial/fungal proteins with NPs. A and B are the crystal structure of PqsR and RstA (BmfR) (ribbon structure), respectively. A.1, A.2, A.3, A.4, and A.5 (upward) showed PqsR interactions and hydrogen bonding (green thin line with distance) with ligand ZnO (Zn -Blue), CuO (Cu-peach), ZnO-CuO, ZnO-SnO₂ (Sn-lime green) ZnO-Ag₂O (Ag-Coral), respectively. B.1, B.2, B.3 B.4 and B.5 Crystal structure BmfR interacted with ligands such as ZnO (Zn -Blue), CuO (Cupeach), ZnO-CuO, ZnO-SnO₂ (Sn-lime green), and ZnO-Ag₂O (Ag-Coral), respectively. Downward figures represent the interacting residues of amino acids of active pocket and Figure 3.12: Molecular interactions of bacterial/fungal proteins with NPs. C and D represented the crystal structures of FosA and Hsp90 (ribbon structure), respectively. C.1, C.2, C.3, C.4 and C.5 (upward) showed FosA interactions and hydrogen bonding (green thin line with distance) with ligand ZnO (Zn -Blue), CuO (Cu- peach), ZnO-CuO, ZnO-SnO₂ (Sn-lime green) and ZnO-Ag₂O (Ag-Coral), respectively. D.1, D.2, D.3 D.4, and D.5. Crystal structure Hsp90 interacted with ligand ZnO (Zn -Blue), CuO (Cu- peach), ZnO-CuO, ZnO-SnO₂ (Sn-lime green) ZnO-Ag₂O (Ag-Coral), and oxygen (red), respectively. Downwards figures represented the interacting residues of amino acids of Figure 3.13: Antibacterial activity results of (Z) ZnO, SZ (ZnO-SnO₂) CZ (ZnO-CuO), Figure 3.14: Antibacterial activity of (Z) ZnO, SZ (ZnO-SnO₂) CZ (ZnO-CuO), and AZ

Figure 3.15: ZOI results obtained for (a) A. baumannii (b) P. aeruginosa (c) C. albicans
and (d) K. pneumoniae. '1', '2', '3', and '5' labels used for the (Z) ZnO, CZ (ZnO-CuO),
SZ (ZnO-SnO ₂), and AZ (ZnO-AgO ₂ /Ag), respectively
Figure 3.16: Bar plot representation of ZOI in different strains obtained using different
metal oxide composite NPs (*P<0.05, **P<0.01, and ***P<0.001)
Figure 3.17: Schematic representation shows the change in the band energy gap for
different composite NP systems and the mechanism involved in the bacterial cell wall
damage through the ROS generation and responsible for the MIC (Table 3.2)
Figure 3.18: (a,b,c, and d) HRTEM micrograph of the Ag-Sn/SnO ₂ composite
nanoparticles obtained from lower to higher magnification, (f) HRTEM image of the Ag-
Sn/SnO ₂ NPs at different positions showing the presence of elemental Ag and Sn/SnO ₂ in
the composite nanoparticle; Fig. (e,g) cross-section/IFFT images obtained from the
HRTEM image for SnO_2 and Ag (e) and for Ag (g) ; (h) SAED pattern of $Ag/Sn-SnO_2$
composite nanoparticles
Figure 3.19: EDS spectra shows the weight percentage of different elements present in
the Ag/Sn-SnO ₂ nanoparticle composite system
Figure 3.20: (a) Powder XRD pattern of the Ag-Sn/SnO ₂ composite nanoparticles; (b)
UV-Vis spectrum of Ag/Sn-SnO ₂ nanoparticles and the inset shows the Tacu plot for
Band gap energy calculation of Ag-Sn/SnO ₂ ; (c) Shows the TGA results of Ag-Sn/SnO ₂
composite nanoparticles (d) DSC thermogram of Ag-Sn/SnO ₂ composite nanoparticles. 97
Figure 3.21:(a) Shows the BET surface area analysis results. N_2 adsorption-desorption
isotherm of Ag-Sn/SnO ₂ nanocomposite particles and the inset shows the BJH pore size

distribution results obtained from the desorption isotherm; (b) FTIR spectrum of Ag/Sn-
SnO ₂ nanoparticles.
Figure 3.22: Shows (a) full-scale XPS spectrum acquired of Ag-Sn/SnO ₂ , (b) XPS
spectrum acquired for Ag 3d; (c) XPS spectrum acquired for O ₂ 1s; and (d) XPS spectrum
acquired for Sn 3d
Figure 3.23: Show the nanoparticles-protein interactions. A): Ag nanoparticles-protein
interactions, B): SnO ₂ nanoparticle- protein interactions. 1, 2, 3, 4, and 5 are the different
crystal structures of molecular protein targets Lpfd, RstA, FosA, PqsR, and Als3 of
E.coli, A. baumannii, k. pneumoniae, P. aeruginosa, and C. albicans, respectively. (Ag-
Coral), (Sn-lime green)
Figure 3.24: Shows the nanoparticle-protein interactions. C: Ag-Sn/SnO ₂ nanoparticles-
protein interactions, 1,2,3,4 and 5, are the crystal structures of molecular protein target
Lpfd, RstA, FosA, PqsR, and Als3 of E.coli, A. baumannii, K. pneumoniae, P.
aeruginosa, and C. albicans, respectively. (Ag-Coral), (Sn-lime green)
Figure 3.25: Results show the antibacterial activity of (a) Ag/Sn-SnO ₂ composite NPs; (b)
Sn/SnO ₂ NPs alone and (c) AgNPs alone in E. coli bacterium obtained by Luria broth
technique; (d) comparative antibacterial activity results calculated from the zone of
inhibition study for Ag NPs, Sn/SnO_2 NPs and for the Ag $-Sn/SnO_2$ composite NPs in
different strains. *P<0.05, **P<0.01, ***P<0.001
Figure 3.26: Results show the antibacterial activity for (a) Ag/Sn-SnO2 NPs composite
system. (b) for Ag NPs alone and (c) for Sn/SnO2 NPs alone in E. coli bacterium by
Luria broth technique

Figure 3.27: Results show the zone of inhibition for (a) Ag-Sn/SnO ₂ composite NPs in C.
albicans; (b) Ag-Sn/SnO2NPs in E. coli; (c) Ag NPs alone (marked as "A") and Sn/SnO2 $$
NPs alone (marked as "S") in C. albicans; (d) Ag NPs alone (marked as "A") and
Sn/SnO ₂ (S) in A. baumannii; and (e) comparative zone of inhibition results obtained for
different microbes against Ag NPs, Sn/SnO ₂ NPs and for Ag -Sn/SnO ₂ composite NPs.
*P<0.05, **P<0.01, ***P<0.001
Figure 3.28: Schematic representation for the inhibition of Candida
Figure 3.29: Shows the molecular interactions associated with molecular target proteins
of C. albicans and Ag/Sn-SnO ₂ NPs. (a), (b), and (c), represent the crystal structures of
Als3, Hsp90, and Cyp51, respectively. The upper part of each panel represents the full
ribbon structure of the protein interacted with nanoparticles while the lower panel shows
the corresponding interaction with amino acid residues and Ag/Sn-SnO ₂ nanoparticles.
Figure 3.30: TEM images of (a-c) CuO/Ag-AgO nanocomposites; (d) SAED pattern of
CuO/Ag-AgO composites nanoparticles; (e-f) TEM image of CuO/Sn-SnO ₂
nanocomposites; (g) HRTEM image showing d-spacing of CuO in CuO/ $Sn-SnO_2$
composite nanoparticles and (h) SAED pattern of CuO/ Sn - SnO_2 nanocomposite 125
Figure 3.31: XRD patterns of (a) CuO/Sn-SnO ₂ nanocomposite (b) CuO-Ag/AgO
nanocomposite. 126
Figure 3.32: EDS spectra of (a) CuO-Ag/AgO nanocomposite and (b)CuO-Sn/SnO ₂
nonocomposito 127

Figure 3.33: Shows (a) Full XPS spectra of CuO-Ag/AgO nanocomposite (inset:
expanded form); (b) Cu 2p spectra of CuO-Ag/AgO nanocomposite and (c) Ag 3d spectra
of CuO-Ag/AgO nanocomposite
Figure 3.34: Shows (a) Full XPS spectra of CuO-Sn/SnO ₂ nanocomposite; (b) Cu 2p
spectra and (c) Sn 3d for CuO-Sn/SnO ₂ nanocomposite
Figure 3.35: BET Curves of (a) CuO-Ag/AgO nanocomposite and (b) CuO-Sn/SnO $_2$
nanocomposite and inset pore size distribution curve
Figure 3.36: UV-Vis spectroscopy of: (a) CuO-Ag/AgO nanocomposites; (c) CuO-
Sn/SnO ₂ nanocomposites; Band gap energy of the (b) CuO-Ag/AgO composite
nanoparticles; (d) CuO-Sn/SnO ₂ nanocomposite
Figure 3.37: TGA Curves of (a) CuO-Ag/AgO nanocomposite (b)CuO/Sn-SnO ₂
nanocomposite and DSC curve of (c) CuO-Ag/AgO nanocomposite; (d) CuO/Sn-SnO ₂
nanocomposite. 133
Figure 3.38: The Zone of Inhibition of (2a) CuO-Ag/AgO NCs; (2c) CuO-Sn/SnO ₂ NCs
and (c) CuO NPs
Figure 3.39: Growth Kinetics study in E. coli bacteria (a) CuO-Ag/AgO Nanocomposite;
(b) CuO-Sn/SnO ₂ Nanocomposite and (c) CuO Nanoparticles
Figure 3.40: Probable mechanism of the composite system of CuO-Ag/AgO and CuO-
Sn/SnO ₂ for the killing of the microbes.
Figure 3.41: TEM image of: (a-b) SAZ, (e-f) ACZ, (i-j) CSZ and (m-n) ACS; HR-TEM
image of: (c) ASZ, (g) ACZ, (k) SAZ and (o) ACS; SAED pattern of: (d) SAZ; (h) ACZ;
(l) CSZ and (p) ACS

Figure 3.42: Particle size distribution of (a) ACS nanocomposite; (b) ACZ
nanocomposite; (c) SAZ nanocomposite and (d) CSZ nanocomposite 145
Figure 3.43: XRD patterns of (a) Ag-CuO-ZnO (ACZ), (b) Ag-CuO-SnO ₂ (ACS), (c)
SnO_2 – Ag - ZnO (SAZ) and (d) CuO- SnO_2 - ZnO (CSZ) nanocomposites
Figure 3.44: (a) FTIR of tri metal oxide nanocomposites: CuO/SnO ₂ /ZnO (CSZ);
$Ag/CuO/ZnO\;(ACZ);\;SnO_2/Ag/ZnO\;(SAZ)\;and\;Ag/CuO/SnO_2\;(ACS);\;(b)\;UV-Vis\;of\;the\; ag/CuO/SnO_2\;(ACS);\;(c)\;UV-Vis\;of\;the\; ag/CuO/SnO_2\;(ACS)\;(c)\;UV-Vis\;of\;the\; ag/CuO/SnO_2\;(ACS)\;(c)\;UV-Vis\;of\;the\; ag/CuO/SnO_2\;(ACS)\;(c)\;UV-Vis\;of\;the\; ag/CuO/SnO_2\;(C)\;UV-Vis\;of\;the\; ag/CuO/SnO_2\;UV-Vis\;of\;the\; ag/CuO/SnO_2\;UV-Vis\;of\;the\; ag/CuO/SnO_2\;UV-Vis\;of\;the\; ag/CuO/SnO_2\;UV-Vis\;of\;the\; ag/CuO/SnO_2\;UV-Vis\;of\;the\; ag/CuO/SnO_2\;UV-Vis\;of\;the\; ag/CuO/SnO_2\;UV-V$
different nanocomposites
Figure 3.45:BET surface area results of :(a) ACZ, (b) SAZ, (c) ACS, (d) CSZ and inset
pore size distribution curve. 149
Figure 3.46: TGA of: (CSZ) CuO-SnO ₂ -ZnO; (ACZ) Ag-CuO-ZnO, (SAZ) SnO ₂ -Ag-
ZnO, and (ACS) Ag-CuO-SnO ₂ nanocomposites
Figure 3.47: DSC profile of (a) CuO-SnO ₂ -ZnO (CSZ), (b) Ag-CuO-ZnO (ACZ), (c)
SnO ₂ -Ag-ZnO (SAZ), (d) Ag-CuO- SnO ₂ (ACS) nanocomposite
Figure 3.48: Full XPS spectra of (a) Ag-CuO-SnO ₂ (ACS) nanocomposite; (e) SnO ₂ -Ag-
ZnO (SAZ) nanocomposite; (i) SnO ₂ -CuO-ZnO (CSZ) nanocomposite; (m) Ag-CuO-
ZnO (ACZ) nanocomposite; XPS spectra of: ACS (b) Cu 2p, (c) Sn 3d, (d) Ag 3d; SAZ
(f) Zn 2p, (g) Ag 3d, (h) Sn 3d; CSZ (j)Zn 2p, (k)Cu 2p, (l) Sn 3d; ACZ (n) Zn 2p, (o) Ag
3d, and (p) Cu 2p
Figure 3.49: Growth kinetics of E. coli (DH5α) in different concentrations of (a) Ag-
CuO-ZnO nanocomposite; (b) SnO ₂ -Ag-ZnO nanocomposite; (c) CuO- SnO ₂ -ZnO
nanocomposites and (d) Ag-CuO- SnO2 nanocomposites. Values are represented as
mean+S.D (n=3)

Figure 3.50: Disk Diffusion method of 3a: Ag-CuO-ZnO nanocomposite; 3b: SnO ₂ -Ag-
ZnO nanocomposite; 3c: CuO-SnO ₂ -ZnO nanocomposites and 2d: Ag-CuO- SnO ₂
nanocomposites
Figure 3.51:TEM image (a-c) of Ag-CuO-ZnO- SnO ₂ nanocomposite material; (g) SAED
pattern of Ag-CuO-ZnO- SnO ₂ nanocomposite; (h-i) HR-TEM image of Ag-CuO-ZnO-
SnO ₂ nanocomposite and inset (c) particle size distribution of the nanocomposite 165
Figure 3.52: XRD pattern of Ag-CuO-ZnO-SnO ₂ nanocomposite
Figure 3.53:(a) UV-Vis spectra of Ag-CuO-SnO ₂ -ZnO nanocomposite and inset Tauc
plot for band gap energy; (b) FTIR spectra of the nanocomposite
Figure 3.54: EDS spectroscopy of the nanocomposite representing the elemental
composition
Figure 3.55: N ₂ adsorption-desorption plot of the tetra oxide nanocomposite material. 169
Figure 3.56: (a) TGA curve Ag-CuO-SnO ₂ -ZnO nanocomposite; (b) DSC curve of the
Ag-CuO-SnO2-ZnO nanocomposite
Figure 3.57: XPS spectra of: (a) Full spectra of CuO-Ag-ZnO-SnO ₂ nanocomposite; (b)
Cu 2p; (c) Zn 2p; (d) Sn 3d, and (e) Ag 3d
Figure 3.58: (a) Growth kinetics in E. coli bacteria by LB broth technique. The plot is
expressed as a mean±SD (n=3); (b) Percentage of inhibition w.r.t. control at a different
time interval. P<0.0001
Figure 3.59: Disk Diffusion of (a) P. aeruginosa; (b) A. baumannii; (c) K. pneumoniae;
(d) C. albicans and (e) graphical representation of the zone of inhibition. ***P<0.0001,
**P<0.001

List of Tables:

Table 1.1: Summary of various composite materials developed for various applications 20
Table 2.1: List of chemicals and Reagents used in this Work
Table 2.2: List of microbial strains used
Table 3.1: Binding energy (kcal mol ⁻¹) and interaction parameters of NPs with interacting
proteins calculated from in silico study. It can be noted that the bold residues represent
active binding sites interacted with inhibitors reported on PDB and earlier publications.73
Table 3.2: MIC values obtained for different samples
Table 3.3: Results show the BET surface area analysis and average pore size distribution
for Ag NPs, Sn/SnO ₂ NPs and for Ag -Sn/SnO ₂ composite NPs
Table 3.4: Zeta Potential (mV) values of Ag-Sn/SnO ₂ NPs measured at different pH of
PBS and in saline solution
Table 3.5: Zeta size analyzed for Ag-Sn/SnO ₂ NPs at different pH of PBS and in the
Saline solution
Table 3.6 Shows the binding energy (kcal mol-1) and interaction parameters of Ag, SnO ₂ ,
and Ag-Sn/SnO ₂ NPs associated with different interacting molecular targets 105
Table 3.7: Show the minimum inhibitory concentration (MIC)
Table 3.8: Zone of inhibition results obtained for the different microbes
Table 3.9: Zone of inhibition values for different NPc composite
Table 3.10: BET surface area and pore size
Table 3.11: Zeta Potential values
Table 3.12: Minimum Inhibitory Constant (MIC) values
Table 3.13: Zone of inhibition (in mm) calculated via disk diffusion method

Table	3.14:	Percentage	of	inhibition	at	different	time	interval	with	diffe	rent
concen	trations	s w.r.t contro	l at t	that particul	lar tiı	ne		•••••			173
Table	4.1: zo	ne of inhibit	ion	and MIC	value	es of all t	he mat	erials syr	nthesize	ed in	this
dissert	ation		•••••								181

CHAPTER 1: Introduction and Literature Review

1.1 Introduction

1.1.1 Basic concept of Nanotechnology and Nanomaterials

When Nobel laureate Richard Feynman in 1959 said: "There's plenty of room at the Bottom", he might not have anticipated the extent Nanoscience and Nanotechnology would develop today. The term 'nanotechnology' was first used in 1974 by Norio Taniguchi who is a Japanese scientist. "Nano" come from a Greek word "nános" meaning dwarf. Nanoscience and its associated technology have a wide area of applications which have been shown in brief in Fig. 1.1.

The major part of Nanoscience and Technology covers the synthesis of nanomaterials and their different properties from their bulk or larger counterpart. Nanomaterials are the materials which have any of the dimensions (x, y or z) in the scale of 10⁻⁹. Now a days the nanotechnology covers all the areas- industrial to biomedical; to improve the efficiency of work with respect to their existing report of efficiencies.

1.1.2 Different types of Nanomaterials

Nanomaterials can be Carbon-based, Metals, inter-metallic compounds, polymers, composites, semiconductors, alloys etc. as enlisted in Fig.1.2. Further nanomaterials are classified as inorganic, organic and hybrid types. Organic NMs are majorly made up with matters such as C, H, O, S etc. Examples of nanomaterial are Fullerenes and Electrospun nanofibres. Carbon Nanotubes come under the organic category and cellulose,

dendrimers etc. comes under the polymer categories. All metal and metallic oxides such as Au, Ag, Cu, Pt, Ag₂O, SiO₂, ZnO, CuO, ZrO, SnO₂, etc. come under the inorganic categories. Functionalized NMs are another type of NMs which can be prepared for developing specific functional properties for specific usage. These can be classified as mentioned in Fig. 1.3.



Figure 1.1 Different uses of Nanomaterials.

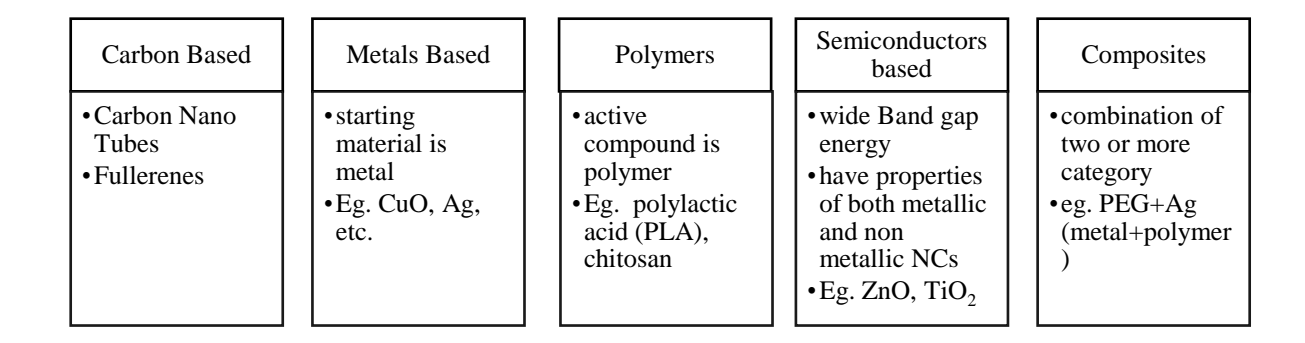


Figure 1.2: Classification of Nanomaterials²

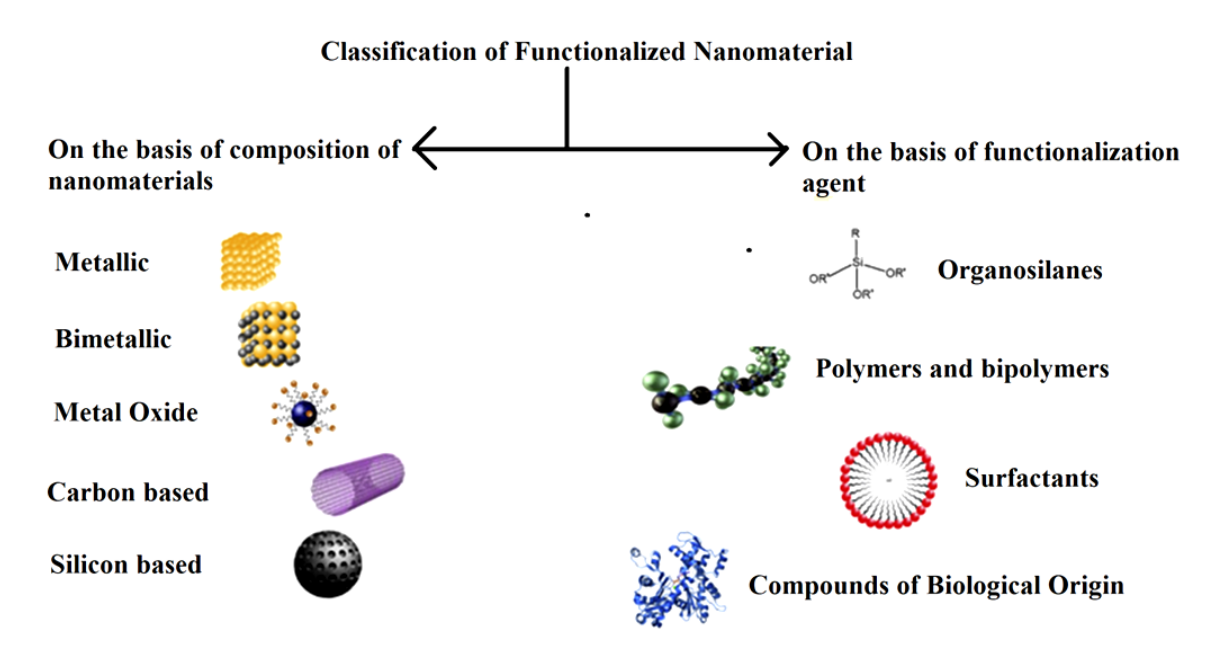


Figure 1.3: Classification of functional Nanomaterials. ³

1.1.3 Different Synthesis approaches of NMs

Nanomaterials can be synthesized via two defined approaches – bottom-up and top-down. Based on other process parameters such as reaction conditions, chemical properties and reactivity, approach and methods, etc. it further can be subdivided into

physical, biological, chemical, green-synthesis, etc.⁴⁻⁶ Briefly the different synthesis routes are enlisted in the Fig. 1.4.

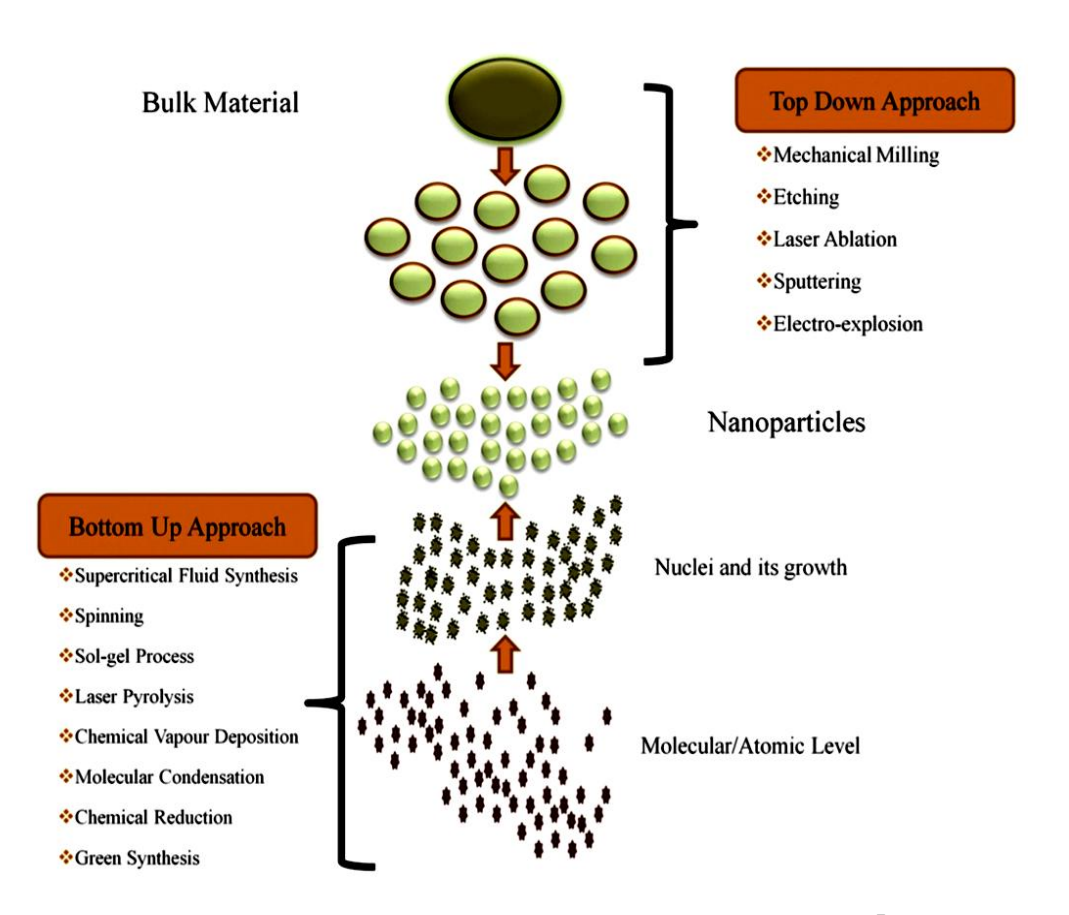


Figure 1.4: Different synthesis routes of Nanoparticles.⁷

1.1.4 Basic concept of Antimicrobial Resistant (AMR) and its importance

Nanotechnology has huge contributions to the biomedical fields and one such important area is the development of new antimicrobial materials apart from the conventional organic antibiotics. Antimicrobial-resistant of conventional antibiotics is one of the major problems in the 21st century. WHO reported that antimicrobial resistance is one of the severe public health concerns which demands immediate attention and thus

the requirement to develop new antibiotics.⁸ WHO also has reported that common infections such as Urinary Tract Infections, Sepsis, etc. are becoming resistant to the existing drugs and this is worrisome. A report on AMR also remarks that by 2050, there could be 10 million deaths only due to AMR and can drive 25 million people in to destitution by 2030.⁹ However, some reports contradict and question this information based on the sample size, data collection, methodology, etc.¹⁰ On 9th June 2021 WHO had reported on GLASS (Global Antimicrobial Resistance and Use Surveillance System) and raised alert on AMR for UTIs and other infectious diseases for many countries.^{11,12}

Irrespective of numbers, for a country like India particularly it is still awful news, because it has the highest cases of bacterial infections with respect to the other parts of the world. India already has a number of problems with several other microbial diseases including typhoid, TB, etc. and AMR is only adding to other social and economic challenges. In a series of data collected from some of the states, it was also found that children are resistant to first-line of antibiotics. ¹³ There is also an enzyme named after the capital city New Delhi (NDM 1) in 2008 and its severity for antibody resistance. Diksit et. al reviewed that since then many steps have been taken to prevent the issues related to this enzyme, yet it is still lacking in many ways like the data are not transparent, lack of coming up of new antibiotics, funding issues, implementations of recent health policies, lack of public awareness, etc.. ¹⁴ WHO has also prepared a priority list (Fig. 1.5) and according to that *A. baumannii*, *E. coli*, etc. are in critical priority list while *S. pneumonia* is in medium. ¹⁵

In a recent study conducted in a tertiary care hospital in Southern India with pediatric samples, it was found that while the cases of *A. baumannii* AMR patterns were

lower; for *E. coli*, *S. aureus*, etc. it was higher. Similarly, other studies conducted in India showed that the high ESBLs (Extended-spectrum beta-lactamases) and Enterobacteriaceae sp. influence on children is concerning. ESBL are those in which current antibiotics no longer work. A similar trend is found in many Asian countries like China, Malaysia, Vietnam, etc. and Mexico too. I Further, ICMR (Indian Council of Medical Research) also prepared data from Jan 2020-Dec, 2020 and found many resistances including fungal resistance has increased. The effective treatment for Tuberculosis has been improved with combination of drugs, however there is always a fear of resistance over the time and there is a need to develop the alternative therapy and drugs addition to the existing drugs.

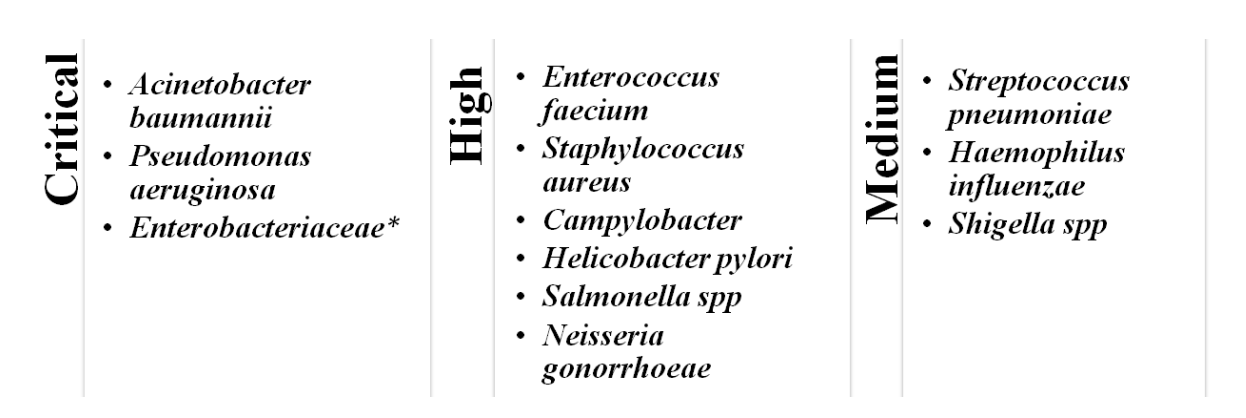


Figure 1.5: WHO reported Antimicrobial priority list.

Some studies reported a significant improvement in this field, however recent review highlights that the scenario is different for lower and middle-income based countries. ^{23–25} Nanomaterials have given hope in this aspect too. ²⁶

It can be noted that it can take around a decade to develop a new antibacterial drug and this is one of the shortest study period compared to the other studies due to the

availability of initial data, efficacy of data which could be generated early, etc. However, it is not as buttery as it should be due to the economical challenges and uncertainty of the use.²⁷We have seen a positive development in the past few years i.e. from 2018 onwards (Fig. 1.6).^{28–30} Yet, it is speculated that since most of these are modified from the existing ones, these drugs might soon be unable to deal with the growing concern of AMR. Also, it does not deal with the critical concern strains like *A. baumannii* and *P. aeruginosa*.^{31,32}

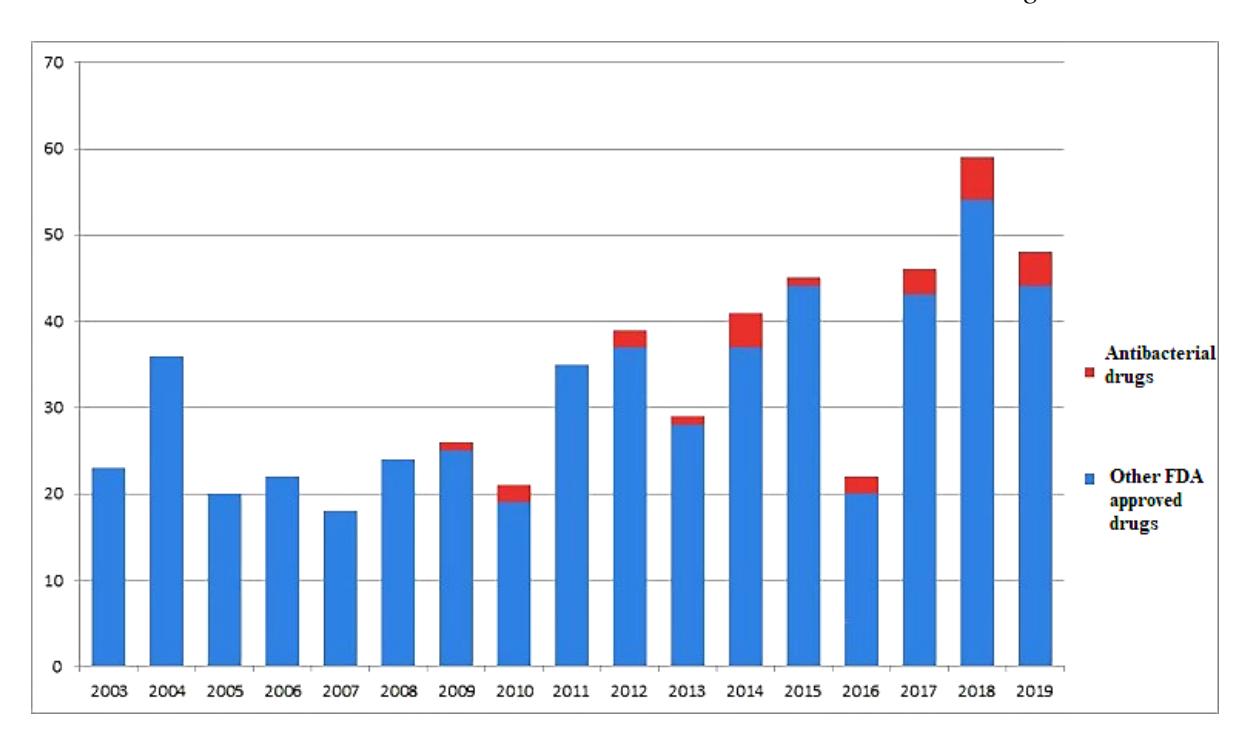


Figure 1.6: Figure shows the year wise novel antimicrobial drugs approved by FDA.²⁸

1.1.5 Antimicrobial Materials

Use of materials for antimicrobial activities is not a new concept as we all know. It was in 1928 when we got our first antibiotics penicillin. Till then India had been using various traditional medicines to treat infections.³³ We also know that inappropriate use of the antimicrobial drugs, natural resistance, and many other factors such as hospital aided infections (HAIs) have escalated the challenges of antimicrobial resistance.²⁵ There are

many classes of antimicrobials, some of which are bactericidal, bacteriostatic, Cell Wall Synthesis Inhibitors, Cell Membrane Function Inhibitors, Protein Synthesis Inhibitors, etc.³³

Antimicrobial materials can be of various types and there have been many signs of progress in this field. Many organic and inorganic materials have been studied such as polymeric nanoparticles, metals nanoparticles, etc. for this purposes. Since its inception, all the nosocomial infections are due to the ESKAPE pathogens and in recent terms, few ways to tackle these problems have been suggested. Out of these, antimicrobial peptides (AMPs), nanomaterials, and combinatorial treatment are the most important ones. AMPs are small proteins consisting of varying amino acids and are present in various cells including humans and microorganisms. AMPs are an effective alternative to the existing AMR. However, the issue with these AMPs is that these are sensitive to proteolytic digestion which might affect their stability and further affect their pharmacokinetics. Although studies suggest that these could be a great alternative, the urgency in tackling the demand has given NPs an advantage over them. Combinatorial treatment includes using a combination of medicines for treatment, combining antibiotics and NPs, etc. Sec.

1.1.6 Importance of nanomaterial as an antimicrobial agent

To elaborate on this, nanomaterial sometimes does not need to penetrate the walls. Instead it comes in direct contact with the cell walls which is not possible for regular antimicrobial drugs. This is mainly due to its small size, and the larger surface to volume ratio, etc.³⁸ Based on previous work, NMs are also reported to be effective in preventing

biofilm formation owing to its desirable physio-chemical characteristics such as morphology, size, and the specific surface area. ^{39,40} As a delivery agent/carrier NMs

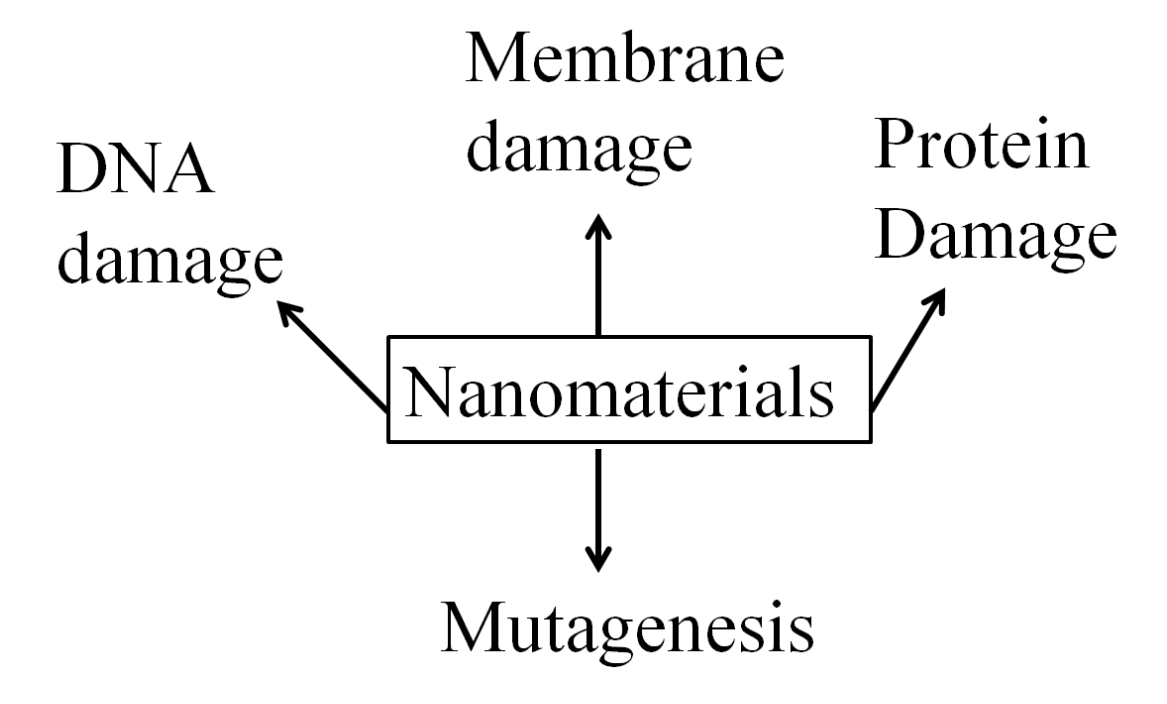


Figure 1.7: Different possible mechanisms in which nanomaterials can affect the various micro-organisms.

function differently than the conventional organic antimicrobial agents in terms of their actions and roles. Size, controllability, combination, protection, and precision are the five crucial reasons why the NMs act as a potential candidate itself as well as they are good delivery system for other antibiotic materials. Due to its size, it can penetrate easily and make the drug release process easier. NPs also can act as a protector to the bulk antimicrobial drug to decrease the resistance of the bacteria. It is a well-known fact that many organic drugs have side effects while treating the main disease. By using NMs as a targeted drug delivery agent, we can also minimize these types of side effects as these materials can travel to the targeted infected site and release only in the desired cells by

recognizing the specific ligands at the place of infection. This is also called active targeting. 44-46 Furthermore, NPs can also be designed in such a way so that the targeted site can have controlled drug release which enhances the stability and avoid the overdose or under dose of the drugs. This has been an effective method in ocular treatment. Finally, the NPs can also be formulated with multiple drugs in a single one, two or more NPs together, etc. It can also be combined in any way to get the best and desired results. 38

Besides these, Krishnapriya et. al⁴⁸ have also added some new factors such as zeta potential, doping modifications, and environmental conditions may affect the suitability of NPs as antimicrobial materials. Hong et. al⁴⁹ synthesized three different sizes of Ag NPs and they observed that nanocubes and nanospheres showed better antibacterial activity compared to the nanowires which they mentioned might be due to the larger specific surface area. In one of the other studies, it is reported that the rate of surface oxidation can affect the antibacterial activity due to the surface roughness and Ag content.⁵⁰ The surface charge or zeta potential of the NMs further can affect the fungal or the bacterial cell wall which can generate severe oxidative stress and thus improve the activity of the NMs by destabilizing the cell membrane.⁵¹ Several other reports on enhanced antimicrobial effects of NPs due to doping can be found. 52-54 Several environmental factors like temperature, pH, osmotic pressure, broth, stirring conditions, etc. also have been found to affect the antimicrobial properties. All these factors make NMs a suitable alternative to meet the challenges against infectious diseases and microorganisms.55,56

1.1.7 Types of antimicrobial Materials and their basic importances in the field of study

NMs are categorized based on their size, synthesis routes, shape, structure, etc and broadly divided into the following:^{2,57}

- Carbon-based NMs
- ➤ Metal and metal oxide NMs
- Nano Composites and composite nanoparticles
- Organic nanoparticles and polymers

Burcu et. al⁵⁸ and a few others^{5,26} also have summarized the different types of antimicrobial materials in their reports which also include lyposomes, dendrimers, and solid-lipid NPs besides the above-mentioned ones.

Among these, metal-based nanoparticles are popular and preferred. Yakoob at. al⁵⁹ have discussed and divided metal base NMs into various types as shown in Fig. 1.8.

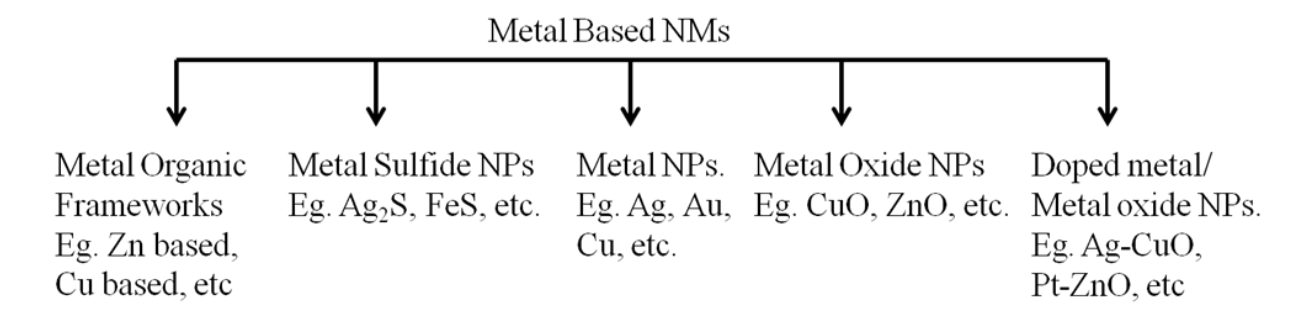


Figure 1.8: Different types of metal-based nanoparticles.

Metal antimicrobials were popular before antibiotics came. Ag, Cu, etc. have been used since ancient ages. Indians and Egyptians have a beautiful history of use of metals as antimicrobial treatment which is why metal-based NPs also have become popular and

being explored for more understanding. 60-62 Metal-based NPs have an effective resistance against microbes and also have high heat resistance compared to their bulk counter parts. 63 The NPs also possess better electronic and optical properties. These also have very good adsorption and diffusion properties which make them suitable for antimicrobial applications.⁶⁴ Murthy et. al⁶ elaborately discuss how each parameter changes or alters the physical, mechanical, chemical, magnetic, etc. properties of the NPs. This is also the reason why Metal-based NPs are preferred over others so that they can be tuned according to our desired needs. Moreover, it has been found in the past that organic NPs cannot withstand heat due to which working with it as an antibacterial agent becomes challenging.⁶⁵ It is also found that MO NPs generate ROS spontaneously whereas some others are capable of only infeasible conditions like selective cells. 66-68 Metal-based NPs are the next generation of antimicrobial treatment options. Furthermore, a recent report highlights the different Metal-based NPs which could be the potential solution to the biofilm treatment. Urinary Tract Infection for example is due to the Uropathogenic Escherichia coli pathogen. Despite antibiotic treatment, these microbes tend to stay in the affected area for a longer period of time and have a tendency to form biofilms which promote in recurring infections and might increase the existing problem. ^{69,70} Many studies have found Ag, Cu, Zn-based metal, and metal oxide NPs to treat chronic wound in a diabetic wound, septic infections, etc.⁵⁵ Due to its several advantages, various metal and metal oxide NPs have been used as antimicrobial agents. e.g. MgO, ⁶⁴ TiO_2 , ⁶³ ZnO, Ag, Ag_2O , Cu, CuO, CeO_2 , Al_2O_3 , etc.. ^{4,6,54,56,60,61,65}

Compared to TiO₂, ZnO have a lower production cost, less toxicity which is why it is preferred over the TiO₂.⁷¹ Zn is recognized as a safe metal by U.S. FDA

(21CFR182.8991). Zn and ZnO have diverse use from paints to sensors, from dental material to fillers, in cosmetics to the food industry. 72 Similarly Cu is considered a safe material since it has been in use since ancient times and it was used as an antiseptic agent much before Ag. 73,74 Even in India Ayurveda has reference to Cu being used as a healing agent. Various medicinal properties of storing H₂O in Cu vessels have been studied before.⁷⁵ Although Cu is required for microbial growth, it still works as an antimicrobial agent. Cu has also been tested against skin issues and found to be non-toxic. 76,77 Moreover, one of the women's contraceptive agents is also composed of Cu. 78 Considering all these facts and ideas, the very reason that it does not harm the mammalian cells when used in permitted quantities makes it an excellent alternative to the current antimicrobial woes. 79 Ag like Cu has been in use for a longer period of time for various purposes including wound healing and water treatment. 80 At low doses, Ag is clinically non-toxic. It has been used in water treatment, fillers, surgical devices, biocatalyst, etc. 81 SnO2 is an n-type semiconductor material with wide energy band gap and it is used in various electronic, gas-sensors, solar energy. The low-cost synthesis techniques make it popular as a promising material. 82,83

Considering these aspects Cu, Ag, Zn and Sn were chosen as our study material based on which various composite NPs were synthesized and studied for antimicrobial activity. Continuous research work is ongoing on these single metals or metal oxide NPs. Attempts have been made in doing the extensive literature review of the published work, and based on the gaps found in literature, the main objectives of this work have been defined in the subsequent section.

1.2 Literature Review

1.2.1 Various metals NPs as antimicrobial Agents

Various NPs such as Ag, Zn, Cu, Au, Ti, Al, Fe, etc. in metallic form or oxide form have been used as an antimicrobial agent as described in various reviews and work. 84–90 Metal NPs with polymers, antibiotics, or metal organic frameworks have been discussed in these reviews extensively. Various modifications in single metal and metal oxide complex either by altering the synthesis process, modifications in morphology, optimization of compositions made by various researchers have been discussed.

ZnO NPs has been used to control the infection of both gram-positive 91 and gramnegative bacteria. $^{91-93}$ Initial work by Lui et. al 92 helped to establish and elaborate ZnO as an antibacterial agent by testing and studied its mechanism in the food borne pathogen, *Escherichia coli* (O157:H7). Similarly, Reddy et al. 93 have synthesized ZnO by precipitation method and tested against *K. pneumoniae* which is also a prominent cause of hospital affected infections (HAIs) and UTI (urinary tract infections). In this study, they calculated the MIC value to be 40 µg/mL. Guo et. al 91 synthesized Ta doped ZnO by Pechini method and tested the synthesized NPs against *P. aeruginosa*, *S. aureus*, *E. coli*, and *B. subtilis*. They found that instead of ZnO alone the 5% Ta doped NPs showed better bacteriocidal results against *P. aeruginosa*, *E. coli*, and *S. aureus* under visible light and bacteriostasis activity against *E. coli*, *S. aureus*, and *B. subtilis* without light. 91 SnO₂ NPs due to their wide energy band gap ($E_g \sim 3.6$ eV) are used for photocatalytic properties and have been explored in antibacterial activities too. One of the earliest literature reported on SnO₂ as an antibacterial agent which was synthesized via

solvothermal method and tested for antibacterial activity against *E. coli* (gram –ive) and *S. aereus* (gram +ive) in which against *E. coli* it showed better activity than *S. aereus*. The variation in results obtained in this might be due to the difference of the cell wall structure of bacteria. More recently, SnO₂ has been synthesized by ultrasonic technique and used against *C. albicans* and *E. coli*. The MIC values for *E. coli* and *Candida* were found to be c.a. 0.5 mg/mL and 8 mg/mL respectively.

Similarly, antibacterial activities of Ag and Ag₂O NPs have been widely studied against different bacterial strains, e.g., Listeria monocytogenes (L. monocytogenes), Escherichia Coli (E. coli), Salmonella typhimurium, and Vibrio Parahaemolyticus (V. parahaemolyticus). However, the effective rate of antibacterial properties depends on the size, shape, and morphology of the Ag NPs. 96,97 Zarei et. al 96 explored commercial Ag against food borne pathogens and had concluded that Ag NPs could be used as cleaning and disinfectant material. They had calculated MIC values for Listeria monocytogenes which was 6.25 µg/mL and 3.12 µg/mL for E. coli, S. typhimurium, and Vibrio parahaemolyticus. Sondi et. al⁹⁷ had synthesized Ag nanoparticles by chemical reduction method using ascorbic acid as the reducing agent and analyzed the NPs for bactericidal activity in E. coli. They also found that when Ag NPs were used in Agar plate and the liquid medium it showed different results. In the agar plate, the Ag NPs were able to inhibit growth and show a biocidal effect with respect to the concentration. However, in LB medium after a certain time even at high concentration, the growth of bacteria was found to have increased. This was further analyzed by SEM and it showed low colloidal stability which means after a certain time the NPs aggregated along with bacteria. Hence, the colloidal stability of NPs is also equally important if it has to be used in a liquid

medium.

Similarly, the antibacterial activity of CuO NPs has been studied against Pseudomonas aeruginosa (P. aeruginosa), Klebsiella pneumonia (K. pneumonia), Salmonella Paratyphi (S. paratyphi), and Shigella Flexneri (S. flexneri) strains, etc. 98,99 It has been noted that the particle size-dependent antimicrobial activities against Staphylococcus aureus (S. aureus), Bacillus subtilis (B. subtilis), P. aeruginosa, and E. coli are also reported and found that this anti-bactericidal efficiency follows the order: ZnO>CuO>Fe₂O₃. The Zone of inhibition (ZOI) for ZnO NPs obtained is highest, c.a. 25 mm against B. subtilis and 19 mm against E. coli. Thus many antimicrobial single oxide NPs are demonstrated. However, the current situation demands newer materials for better efficacy than the reported results.⁸⁹ Due to the ongoing pandemic covid-19, developing coating material with antimicrobial properties has risen and the metal and metal oxide NPs is being explored in those directions too.⁷⁹ The review also focuses on various works done in this aspect. Interestingly, in some cases, Cu has been found to have higher killing efficiency than Ag under ambient temperature and humidity which is due to the "contact killing" phenomena. This means that with the surface contact, the Cu NPs can kill more microbes within short period of time. Grass et. al¹⁰¹ proposed a mechanism that is widely accepted for this phenomenon and is shown in Fig. 1.9. The Fig. 1.9 (A) represents the dissolution of Cu ions which causes the damage to the microbial cells. This damage of the cells can also be due to stress such as depolarization and other intracellular leakages as seen in (B). The ROS-induced damage also might take place due to oxidative degradation (C). And further DNA damage might take place (D). Besides these, there are several other studies that support this and there are some which are a contradictory

mechanisms and can be referred to in detail in the same report by Mitra et. al⁷⁹. However, the conclusion is that despite multiple studies and conclusions on the mechanism of contact killing, it also depends on other factors as well which are: (i) bacterial surface morphology and charges, (ii) buffering agents, (iii) moisture presence, etc. All these reasons make it suitable for the coating material over Ag, especially for indoor use.

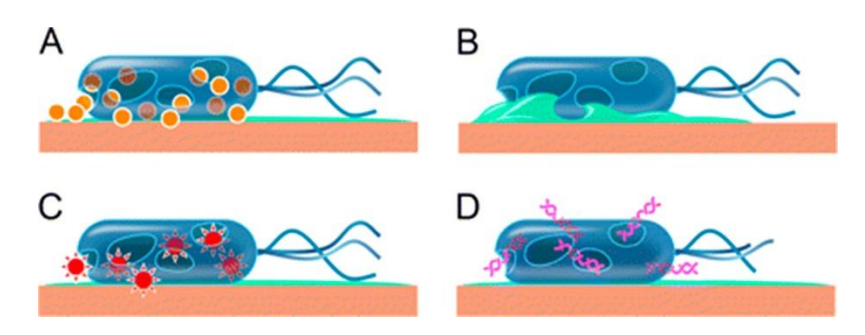


Figure 1.9: Representation of steps of contact killing mechanism of Cu proposed by

Grass et. al¹⁰¹

These metal and metal oxide NPs have shown efficient antimicrobial properties in the food packaging industry, cosmetics, paints; agriculture sectors, etc. yet the rate at which microbes are surpassing the effect of any new treatment and getting resistant to it is increasing. There are already reports of bacteria that growing resistant to Ag due to indiscriminate use. Graves et. al cultured *E. coli* to see the kind of resistance Ag can develop and it was surprising to see that it took only few mutations for Ag to develop resistance. They concluded in their findings that Ag is not a miracle antimicrobial agent and it also needs modifications. Gunawan et. al control to address two questions in their research: (i) whether the prolonged exposure of bioavailable nano-Ag(NAg) or Ag develop resistance or not and (ii) if yes, how would this develop. From the series of studies, it was found that applications of NAg/Ag indeed increased the chance of developing resistance due to

prolonged exposure. The fact that these resistance potentials were detected in microorganisms collected from the various common areas such as the hospitals is one of the major concern. They even summarized the potential risk in humans which is shown in Fig. 1.10. It is thus advisable to have constant check and judicious use of the Ag NPs.

Further, this also means to keep exploring new and desired antimicrobial materials. Panáček et. al¹⁰⁴ prepared Ag NPs with 28 nm in diameter by modified Tollens process. *E. coli*, *P. auruginosa* were tested and found that with many repeated exposure

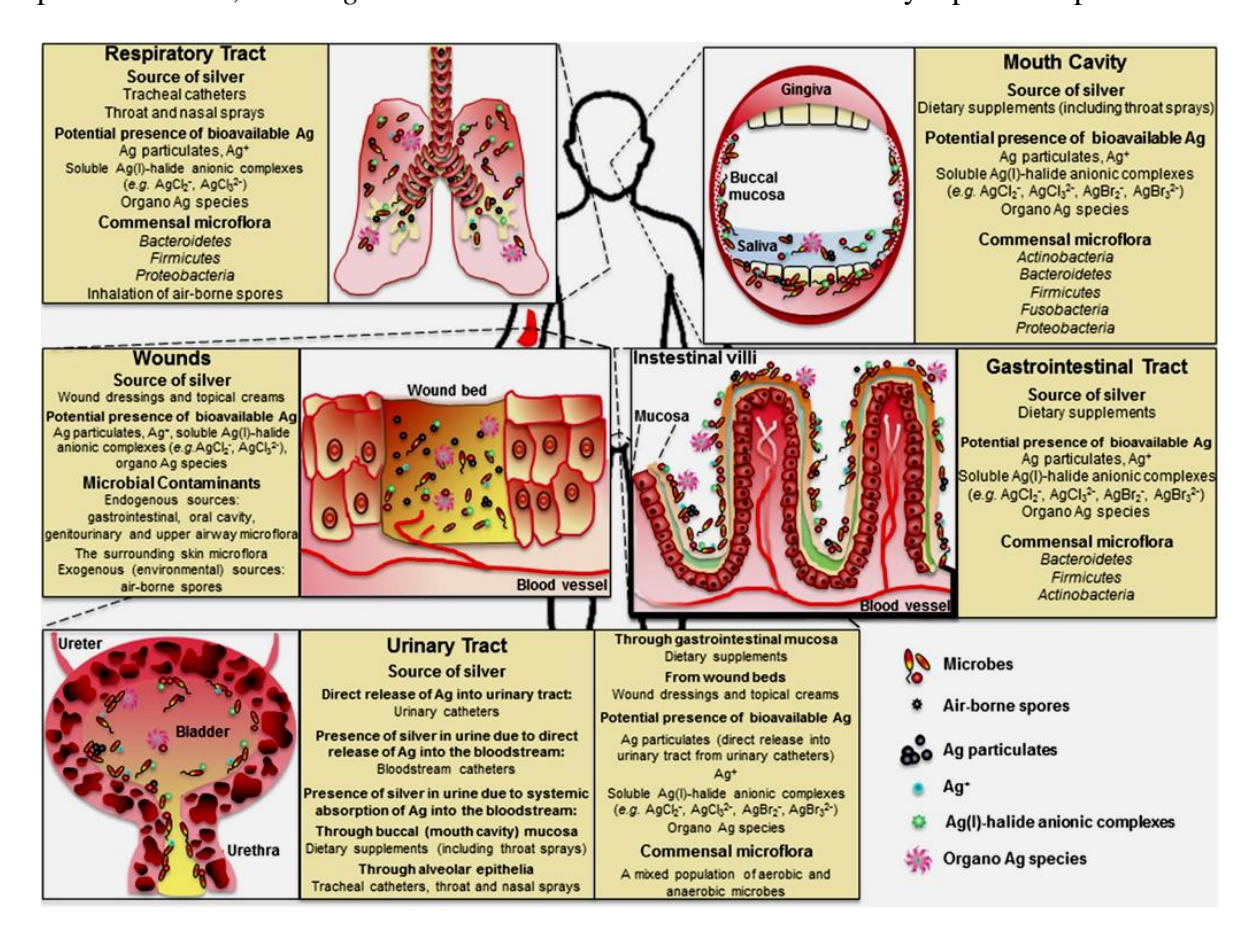


Figure 1.10: Potential risk sites of NAg/Ag in the human body. This is mainly due to the bioavailablity of Ag. The Ag species from Ag NPs products release, absorb, accumulate Ag which increases the Ag bioavailability. ¹⁰³

resistance is developed. This resistance cannot be prevented by using the stabilizing agents such as polymers or surfactants. They also reported that this resistance developed due to flagellin protein which promotes aggregation of the NPs.

Thus the need to find suitable and develop new materials is always in demand besides practical approaches such as judicious use. Currently, researchers have also been focused on the combination of two or more metals/metal oxide NPs for many purposes such as photocatalytic activity, ¹⁰⁵ antibacterial purposes, ^{106–109} making optical devices, ¹¹⁰ energy harvesting, ¹¹¹ to solve the environmental issues ¹⁰⁹, etc. which is summarized in Table 1.1.

Basically, during the development of metal oxide, metal alloy, and metal/ metal oxide, cooperative exchange of charges among the mixed oxide or metals/alloys¹¹² and difference in the electronic potential/energy band gap has been observed. And hence it is considered that a combination of two or more metals/metal oxide could provide significant results in the treatment of microbial strains efficiently. Few articles can be found which describes these multi metallic NPs synthesis, benefits, strategies, etc. in detail. Basavegowda et. al¹¹³ discusseed in detail the latest in-vitro related experiments in multi-metal composites system for treatment of MDR and has shown various developments that have taken place. The appropriate discussions of their benefits have also been articulated. Similarly, Arora et. al¹¹⁴ discussed different synthesis routes, properties, antimicrobial activities of bimetallic NPs both support assisted and non-support based on different materials such as zeolites, polymers, fibers, graphene, etc.

Both these articles conclude the importance of NPs composite systems of multimetal or its oxides.

Table 1.1: Summary of various composite materials developed for various applications

Material	Method	Applications	Size	Inference drawn	Ref
SnO ₂ -ZnO	Sol-gel	Photocatalytic	3-7 nm		105
)Quantum dot)					
SiO ₂ @Cu	Stöber	Antibacterial	200 nm	ZOI:	106
	method		of SiO ₂	<i>E.coli</i> =~10-17 mm	
			core	S. aureus=~9-16	
				mm	
				C. albicans=~9-11	
				mm	
ZnO-SnO ₂	Sol-gel	Optical devices	~28 nm		110
ZnO-SnO ₂ :F	atmospheric	Energy	Grain		111
	spray	harvesting	size		
	pyrolysis	/transparent	~100		
		electrodes	nm		
Ag:Cu	nano casting	Catalytic and	25 nm	E. coli and B.	107
		antibacterial	shell	Subtilis EC50 c.a.	
			with	22.87 ± 0.015 and	
			3.7 nm		
			of Cu	respectively	
			core		100
Ag/Cu	CVD	Antibacterial in	3 nm		108
bimettalic and		E. coli (strain			
Cu & Ag		DH5α)			
monometallic					
on graphene					
support					100
Ag@SiO ₂	Stober	Antibacterial	20 nm	ZOI: Ag@SiO ₂	109
	method	and	of core	(0.5 ml of TEOS)=	
		environmental	Ag and		
			21 nm	/	
			of shell	<i>E. coli</i> at 1000	
			SiO ₂	μg/ml	
				concentration.	

Furthermore, researchers have explored the mixed metal oxide composites e.g., CaCO₃/MgO against *S. aureus* and *E. coli*, ¹¹⁵ mixed ZnO–MgO component against *B. subtilis* and *E. coli*, ¹¹⁶ bimetallic Ag-Cu NPs¹¹⁷ against the *C. albicans*, *E. coli*, and *S.*

aureus, which showed both bacteriostatic and bactericidal activities, and exhibited lower anti-fungicidal activities. Ag-ZrO₂ NPs have also been studied for antifungal activity in which ZOI was calculated between 8 mm-18 mm.¹¹⁸ The Ag-ZrO₂ NPs were synthesized by sol-gel technique and the size was between 14-45 nm (calculated by DLS). This study, also found that mixing of metal oxide ZrO₂ prevented agglomeration and improved antifungal activity compared to single Ag. In another recent study, ZnO-ZrO₂ bimetallic NPs have been synthesized by sol-gel method and antifungal studies on *Candida sp.* were done. The ZOI was found to be between 1-5.4 mm and it was found to be dependent on ZnO concentration.¹¹⁹ However, this study also showed ZOI to be better in monometallic ZnO compared to ZrO₂-ZnO in *C. albicans*. Using metal NPs as antiviral materials are also on the rise. We may find many data on bacterial study but a decade back finding data on antiviral nanomaterials was difficult. However, Ag and Au NPs were initially used for antiviral activity especially of the HIV virus.¹²⁰

Recent reports on how ZnO, Ag, Cu, CuO, etc. are being explored for various antiviral activities are available. These NPs have been used in a spray, as coating material, and also to find treatment for Zika Virus. ^{121–125} Abinaya et. al ¹²⁵ had synthesized ZnO NPs by co-precipitation method using exopolysaccharides (EPS) as reducing and stabilizing agents. These NPs are biocompatible and showed an effective larvicidal property which makes them an effective tool to control the mosquito population and prevent the spread of the Zika virus. This also can be used as pharmaceutical and biomedical materials. Tortella et. al ¹²¹ have reviewed in detail the antiviral use of Ag, Cu, and CuO. The availability of in-vitro studies is an advantage but to use it as human

medical material, more in-vivo experiments, and their uses needs to be studied. Merkl et. al¹²² have studied the coating properties of Ag, ZnO, CuO by synthesizing the material via flame spray pyrolysis technique. These NPs were deposited on flat surfaces and in porous filter media to understand their antiviral activity. Given the pandemic SARS-CoV-2, the development of coating material needs has increased many folds. Hence the authors tried to study these materials against SARS-CoV and found that while Ag showed maximum efficiency, CuO was effective but ZnO was considered unsuitable. Respiratory infections caused by RNA viruses such as influenza are increasing so Jana et. al¹²³ tried to find a solution in Cu-Graphene nanocomposite materials. This nanocomposite prevents the entry of viruses into the host cells. When this composite was blended with PVA, it became transparent which makes it suitable for use in a wide range of surfaces such as face shields, masks, etc. Megharbel et. al¹²⁴ synthesized ZnO by precipitation technique to study its potent antiviral activity against SARS-CoV-2 and it was found that at 525 ng/mL, these NPs causes oxidative stress due to the release of free radicals and induce the membrane damage of the virus which is a promising development. However, Merkl et. al¹²² had found ZnO to be ineffective and the current study by Megharbel et. al¹²⁴ have also found ZnO to have cytotoxic level maximal half concentration ($CC_{50} = 292.2 \text{ ng/mL}$) against VERO-E6 cells. The authors thus suggested that further studies are required to make it more appropriate and use of biological/natural reagents to reduce cytoxicity for improving efficiency.

Furthermore, tri and tetra metal composite NPs have also been synthesized and studied for antimicrobial and anticancer activities recently ^{126,127} and it has always shown

enhanced antimicrobial activity than the mono metal or MO NPs. 128-130 Recently Saranya et. al¹²⁶ have reported CeO₂/ZnO/GO nanocomposite as an effective anticancer material. Similarly, Ahmed et. al¹²⁷ have reported CdO-NiO-Fe₂O₃ nanocomposites synthesized by self-combustion method to have effective antibacterial activity against both gramnegative and gram-positive bacteria. The size of the nanocomposite was affected by the concentration of Ethylene glycol (EG) used. The size was inversely proportional to the concentration of the EG. Jang et. al 128 have synthesized Graphene oxide and Ag/Cu bimetallic NCs to prevent the formation of biofilms on the surface and use it as an antimicrobial material. This nanostructure could be used as a wound-healing material too. Sivaranjan et. al¹²⁹ synthesized mono and bimetallic Pd:Au NPs of various ratios anchored over reduced GO-PANI composites by chemical reduction method. These materials was tested against both bacterial (S. aureus and S. typhi) and fungal strains (C. albicans and C. kruesi) and found to be an efficient antimicrobial agent against all the strains. Akhtar et. al¹³⁰ synthesized spherical CdS, ZnO and CdS loaded ZnO. The size of ZnO was ~50 nm and CdS ~12 nm in the composite nanostructure. In this study, monometallic ZnO had better anticancer activity in colorectal cells (HCT-116) however the antifungal activity in C. albicans was better in CdS/ZnO composite material which had MIC values of 0.5 mg/mL and minimum fungicidal concentration (MFC) of 1 mg/mL. Apart from hospital set-up, coating materials, etc. these NPs and NCs also will be a solution to wastewater treatment. Rehman et. al 131 synthesized binary nanocomposite material of TiO₂-SnO₂ and used it for lead absorption besides its antimicrobial testing. The NCs was of around 15±2 nm and could effectively absorb Pb and showed ZOI

between 12-19 mm for different strains depending on the weight of the sample and strains (S. aureus, P. aeruginosa, C. albicans, and Trichophytons)

Despite the various development and advanced studies of NPs as antimicrobial agents, there remains a challenge to improve their properties, pharmacokinetic profiles, and studies on effects on mammalian cells. Some studies also proposed to develop nanohybrid materials by combining different metals. Therefore, it is always an open field to study more and develop new NPs which can tackle and give hope to the existing crisis of AMR as mentioned in several recent literatures including the one by León-Buitimea et. al.³⁵

Interestingly, transition metals are promising materials since they are capable of generating rapid and significant toxicity in different microbes. Synergistic effects of transition metals and Ag have been studied before which showed improved antibacterial activity compared to the single metal. Garza-Cervantes et. al¹³² in their study showed 8 fold increase in the antimicrobial activity against *E. coli* and *B. subtilis* when transition metals Zn, Co, Cd, Ni, and Cu were used with Ag.

Hence, we aimed to develop NPs composite consisting of elemental Ag, Sn, Cu, and Zn in their metallic and oxide forms by one step facile chemical reduction method and without using any surfactant/capping agent or stabilizer.

1.3 The choice of the Synthesis Route:

There are several synthesis methods available to develop NPs. Here we have chosen the chemical method over others i.e. biological or mechanical. Mechanical

processes include ball milling, laser abrasion, etc. The mechanical route prevents solvent contamination issues. ¹³³ However, the production cost, rate, and energy consumption are not feasible. Similarly, biological synthesis is gaining popularity due to the increased concern of toxicity in NPs synthesis via chemical route. ¹³⁴ The challenge in the green synthesis method is that it is time taking, large-scale production is not easy and adverse reactions in some cases. In short, this method still is in progressing stage in terms of translational research. However, it is an interesting alternative that might give us a breakthrough in the future if certain aspects like physiochemical studies, reaction time, optimization, stability, etc. are studied upon. ¹³⁴ Yet, at this stage chemical synthesis is preferred due to these limitations in biological as well as mechanical synthesis. Even out of the various chemical synthesis techniques, chemical reduction is chosen due to its simplicity and cost-effectiveness. ¹³⁵

1.4 Choice of reducing agent:

There are various organic and inorganic reducing agents such as $NaBH_4$ (sodium borohydride), $Na_3C_6H_5O_7$ (Sodium citrate), Tollens reagent, etc. $NaBH_4$ was chosen as the reducing agent because it has a dual role. It not only reduces the metal salts to ions, but it also stabilizes when used in an adequate quantity. This also reduces the overall costs.

Furthermore, the composite NPs synthesized in this work are surfactant/capping agent-free. The surfactant or capping agents are used to increase the stability and prevent agglomeration in metal NPs. These materials should be biocompatible and hence they should be chosen according to the desired output and additional care has to be taken.

Various types of surfactants used are chitosan, CTAB, polyethylene analyine, PEG, etc. Since these materials have their properties and alter the overall properties of the NPs and composite materials, they have certain limitations. These might have non-specific interactions which might increase the toxicity. Further, it also increases the synthesis time and increases the overall experimental steps. ^{136–139} In one of the studies it was also found that the capping agent had a negligible effect on antibacterial activity. ¹³⁷ Similarly nanocomposite materials with high stability and effective antibiofilm formation has also been developed by Zhao et. al. ¹³⁹ Muhammad Ahmad et. al ¹³⁶ have synthesized surfactant-free Ag-GO nanocomposite and they observed ~41% of bacterial growth inhibition in *E. coli* bacteria with 100 μg/mL of dose concentration which is quite significant in the surfactant-free synthesis of nanocomposite materials for antibacterial activity.

Thus, exploring surfactant-free facile synthesis methods for antimicrobial activity is preferred. This also enables us to investigate if we can come up with suitable antimicrobial NPs effectively for different metal nanocomposites.

1.5 Different Antimicrobial Mechanisms and their justification

Nanomaterials have multiple mechanistic ways to inhibit microbial growth. There are various suggested ways in which metal-based NPs affect the antimicrobial activity which is as follows (also shown in Fig. 1.11)⁸⁴:

❖ Generation of ROS (Reactive oxygen species): hydroxyl radicals, H₂O₂, superoxide anions, etc are produced resulting in DNA replication, membrane damage, etc.

- ❖ Releasing Metal ions to damage bacterial membrane: since bacterial walls are sensitive to metal ions, NPs like Ag⁺ are said to interact with enzymes, Cu⁺⁺ with carboxyl groups, etc. which helps in cell wall damage.
- ❖ Interaction with DNA: NPs like Ag and Cu have also been observed to interact with DNA which further inhibits its replication and damages it.
- ❖ Adsorption: NPs get adsorbed on the surface of the bacterial cell due to their electrostatic interactions. This results in protein damage and causes oxidative stress, etc.

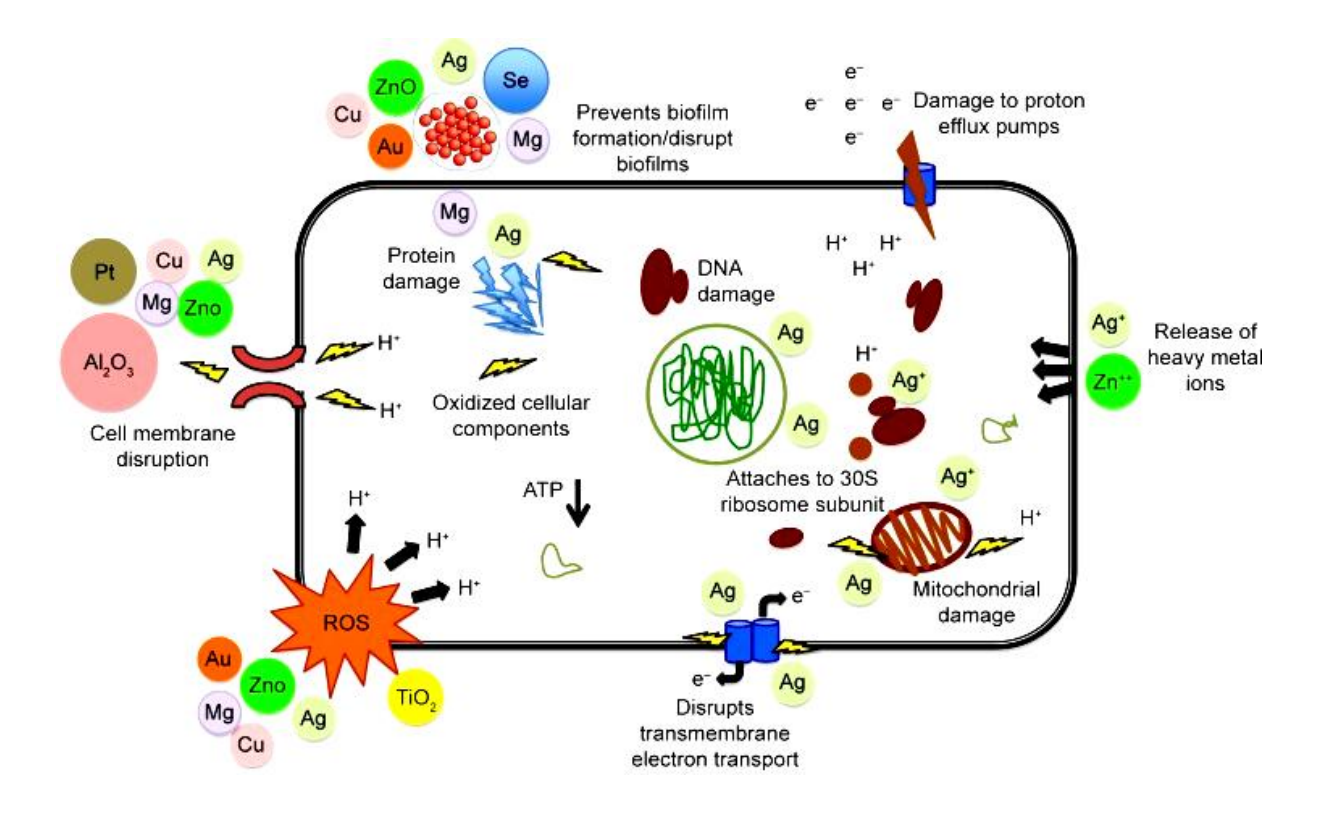


Figure 1.11: Various mechanisms of antibacterials activity using metal-based nanoparticles. ⁸⁴

- ❖ Change in permeability: many metals like Ag and ZnO have been found to increase the permeability, change viscosity, imbalance in the transport system, etc. ultimately leading to cell death.
- ❖ Penetration due to surface charge: NPs surface charge promotes toxicity to the membrane and further it can reach cytoplasm which can then affect the ribosome of the microbes.
- ❖ Biofilm damage/disruption: biofilms are formed when quorum sensing molecules i.e., the molecules which communicate with the cells are produced. When these molecules grow, they detach and spread the infections. NPs like Ag. TiO₂, Fe, etc. are found to interrupt the formation of these molecules and thus disrupt the biofilm formation.

1.6 The motivation behind the work:

The AMR is increasing and this also has led to the ever-increasing burden of Multi Drug-Resistant Tuberculosis. MDR-TB which now is XDR is one of the concerns in India. India is one of the highest consumers of antibiotics in the world. Sikkim, a tiny Himalayan state with a population of around 7-8 lakhs has the highest number of TB patients in India. Few reports state that there are almost 38 deaths lakh⁻¹ year⁻¹. 9% of people do not respond to the first line of drugs. There are cases of relapse even after proper management and mitigation channel. Gautam et. al¹⁴⁰ have done extensive work on studying the TB treatment and diabetes relationship in South East Asia with the maximum data from India. In their study it was found that diabetic-TB patient have higher mortality rate compared to non-diabetic TB patients. Sikkim, a Himalayan state in

North East India with the least population in the country has one of the highest burdens of TB. Singhai et. al¹⁴¹ had conducted their study and according to their findings, 9% patients out of the 1508 enrolled did not respond to treatment.

Recent study shows that 62.41% of TB cases in Sikkim is due to the Beijing strain of *Mycobacterium tuberculosis* complex (MTBC) and about 30% of MDR-TB is due to it¹⁴³ which is alarming because this particular strain is resistant to treatment, has a tendency to cause an epidemic, and has a high degree of transmission and is ineffective against BCG vaccine.^{144–146}

Although there are only a few reports available but the MDR also affects mental health. Sikkim is also one of the states in India with the highest rate of suicide. Local media have reported these incidents from people who were under treatment (Sikkim Chronicle dated 8th July 2019). This led me into thinking about whether AMR, TB, and other bacterial infections and mental health are co-related.

Swati et. al¹⁴⁷ have prepared a report based on this and it is available on the Directorate Of Economics, Statistics & Monitoring And Evaluation (**D.E.S.M.E**) website. According to the report, MDR-TB patients do tend to fall victim to mental health and one of the reasons for suicide in the state. Hence finding solutions to AMR and developing new material is even more important.

1.7 Objectives of this work:

Based on the literature review and the current needs the main objectives fixed for this dissertation are as follows:

- 1. **Objective I**: Study the targeted and Enhanced Antimicrobial Inhibition of mesoporous ZnO-Ag₂O/Ag, ZnO-CuO, and ZnO-SnO₂ composite nanoparticles.
- 2. **Objective II**: Study the target specific inhibition of bacterial and Candida species by mesoporous Ag/Sn-SnO₂ composite nanoparticles: *in silico* and *in vitro* investigation.
- 3. **Objective III**: Preparation of CuO-Sn/SnO₂ and CuO-Ag/AgO nanocomposites and study their comparative antimicrobial activity.
- 4. **Objective IV**: Synthesis and characterization of ternary metal oxide nanoparticles and their in-vitro antimicrobial studies.
- 5. **Objective V**: An attempt to synthesize quaternary metal oxide nanocomposite and study its antimicrobial activity.

CHAPTER 2:Materials, Methods of synthesis and Characterization Techniques

2.1 Materials

The list of chemicals and reagents used in this work and the microbial strains has been listed in Table 2.1 and Table 2.2 respectively.

Table 2.1: List of chemicals and Reagents used in this Work

S. No.	Chemicals and Reagents	Molecular weight	Purity	Make
1.	Zinc Chloride anhydrous (ZnCl ₂)	136.3 g mol ⁻¹	98%	NICE Chemicals
2.	Stannous Chloride (SnCl ₂ .2H ₂ O)	225.64 g mol ⁻¹	95%	SRL
3.	Cupric Chloride A.R (CuCl ₂ .2H ₂ O)	170.48 g mol ⁻¹	99%	NICE
4.	Silver Chloride extra pure (AgCl)	143.32 g mol ⁻¹	99%	NICE
5.	Sodium Borohydrate extrapure (NaBH ₄)	37.83 g mol ⁻¹	95%	SRL
6.	Methanol (CH ₃ OH)			Hychem
7.	Sodium Phosphate Dibasic	141.96 g mol ⁻¹		
8.	Sodium Phosphate Monobasic	119.98 g mol ⁻¹	99%	
9.	NaCl	58.44 g mol ⁻¹	99%	Himedia Ltd
10.	Potassium Chloride	74.55 g mol ⁻¹	99%	
11.	1 M Sodium Hydroxide solution	40 g mol ⁻¹		

All the chemicals were purchased from the supplier and used without further purification.

Table 2.2: List of microbial strains used

S. No.	Microbial strain used		
1.	E. coli (DH5α)		
2.	C. albicans ATTC 90028		
3.	K. pneumoniae AT CC 700603		
4.	P. aeruginosa ATCC 27853		
5.	A. baumannii (clinical strain)		

2.2 Methods of preparation

2.2.1 Synthesis procedure

The synthesis procedure for all the composite NPs will be discussed in subsequent chapters according to the composition of the materials used. The synthesis procedure has also been shown in Fig. 2.1. In brief, equal mmol of respective chemicals were taken in a beaker containing 50 ml of MeOH under continuous stirring. In a separate beaker, 30 mmol of NaBH₄ was taken and dissolved in 50 ml of MeOH at RT. This was then added dropwise under continuous stirring in RT until colour changed fully. After 2 hrs, this was removed, centrifuged and washed with DI water several times and dried in 80°C and sent for characterizations.

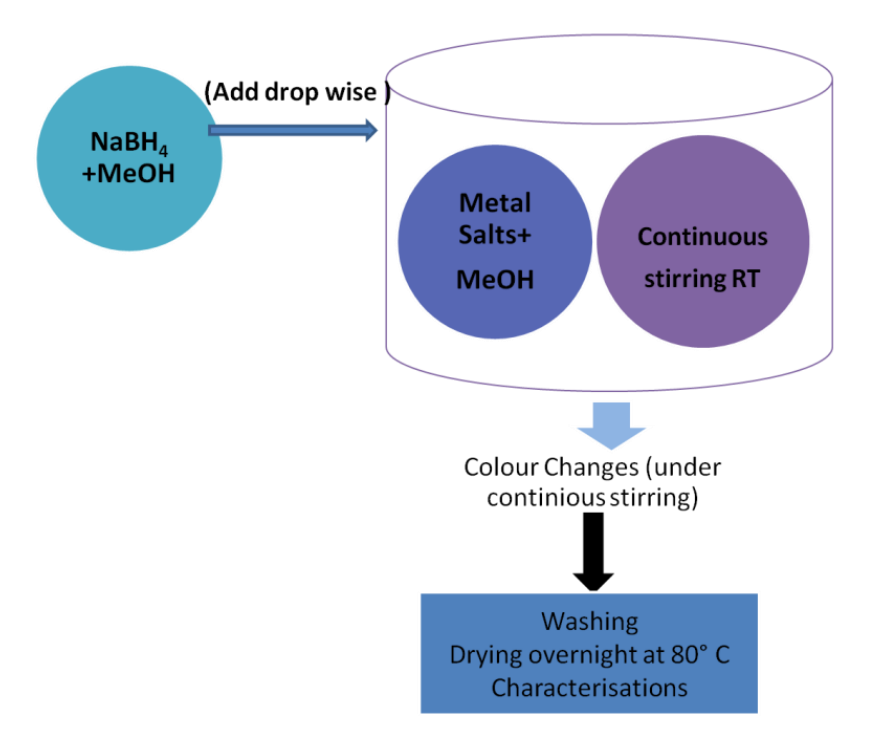


Figure 2.1: Schematic representation of Synthesis Procedure

2.2.2 Preparation of Phosphate Buffer Solution (PB) and Phosphate Buffer Saline (PBS)

In brief, a stock solution 'A' was prepared by adding 13.8 g Sodium Phosphate Monobasic in 500 mL dd-H₂O. Then, stock solution 'B' was prepared by adding 26.81 g of Sodium Phosphate Dibasic in 500 mL of dd-H₂O. Then 'A' and 'B' mixed well.

1X PB was prepared by adding 100 mL stock solution of 'A' with 400 mL stock solution of 'B' and 500 mL of ddH₂O was added to make total 1L.

1X PBS: 10X PBS was prepared by adding 100 mL stock solution of 'A' with 400 mL stock solution of 'B' and then 100 mL of 9% NaCl solution was added into another 400

mL ddH₂O. Further, 1X PBS was prepared by mixing prepared by adding 1 M Potassium Chloride and 1 M Sodium Hydroxide solution.

2.3 Antibacterial evaluation techniques

2.3.1 Disk Diffusion method

For the disk diffusion method, modified procedure has been chosen for antibacterial activity. First, fresh microbial culture was made in normal saline (0.9%) to achieve two different concentrations of 10⁶ cfu/mL and 10⁸ cfu/mL. Sterile cotton swab was used to spread this prepared suspension and it was left for drying for 5 minutes. Then the sterile discs (Whatman filter paper No.1) of size 4 mm diameter was placed on the medium surface. After that, 3mg/ml of each of the nanomaterials were dispensed, and then allowed to diffuse for 5 min. Then the plates were incubated for 24 h at 37°C. After the incubation ZOI were measured around the discs. All the assays were conducted in triplicate and statistically significant results were obtained.¹⁴⁸

2.3.2 Calculation of Minimum inhibitory concentration:

Broth dilution method has been used to determine the MIC for *A. baumannii*. ¹⁴⁹ Equal quantities of NPs were placed with different dilutions of cultured microorganism. The nutrient broth was mixed in 96 well plates and incubated at 37 °C for 24 h. The preparation was carried out in a round bottom microtiter plate containing 100 μl of diluted antibacterial nanomaterials. Ten different concentrations such as, 10 μg/mL, 5 μg/mL, 2.5 μg/mL, 1.25 μg/mL, 0.625 μg/mL, 0.312 μg/mL, 0.156 μg/mL, 0.07 μg/mL, 0.03 μg/mL and 0.019 μg/mL for each material were used for the experimentation. The

MIC values were calculated based on lowest concentration of sample that prevent any noticeable growth of *A. baumannii*.

2.3.3 Luria Bertani (LB) Broth Dilution Method:

The antibacterial activity of each sample was investigated against *E. coli* strain DH5α by LB broth method. The stock solution was prepared by dispersing the NPs in DI water. In 10 ml of LB medium, bacterial culture was inoculated along with different concentrations with NPs and without NPs as control. Further, the culture tubes were incubated at 37° C in shaker incubator at 3500 RPM for 12 h. OD values were measured at 600 nm at different time intervals and finally at 12 h.

2.4 Physiochemical Characterizations Techniques

Various characterization techniques were used to understand the properties of the assynthesized material. HR-TEM, XRD analysis, UV-Vis, BET, FTIR XPS, etc were done to understand the morphology, crystal structure, absorption, specific surface area, composition, oxidation state, respectively. Each technique has been described in this section.

2.4.1 X-Ray Diffraction

X-ray Diffraction (XRD) is used to understand the structure of the materials. The wavelength of the X-ray and the atomic spacing in the crystalline material/solids are in the same order i.e. 10^{-10} m. This is why it is used as a source to understand the crystal structure of the material. When the sample is placed in sample holder and exposed to the x-rays, some diffraction takes place. This diffraction is unique for each sample and this

further gives us information about the sample characterized. W H Bragg and W L Bragg studied this and came up with simple formula to understand this constructive interference. Commonly called as Bragg's law is expressed in equation (2.1):

$$n\lambda = 2(d_{hkl})Sin\theta \dots (2.1)$$

Where, n= integer

d_{hkl}=space between the atoms,

 θ =angle b/w the scattering plane and the X-ray beam

 λ = wavelength of the X-ray

The X-Ray Diffraction (XRD) was measured in X-ray diffractometer (Bruker AXS Model D8) with a Cu K α source, λ =1.54 Å and step size of θ =0.02 between 2 θ =10 $^{\circ}$ -90 $^{\circ}$.

2.4.2 UV-Vis absorption spectroscopy

UV-Vis Spectroscopy is based on the principle that when a light is passed through a sample it absorbs Ultraviolet (UV) or Visible (Vis) lights and gives a unique spectrum which helps in determining the various properties based on it. When light interacts with the matter or $e^-(\pi)$ electrons or n-electrons), it gets excited to higher anti-bonding orbitals. The possible transition from ground state to excited state is of four types- π - π *, n- π *, σ - σ *.

According to the **Beer Lambert Law** (equation 2.2) when the monochromatic light is passed through the substance, the absorption of the solution is directly proportional to concentration of the molecules present in the solution and the path length.

$$A = log_{10} \frac{I_0}{I} = \varepsilon * c * L \qquad (2.2)$$

Where, A= absorbance

Io= intensity of the incident light

I= transmitted intensity

 ε = molar absorptivity

c= concentration of the absorbing molecules

L= the path length.

Sample preparation and measurement

About 1 µg of the sample was dispersed in methanol and sonicated for 10 min. UV-Vis was observed between 190 nm-800 nm using a UV-Vis-NIR spectrometer (Perkin Elmer: LAMBDA 750 instrument). The absorption of the prepared material was measured in quartz cuvette of 1 cm optical path length.

2.4.3 Transmission Electron Microscopy (TEM)

The shape, size, morphology, and the particle distribution can be obtained by TEM. Transmission electron microscopy (TEM) images and selected area electron diffraction (SAED) images were obtained using a high-resolution transmission electron microscopy (HRTEM) (FEI TECNAI G2).

To obtain images via TEM, e⁻ source are transmitted through the specimen. When the e⁻ beams pass, the electrons particles scatter and electromagnetic lens creates image. The TEM instrument consists of- electron source, electromagnetic lens system, sample holder, and imaging system.

Selected Area Diffraction Pattern (SAED) can be obtained from the same instrument. The atoms in the specimen diffract the electrons in a particular angle. This angle forms spots in

the screen which determines the structure and crytallinity of the specimen. The highly crystalline material forms clear spots and the semi crystalline forms ring pattern.

Preparation of sample: a pinch of samples was taken and dispersed in IP and sonicated for 15 minutes. It was then drop casted on Carbon coated Cu grids (200 Mesh). The elemental compositions were confirmed by the EDS attached with the instrument.

2.4.4 Dynamic Light Scattering (DLS) and Zeta Potential

Sample preparation: 1 μ g/ mL sample was dispersed in water, sonicated for 10-15 min and using a MS3000 model (Malvern Instruments Ltd, UK) the hydrodynamic size and the zeta potential was measured. The instrument has 632 nm HeNe laser operating at a 173 degree detector angle.

2.4.4.1 DLS

DLS is based on the Brownian movement of the particles. When particles are dispersed in a solvent, they move constantly. This movement is due to the energy transfer between the molecules of the solvent and the molecules of the particles. Depending on their size they can move faster or slower and if all the other parameters are known, the hydrodynamic diameter can easily be measured based on the speed of the particle movement.

This particle size is measured by Stoke's equation shown in equation 2.3.

$$D = \frac{k_B T}{6\pi \eta R_H}.$$
 (2.3)

Where, D = Diffusion coefficient

 k_B = Boltzmann constant

T = Temperature

 $\eta = Viscocity$

 R_H = Hydrodynamic radius

2.4.4.2 Zeta Potential (ζ- potential)

The electrostatic charge between the particles is measured by Zeta Potential and is an important factor which affects stability of the NP. Zeta cells have Au coating. The particles inside the cell are in motion and are directly proportional to their zeta potential. The frequency shift occurred due to the scatter of the light when a laser beam is passed through the sample is converted into electrophoretic mobility. Zeta potential is calculated via electrophoretic mobility given by the Henry equation 2.4:

$$U_E = \frac{2\varepsilon\zeta}{3\eta} f(Ka)....(2.4)$$

Where,

 U_E = electrophoretic mobility

 ε = dielectric constant

 η = viscosity

 ζ = zeta potential

 $f(K_a)$ =Henry's function

2.4.5 Brunauer-Emmett-Teller (BET) Specific Surface Area

BET theory is based on the adsorption of the gas taking place in the surface of the material. The adsorption depends on temperature, gas pressure and strength of the interaction. Liquid N_2 is used to cool down the temperature of the sample and herein N_2 gas also called the probing gas is released step wise into the sample cell. The amount of N_2 gas adsorbed by the surface of the sample is measured by the following equation (2.5):

$$\frac{1}{V_{a(\frac{P_0}{P}-1)}} = \left[\frac{C-1}{V_m C} * \frac{P}{P_0}\right] + \frac{1}{V_m C}$$
 (2.5)

Where, V_a = volume of the gas adsorbed at STP

P= partial vapour pressure of N_2 gas at 77.4 K

 P_0 = saturated pressure of the N₂ gas

 V_m =volume of the gas adsorbed at STP to produce monolayer on the sample

C=constant

BET equation uses the information from the above equation to measure specific surface area of the sample. V_a is measured at each relative pressure (P/P_0) and specific surface area is calculated with the following equation (2.6):

$$SSA = \frac{V_m N_a}{m22400}$$
 (2.6)

Where, $N = \text{Avogadro constant } (6.022 \times 10^{23} \text{ mol}^{-1})$

m= mass of test sample

 N_a = cross-sectional area of one adsorbate molecule (0.162 nm² for nitrogen)

22400 is the volume occupied by 1 mole of the probing gas at STP.

Sample measurement

BET specific surface area and BJH (Barrett-Joyner-Halenda) average pore width of the samples were analyzed by N₂ gas adsorption-desorption isotherms at 76.5 K with a Tristar 3020 physiorption analyzer **TriStar II 3020** (Micromeritics Instrument Corporation, USA).

2.4.6 Thermogravimetric analysis (TGA) and Differential Scanning Calorimetry (DSC)

TGA measures the samples mass with respect to Temperature and DSC measures the heat flow of the sample with respect to Temperature. TGA and DSC are measured by gradually increasing the temperature of the sample and the curves are obtained as a function of Temperature with respect to the reference sample. DSC is based on the principle that when there is change of phases or some form of change, there is difference of the heat supplied which then is recorded and gives information about transition such as melting, crystallization, etc.. TGA is based on the principle that mass loss occurs when there is loss of volatile matter or mass can also increase if there is oxidation. With some change in temperature, mass of a substance can increase or decrease.

Measurement

The thermal study was done by TGA/DSC (Thermo ONIX Gaslab 300) in inert N_2 atmosphere from 10 to 1000°C at a heating rate of 10°C by taking around 5 mg of the sample.

2.4.7 X-ray Photoelectron Spectroscopy (XPS)

It is also called ESCA (Electron Spectroscopy for Chemical Analysis). X-rays are bombarded on the samples from which electrons near the surface will emit. This energy that is emitted from these electrons is analyzed. The energy spectrum of these is obtained by scanning over the kinetic range from 0 eV. This is then also used to find the binding energy with the following relationship (equation 2.7):

$$hv = KE + BE + \varphi \qquad \dots (2.7)$$

Where:

hv= energy of the X-ray

KE= kinetic energy

BE= Binding energy

φ=work function of the spectrometer

Every e has a unique Binding energy which is then used to identify chemical bonds, oxidation state, etc. XPS study was performed from 0-1200 eV using KRATOS Analytical Axis SUPRA model.

2.4.8 Fourier Transform Infra-red Spectroscopy (FT-IR)

Every molecule has their characteristic frequencies which are unique for their structure. When samples are passed through the IR radiation, some of these frequencies are absorbed and are used to identify the molecules. FTIR instrument sends radiation through the sample and the absorbed radiation converts into vibrational or/and rotational energy depending on the composition of the samples. So once this is done, a fingerprint in the form of spectrum is presented for interpretation and analysis which is unique for every molecule.

Sample preparation

The FTIR of the sample was recorded with Perkin Elmer-model: Impact-410 frequency between 400 cm⁻¹ to 4000 cm⁻¹. The dried samples were mixed with KBr in the ratio of 1:4 using a pestle and mortar, and then pressed into disks before taking the readings.

2.5 Time scale dissolution and stability Studies

2.5.1 Time scale Zeta study

The time scale stabilities of the composite NPs were investigated for 3/7 days through zeta potential measurement considering defined time interval. The following experiments were performed:

- > 5μg/ml of each sample was prepared in 1X PBS (Phosphate Buffer Saline) for different pH of 5, 6.9, 7.4 and 8 of bimetallic NPs discussed in subsequent chapters.
- > 5μg/ml of each sample was prepared in PB (Phosphate Buffer Solution) for different NPs discussed in chapter 3.
- > 5μg/ml of sample was dispersed in 0.9 % W/V Saline solution (medical saline available in medical store).

2.5.2 Time scale dissolution study through DLS:

The time scale dissolution and stabilities of the composite NPs were investigated for 3/7 days through DLS. The sample preparation has been conducted as similar to the above mentioned in zeta potential and stability study for different NPs in pH 5, 6.9, 7.4 and 8. Further, DLS readings were taken for all the samples at different time intervals. Samples were sonicated for 10 min to disperse before starting the experiments/measurements.

CHAPTER 3: Results and Discussions

Part I: Targeted and Enhanced Antimicrobial Inhibition of mesoporous ZnO-Ag₂O/Ag, ZnO-CuO and ZnO-SnO₂ composite nanoparticles.

Outcome of this chapter: Published in ACS Omega.

Part II: Target specific inhibition of bacterial and Candida species by mesoporous Ag/Sn-SnO₂ composite nanoparticles: *in silico* and *in vitro* investigation

Outcome of this chapter: Published in RSC Advances.

Part III: Study of comparative antimicrobial activity of CuO-Ag and CuO-SnO₂ Nanocomposite and find an alternative to Ag NPs.

Outcome of this chapter: manuscript ready for submission

Part IV: To synthesize three metal oxide NPs and their comparative antimicrobial activities.

Outcome of this chapter: manuscript ready for submission

Part V: an attempt to synthesize tetra-metal oxide NPs for their antimicrobial activity. **Outcome of this chapter:** manuscript ready for submission

Chapter 3: PART I

3.1 Targeted and Enhanced Antimicrobial Inhibition of mesoporous ZnO-Ag₂O/Ag, ZnO-CuO and ZnO-SnO₂ composite nanoparticles

3.1.1 Abstract

In this part, mesoporous (pore size below 4 nm) composite NPs of ZnO-Ag₂O/Ag, ZnO-CuO, and ZnO-SnO₂ of size $d \le 10$ nm (dia.) have been synthesized through the in situ chemical reduction method using NaBH₄. These composite NPs exhibited excellent killing efficacy against Gram-positive/negative bacterial and fungal strains even at a very low dose of 0.010 µg/mL. Additionally, by applying the in silico docking approach, the NPs and microorganism-specific targeted proteins and their interactions have been identified to explain the best anti-bacterial/anti-fungal activities of these composites. For this purpose, the virulence and resistance causing target proteins such as PqsR, RstA, FosA, and Hsp90 of P. aeruginosa, A. baumannii, K. pneumoniae, and C. albicans have been identified to find out the best inhibitory action mechanisms involved. From the in vitro study, it is revealed that all the composite NPs types used here can act as potent antimicrobial components. All the composite NPs have exhibited excellent inhibition against the microorganisms compared to their constituent single metal or metal oxide nanoparticles. Among the NPs types, the ZnO-Ag₂O/Ag composite nanoparticles exhibited the best inhibition activity compared to the other reported nanoparticles.

3.1.2 Introduction

Microbial contamination, adhesion, persistence colony formation on surfaces, and associated infections have become detrimental to public health and are causing massive alarm. ⁸⁶ The usages of antibiotics lead to the development of resistant microbial strains which are the main cause of antimicrobial resistance and persistent infection. ¹⁵⁰ Thus, there is a high demand for efficient antimicrobial components that can resist the infection level. There are many organic, inorganic, and polymeric antibiotics and each of them has its own advantages and disadvantages. Organic and polymeric antimicrobial agents are very temperature sensitive, possess a shorter lifetime, can degrade easily, and manifest various side effects in the long run. ⁸⁹ Therefore, constant efforts are necessary towards the development of new antimicrobial components to address these challenges with minimum side effects.

NPs have also been explored as an efficient antimicrobial component mainly due to their unique mechanism of action, contact killing effect, the generation of reactive oxygen species (ROS), disruption of DNA, disruption of the cell membrane, etc. 90,94,150–154 However, the field of material research is constantly progressing to accomplish the best antibiotics with optimum results. Materials such as metal and metal oxide NPs like ZnO, 151 CuO, 155 SnO₂ 156, and Ag₂O 157,158, and different polymeric NPs have been reported and used for their antimicrobial properties for a long time now. By interacting with the thiol groups of enzymes, metallic/metal oxide NPs inactivates the cellular activities of proteins. 159 Hence, further development of inorganic antimicrobial agents

such as metal and metal oxide NPs could become an alternative simple, and cost-effective strategy to address the problems related to the microbial infections and associated issues.

Furthermore, many researchers have explored metallic oxides for their wide applications, especially for antimicrobial efficiency. For example, ZnO NPs were used for electronic applications as well as to control the infection of both gram-positive⁹¹ and gram-negative bacteria. $^{91-93}$ SnO₂ NPs due to their wide band energy gap (E_g~3.6 eV) are used for photocatalytic properties and have been explored in antibacterial activities too. Similarly, antibacterial activities of Ag and Ag₂O NPs have been widely studied against different bacterial strains, e.g., L. monocytogenes, E. coli, S. typhimurium, and V. parahaemolyticus. However, the effective rate of antibacterial properties depends on the size, shape, and morphology of the Ag NPs. 96,160 Similarly, the antibacterial activity of CuO NPs have been studied against P. aeruginosa, K. pneumonia, S. paratyphi and S. flexneri strains, etc. 98,99 It has been noted that the particle size-dependent antimicrobial activities 100 against S. aureus, B. subtilis, P. aeruginosa, and E. coli are also reported and found that this anti-bactericidal efficiency follows the order: ZnO>CuO>Fe₂O₃. The Zone of inhibition (ZOI) for ZnO NPs obtained is highest, c.a., 25 mm against B. subtilis and c.a., 19 mm against E. coli. Thus many antimicrobial single oxide NPs are demonstrated, however current situation demands newer materials for better efficacy than the reported results. 89 Presently researchers have also been focused towards the combination of two or more metals/metal oxide NPs for many purposes such as photocatalytic activity, 105 antibacterial purposes, 108,109,161,162 making optical devices, 110 energy harvesting, 111 to solve the environmental issues 109, etc. These NPs can be synthesized through various

methods e.g., solvothermal, sol-gel, microwave-assisted, etc. It has also been noticed that the antimicrobial properties of NPs depend on the size, shape, morphology, and synthetic methods. Basically, during the development of metal oxide, metal alloy, and metal/ metal oxide, cooperative exchange of charges among the mixed oxide or metals/alloys¹¹² and difference in the electronic potential/energy band gap has been observed. And hence it is considered that a combination of two or more metals/metal oxide could provide significant results in the treatment of microbial strains efficiently. Furthermore, researchers have explored the mixed metal oxide composites e.g., CaCO₃/MgO against *S. aureus* and *E. coli*, ¹¹⁵ mixed ZnO–MgO component against *B. subtilis* and *E. coli*, ¹¹⁶ bimetallic Ag-Cu NPs¹¹⁷ against the *C. albicans*, *E. coli* and *S. aureus*, which showed both bacteriostatic and bactericidal activities, and exhibited lower anti-fungicidal activities.

Thus the challenges of the present situation are to find out newer broad-spectrum antimicrobial agents, which will be having efficient microbial killing efficacy within minimum dose, without exhibiting side effects and having longer stability. In the present context of the health care demands, the objective of this work is to synthesize mixed oxide/composites such as ZnO-CuO, ZnO-Ag₂O/Ag, and ZnO-SnO₂NPs with smaller size and with porous structure by the in-situ chemical reduction method to achieve very high surface area to volume ratio as well as effective antimicrobial activities. Further, docking prediction has been performed to evaluate and predict the interactions of the composite nanoparticles for their enhanced activity compared to the single metal/metal oxide NPs. It has also been observed that NPs could act as a potential antimicrobial agent

against drug-resistant microorganisms. Further, it has also been observed that in microorganism resistance development, enhanced virulence capacity, biofilm formation, and quorum sensing mechanisms are regulated by the various proteins. Such as, (i) PqsR is involved in the quorum-sensing pathway of P. aeruginosa, and it controls virulence, 163 and (ii) FosA gene and RstA (BfmR) are involved in controlling the stress response and multidrug resistance issues. 164 It has been observed that the FosA gene was found in 7 types of *E.coli* pathogenic strains, 165 which controls the metabolization of fosfomycine via regulating the expression of metal-dependent glutathione transferase. 166 It is known that the K. pneumoniae and P. aeruginosa are inherently resistant to fosfomycine, while in A. baumannii stain, BfmR is a conserved gene. Interestingly, targeting BfmR can decrease the survival of A. baumannii and it can increase the sensitivity of organisms towards the antimicrobial and anti-biofilm formation. ¹⁶⁷ In candida, conserved molecular chaperone Hsp90 governs the key functions like thermal stability, cell cycle regulation, morphogenesis, expression of virulence traits, and drug resistance. 168 Therefore, for the conformation of enhanced antibacterial and antifungal activities of the metallic nanocomposite, we have carried out interaction studies using the quorum sensing proteins PqsR, ¹⁶³ RstA response regulator ¹⁶⁷, and resistance causing FosA proteins. ¹⁶⁶ Then, in vitro differential antibacterial and antifungal activities have been studied in this work by KB test. The efficacies of inhibiting the microorganism of our materials have been evaluated by calculating the MIC and the ZOI in different strains. Additionally, we have tested the antimicrobial properties of individual metal oxides such as ZnO, Ag₂O/Ag, CuO, and SnO₂ NPs separately, which were synthesized using the same approach. Finally, the antimicrobial properties of Ag₂O, CuO, SnO₂, and ZnO NPs and ZnO-CuO,

ZnO-AgO₂/Ag, and ZnO-SnO₂ NPs have been compared using the *in silico* and *in vitro* studies. Thus, in the present study, we have focused mainly on the composite NPs doped with metal/metal oxide NPs and their antimicrobial results were compared with the ZnO NPs which could challenge different microorganism-based infections and diseases.

3.1.3 Experimental

3.1.3.1 Synthesis of Zinc oxide (ZnO) NPs

In brief, 10 mmol of ZnCl₂ was added in 50 mL of alcohol under continuous stirring. Simultaneously, 20 mmol of NaBH₄ was added in 10 mL alcohol under an ice bath. Further NaBH₄ solution was added drop wise at the rate of 1 drop/2-sec in the solution of zinc chloride under continuous stirring (300 RPM). The color change from transparent to milky white was observed. The solution was centrifuged (8000 RPM) and washed with deionized (DI) water three times and dried overnight at 80° C. This sample is designated as Z (ZnO).

3.1.3.2 Synthesis of Zinc Copper bimetallic oxide NPs (ZnO-CuO)

In brief, 10 mmol each of ZnCl₂ and CuCl₂.2H₂O was added in 50 mL of alcohol under continuous stirring (300 RPM) at room temperature (RT). 50 mmol of NaBH₄ was added in 20 mL alcohol and the exothermic reaction was taken place at RT in the ice bath. The solution was added drop wise at the rate of 1 drop per 2 sec to the first solution. The color changed from greenish to dark green more like a shade of black. The solution was centrifuged and washed with DI water thrice and dried overnight at 80° C. Details of the

synthesis method can be referred to the applications of Indian Patents. ^{169,170} This sample is designated as CZ (ZnO-CuO).

3.1.3.3 Synthesis of Zinc Silver bimetallic oxide NPs (ZnO-Ag₂O/Ag)

In brief, chloride salts of silver and zinc were taken in the same quantities as above and the same procedure was adopted. After the drop wise addition of NaBH₄ solution, a change in color from dark-green to greenish-black has been observed. The solution was centrifuged and washed with DI water three times and dried overnight at 80°C. This sample is designated as AZ (ZnO-Ag₂O/Ag).

3.1.3.4 Synthesis of Zinc Tin bimetallic oxide NPs (ZnO-SnO₂)

In brief, 10mmol of zinc and stannous chloride salts were taken and the same procedure was followed as above. On addition of the NaBH₄ solution, the color changed from milky transparent to brownish and then greyish. The solution was washed with DI water three times and dried overnight at 80° C. ^{169,170} This sample is designated as SZ (ZnO-SnO₂).

3.1.3.5 Antibacterial Evaluation study

In silico Molecular interactions of metallic oxide Nanoparticles and the target protein of micro-organism

Investigation of molecular interaction of ZnO-Ag₂O/Ag, ZnO-CuO and ZnO-SnO₂ and single oxide Ag, SnO₂and Zn were carried out by applying Lamarckian genetic algorithms (LGA) using AutoDock4.2 tool. The structure of the NPs was modeled and optimized by using VESTA version 3, freely available software.¹⁷¹ The crystal structure of Quorum sensing regulator PqsR (PDB ID: 4JVI), *P. aeruginosa*, response regulator

RstA (PDB ID: 5E3J) *A. baumannii*, fosfomycin resistance protein (PDB ID: 5WEW) of *K. pneumoniae*, Heat Shock protein 90 (HSP90) (PDB ID-6CJP) of *C. albicans* were retrieved from the protein data bank. Macromolecule preparation was carried by adding the polar hydrogen atoms, Kollman charges, solvation parameter, and defaulted grid box was generated. Computational flexible docking was performed using the optimized geometry of NP and protein molecules. Docking parameter set defaulted, number of GA run set 30 and maximum amount of generation was set at 27,000 for each study. Further Analysis was conducted using AutoDock and Chimera software.

ii. Disk Diffusion method

The method has been described in the experimental section in Chapter 2 (Page 33).

iii. Calculation of Minimum inhibitory concentration

The method has been described in the experimental section in Chapter 2 (Page 33).

iv. Luria Broth (LB) Dilution Method

The method has been described in the experimental section in Chapter 2 (Page 34).

3.1.3.6 Statistical Analysis:

Data are expressed as mean values (± SD). Analysis of variance followed by Bonferroni post tests comparisons in different time intervals for multiple comparison tests in two ways ANOVA was done. In all cases, the p value was obtained from the ANOVA table and the conventional 0.0001 level was considered to express the statistical significance.

3.1.4 Results and Discussions

3.1.4.1 Synthesis and Characterizations

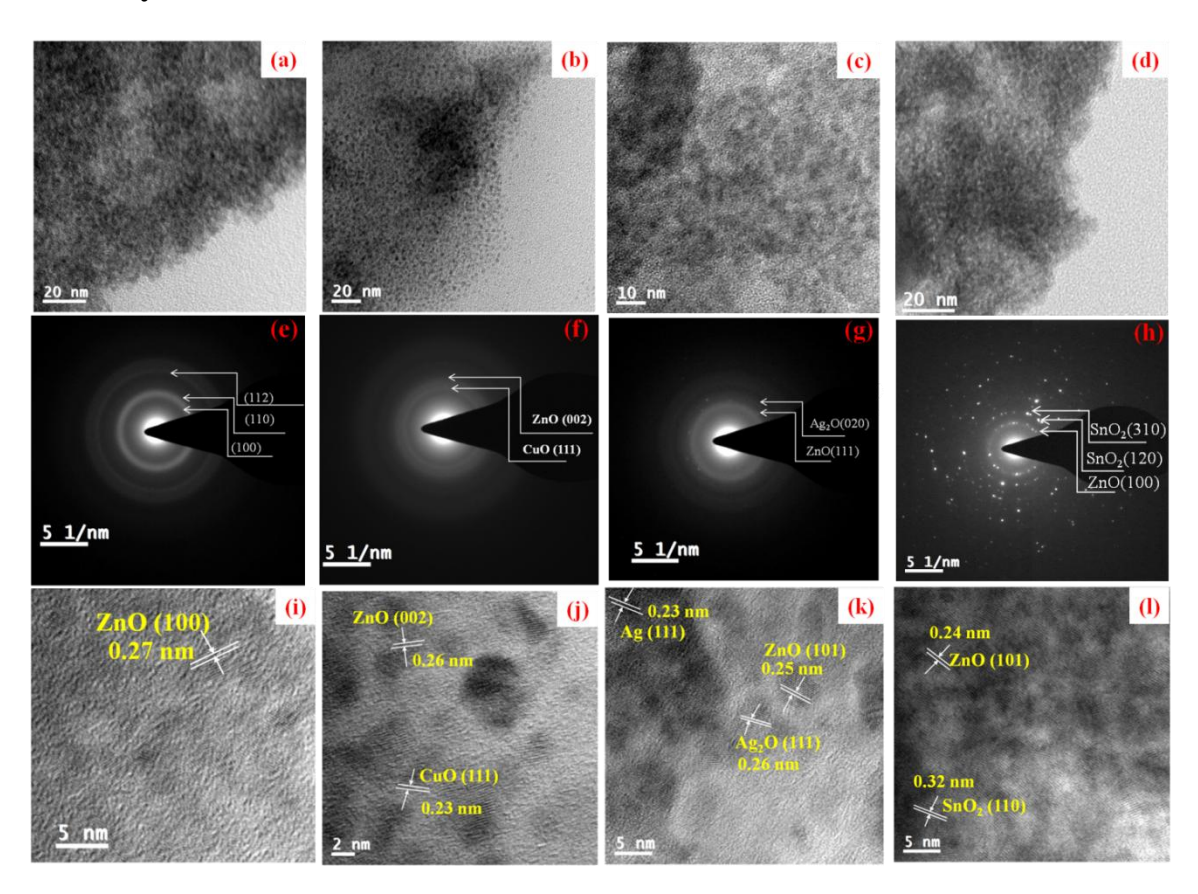


Figure 3.1: HRTEM micrographs for (a) ZnO, (b) ZnO-CuO, (c) ZnO-Ag₂O/Ag, and (d) ZnO-SnO₂; SAED pattern for (e) ZnO; (f) ZnO-CuO, (g) ZnO-Ag₂O/Ag, and (h) ZnO-SnO₂; and d-spacing for (i) ZnO, (j) ZnO-CuO, (k) ZnO-Ag₂O/Ag, and (l) ZnO-SnO₂.

The ZnO-CuO, ZnO-Ag₂O/Ag, and ZnO-SnO₂ NPs were synthesized by *in-situ* solvo-chemical reduction method using NaBH₄ as mentioned in the experimental section. Detailed synthesis methods for different samples have been filed for patents. ^{169,170} The HRTEM micrographs of ZnO, ZnO-CuO, ZnO-Ag₂O/Ag, and ZnO-SnO₂ NPs are shown in Fig. 3.1 (a) to (d), respectively, where all the NPs are observed in well-dispersed form.

Size and morphology of the NPs are observed from HRTEM (Fig. 3.1) which shows ZnO NPs are quasi-spherical in shape with an average size of c.a., 2.25±0.3 nm in diameter. The ZnO-CuO NPs (Fig. 3.1 (b)) show an average size of 2.1±0.2 nm in diameter. The mono dispersed ZnO-Ag₂O/Ag NPs (Fig. 3.1 (c)) are of the size 3.2±0.2 nm in diameter and ZnO-SnO₂ NPs (Fig. 3.1 (d)) are of the size 5±0.2 nm in diameter. The SAED pattern for ZnO, ZnO-CuO, ZnO-Ag/Ag₂O, and ZnO-SnO₂ are shown in Fig. 1(e), (f), (g), and (h), respectively. The d-spacing values were calculated from the HRTEM image and it is found to be 0.27 nm corresponds to the ZnO (100) (in Fig 3.1 (i)) and this value is matching well with the pure ZnO NPs. For ZnO-CuO, the d-spacing is calculated to be 0.23 nm for CuO (111) and 0.26 nm for ZnO (002) as shown in Fig. 3.1 (j). For ZnO- Ag_2O/Ag , the d-spacing ~0.25 nm corresponds to ZnO (101), 0.23 nm for Ag (111), and 0.26 nm for Ag₂O (111) as is shown in Fig. 3.1 (k). For ZnO-SnO₂, d-spacing is calculated to be 0.24 nm for ZnO (102) and 0.32 nm corresponding to the SnO₂ (110) as shown in Fig. 3.1 (1). Thus, the samples are mixed with oxide components. These results are in good agreement with the XRD results which are represented in the subsequent section.

The UV-visible spectra were acquired in the range of 190-800 nm for all the NPs to find out the surface plasmon behavior (Fig. 3.2). All the samples exhibited a single distinct absorption band at 382 nm (Fig. 3.2a), 262 nm (Fig. 3.2 b), 224 nm (Fig. 3.2c), and 358 nm (Fig. 3.2 d) for ZnO-CuO, ZnO-SnO₂ and for ZnO-Ag₂O/Ag, respectively. The appearance of a single absorption band instead of double peaks denotes that the bimetallic-oxide composites have been formed in the presence of NaBH₄, which

are further converted into oxides since the synthesis process was conducted in the oxidizing environment and the overall composition of the various samples are with uniformly mixed phase.¹⁷² Another important can be pointed out from the UV-Vis spectra that for ZnO-SnO₂ (SZ) (Fig. 3.2 c) and for ZnO-CuO (CZ) (Fig. 3.2b) there is a significant decrease in intensity of the absorption band. This could occur since SnO₂ and CuO are the dominant phases over the ZnO in SZ and CZ, respectively. This also can be verified from the EDS results (Fig. 3.3).

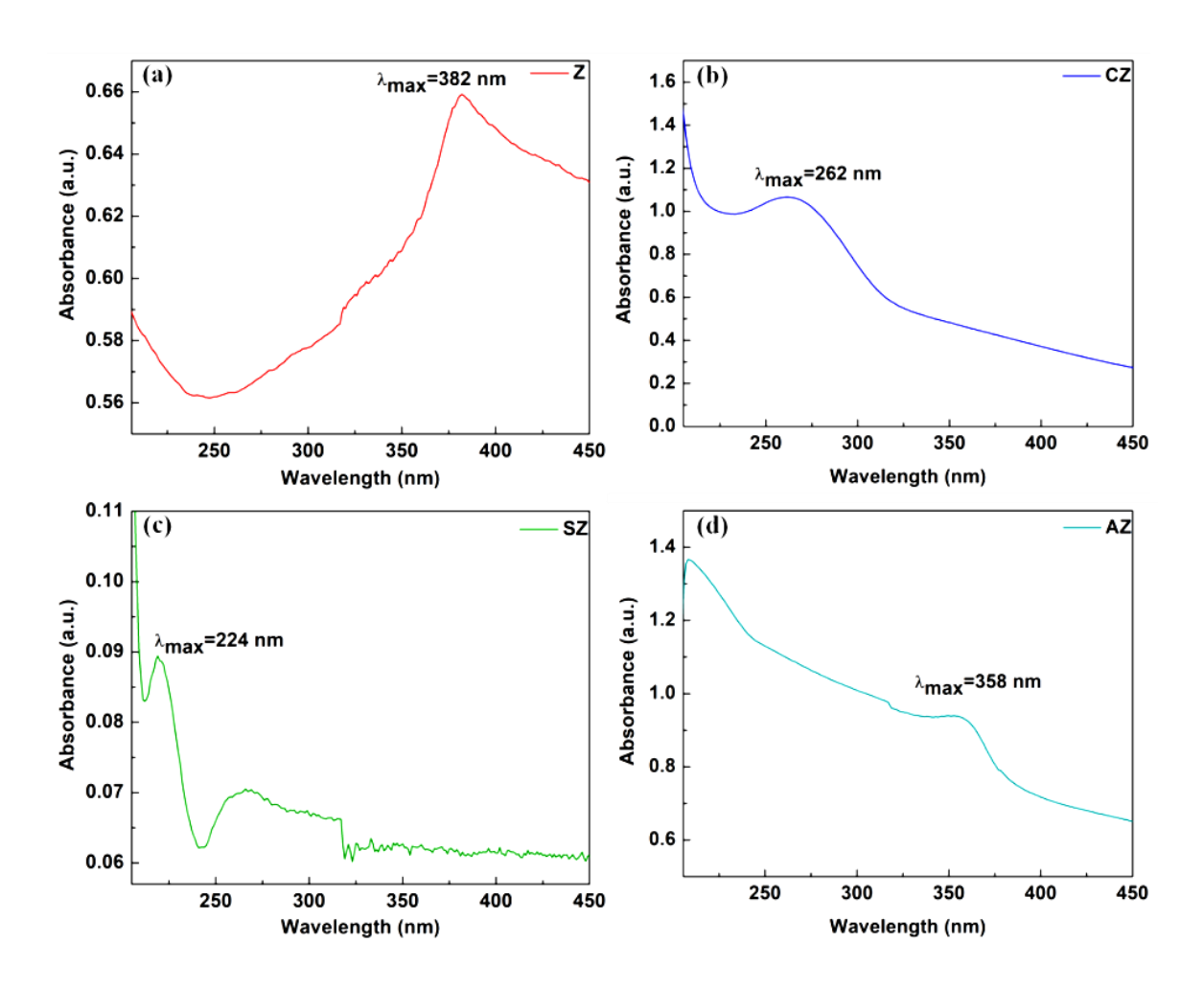


Figure 3.2: UV-Vis spectra of composite NPs: (a) ZnO NPs, (b) ZnO-CuO NPs, (c) ZnO-SnO₂ NPs and (d) ZnO-Ag₂O/Ag NPs.

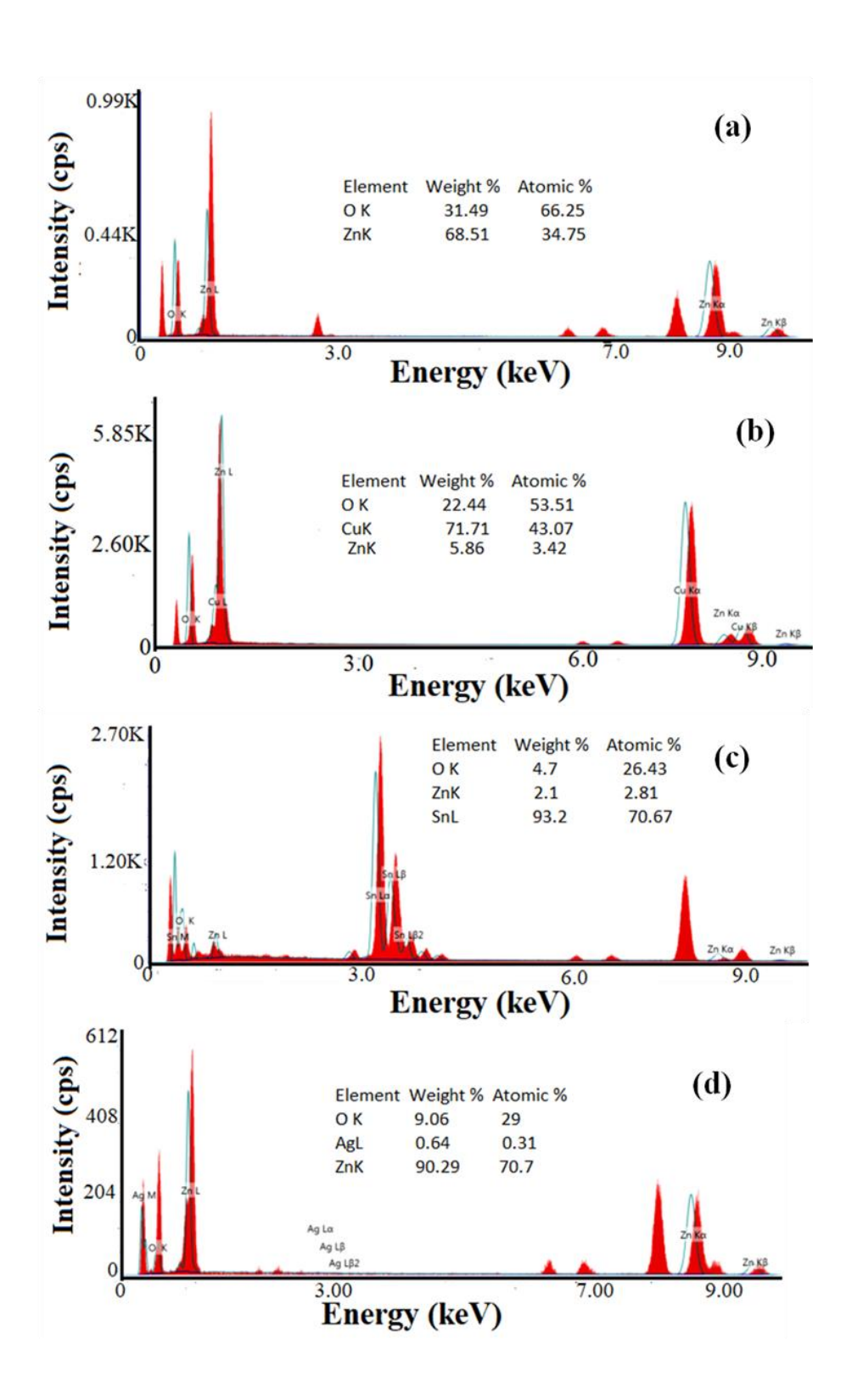


Figure 3.3: EDS spectrum of: (a) ZnO, (b) ZnO-CuO, (c) ZnO-SnO₂ and (d) ZnO- Ag/Ag_2O .

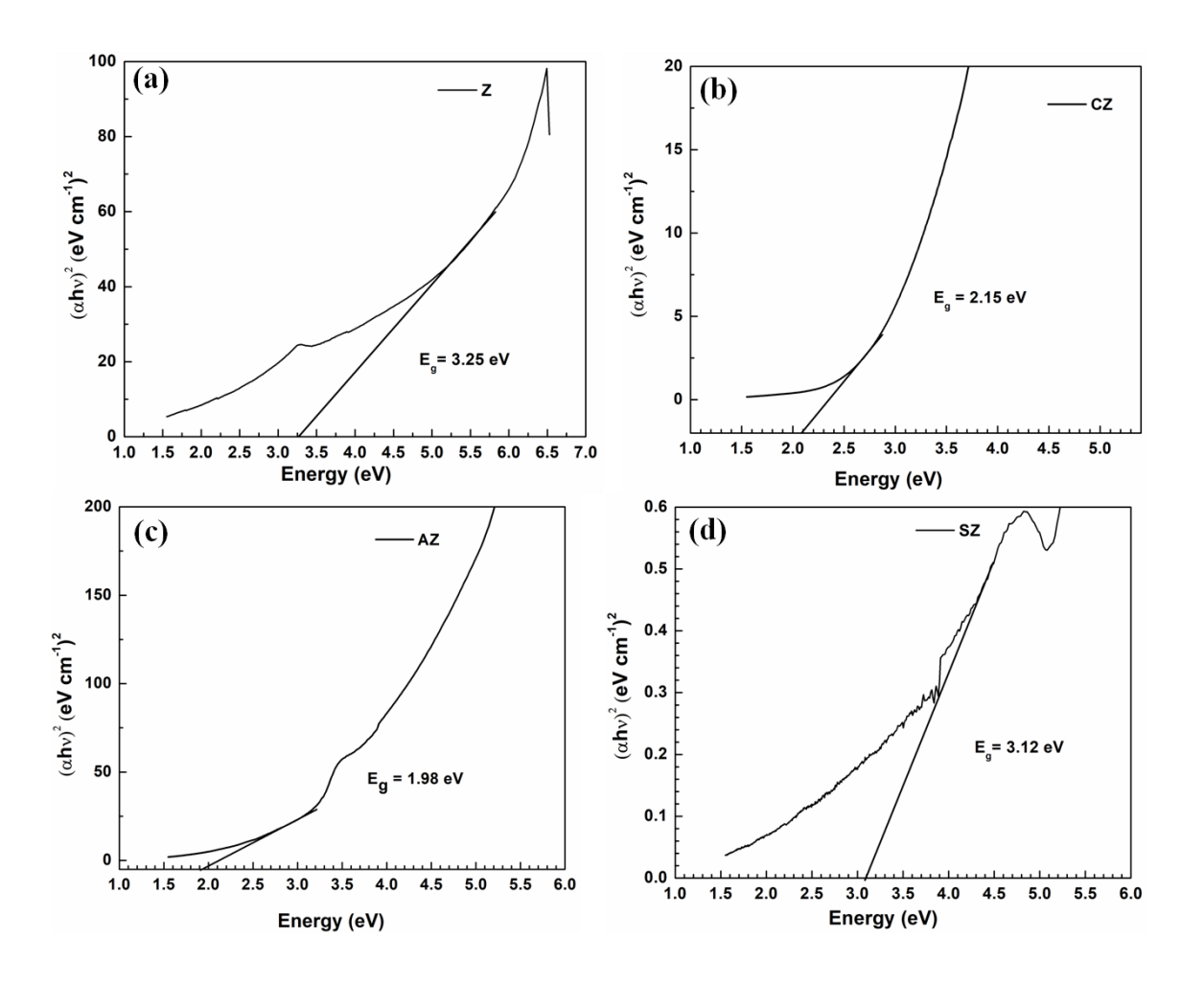


Figure 3.4: Calculation of band gap (Eg) for different samples, of (a) ZnO (Z); (b) ZnO-CuO (CZ); (c) ZnO-Ag/Ag₂ O (AZ) and (d) ZnO-SnO₂ (SZ).

The energy band gap values (E_g) were calculated for all the samples and found to be around 3.25 eV, 2.15, eV, 1.98 eV, and 3.12 eV for Z, CZ, AZ, and SZ, respectively (Fig. 3.4). This variation in E_g could be responsible for the electronic transition that occurs during the interaction between NPs with micro-organisms and differentiated their killing efficiency, which has been discussed in detail in the subsequent section (see Fig. 3.17).

Further, to check the chemical functionality, the FTIR experiments were performed for all the samples. The FTIR of the materials is shown in Fig. 3.5. The stretching bands observed at around 3500 cm⁻¹ and around 1300 cm⁻¹ are due to the presence of the O-H bonds. The stretching bands appeared at around 457 cm⁻¹, 452 cm⁻¹, 500 cm⁻¹, and 719 cm⁻¹ are due to the Zn-O bond, Cu-O bond, Ag-O, and O-Sn-O bond, respectively.

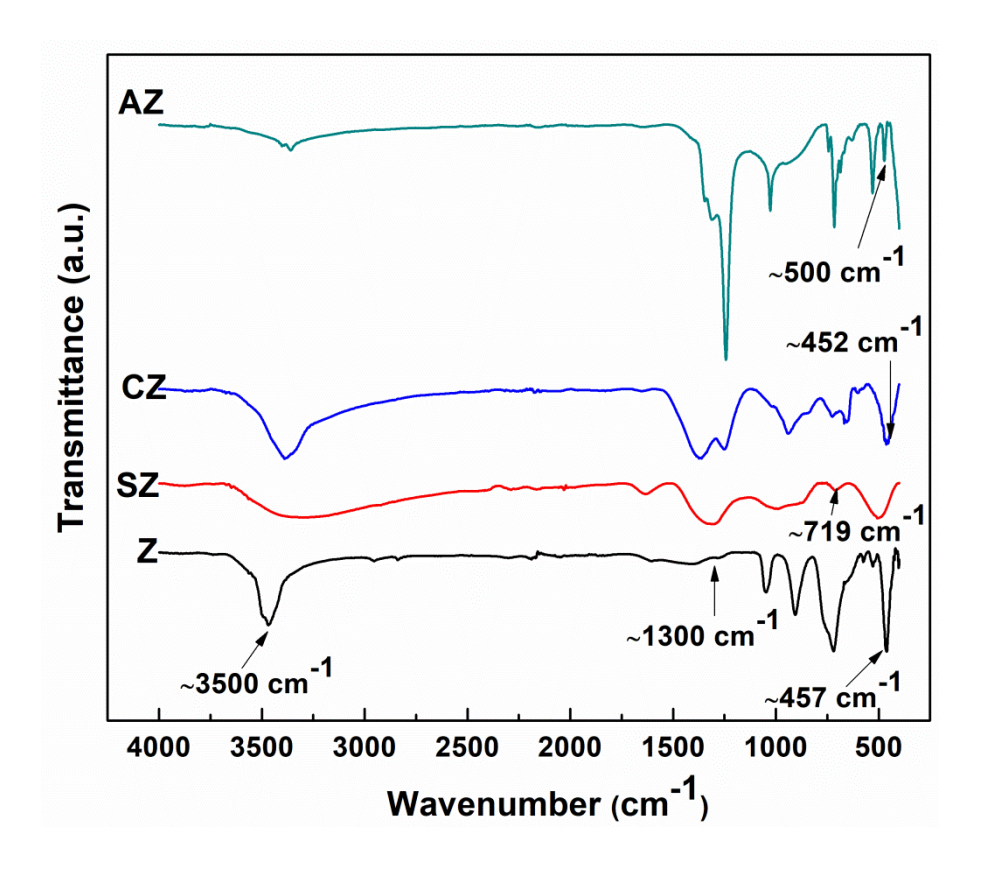


Figure 3.5: Shows the FTIR spectra for the materials.

The solid state crystal structure and phases of the synthesized materials have been examined through the powder XRD patterns (Fig.3.6). XRD pattern of ZnO NPs (Fig.

3.6(a)) is matching well with the previous report corresponding to the hexagonal Wurtzite phase of the ZnO NPs (JCPDS data card 89-0510). The peaks at $2\theta = 32.1^{\circ}$, 33.1° , 36.3° , 45.1°, 57.9°, 68.8°, 70.6° and 77.1° correspond to the (100), (002), (101), (102), (110), (201), (004) and (202) diffraction planes, respectively. The XRD pattern of ZnO-CuO NPs is shown in Fig. 3.6(b) and the diffraction peaks appearing at $20 \sim 34.4^{\circ}$ and 34.9° correspond to the (100) and (002) planes of ZnO Wurtzite hexagonal phase, respectively. Further, the peaks at $2\theta \sim 36.7^{\circ}$, 53.2° , and 74.3° correspond to the (111), (020), and (004) planes, respectively for the monoclinic crystalline phase of CuO (JCPDS file number 48-1548). 173 A trace amount of cubic Cu₂O is also present in the composite system (Fig. 3.6(b)). Fig. 3.6(c) shows the XRD pattern for ZnO-SnO₂, which is matching well with the previous report. The peaks appeared at $20\sim30.8^{\circ}$ and 34.5° correspond to the hexagonal phase of ZnO with (100) and (101) diffraction planes, respectively. Whereas, the peaks appeared at $2\theta \sim 32.1^{\circ}$, 42.7° and 62.7° correspond to the tetragonal crystalline phase of SnO₂ with (101), (120), and (310) planes, respectively. Further, it can be seen from Fig. 3.6(c) that the peak appeared at $2\theta \sim 80.17^{\circ}$ correspond to the (400) planes of SnO₂ and (014) of ZnO which are co-existed. Further, a trace amount of SnO (200) is also found. Additionally, Fig. 3.6(d) depicts the XRD peaks for ZnO-Ag₂O/Ag which consists of cubic phase of ZnO and cubic phase of Ag₂O as found out from the MATCH software pdf no. 16-153-7876 and 96-101-0605, respectively. The diffraction peaks appeared at $2\theta \sim 32.5^{\circ}$, 38.2° , 54.8° and 74.5° resemble the (111), (020), (202) and (231) diffraction planes, respectively that correspond to the cubic phase of Ag₂O. The peaks that appeared at $2\theta \sim 33.5^{\circ}$, 56.3° , and 67.4° are typically for cubic ZnO phase belong to the (111), (202), and (311) planes, respectively. Further, from XRD it is

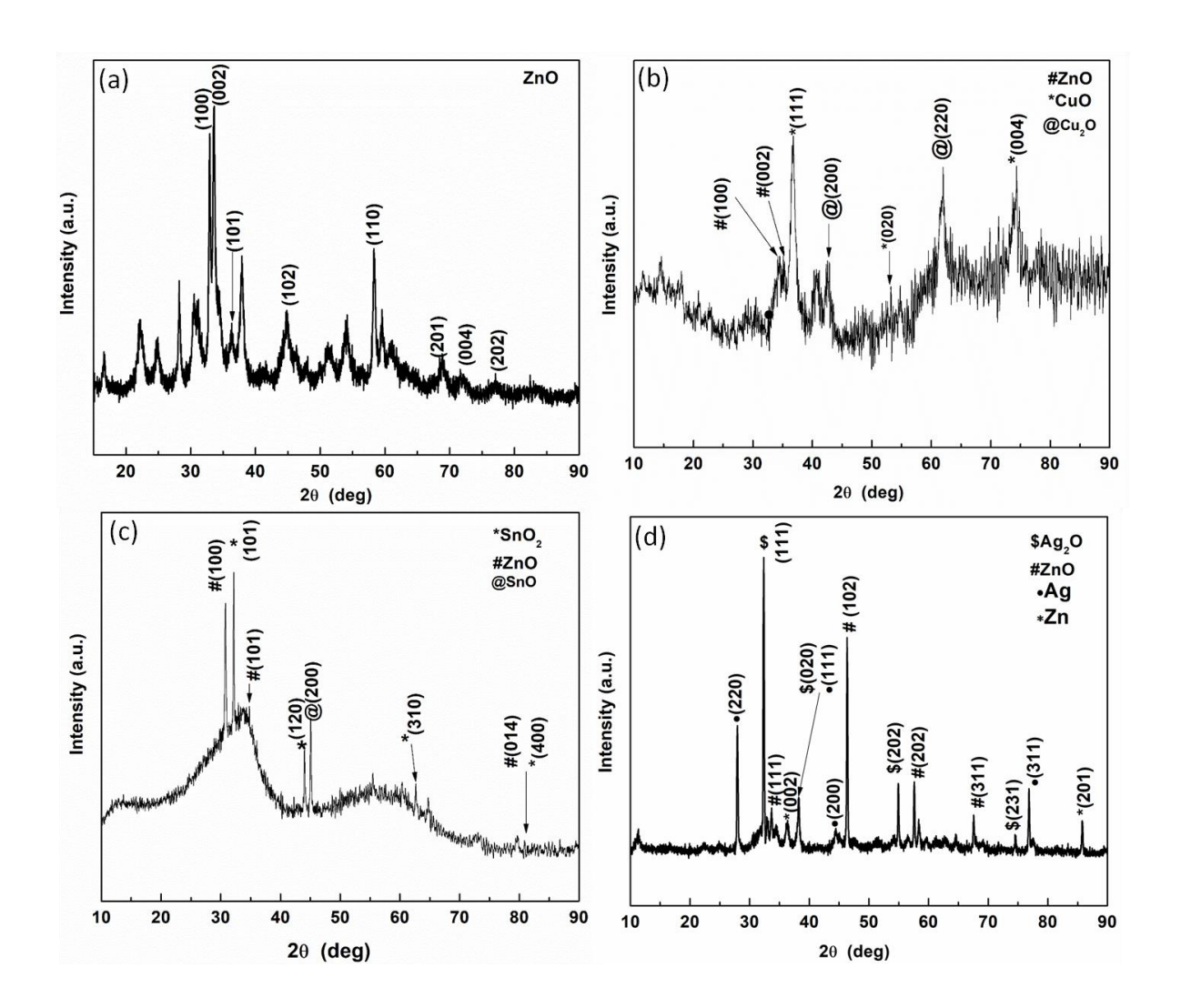


Figure 3.6: XRD patterns of (a) ZnO (b) ZnO-CuO (c) ZnO-SnO₂ (d) ZnO-Ag₂O/Ag NPs.

confirmed that the composite (i.e., ZnO-Ag₂O/Ag) consists of metallic Ag and the corresponding diffraction peaks appeared at $2\theta\sim28^{\circ}$, 38.2, 42.5° , and 77° for (220), (111), (200) and (311) diffraction planes, respectively. Therefore, obtained results prove that there are significant diffraction peaks present as evidence for the presence of

 AgO_2/Ag^0 , SnO_2 , and CuO in the final composition. Notably, there are no significant diffraction peaks observed that could be due to the lattice site substitution of ZnO or for the other elements.¹⁷⁵ In conclusion, the XRD pattern showed that the NPs combination system comprises of elemental Ag_2O/Ag^0 , CuO, and SnO_2 in different combinations with ZnO and the NP systems are crystalline in nature.

These results are further matching well with the TEM results (fringes are visible Fig. 3.1). Elemental analysis results are also matching well with the results obtained from the EDS (Fig. 3.3) and XPS experiments (Fig. 3.10). The EDS results as shown in Fig. (3.3), are also the evidence for the presence of elemental Zn and O in ZnO; Cu, Zn, and O in ZnO-CuO; Ag, Zn and O in ZnO-Ag₂O/Ag and Sn, Zn and O in ZnO-SnO₂.

To find out the physical properties such as surface area and porosity the BET surface area analysis has been conducted for all the samples and surface areas were calculated to be 61.0 m²/g, 40.1 m²/g, 23.4 m²/g, and 10.3 m²/g for the samples ZnO, ZnO-CuO, ZnO- Ag₂O/Ag and ZnO-SnO₂, respectively. Further, all the samples prepared for this work are found to be porous in nature. The BJH average pore size is found to be 3-4 nm for all the samples (see in-set of Fig. 3.7). The porous nature of the samples is further confirmed through the BJH-isotherm (adsorption-desorption), which is of the type IV category (Fig. 3.7) and the average pore size range shows that the materials are mesoporous in nature which is matching well with the porosity results obtained from the HRTEM images. It is noticed that the specific surface area has decreased in mixed oxide NPs compared to the ZnO NPs which might be due to the blocking of many micro-pores due to the presence of the tiny metal oxide NPs.¹⁷⁶ Further, the surface area of the ZnO-

CuO decreases with an increase in the average pore size. The reason behind this phenomenon is that the crystallinity/particle size is inversely proportional to the surface area and the XRD pattern shows that the ZnO-CuO (Fig. 3.6b) is quite amorphous in nature due to the smaller particle size. It can be further noted that the porous structure and the particle size strongly influence the antimicrobial properties due to the change in the

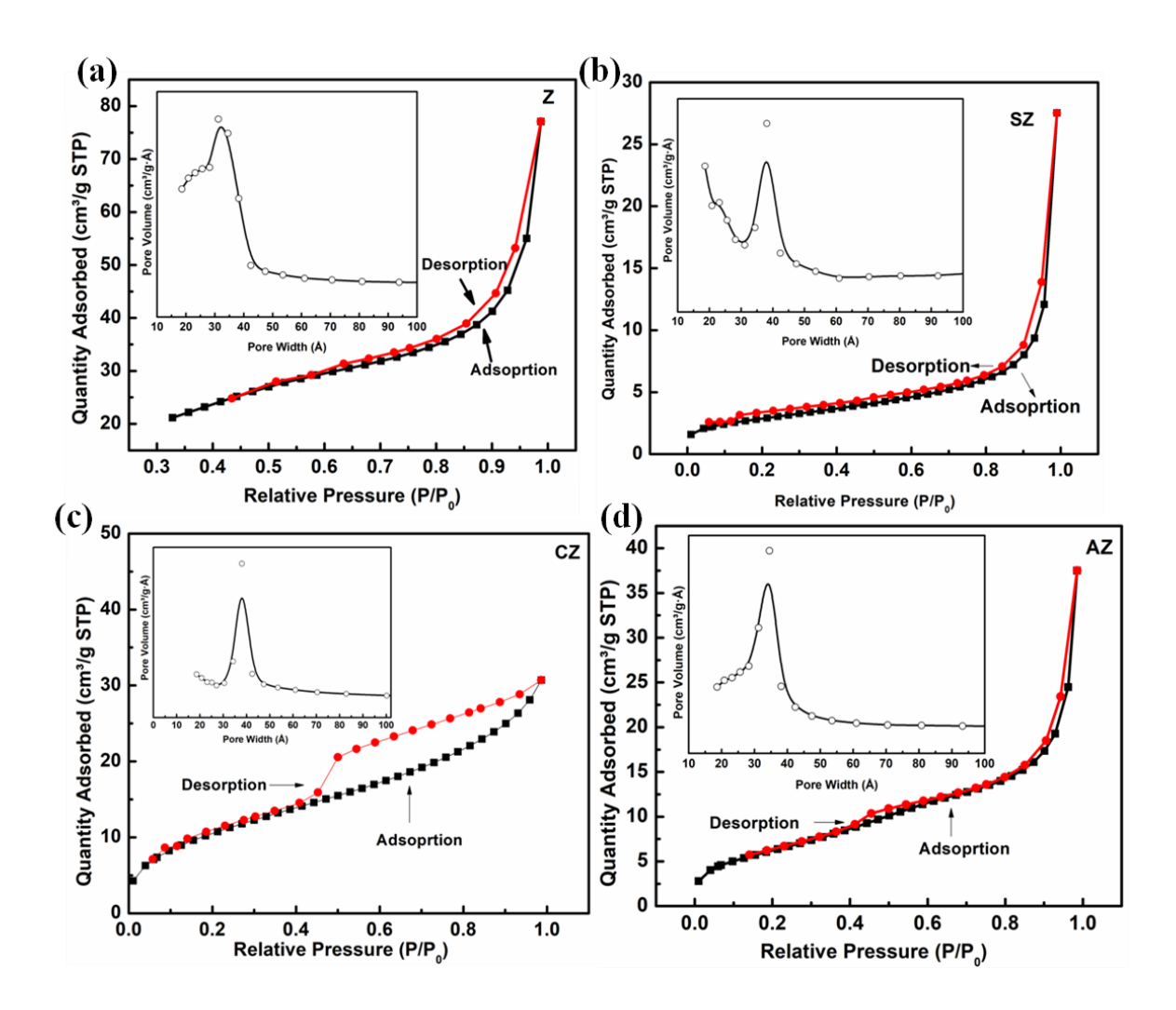
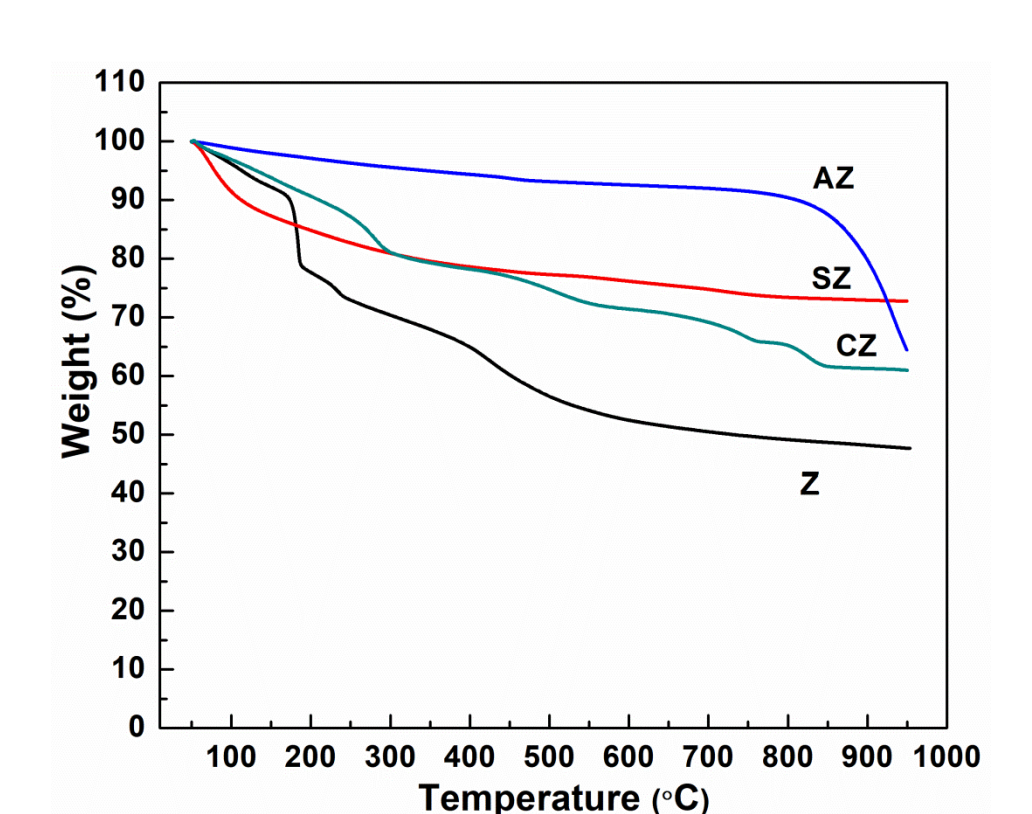


Figure 3.7. BET surface area analysis results: N_2 adsorption-desorption isotherm plots of (a) ZnO (Z); (b) ZnO-SnO₂ (SZ); (c) ZnO-CuO (CZ); and (d) ZnO-Ag₂O/Ag (AZ). Inset represents the pore size distribution results calculated from the BJH desorption pore volume data for the respective sample.



surface area as well as the availability of active sites of interactions with them.

Figure 3.8: Shows TGA results for Z (ZnO), CZ (ZnO-CuO), SZ (ZnO-SnO₂), and AZ (ZnO-Ag₂O/Ag. Experiments performed in N_2 gas environment

The thermal stability of the samples was investigated through the TGA analysis (Fig. 3.8). Results showed that the weight loss for all the samples occurred in the temperature range of 40°C≤T≤200°C due to the evaporation of unbound moisture present in the samples. The weight loss continues up to 619 °C for ZnO, 848 °C for ZnO-CuO, 745 °C for ZnO-SnO₂, and 459 °C for ZnO-Ag₂O/Ag until they become stable. The weight loss at the higher temperature occurred due to the creation of oxygen vacancy in ZnO. From the above results, we also noticed that for ZnO-Ag₂O/Ag a sharp decline or

intense exothermic peak was observed at ~800 °C (in DSC results, Fig. 3.9) which attributed to the re-crystallization of the NPs¹⁷⁷ and found stable between 459 °C \geq T \leq 800 °C. However, the obtained results describe that the mixed oxides are more stable than the single oxide (ZnO). From Fig. 3.9 (d), we observed that there is a small endothermic peak at ~438 °C and this occurred due to the release (evaporation) of Zn metal (the melting point of pure Zn is around 420°C). From Fig. 3.8, it is also clearly noticed that there is no substantial change in the thermogram. However, one endothermic peak at 190°C for Z

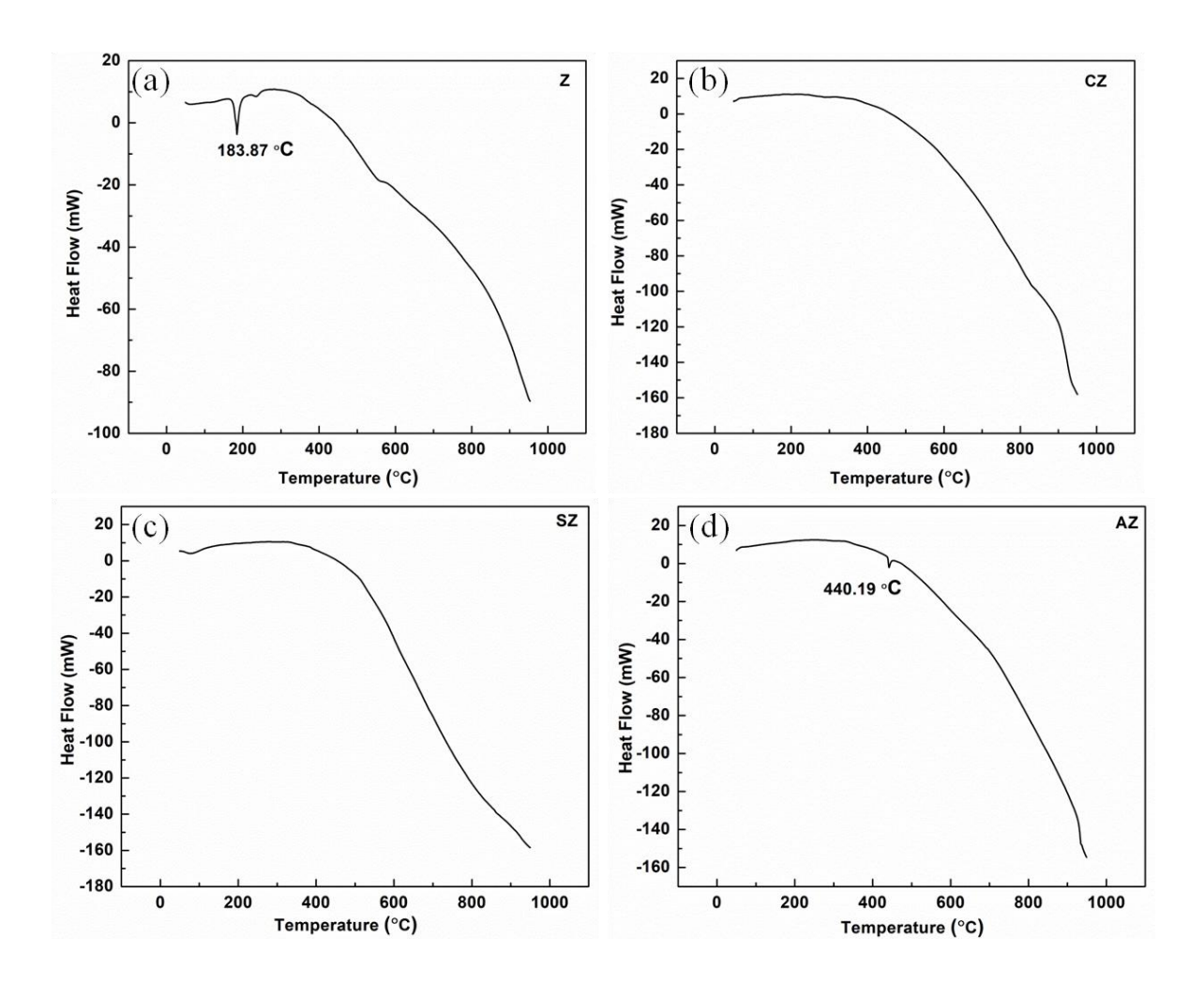


Figure 3.9:DSC of (a) ZnO; (b) ZnO-CuO; (c) ZnO-SnO₂; and (d) ZnO-Ag/Ag₂O Nanoparticle system.

(ZnO) and AZ (ZnO-Ag₂O/Ag) is observed, which may be due to the loss of moisture (from Zn-OH) (FTIR spectra Fig. 3.5).

To check the colloidal stability of the NPs, the surface charge potential was measured through surface charge zeta potential (ς) measurement of the samples without any surface modification or adding surfactant, and the \(\zeta \) values varied in the order of ZnO-SnO₂<ZnO-Ag₂O/Ag<ZnO-CuO<ZnO. The result shows that the ς values are in a broad range and colloidal stability is varied on the types of particles 178 and the NPs are suitable for biological applications. 179 Further, the stability of the composite NPs was investigated in PB, PBS (pH, 5, 6.9, 7.4, and 8), and saline solutions for seven days by keeping the fixed concentration of the samples. The obtained results have been tabulated in Table A1 to Table A4 in the Appendix section. From Table A1 it is observed that zeta potential values for ZnO (Z) in PBS of (1) pH 5 varied in between -12.0 mV to -10.9 mV for seven days; (2) for pH 6.9, potential values varied in between -15.3 mV to -20 mV; for pH 7.4 potential values varied in between -15.5 mV to -16.1 mV, and for (4) pH 8 the potential values varied from -23.4 mV to -30 mV. However, for longer period of time the potential values decreased within the time period of 2-7 days. Zeta potential values for the ZnO-Ag₂O/Ag (AZ) sample were measured in PBS and the values are tabulated in Table S3 over a time period of seven days and the values obtained to be (i) -10.9 mV to -12.3 (for pH 5), (ii) -14.2 mV to -20.8 mV (for pH 6.9); (iii) -16.2 mV to -10.1 mV (for pH 7.4) and (iv) -1.9 mV to -4.1 mV (for pH 8), respectively. Till the time period of 7th day and at higher pH (pH 8) the sample becomes unstable in PBS. In Table A2 the zeta potential values for all the samples in Saline solution have been shown and it was found

that all the samples are stable at least up to 2 days. However, over the time period of seven days their zeta potential values were decreased. Zeta potential for all the samples in Phosphate Buffer Solution (PB) have been investigated (see Table A4) and found that ZnO-Ag₂O/Ag (AZ) are quite stable in the physiological pH 6.9 and pH7.4. All the other samples are found stable in PB at different pH. In conclusion, all samplers are stable in Saline solution up to 48 h and ZnO-Ag₂O/Ag (AZ) is very stable among all the samples. Details zeta potential values are tabulated in Table A1 to Table A4.

Time scale dissolution studies for all the samples were conducted through DLS for 7 days, using Saline, PBS, and PB solutions of different pH 5, 6.9, 7.4, and 8, and the results are represented in Table A5-A11. It is evident that the hydrodynamic diameters of the particles varied in Saline, PBS, and PB. The hydrodynamic diameters have been calculated for all the samples dispersed in PBS and it shows that particle size of ZnO-Ag₂O/Ag (Table A6) is found to be quite stable, whereas for ZnO it was fluctuating (Table A5) at different pH, 5 6.9, 7.4 and 8. In Saline solution, all the types of NPs are quite stable at least for 7 days, and the stability is found more for ZnO-Ag₂O/Ag with respect to the other samples, such as ZnO, ZnO-CuO, and ZnO-SnO₂ (Table A7). For ZnO, ZnO-CuO, and ZnO-SnO₂ the increase in hydrodynamic diameters was observed, which may be due to the settlement of the particles or due to their coagulation.

Further, hydrodynamic diameters of all types of particles in PB solution of different pH (5, 6.9, 7.4, and 8) have been evaluated. More fluctuation of the size has been observed for ZnO for different pH in the entire period (Table A8), while for ZnO-Ag₂O/Ag the variation of the particle size is found to be in the considerable range (see

Table A9). A similar phenomenon was observed for ZnO-CuO (Table A10) and ZnO-SnO₂ (Table A11) at different pH and time periods. As per our analysis, this variation of the size observed may be due to the change in the pH which has further affected the dissolution of particles, as we observed the change in color of the solution. In acidic conditions, the NPs may be agglomerated at a faster rate and it is also observed that the rate of agglomeration varied for the different samples. However, we should not compare the particle size results obtained from TEM and DLS, since DLS samples were dispersed in different solutions (Saline, PB, and PBS) for up to 7 days at different pH, whereas, the TEM/HRTEM experiments were performed by dispersing the samples in iso propanol followed by drying on TEM grids (former/C coated Cu grid, Mess size 200). Therefore, from the time scale zeta potential and dissolution studies, it can be concluded that the mixed oxide NPs prepared for this work are more stable compared to the ZnO alone and good bioavailability can be achieved during any biological as well as antimicrobial applications.¹⁷⁸

XPS analysis was performed for the determination of the elemental composition of the samples and Fig. 3.10 shows the XPS spectra of the mixed oxide composites in which Fig. 3.10 (a-c) represent spectra of ZnO-CuO; Fig. 3.10 (d-f) of ZnO-SnO₂; and Fig. 3.10 (g-i) of ZnO-Ag₂O/Ag. The appeared band at ~530 eV signifies the presence of oxygen (O 1s) in each nanocomposite. In Fig. 3.10 (a) the bands appeared at energy level 933.4 eV, 77 eV, 1020.3 eV and 1043.3 eV, correspond to the binding energies for Cu 2p_{3/2}, Cu 3p_{3/2}, Zn 2p_{3/2} and Zn 2p_{1/2}, respectively. Further, a minor shift in the binding energy band of Zn, and splitting energy bands (~23eV) between Zn 2p_{1/2} and Zn 3p_{3/2}

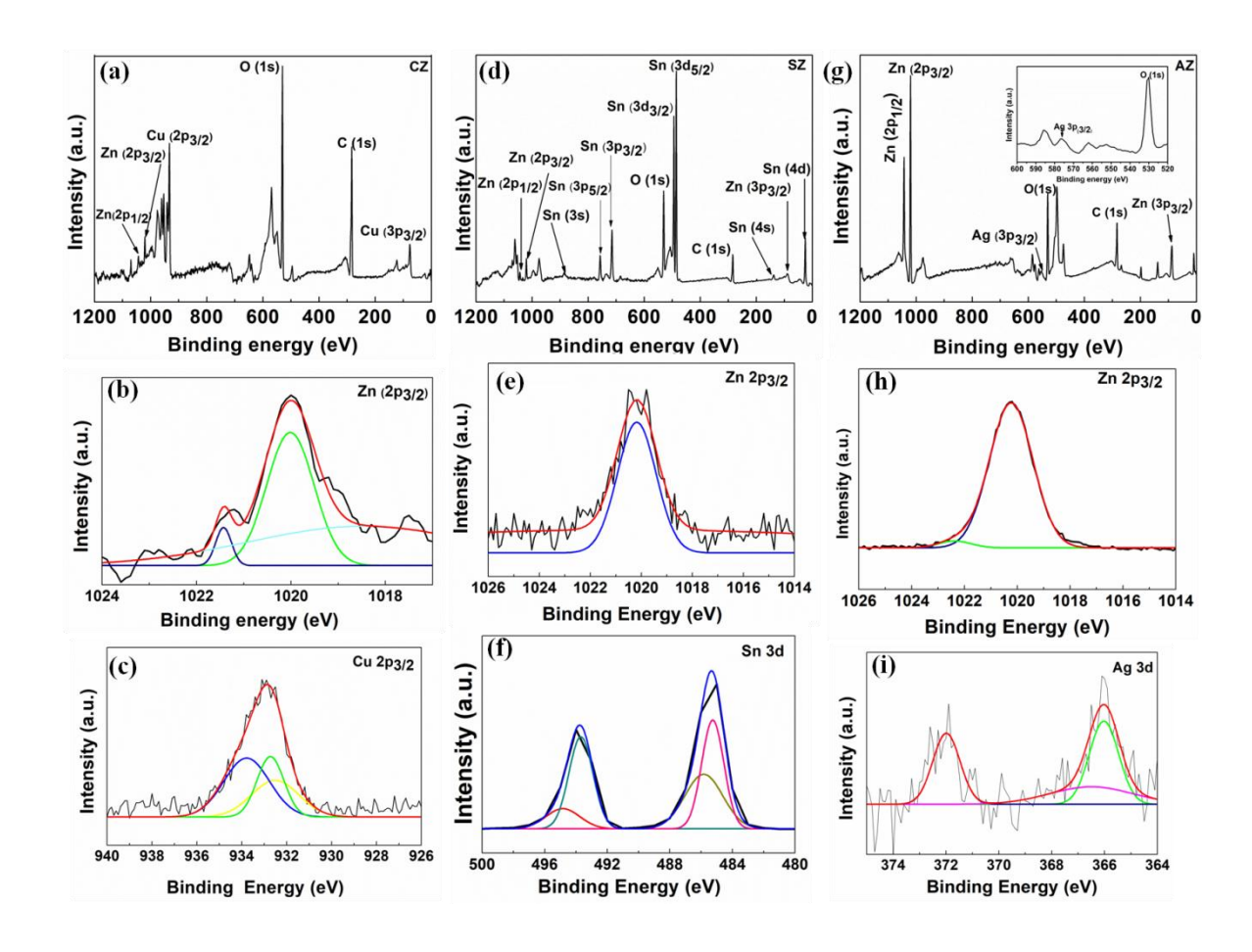


Figure 3.10: XPS spectra of (a) full range for ZnO-CuO; (b) Zn $2p_{3/2}$ of ZnO-CuO; (c) Cu $2p_{3/2}$ of ZnO-CuO. Fig.(d),the full range spectra for ZnO-SnO₂; (e) Zn $2p_{3/2}$ of ZnO-SnO₂; and (f) Sn 3d of ZnO-SnO₂. Fig. (g) shows the full range spectra for ZnO-Ag₂O/Ag; (h) Zn $2p_{3/2}$ of ZnO-Ag₂O/Ag and (i)Ag 3d of ZnO-Ag₂O/Ag

indicate the strong interactions that occurred between the CuO and ZnO due to the local difference in the atomic environment.¹⁸¹ Fig. 3.10 (c) represents the bands for Cu 2p_{3/2} of ZnO-CuO, which can be de-convoluted into three energy bands and it confirms the presence of three oxidation states of the elemental copper, i.e., Cu⁺², Cu⁺¹ and Cu⁰ in the composite system. The formation of Cu⁰ (copper zero) subsequently translated into Cu₂O (Cu⁺¹) and CuO (Cu⁺²) due to the use of strong reducing agent NaBH₄ and as the entire

reaction has been performed in the oxygen environment. The Fig. 3.10 (b) shows the XPS spectra for Zn 2p_{3/2} and the binding energy bands observed at ~1021.70 eV and ~1020 eV, which are the characteristics bands for the ZnO. From the full range of the XPS spectrum of ZnO- Ag₂O/Ag (in Fig. 3.10 (g)), it is identified that the energy bands appeared at 87 eV, 576 eV, 1020.2 eV, and 1043.2 eV corresponding to the presence of Zn $3p_{3/2}$, Ag $3p_{3/2}$, Zn $2p_{3/2}$, and Zn $2p_{1/2}$ states, respectively. Fig. 3.10 (g) has been expanded into the region between 520-600eV (represented in inset), which supports the presence of O1s and Ag 3p_{3/2}. Fig. 3.10 (i) shows the XPS energy band for Ag 3d and Fig. 3.10 (h) shows for Zn 2p_{3/2} present in ZnO-Ag₂O/Ag, which further shows that the presence of Ag₂O corresponds to the band appeared at ~367.6 eV. Interestingly, Fig. 3.10 (h) also shows the presence of Ag (~371.9 eV) and AgO (367.4 eV) in ZnO-Ag₂O/Ag. ^{182,183} This means that Ag₂O was formed during the reduction reaction and the same was transformed into the Ag⁰. Fig. 3.10 (h) shows the Zn 2p_{3/2} peak at 1020.2eV, which is matching well with the previously reported results. For XPS spectra of ZnO-SnO₂, bands for Zn 2p and Sn 3d are depicted in Fig. 3.10 (d), (e), and (f), respectively. The bands appearing at 88eV, 139.9eV, 485eV, 494eV, 715eV, 757eV, 884.8eV, 1020eV and 1043eV correspond to the presence of Zn $3p_{3/2}$, Sn 4s, Sn $3d_{5/2}$, Sn $3d_{3/2}$, Sn $3p_{3/2}$, Sn $3p_{5/2}$, Sn 3s, Zn $2p_{3/2}$ and Zn $2p_{1/2}$, respectively. The band observed at 25.1eV is a characteristic peak for Sn 4d (Sn⁺²) state, which suggests that it indeed formed SnO₂ NPs. 184 It is also evident for the presence of Sn and SnO which has been confirmed from XRD results (Fig. 3.10 (c)). The binding energy of elemental oxygen at 530eV also suggests that it appeared due to the presence of metal oxide. 184,185 The minor peak shifting for Sn 3d is observed, which might be due to the chemical modification and

lattice interactions between the elemental Zn and Sn, which further has been supported by the TEM results (Fig. 3.1(c)). All these results are interesting for their use as an antimicrobial component, which has been explained in the subsequent section.

3.1.4.2 In-silico studies results

Then the in silico computational approach was taken into consideration to determine the bactericidal/fungicidal activities of bimetallic composite NPs compared to the single metal oxide NPs. Molecular interaction between NP with Quorum sensing regulator PqsR (PDB ID: 4JVI), response regulator RstA (PDB ID: 5E3J), fosfomycin resistance protein (PDB ID: 5WEW), and Heat Shock protein 90 (PDB ID-6CJP) have been analyzed. The binding energy and affinity, inhibitory constant, interacting polar bonds, and interacted amino acids for the single metallic/oxide and bimetallic/oxide NPs have been represented in Table 3.1, Fig. 3.11, and Fig. 3.12. For single metallic/oxide NPs the highest binding energy affinity was observed when CuO NPs interacted with the PqsRA, RstA, and Hsp90 and the values are -7.50, -5.33, and -5.72 (kcal/mol), respectively, While ZnO NPs interacted with the FosA with a required binding energy affinity of -5.17 kcal/mol (see Table 3.1). It is further observed that a very low binding energy for Ag and SnO₂ NPs required, while ZnO NPs were required almost in an equivalent amount of binding energy for PqsR, RstA, FosA, and Hsp90, such as -5.61, -4.83, -5.17, and -4.97 kcal/mol, respectively. It is also found out that the higher polar interactions played with ZnO nanoparticles along with all the listed proteins. Therefore, a combination of ZnO-CuO, ZnO-SnO2, and ZnO-Ag2O/Ag have been chosen for further protein-ligand interactions analysis (Ribbon structure in Fig. 3.11 and Fig. 3.12),

hydrogen bond (thin green line with) polar and nonpolar interactive amino acid (spherical) have been represented in Fig. 3.11 and Fig. 3.12. Inhibition constants are calculated for the interactions between ZnO with PqsR, RstA, FosA, and Hsp90, which are as follow: 77.18 μM, 289.86 μM, 163.38 μM, and 227.87 μM, respectively. CuO NPs also interacted with the PqsR, RstA, FosA, and Hsp90 and the interaction constants obtained to be 3.17 µM, 123.94 µM, 4.43 µM, 64.22 µM, respectively. While for all the bi-metallic/oxide NPs, during the interaction with PqsR, RstA, FosA, and Hsp90 the inhibition constants decreased to nanomole with the increase in the binding energy affinity. Among these three nanoparticle systems such as ZnO-CuO, ZnO-SnO₂, and ZnO-Ag₂O/Ag, the highest binding energy affinity was observed for ZnO-Ag₂O/Ag, while it was interacting with the PqsR, RstA, FosA, and Hsp90 and the values calculated to be -9.79, -12.0, -11.57 and -11.32 (kcal/mol), with minimum inhibition constants of 66.48 nM, 1.61 nM, 3.33 nM, and 5.06 nM, respectively. It is also noticed that ZnO-CuO, ZnO-SnO₂ and ZnO-Ag₂O/Ag NPs possessed excellent antimicrobial and antifungal activities with higher efficiencies compared to the single metal or metal oxide NPs. However, among these NPs the ZnO-Ag₂O/Ag NPs exhibited the highest antimicrobial efficacy compared to the other samples used. It can also be noticed that the presence of octahedral and cubic phase of Cu₂O can affect the antibacterial activity, ¹⁸⁶ however the extent of Cu₂O present in our composite system is very less/negligible.

Further, the intermolecular interacting amino acids and the hydrogen bonding resulting with ZnO, CuO, ZnO-CuO, ZnO-SnO₂, and ZnO-Ag₂O/Ag are shown in Fig. 3.11 and Fig. 3.12, and for *P. aeruginosa* (Fig. 3.11A), *A. baumannii* (Fig. 3.11B), *K.*

pneumoniae (Fig. 3.11C) and C. albicans (Fig. 3.11D), respectively. P. aeruginosa (gram-negative) bacterium is a causative agent of nosocomial infection. Virulence factor PqsR involved in the pathogenicity belongs to the family of LysR type transcriptional regulators. The active motif of PqsR can interact with the various inhibitors such as (i) quinolone derivative interacting amino acids including Asn206(H), Arg209(H), Leu197(H), Glu259(H), Phe221, Leu207(H), and Ser196, 187 (ii) Stigmatellin Y interacting amino acids including Pro129, Ala187, Ala190 and Val211, 188 and (iii) Zingerone interacting amino acids including Leu208(H), Gln194(H) Met 224 Ile236 and Leu207, Val211, Pro210 Arg209 and Ser196. From our study, it is observed that except ZnO-Ag₂O/Ag, other NPs (Fig. 3.11 (A.1, A.2, A.3 and A.4,)) interacted with the active motif of PqsR (represented in bold in Table 3.1) and it showed the anti-biofilm activity. ZnO forms hydrogen bonding with the Gln194, Leu19, and Ile236 and with other intermolecular interactions with Val211, Pro210, Arg209, and Leu208 (Fig. 3.11 A.1). While shows that the ZnO-Ag₂O/Ag NPs interact at different motifs with higher affinity forming the hydrogen bonds with Tyr240, Ser106, and other interacting nonpolar interaction proteins including Gly296, His239, Lys167, Thr166, and Pro104 (Fig.3.11 A.5). RstA(BfmR) is a master regulator of bio-film initiation in A. baumannii which is regulated by csu operon and increased the resistance towards the erythromycin, colistin, imipenem, rifampin. The csu operon was involved in the attachment of biofilms to abiotic surfaces both in nature and in the clinic. Molecular dynamic stimulation showed the α4β5-α5 segments of BfmR is an active motif. 190 Crystal structure of BfmR is an active homodimer conformation consisting of two active residues such as Thr85 and Tyr104. Previous studies showed strong binding hot spot residues including Arg124 and His78,

while Glu98, Arg112 and Arg119; Asp102 and Arg124; and Asp103 and Arg117 residues were involved in the salt bridge formation. As represented in Fig. 3.11 (B.1, B.2, B.3, B.4 and B.5) and Table 3.1, our *in silico* studies showed that the ZnO, CuO, ZnO-CuO, ZnO-SnO₂, and ZnO-Ag₂O/Ag NPs interacted at an active site of BfmR and it is represented in bold.

Expanded clinical usages of fosfomycine result in the development of fosfomycine resistant K. pneumoniae strain. Fosfomycine shows a bactericidal effect only when the fosA gene is deleted. Investigation of FosA inhibitor will help in overcoming multidrug resistance. 166 Important interacting residue of FosA includes \(\beta 2 - \beta 3 \) from residues 31 to 46 and β 6- α 3 helix residue from 115 to 135. The interactions with 5WEW between NPs such as ZnO, CuO, ZnO-CuO, ZnO-SnO2, and ZnO-Ag2O/Ag have been shown in Fig. 3.12 (C.1, C.2, C.3, C.4 and C.5). Polar interactions formed between (i) CuO with Tyr131; (ii) ZnO with Arg55, Thr58, Ser63, and Lys111; (iii) ZnO-CuO with Ser63 and Lys111, (iv) ZnO-SnO₂ with Asp64 and His110, and (v) ZnO-Ag₂O with leu119 and Gln121 with highest binding affinity -11.57 (kcal/mol). Other interacting amino acids are represented in Table 3.1 and Fig. 3.11 and Fig. 3.12 can also interact. Further, molecular chaperone Hsp90 governs the key function of morphogenesis, and inhibition of Hsp90 alters the capsule assembly and virulence property of the pathogen. The co-crystal structure of the Hsp90 nuclear binding domain of C. albicans with CMLD013075 showed the unique target specific structural rearrangement. 192 Hsp90 inhibitor showed antifungal activity when it was bound to the ATPase domain form residues 29-184. 192,193

Table 3.1: Binding energy (kcal mol⁻¹) and interaction parameters of NPs with interacting proteins calculated from *in silico* study. It can be noted that the bold residues represent active binding sites that interacted with inhibitors reported on PDB and earlier publications.

Sr. No		Ligand NPs	Binding energy (kcal/mol)	Inhibition Constant	Hydrogen Bond/ amino acid residue	Amino acid interaction
1	P. aeruginosa PqsR (MvfR) PDB ID 4JVI	Ag	-1.64	63.28 mM	-	SER205, GLN203, HIS204, LEU208, ASP150, ASP131, SER199, SER201
		SnO2	-3.92	1.33 mM	ILE155 (1.766 Å)	LYS154, ILE155, GLN160, TYR270,
		ZnO	-5.61	77.18 μM	GLN194 (2.085 Å) LEU197 (1.922Å) ILE236 (2.173Å)	VAL211, PRO210, GLN194, ARG209, LEU208, LEU197, ILE236, LEU197
		CUO	-7.50	3.17 μΜ	LEU197 (1.931Å) ILE236 (1.875Å)	GLN195, LEU208,LEU197, SER196,PHE221, MET224, ILE236
		ZnO-CuO	-9.03	241.04 nM	LEU197 (2.248Å)	GLN194, LEU208 , SER196, LEU197 ILE236 , ILE149, ALA168, ALA237, PHE221
		ZnO-SnO ₂	-9.07	224.6 nM		ILE186, LEU189, VAL211, TRP234, TYR258, ILE236
		ZnO-Ag ₂ O/Ag	-9.79	66.48 nM	SER106 (2.099Å) TYR240 (2.096Å)	TYR240, SER106, GLY296, HIS239, LYS167 , THR166, PRO104
2	A. baumannii RstA PDB ID- 5E3J	Ag	-1.73	53.94 mM	-	THR23, ALA20, ILE12, VAL56,VAL13,GLU14, ASP58, LEU84
		SnO2	-3.90	1.39 mM	-	ILE12, VAL56
		ZnO	-4.83	289.86 μΜ	ALA106 (1.905 Å) ARG117 (2.162 Å) GLN93 (2.106 Å) ALA106 (2.143 Å)	ARG117, VAL105, ALA106,GLN93, TYR104
		CuO	-5.33	123.94 μM	ARG124 (2.207 Å) HIS78 (2.151 Å)	HIS78, ARG123, ARG124, GLY100, ARG74
		ZnO-CuO	-7.50	3.18 μΜ	ARG117 (2.096 Å) GLN93 (1.873 Å)	VAL104, ALA106, VAL109, GLN93, ARG117, VAL113, GLN110
		ZnO-SnO ₂	-10.72	13.94 nM	GLN93 (1.754 Å) ALA106 (2.022 Å)	VAL113 , GLN93, TYR104 , ARG117 , VAL105, ALA106 TYR104
		ZnO-Ag ₂ O/Ag	-12.0	1.61 nM	ALA106 (2.034 Å) GLN110 (2.207 Å) ALA106 (1.893 Å)	VAL105, VAL109, VAL113 , ALA106, LYS107, GLN93 , ARG117 , TYR104 , GLN110, ALA106
3	K. pneumoniae/ FosA PDB ID- 5WEW	Ag	-1.48	82.78 mM	-	LEU114, ILE72, PHE70, SER71, MET28, CYS42
		SnO2	-3.60	2.31 mM	LYS111 (1.914 Å)	LYS111, THR66, HIS110
		ZnO	-5.17	163.38 μΜ	ARG55 (1.830 Å) THR58 (2.232 Å) SER63 (1.626 Å) LYS111 (1.761 Å)	ARG55, GLY109, THR58, LYS111, THR66, ASP64, SER63
		CuO	-3.21	4.43 mM	TYR131 (2.209 Å)	ARG96, GLN129, TYR131, GLN129
		ZnO-CuO	-7.44	3.54 μΜ	SER63 (1.661 Å) LYS111 (1.839 Å)	SER63, LYS111, ARG55, GLY109, HIS110, THR66, TYR68
		ZnO-SnO ₂	-8.04	1.28 μΜ	ASP64 (1.948 Å) HIS110 (2.238 Å)	SER63, THR58, ARG55, TYR68, HIS110, THR58, ASP64
		ZnO-Ag ₂ O/Ag	-11.57	3.33 nM	LEU119 (1.852 Å) GLN121 (2.119 Å)	LEU119, SER118, HIS115 , GLY117,VAL116, ILE72, SER71, GLU74, GLN121
4	C. albicans Hsp90 PDB ID - 6CJP	Ag	-1.63	63.89 mM		LEU176, ASN40 , THR174 , ILE80, ASP82 , ALA41, ARG81, ILE67
		SnO2	-4.14	926.71 μM	ILE99 (2.024 Å)	ILE99
		ZnO	-4.97	227.87μΜ	GLN5 (2.049 Å) ILE99 (2.046 Å)	THR98, ILE99, ILE15, THR12, GLN5, PHE4
		CuO	-5.72	64.22 μΜ	LYS47 (2.174 Å) GLY86 (1.920 Å)	MET87, ASN40, GLY86, LYS47, ILE85, ALA44
		ZnO-CuO	-8.61	486.66 nM	GLN5 (2.194 Å) ILE99 (1.825 Å)	ALA13, GLY157, PHE159 , HIS9 , THR12, SER16, GLN5, ILE15, PHE4, GLY97, ILE99
		ZnO-SnO ₂	-9.31	149.24 nM	ASN95 (2.220 Å) GLY126 (2.148 Å)	PHE127, THR98, GLY126, GLY124, ASN40, ASN95
		ZnO-Ag ₂ O/Ag	-11.32	5.06 nM	THR12 (2.018 Å) LYS89 (2.055 Å)	LYS158, THR160, PHE159, VAL161, ALA13, HIS9, THR12, GLU10, VAL93, LYS89, GLU7, THR8

Single or bimetallic oxide NPs interacted with ATPase domain residues as they are shown in Fig. 3.12 (D.1, D.2, D.3, D.4, and D.5). Polar interactions occurred for (i) CuO with Lys47 and Gly86; (ii) ZnO with Gln5 and Ile99, (iii) ZnO-CuO with Gln5 and Ile99,

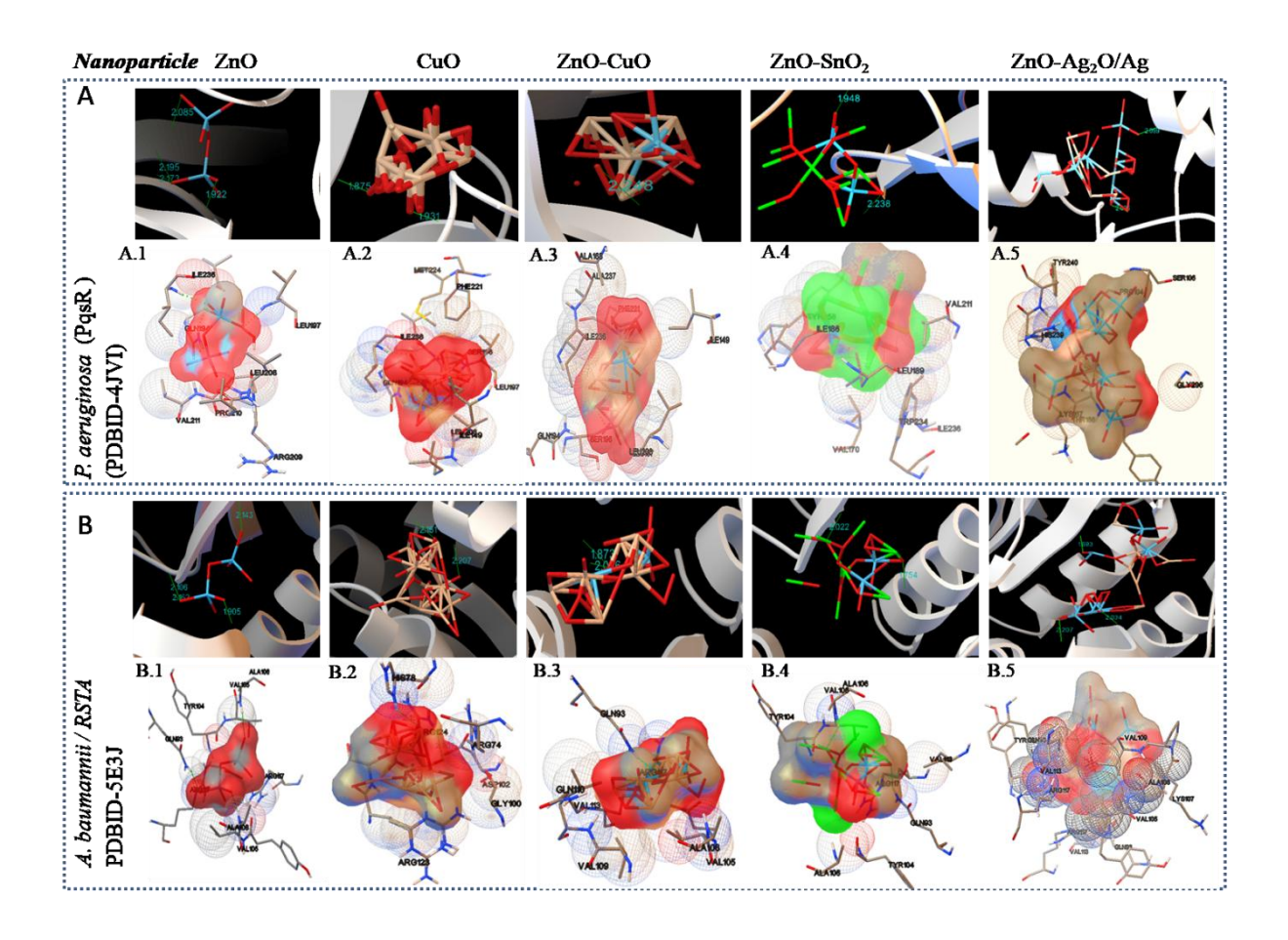


Figure 3.11: Show molecular interactions of bacterial/fungal proteins with NPs. A and B are the crystal structure of PqsR and RstA (BmfR) (ribbon structure), respectively. A.1, A.2, A.3, A.4, and A.5 (upward) showed PqsR interactions and hydrogen bonding (green thin line with distance) with ligand ZnO (Zn -Blue), CuO (Cu-peach), ZnO-CuO, ZnO-SnO₂ (Sn-lime green) ZnO-Ag₂O (Ag-Coral), respectively. B.1, B.2, B.3 B.4 and B.5 Crystal structure BmfR interacted with ligands such as ZnO (Zn -Blue), CuO (Cu-peach), ZnO-CuO, ZnO-SnO₂ (Sn-lime green), and ZnO-Ag₂O (Ag-Coral), respectively. Downward figures represent the interacting residues of amino acids of active pocket and oxygen molecules (red).

(iv) ZnO-SnO₂ with Asn95 and Gly126 and (v) ZnO-Ag₂O/Ag with Thr12 and Lys89. Many interactions observed with other residues are represented in Table 3.1 and Fig. 3.12.

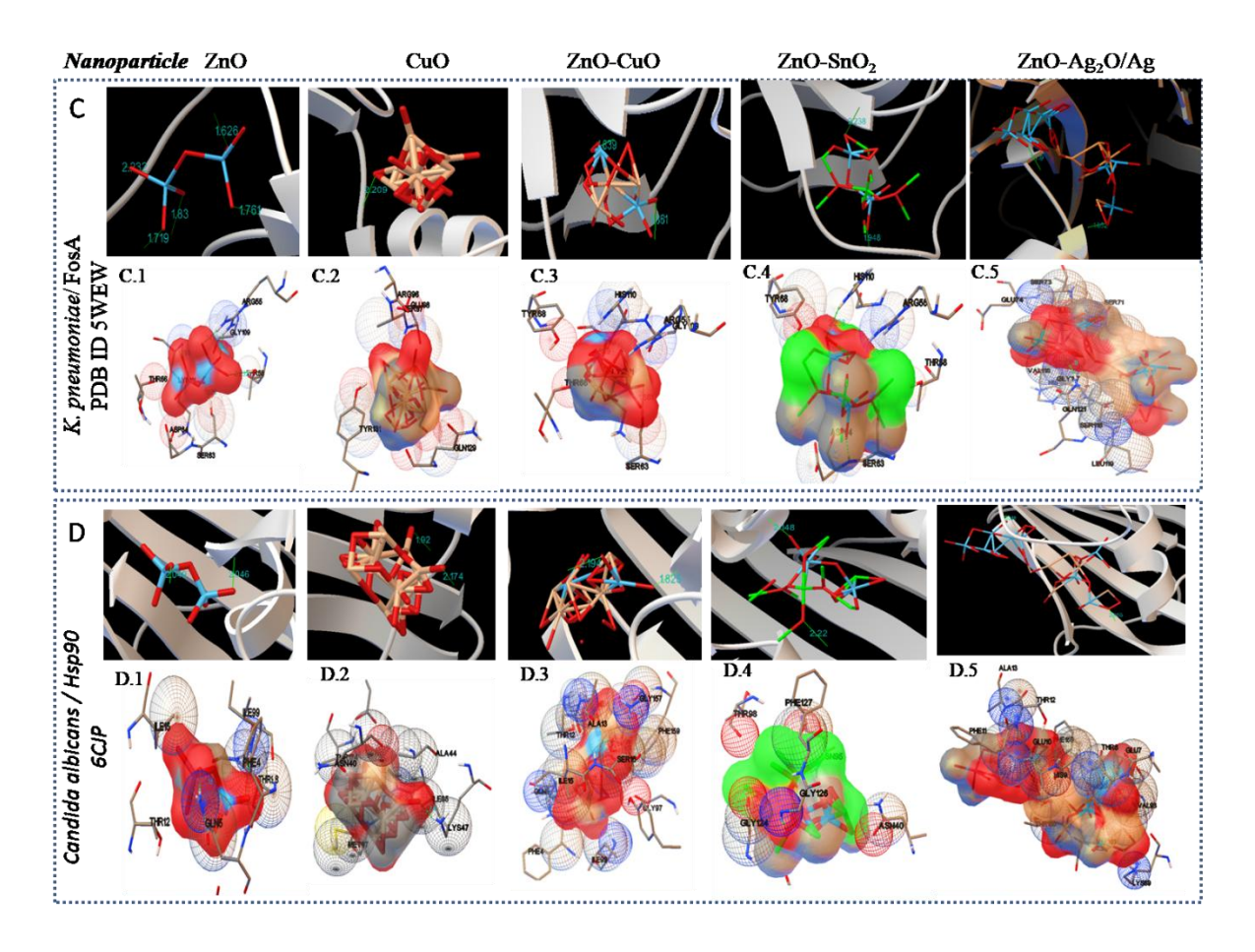


Figure 3.12: Molecular interactions of bacterial/fungal proteins with NPs. C and D represented the crystal structures of FosA and Hsp90 (ribbon structure), respectively. C.1, C.2, C.3, C.4 and C.5 (upward) showed FosA interactions and hydrogen bonding (green thin line with distance) with ligand ZnO (Zn -Blue), CuO (Cu-peach), ZnO-CuO, ZnO-SnO₂ (Sn-lime green) and ZnO-Ag₂O (Ag-Coral), respectively. D.1, D.2, D.3 D.4, and D.5. Crystal structure Hsp90 interacted with ligand ZnO (Zn -Blue), CuO (Cu-peach), ZnO-CuO, ZnO-SnO₂ (Sn-lime green) ZnO-Ag₂O (Ag-Coral), and oxygen (red), respectively. Downwards figures represented the interacting residues of amino acids of active pocket with NPs.

In comparison to ZnO, when ZnO is doped with CuO, SnO₂, and Ag₂O, the antibacterial and antifungal properties are found enhanced significantly in many folds. Among these three doped compositions, *in silico studies* conclude that ZnO-Ag₂O/Ag is an effective component having the highest antimicrobial properties. Further, we have performed *in vitro* studies for all the components since all are indicating good targeted results.

3.1.4.3 In-vitro studies results and mechanism:

Finally, the *in vitro* antimicrobial study was conducted against *E. coli* according to the method mentioned in the experimental section. The OD₆₀₀ values were calculated with a regular interval of three hrs for up to 12 hrs for each set of samples and at various concentrations, i.e., 0µg/ml, 50µg/ml, 250µg/ml, 500µg/ml, 750µg/ml and 1000µg/ml. The antibacterial activity results of different NPs in different concentrations with different time intervals have been shown in Fig.3.13. All the NPs exhibited regular trends that increase in the concentration from 50 µg/ml to 1000 µg/ml the antibacterial activity or rate of inhibition increases after 3 h and the highly effective results have been obtained. The ZnO acts as an antibacterial agent in two ways: (i) by ROS generation and (ii) by Zinc ions release/diffusion, ¹⁵¹ Similarly, many antimicrobial mechanisms have been proposed using silver nanomaterials.¹⁵² Ag NPs can penetrate bacterial cell walls through pits formation and release silver ions that inhibit the growth of micro-organisms. For CuO and SnO₂ NPs, the antibacterial mechanisms have also been discussed and it also has been narrowed down to ions release as well as ROS formation, which attack the important cellular components and kill the microorganisms. 94,153

Metallic NPs can also inhibit the growth of the micro-organism. 154 And similarly

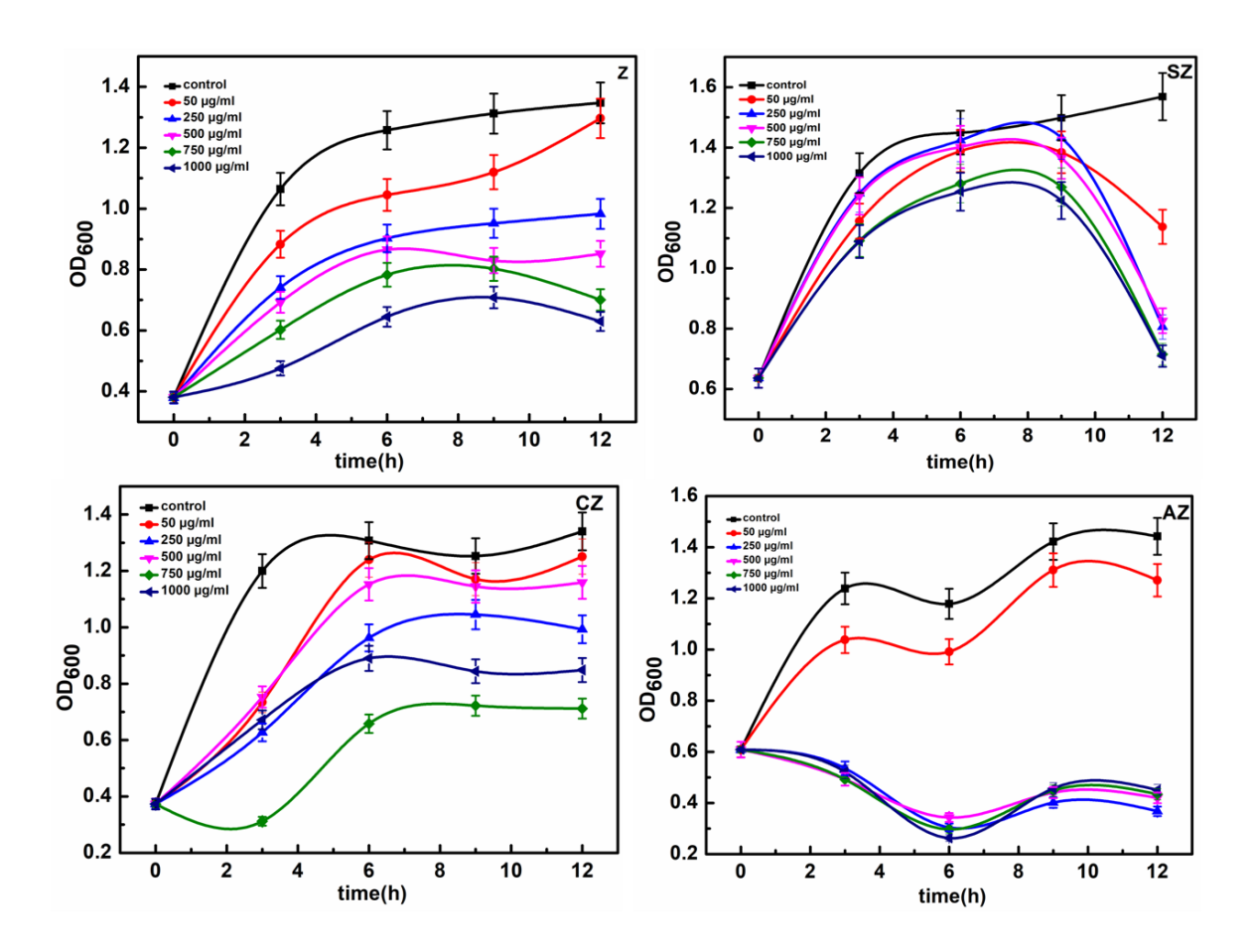


Figure 3.13: Antibacterial activity results of (Z) ZnO, SZ (ZnO-SnO₂) CZ (ZnO-CuO), AZ (ZnO-AgO₂/Ag) in different time intervals with E. coli.

we can conclude that the present antibacterial materials also follow the ROS mechanism which subsequently has been discussed (Fig. 3.17).

However, mixed bimetallic oxides combination with tiny metallic NPs (of size 2-3 nm) accelerated the antimicrobial activities much more through a cooperative electrochemical mechanism and the band energy gap (E_g) altered and subsequently promoted the ROS formation.

Further, in vitro studies were conducted for screening of antimicrobial and

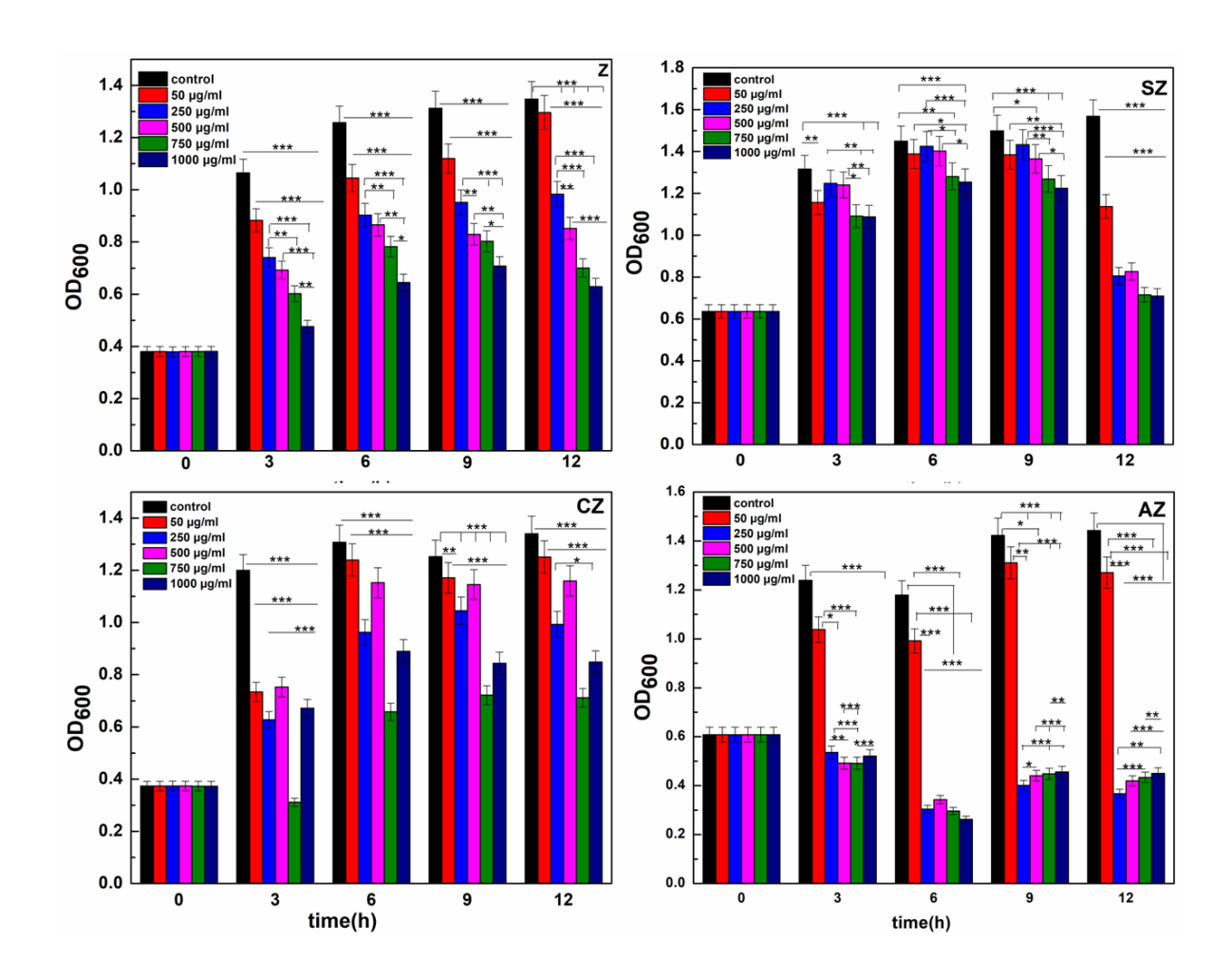


Figure 3.14: Antibacterial activity of (Z) ZnO, SZ (ZnO-SnO₂) CZ (ZnO-CuO), and AZ (ZnO-AgO₂/Ag) in different time intervals with E. coli (Dh5 α).

antifungal activities of synthesized NPs through ZOI studies (Fig. 3.15-3.16) and their efficacy was evaluated through the calculation of MIC.

Some nosocomial bacterial strains were selected for this study because these bacteria and fungus can form bio-films on the biomedical implants in the hospital quickly and increase the infection levels. Herein, we have calculated the MIC values for all the synthesized mixed metal oxide/metal NPs and their results were calculated with their single metal

oxide NPs keeping the molar equivalent metallic components. Few mixed oxides NPs exhibited excellent MIC results as it is shown in Table 3.2. From Fig. 3.15-3.16, it is evident that the mixed metal oxide composite NPs (ZnO-Ag₂O/Ag) exhibited excitingly a maximum of 17 mm ZOI in P. aeruginosa, 11.2 mm in K. pneumoniae, 14 mm in A. baumannii, and with 10.5 mm inhibition in C. albicans. Consequently, ZnO-CuO NPs exhibited ZOI of 9.25 mm in A. baumannii, 8.1 mm in P. aeruginosa, 8.2 mm in K. pneumoniae, and 8 mm inhibition against the C. albicans. For ZnO-SnO₂, the ZOI was calculated to be 8.5 mm, 6.25 mm, 9 mm, and 7 mm for C. albicans, K. pneumoniae, A. baumannii, and P. aeruginosa, respectively. These results were compared with the results obtained for ZnO NPs alone with an equivalent molar concentration of metallic Zinc and found the ZOI results obtained to be 8 mm in P. aeruginosa, 6.5 mm in K. pneumoniae, 8 mm in A. baumannii and 9.5 mm in C. albicans. Thus mixed metal oxide NP system with ZnO exhibited noticeably very high antimicrobial activities compared to the ZnO NPs alone. Thus, it can be concluded that the mixed oxide composite NPs are excellent in preventing bacterial and fungal growth as well as act as better fungicidal and bactericidal activities compared to a single oxide system such as ZnO, CuO, Ag₂O, AgO, or SnO₂. It can only be possible when mixed oxide NPs can rupture or distort the phospholipid bilayer membrane of bacteria cells with higher penetration rates and with higher electronic interaction in a cooperative manner and consequently gives excellent results as a whole. Further, mixed oxide NPs can alter or block the ion channels present on the membrane better than a single type of oxide. Additionally, it can be assumed that the tiny mixed oxide NPs (size below 5 nm, about 2-5 nm size) can easily penetrate through the cellular membrane directly with a cooperative understanding which further creates more

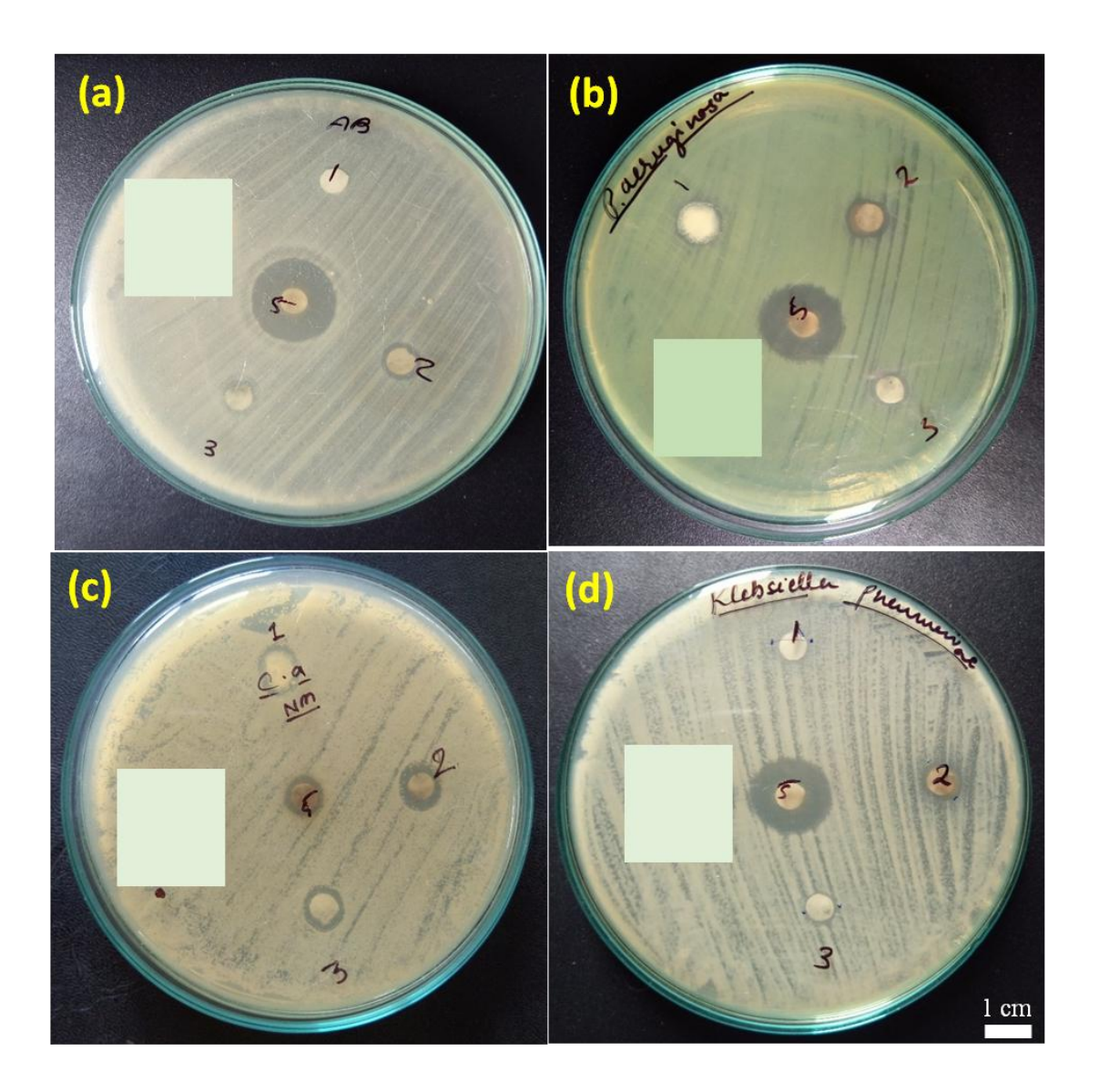


Figure 3.15: ZOI results obtained for (a) A. baumannii (b) P. aeruginosa (c) C. albicans and (d) K. pneumoniae. '1', '2', '3', and '5' labels used for the (Z) ZnO, CZ (ZnO-CuO), SZ (ZnO-SnO₂), and AZ (ZnO-AgO₂/Ag), respectively.

oxidative stress through participation in physiochemical reactions and disturbs the overall balance of the inter cellular environment and subsequently damages the genetic materials of microorganisms and promote the leakage of internal components of microorganism.¹⁹⁴

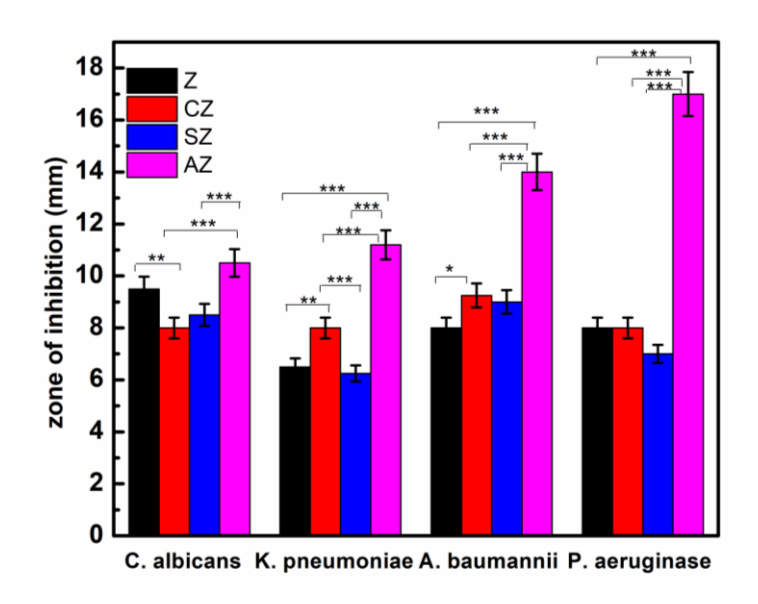


Figure 3.16: Bar plot representation of ZOI in different strains obtained using different metal oxide composite NPs (*P<0.05, **P<0.01, and ***P<0.001).

Raghunath *et al.*¹⁵⁰, reported that antibacterial properties increased with the decrease in the particle size for single metal oxide NPs. In this line, we can propose that not only the particle size, electrochemical environment of mixed oxide also have a great role in the killing of microorganisms with better efficacy with creating a unique electrochemical reaction. Further, smaller sized mixed oxide NPs may have more permeability and penetration efficiency compared to the bigger sized particles, which further excel the antibacterial activity or ZOI.¹⁹⁵ Fig. 3.16 graphically represents the ZOI obtained by plotting the average value of multiple experiments through the disc diffusion method. Herein, the results obtained using the different metal oxide combinations against the fungi and various bacterial strains are quite interesting. AZ which is the combination of elemental Ag₂O/Ag and ZnO had a good antifungal and antibacterial efficiency. Both the

metal oxide could reduce the growth of fungal and bacterial together compared to the ZnO alone.

Table 3.2: MIC values obtained for different samples

Materials	Z (ZnO)	CZ (ZnO- CuO)	AZ (ZnO- Ag/Ag ₂ O)	SZ (ZnO- SnO ₂)	A(Ag/Ag ₂ O)	C (CuO/Cu ₂ O)	S(SnO ₂)
E _g (band energy), eV	3.25	2.15	1.98	3.12	-	2-2.4 (1.2 CuO)	3.6
MIC values (μg/ml)	0.312	0.312	0.010	0.019	0.039	1.25	1.25

Further to qualify the materials synthesized in this work for biomedical applications, the MIC values have been evaluated. MIC is the minimum concentration of compound or drug which inhibits the growth of bacteria. A. baumannii was chosen to study the MIC as it exhibited a higher ZOI value compared to the other bacterial and fungal strains. And from the above results, it can be seen that the MIC values obtained for the mixed oxide are very low compared to the results obtained for single oxide (Table 3.2). Further, it can be noted that AZ (ZnO-Ag₂O/Ag) and SZ (ZnO-SnO₂) show excellent MIC values of 0.010 μg/mL and 0.019 μg/mL, respectively.

Thus it can be concluded that the AZ and SZ have maximum killing efficiency compared to the CZ (CuO-ZnO), A (Ag₂O/Ag), C (CuO), S (Sn/SnO₂), and Z (ZnO) as shown in Table 3.2. Thus, we can conclude that the present antibacterial materials also

follow the ROS mechanism which subsequently has been shown in Fig. 3.17. If we compared the band energy gap (E_g), then it is observed that ZnO-AgO₂/Ag has the lowest value of 1.98 eV and exhibited maximum antimicrobial activities compared to the ZnO-CuO (E_g: 2.15 eV), and ZnO-SnO₂ (E_g: 3.12 eV). Therefore, E_g may have a good relation to antimicrobial activities.

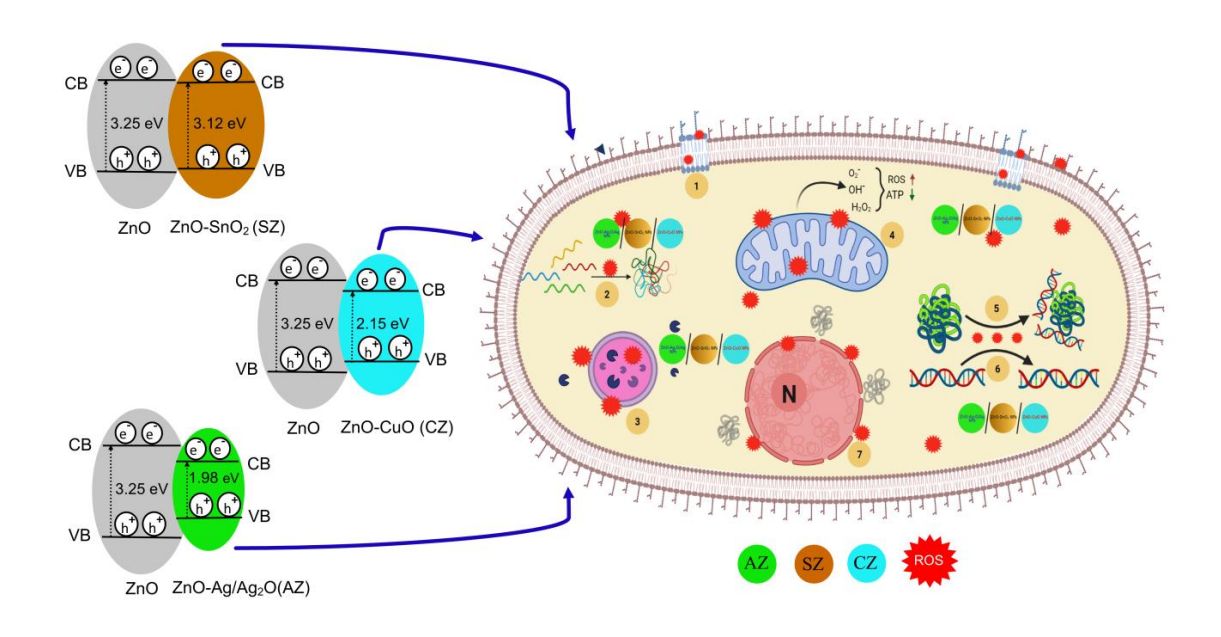


Figure 3.17: Schematic representation shows the change in the band energy gap for different composite NP systems and the mechanism involved in the bacterial cell wall damage through the ROS generation and responsible for the MIC (Table 3.2).

3.1.5 Conclusions for this part

Bimetallic oxide composites NPs have been synthesized in absence of any surfactant for broad-spectrum application. The 'in silico' investigation for targeted proteins with these

NPs and their nature of interactions have been studied for the determination of NPs mediated antibacterial and antifungal activities. Molecular docking studies predicted the binding affinity of composite NPs to its molecular target proteins of microbes and the study revealed that the composite NPs enhanced the antimicrobial activities compared to the single metal/metal oxide NPs. For the conformation of enhanced antibacterial and antifungal activities of the synthesized composite NPs against the drug resistance, we have found out interaction using quorum sensing PqsR, 163 RstA response regulator 167, and FosA gene involved in multidrug resistance development. ¹⁶⁶ In vitro study revealed that the antimicrobial activity significantly improved with the use of composite NPs instead of single oxide NPs alone even in very low concentrations of the sample used. Significantly, the combination of metallic Ag/Ag₂O and ZnO systems gives the best results as antifungal and antibacterial materials. The combination of two metals/metal oxides composite NP systems undoubtedly enhanced the antimicrobial efficacy due to the electronic interactions played between the NPs virulence/quorum sensing proteins. Based on these results, it can be concluded that these materials can be used in broad prospective development of the health care technology, for preventing the bio-film formation and to prevent the growth of infections caused by the microorganisms. Further, these NPs could act as potential antimicrobial agents against the resistance of drugs and could be effective in fabricating personal protective kits for health care management. However, the authors are committed to detailed studies on the action mechanism and *in vivo* studies which will be communicated later.

CHAPTER 3- PART II

3.2 Target specific inhibition of bacterial and Candida species by mesoporous Ag/Sn-SnO₂ composite nanoparticles: *in silico* and *in vitro* investigation

3.2.1 Abstract:

This study has been designed to evaluate the advantage of Ag/Sn-SnO₂ composite nanoparticles over the single oxide/metallic nanoparticles. By using *In silico* molecular docking approaches, herein the effects of Ag/Sn-SnO₂ nanoparticles on adhesion and invasion responsible molecular targets such as LpfD (E.coli), Als3 (C. albicans), and virulence/ resistance causing PqsR (P. aeruginosa), RstA (Bmfr) (A. baumannii), FoxA (K. pneumonia), Hsp90 and Cyp51 (C. albicans) has been evaluated. This Ag/Sn-SnO₂ nanoparticles exhibited higher antimicrobial activities, especially against the C. albicans, which is the highest ever reported. Further, Ag/Sn-SnO₂ NPs exhibited interaction with the heme propionate residues such as Lys143, His468, Tyr132, Arg381, Phe105, Gly465, Gly464, Ile471, and Ile304 by forming the hydrogen bonds with the Arg 381 residue of Lanosterol 1 4α-demethylase and increase the inhibition of the candida strains. Additionally, the Ag/Sn-SnO₂ nanoparticles exhibited extraordinary inhibitory properties by targeting different proteins of bacteria and Candida species followed by several molecular pathways which directed us that it can be used to eliminate the resistance of traditional antibiotics.

3.2.2 Introduction:

The multidisciplinary effort to develop new antimicrobial nanocomposites with efficient activities is one of the most promising advancements in composite science and has a tremendous societal and global health impact. The incorporation of known antimicrobial nanoparticles into polymeric, ceramic, or metallic matrices has given rise to a new generation of materials with improved properties/antibacterial activities. Nanocomposites have great importance in the field of water treatment, food industries, biomedical and hospital management, and textile industries. Rapid development of these newly manufactured materials prevents microbial growth and is useful in resolving the current global health care crisis of antimicrobial resistance. Different nanoparticles (NPs) are increasingly used to target microbes as anti-microbial agents and are advantageous in preventing adhesion as well as treating microbial infections.

As an example, metallic or its oxide nanoparticles are in huge demand due to their physiochemical properties which are useful in fulfilling the various biomedical demands. ²⁰² Such as ZnO nanoparticles eliminate the possibilities of biofilm formation in medical instruments. ²⁰³ Similarly, various types of nanomaterials are now extensively being explored as antimicrobial agents details of which have been reported by many research groups. ^{204,205} These nanoparticles can bind to any polymers, ligands, or drugs which makes them diverse and accessible for the inhibition of the microorganisms.

Since time immemorial the metallic silver (Ag) has been used due to its antibacterial properties.^{206,207} It can be noted that the concept of using the Ag for storing water or for use it as a medical material existed even before the concept of antibiotic

properties came to light.²⁰⁸ With the increase of multidrug-resistant bacteria, it is being explored more to develop alternative antibiotics to manage the impact of infection level.²⁰⁷

It is well known that Sn and SnO₂ nanomaterials have good optical and electronic properties.²⁰⁹ These materials are used in gas sensors applications, solar cells, Li batteries, solid-state sensors, and other optical-electronic systems due to their promising optoelectronic, electrochemical, and catalytic properties^{209–213} and recently it is also being used as an antibacterial agent.²¹⁴

Currently, with the advancement of material science and nanotechnology, the fabrication of semiconductor material with a noble metal has gained popularity due to its unique nature especially optical and electrical properties²¹⁵ due to which Ag-SnO₂ composites have been developed for several reasons, one of which is the study in antimicrobial activity.

Ag-SnO₂ has been reported as an antimicrobial agent against *E. coli*, ²¹³ *S. aureus*, *P. aeruginosa*, *K. pneumonia*, *B. cereus*, *and E. faecalis*. ²¹⁶ It is observed that the MIC values for antimicrobial activities are particle size-dependent and depend on the constituents. Hence, there is always a need to develop a suitable composite material that may overcome such challenges of infection due to the bacteria or fungus.

Many methods such as co-precipitation,²¹⁶ sol-gel,²¹³ horizontal vapour phase growth techniques,²¹⁷ solid-state electroreduction,²¹⁸ green synthesis by UV-irradiation,²¹⁹ in-situ reduction and hydrothermal,²²⁰, etc. have been used to achieve the Ag-Sn or Ag-SnO₂ NPs for various applications including antimicrobial. However, there is still a constant need for research to develop a suitable composition that can exhibit

better anti-microbial properties and have a lower minimum inhibitory concentration (MIC) than the existing compositions to get better efficacy and the method of preparation should be cost-effective, simple, and fast.

As per the current understanding, the ionization of silver releases biologically active silver ions (Ag⁺) which exhibit antimicrobial, bactericidal, anti-biofilm activities.²²¹ In a recent review recently published mentioned that while Au NPs are found to have excellent antimicrobial activity against *C. albicans*, Ag NPs have shown considerable effect and TiO₂ has prevented biofilm formation.²²² Sn-SnO₂ related antifungal and antibacterial effects had not been reported to date. Researchers these days are also targeting bimetallic nanoparticles for estimation associated antifungal and antibacterial properties. In bimetallic nanocomposite, Ag/ZnO is majorly studied. Substantially Ag-ZnO nanocomposite showed antimicrobial activity against *Candida krusei*.²²³ In another study it is reported that 5%-(Ag/ZnO)-chitosan was found optimal for the inhibition of Candida albicans²²⁴ where Ag:ZnO was used in 1:1 ratio in Ag-ZnO.

In the present work, analysis of the antifungal and antibacterial activity Ag/Sn-SnO₂ composite NPs is targeted where noticeably both the metallic Ag and Sn were present along with the SnO₂ in the matrix phase. We performed an *in-silico* molecular docking study using these composite nanoparticles (Ag/Sn-SnO₂) using molecular targets Long Polar fimbriae adhesion (LpfD) protein of *E.coli*, Response regulator RstA (Bmfr) of *A. baumannii*, FoxA of *K. pneumonia*, PqsR of *P. aeruginosa*, and Heat shock protein Hsp90, Cytochrome P450 monooxygenase (Cyp51) and Agglutinin like protein 3 (ALS3) of *Candida albicans* for finding out the antibacterial and antifungal activities. The Bmfr gene of *A. baumannii* is usually involved in biofilm formation and resistance

development as it regulates stress-related proteins.²²⁵ FosA expression is responsible for the K. pneumonia resistance. 166 While in nosocomial infection causing P. aeruginosa (Gram-Ve) bacterium, PqsR controls the virulence and increases the pathogenesis. 163 In humans, pathogenesis caused by the enteropathogenic E. coli and opportunistic C. albicans are the major concern due to its high prevalence, morbidity, and mortality. It is observed that Crohn's disease patients are found prevalently infected in different areas of the digestive system by the adherent/invasive E. coli and these days it is in the highest demand to develop new therapeutics to manage the inflammation of the digestive tract.²²⁶ Similarly, Candida albicans infection is a highly prevalent fungal infection (~14-35%) and resistant to Fluconazole and it is alarming for the need of suitable antifungal components on a priority basis. 227,228 It can be noted that the increased expression of long polar fimbriae adhesion (LpfD) protein in E. coli fimbriae is mainly responsible for the invasive pathogenesis and the invasive pathogenesis mediated by the strong interaction between fimbriae expressed LpfD protein with extracellular matrix fibronectin. 229 Hence, targeting to the LpfD protein is commendable in designing the new antibacterial drug. For candida, the target protein Als3 is involved in the adhesion of Candida albicans to the host cell. Therefore, the deletion of Als3 of Candida albicans can reduce its adhesion property.²³⁰

To check whether the infection of the above bacteria and fungus can be prevented or not, prepared Ag/Sn-SnO₂ NPs were used to find out the antibacterial/ antifungal activities along with their inhibitory mechanisms through the in silico and in vitro methods. Further, analysis of the possible adhesion/inhibitory mechanisms for finding out the best inhibitory mechanism involved using Ag/Sn-SnO₂ composite nanoparticles

against the candida as the best model has been done. For this more different target proteins of *C. albicans* such as Hsp90 and Cytochrome P450 monooxygenase (Cyp51/Erg11) were selected for this study since conserved molecular chaperone Hsp90 governs the key functions like thermal stability, cell cycle regulation, and morphogenesis, expression of virulence trait and drug resistance. From the *in silico* molecular docking studies we focused to evaluate the efficacy of antifungal activity using Ag/Sn-SnO₂ composite NPs and the results have been compared with the results obtained for the individual metal and their oxides considering the same targets of various molecular proteins of the various microorganisms.

To perform the in vitro work the composite NPs have been tested against pathogenic bacteria such as *A. baumannii and E. coli*, and the *C. albicans* for finding out the effective antimicrobial efficiency. Further, to decide the dose of inhibition minimum inhibitory concentration (MIC) has been evaluated through a series of experiments. Results have been compared with the pure SnO₂ and Ag NPs of similar size that was prepared through the same procedure. Finally, we have manifested a clear direction for the antimicrobial mechanism using the Ag/Sn-SnO₂ composite NPs system.

3.2.3 Methodology

3.2.3.1 Synthesis of composite nanoparticles

In brief, 10 mmol SnCl₂.H₂O and 10 mmol AgCl were taken in a beaker and stirred in 50 ml alcohol. After 20 min, 50 mmol NaBH₄ was added drop wise and the colour changed from milky white to brown. The reaction mixture was then kept under stirring for 4 hours at room temperature (25° C). It was then washed thoroughly, centrifuged (20 min, 12,000 min, 12,000 min).

RPM) several times with methanol and water mixture (1:1) to remove the unreacted components. The solid residue then was dried at 80° C overnight (12 hr) and kept for characterizations. The detailed methodology has been referred to the Indian Patents filed by us (Indian Patent Application No. 202011031802 and 202011017968, dated July 24, 2020, and April 27, 2020, respectively).

3.2.3.2 Time scale surface zeta potential and stability Studies

The time scale stabilities of the composite NPs were investigated for three days through zeta potential measurement considering defined time intervals. Three sets of experiments were performed (1) 5μg/ml of each sample was prepared in 1X PBS (Phosphate Buffer Saline) for different pH of 5, 6.9, 7.4, and 8. Similarly, (2) 5μg/ml of each sample was prepared in 1X PB (Phosphate Buffer Solution) for Ag-Sn/SnO₂ in pH 6.9 and 7.4 and (3) 5μg/ml of each sample was dispersed in 0.9 % W/V Saline solution. Further, DLS readings were taken for all the samples at different time intervals for up to three days. Before starting the measurement all the samples were sonicated for 10 mins to disperse. Finally, Both DLS and zeta potential readings were taken for all of the above samples at different time intervals and the results are discussed in the subsequent section.

3.2.3.3 In-silico molecular docking study

Then we have analyzed the potential antibacterial/antifungal activity of Ag/Sn-SnO₂ nanoparticles through the *In silico* molecular docking. 3D chemical structures of Ag NPs, SnO₂ NPs, and Ag/Sn-SnO₂ NPs were generated using VESTA software. 3D protein structure of molecular target protein includes LpfD (PDBID-5AFO) Bmfr (PDBID-5E3J), FoxA (PDBID-5WEW), PqsR (PDBID-4JVI) Als3 (PDBID-4LEB), HSP90

(PDBID-6CJP) and Cyp51 (PDBID-5V5Z) were retrieved from RCSB- protein data bank. Ligand preparation and macromolecular preparation were conducted by adding the polar hydrogen atoms, kollman charges, solvation parameter and by generating the grid box. Molecular docking was performed using the Autodock 4.2 tool. A Lamarckian genetic algorithm was used in this study. 30 independent runs and a maximum number of 27,000 GA operations were conducted. Protein and nanoparticle interactions and images were acquired by the Pymol software.

3.2.3.4 In-vitro Antimicrobial activity study:

These studies have been done as described in the procedure in Chapter 2 (Page 33 and 34)

3.2.3.5 Statistical Analysis:

All the necessary data were represented with mean values (\pm SD). Two-way ANOVA used for statistical analysis followed Bonferroni's method for multiple comparison tests was conducted using the software GRAPH PAD PRISM. In all cases, a p-value was obtained from the ANOVA analyses; the conventional value of 0.001 was considered to express statistical significance.

3.2.4 Results and Discussions:

3.2.4.1 Synthesis and Characterizations

The TEM image is shown in Fig. 3.18 (a-d) on a different scale from 1 μ m-10 nm. The TEM images show the presence of small particles between 1-18 nm in size. They are

porous and the particles are strongly bonded as seen from Fig. 3.18 (b-c). This result is also supported by BET results in Fig. 3.18 (a). They are rod-type, chain-like, and interlinked with each other. The lattice fringe can be seen in Fig. 3.18(f) from which the d-spacing is calculated to be ~0.202 nm, ~0.234 nm, and ~0.237 nm for Ag (200), Ag (111), and SnO₂ (200), respectively. This is further expanded to the IFFT image (Fig. 3.18 (e, and f)) to clearly show the fringes. From Fig. 3.15 (e), the cross-section can be clearly seen, which further shows the presence of two different types of fringes, for SnO₂ (200) and Ag (200). The SAED pattern (Fig. 3.18 (h)) shows the presence of Ag (111), SnO₂ (220), Ag (311), and Sn (301). All these results match well with the XRD pattern

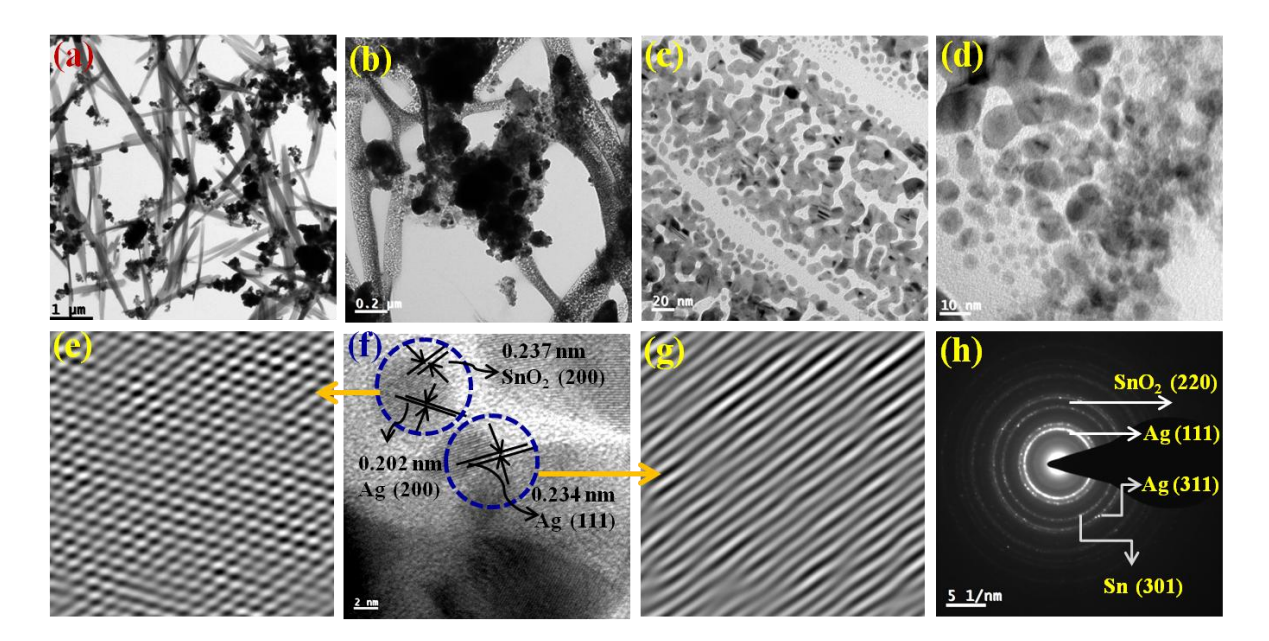


Figure 3.18: (a,b,c, and d) HRTEM micrograph of the Ag-Sn/SnO₂ composite nanoparticles obtained from lower to higher magnification, (f) HRTEM image of the Ag-Sn/SnO₂ NPs at different positions showing the presence of elemental Ag and Sn/SnO₂ in the composite nanoparticle; Fig. (e,g) cross-section/IFFT images obtained from the HRTEM image for SnO₂ and Ag (e) and for Ag (g); (h) SAED pattern of Ag/Sn-SnO₂ composite nanoparticles.

(Fig. 3.20) and it also matches with the literature.²³¹ Similarly, the rod type of morphology has also been found in the previous report.²¹⁷ However, these rods or needle types of shape are formed due to the self-assembly grain growth of the tiny nanoparticles as is shown in the enlarged TEM micrographs, i.e., in Fig. 1 (c), and (d). These nanoparticles are also aligned in a single direction.

The elemental analysis of the sample was performed from TEM to find out the composition as it is shown in Fig. 3.19. From the analysis, it can be observed that the atomic percentage (by wt.) of Ag, Sn, and O are 51%, 42.63%, and 6.37%, respectively. From this result, we can confirm the presence of Ag, Sn, and O₂ which also supports the formation of Ag, Sn, and SnO₂ as identified from XPS results and it is also supported by the SAED pattern and HRTEM micrographs as it is shown in Fig. 3.18 (e-h). This has been confirmed further from the XRD pattern.

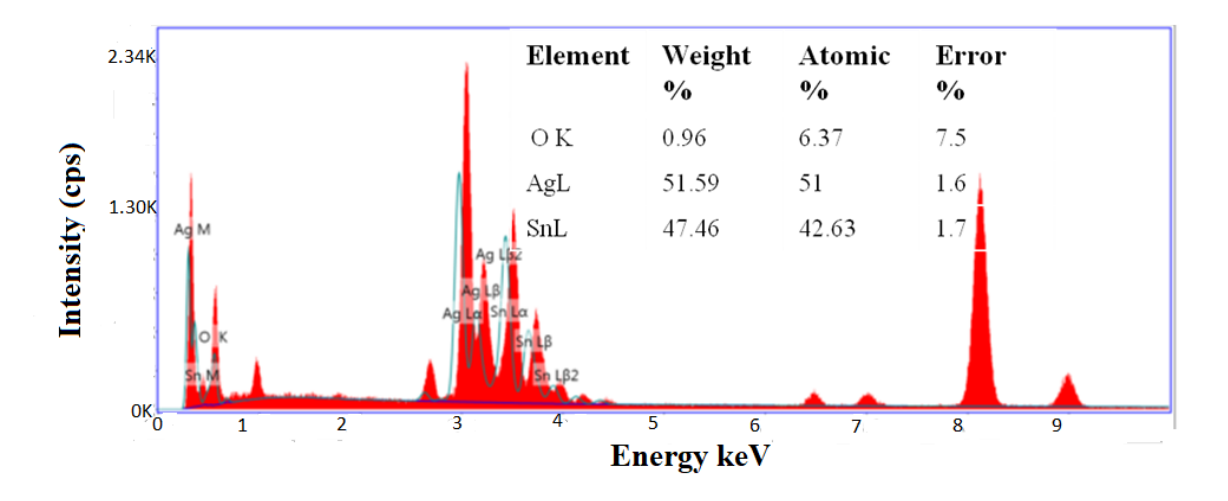


Figure 3.19: EDS spectra shows the weight percentage of different elements present in the $Ag/Sn-SnO_2$ nanoparticle composite system

The solid-state XRD pattern of the composite nanoparticles is represented in Fig.

3.20 (a) and the diffraction peaks appeared at $2\theta = 27.9^{\circ}$, 38.2° , 44.4° , 46.50° , 64.6° , 77.6° and 81.7° corresponds to the diffraction plans of (210), (111), (200), (231), (220), (311) and (222), respectively, which further closely resembles the FCC cubic crystal structure of Ag nanoparticles (as per JCPDS 04-0783). The peaks appeared at $2\theta = 54.9^{\circ}$, 57.6° and 38.1° correspond to the diffraction planes (220), (002), and (200), respectively, and resemble the tetragonal crystalline phase of SnO₂ (JCPDS 41-1445). It also can be seen that there is elemental Sn⁰ (zero Valence) present as evidence for Sn (101) diffraction plane and the diffraction peak appeared at around $2\theta = 32.1^{\circ}$. These XRD results were correlated and it is in concordance with the SAED results obtained from the TEM experiments as is shown in Fig. 3.18 (h).

The UV-Vis absorption study was conducted in a solution medium of $Ag/Sn-SnO_2$ nanoparticle composite system and the results are shown in Fig. 3.20 (b). A broad-spectrum is observed at the wavelength of λ = 271 nm (see Fig. 3.17 b). Usually, the Surface Plasmon Resonance is observed above 400 nm for Ag nanoparticles, and for Sn and SnO₂ is found to be at ~ 270 nm, which means that the UV-Vis shows the effect of Sn and SnO₂ NPs. However, the appeared broad spectrum depicts the formation of the composite material which is mainly due to the electronic environment and due to the possible defects present in the composite nanoparticle system. Further the appearance of only one spectral band indicates that Ag, Sn, and SnO₂ are blended well with each other and there is a rare possibility of formation of alloy since the HRTEM micrograph exhibited clear fringes for Ag, and Sn/SnO₂. The energy band gap (Eg) has been calculated with constituting Tauc plot for the direct transition and Eg value is found to be 3.75 eV, which is slightly higher than the bulk SnO₂ (3.6 eV)²³⁴ and higher than the Ag

nanoparticles (2.8 eV). This might be due to the synergistic effects of the composite nanoparticle system that is developed and the size of the nanoparticles.^{213,215,235,236}

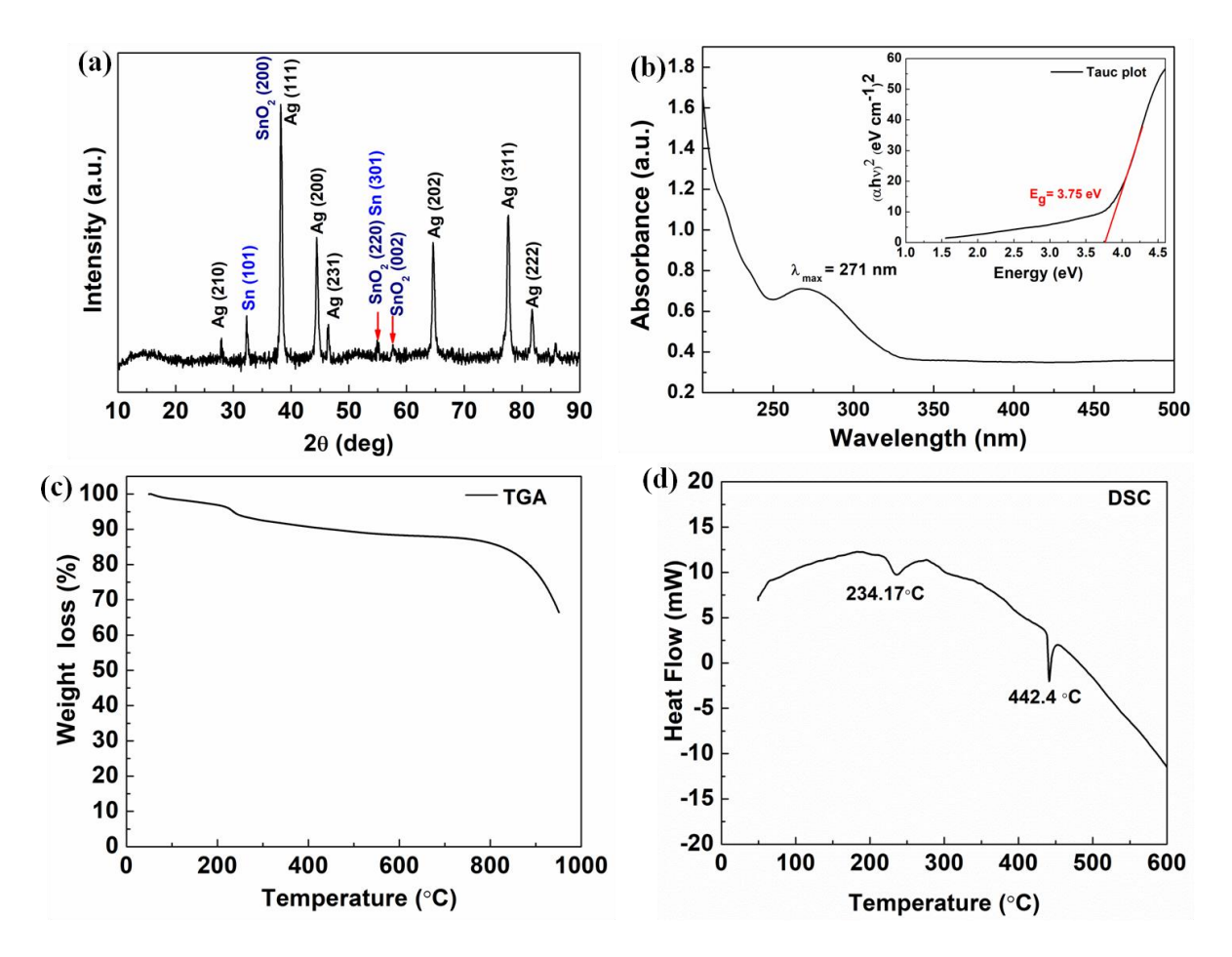


Figure 3.20: (a) Powder XRD pattern of the Ag-Sn/SnO₂ composite nanoparticles; (b) UV-Vis spectrum of Ag/Sn-SnO₂ nanoparticles and the inset shows the Tacu plot for Band gap energy calculation of Ag-Sn/SnO₂; (c) Shows the TGA results of Ag-Sn/SnO₂ composite nanoparticles (d) DSC thermogram of Ag-Sn/SnO₂composite nanoparticles.

The thermal stability of Ag/Sn-SnO₂ NPs has been studied through TGA. The TGA analysis as shown in Fig. 3.20 (c) shows a weight loss (~7%) at around 200 °C, which occurred due to the adsorbed surface water/moisture. Weight loss beyond 200 °C has occurred due to the creation of oxygen vacancies in SnO₂ or loss of Sn due to

evaporation. It can be noted that the melting of Sn occurred at ~234.17 °C, as is evident from the DSC curve (see Fig. 3.20 (d)). The change of weight beyond this temperature has occurred due to the evaporation of melted Sn (shown in Fig. 3.20 (d)). The endothermic peaks appeared at 234.17 °C and 442.40 °C in Fig. 3.20 (d) are due to the melting of metallic Sn and Ag, respectively. This depression of melting for both Sn and Ag is observed due to their size reduction and is lower in value than their bulk. Thus TGA and DSC result further supports the formation of Ag/Sn-SnO₂ nanoparticle system as shown in TEM and XRD (see Fig. 3.15 and Fig. 3.17 (a), respectively.

To understand the specific surface area and porosity of the Ag/Sn-SnO₂, BET surface area analysis was performed and the results are shown in Fig. 3.21 (a). From the N₂-adsorption-desorption study a clear hysteresis of type-IV isotherm is seen and it is evident for the mesoporous structure of the solid Ag/Sn-SnO₂. The specific surface area of the composite has been calculated and found to be \sim 70.88 m²/g and the average pore diameter is \sim 3.9 nm as seen from Fig. 3.21 (a) (inset). Thus from the BET experiment, it can be concluded that the Ag/Sn-SnO₂ nanoparticle composite system is porous and the results are matching well with the TEM results. The specific surface area values are also shown in Table 3.3 for comparison.

To find out the surface chemical structure of the synthesized Ag/Sn-SnO₂ FTIR analysis has been performed and is shown in Fig. 3.21 (b). The absorption band appeared at ~3600 cm⁻¹ belongs to the O-H group of surface hydroxyl, which could be due to the absorbed moisture. Bands that appeared ranging from 900 cm⁻¹ -1500 cm⁻¹ correspond to the stretching and bending vibration of oxygen²³⁸. Bands that appeared at ~1600 cm⁻¹ might be due to the bending vibration of H₂O molecules. The band appeared at ~869 cm⁻¹

might be due to the presence of Sn-OH.^{239,240} Further absorption band appeared at ~712 cm⁻¹ is due to the stretching vibration of Sn-O bond^{241,242} and the band observed at ~520 cm⁻¹ corresponds to the stretching vibrations of Ag-O.

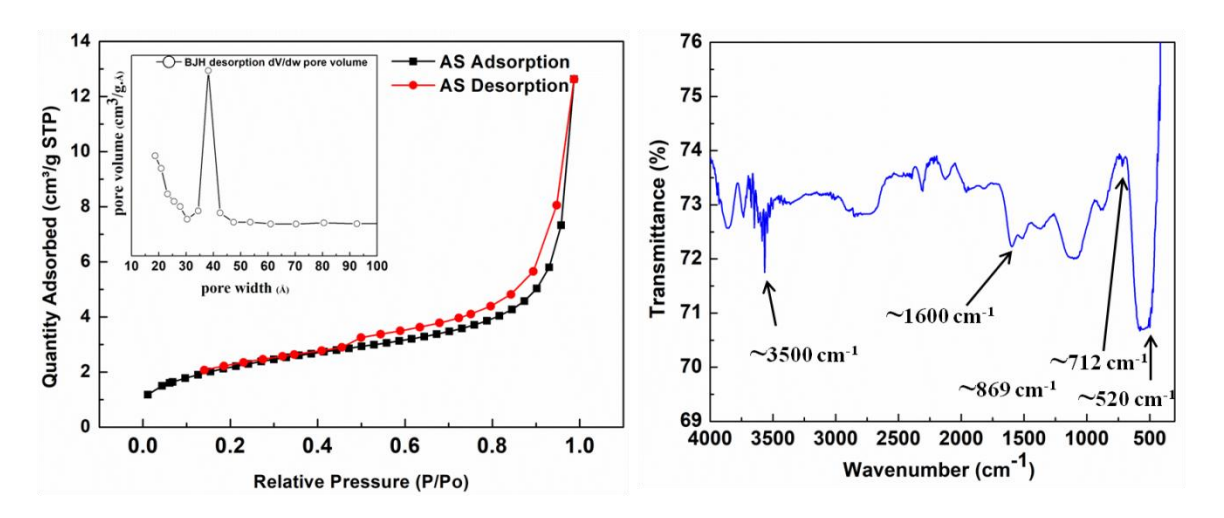


Figure 3.21:(a) Shows the BET surface area analysis results. N_2 adsorption-desorption isotherm of Ag- Sn/SnO_2 nanocomposite particles and the inset shows the BJH pore size distribution results obtained from the desorption isotherm; (b) FTIR spectrum of Ag/Sn- SnO_2 nanoparticles.

Table 3.3: Results show the BET surface area analysis and average pore size distribution for Ag NPs, Sn/SnO₂ NPs and for Ag -Sn/SnO₂ composite NPs.

Sample name	Sample composition	BET surface area (m²/g)	BJH Desorption average pore width	
2b	Ag-Sn/SnO ₂	70.88	38.1 Å	
A	Ag	0.45	18.1 Å	
S	Sn	18.43	38.2 Å	

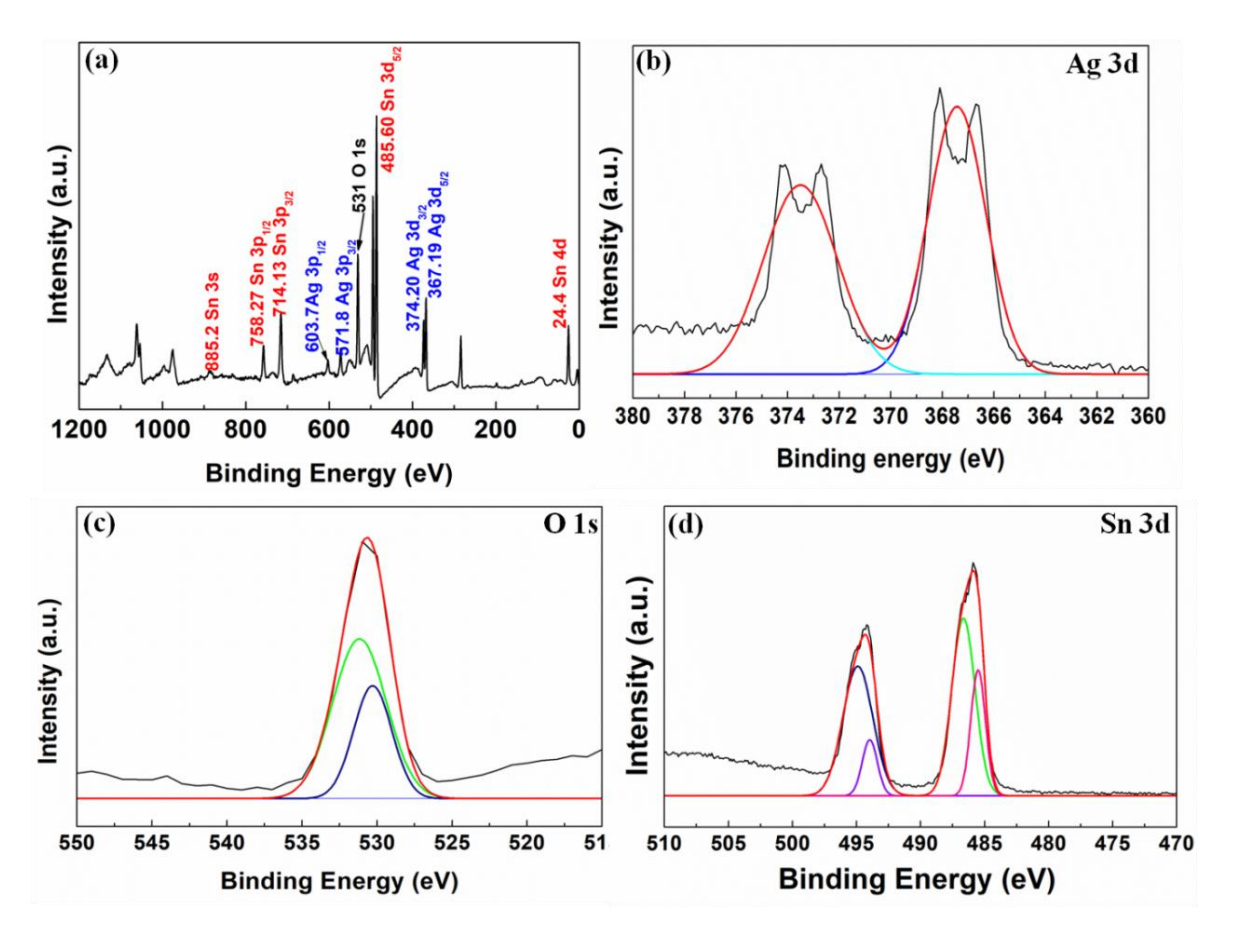


Figure 3.22: Shows (a) full-scale XPS spectrum acquired of Ag-Sn/SnO₂, (b) XPS spectrum acquired for Ag 3d; (c) XPS spectrum acquired for O₂ 1s; and (d) XPS spectrum acquired for Sn 3d.

To find out the elemental composition of the synthesized nanocomposite, XPS analysis was performed (see Fig. 3.22). The full spectrum (Fig. 3.22 (a)) shows the presence of Sn 3d, Ag 3d, and O 1s. The binding energy at 24.4 eV, 367.19 eV, 374.20 eV, 485.60 eV, 531 eV, 571.8 eV, 603.7 eV, 714.13 eV, 758.27 eV and 885.2 eV are the binding energy of Sn 4d, Ag 3d_{5/2}, Ag 3d_{3/2}, Sn3d_{5/2}, O 1s, Ag 3p_{5/2}, Ag 3p_{3/2}, Sn 3p_{3/2}, Sn 3p_{5/2}, and Sn 3s, respectively. The energy band fitting of the O 1s in Fig. 3.22 (c) shows the presence of elemental oxygen at 531.2 eV and the band appeared at 530.6 eV which

might be due to the surface oxygen and metal oxide (here SnO_2), respectively.²¹⁶ From Fig.3.22 (b), the presence of Ag can be confirmed through the presence of band energy at 367.4 eV and 374.5 eV, which are bands of Ag^0 . The bands for Sn 3d in Fig. 3.22 (c) can be seen as evidence for the formation of Sn^0 and Sn^{+2} . All these results are in agreement with the TEM (Fig. 3.18), EDS (Fig. 3.19), and XRD (Fig. 3.20 a) results as discussed previously.

Thus all the above results are strongly supporting for the formation of Ag-Sn/SnO₂ nanocomposite. A multidisciplinary effort to find out antimicrobial/antifungal nanocomposites is one of the most promising advancements in composite materials and has a tremendous impact on the development of new health care technology. Further to achieve the best antimicrobial/antifungal nanocomposites of Ag-Sn/SnO₂ the colloidal stability is important. To check the colloidal stability of the NPs, the surface charge potential was measured in PBS and saline solution through surface charge zeta potential (ζ) measurement of the Ag-Sn/SnO₂ NPs without any surface modification or adding surfactant. ζ values were recorded up to three days with different time intervals and the ζ values were found to be varying with change in the pH of PBS solution and it is different at different times (see Table 3.4). From Table 3.4 it is noticed that ζ values are observed to be consistent in pH 7.4 (PBS) and saline solution followed by pH 6.9 (PBS). For acidic PBS (pH 5), it is below -5 mV and for basic PBS (pH 8) it is below -10 mV. In saline solution ζ values vary mostly in between -18.4 mV (at 45 min) to -17.3 mV (after 3 days), which means it is quite stable. Similarly from the zeta size results of the particles, a similar conclusion can be drawn (Table 3.5). The Ag-Sn/SnO₂ NPs are stable in saline for up to 2 days. Whereas the NPs are stable in PBS pH 7.4 and in pH 6.9 for up to 3

days, for 24 h in pH 5, and 48 h in pH 8. Out of 6.9 and 7.4, we can see hydrodynamic diameters are consistently better stable in pH 7.4 for PBS. The Zeta Potential values at nonphysiological pH are important for certain biological environments. As an example, oral drugs interact with the gastric juice in the stomach at an acidic pH. The zeta potential of our nanocomposites seems to be decreasing in nonphysiological pH. Therefore, our material (NPs) may not be suitable for oral drug delivery. Additional experiments need to be performed to explore such areas of applications that are beyond the scope of our present investigation. Further, the decrease in zeta potential values in nonphysiological pH leads to the agglomeration/aggregation for our nanocomposite. This phenomenon is also noticed from the results obtained from the DLS (Table 3.5).

Table 3.4: Zeta Potential (mV) values of Ag-Sn/SnO₂ NPs measured at different pH of PBS and in saline solution

Time	Zeta Potential (mV) of Ag-Sn/SnO ₂ in pH							
	PBS pH 5	PBS pH 6.9	PBS pH 7.4	PBS pH 8	Saline			
0 min	-5.41	-5.14	-13.1	-5.1	-10.1			
15 min	-5.7	-5.8	-14.9	-5.2	-11.6			
30 min	-5.7	-5.2	-15.2	-5.7				
45 mi	-6.13	-16.1	-16.6	-8.06	-18.4			
60 min	-5.1	-17.7	-15.6	-6.66	-16.8			
1.5 h	-6.2	-18.4	-9.86	-4.5	-16			
2 h	-5.6	-17.4	-14.9	-8.1	-17.9			
2.5 h	-5.7	-17.7	-14.3	-6.2	-17			
3 h	-5.5	-17.1	-15.2	-5.3	-17.8			
24 h	-4.6	-14.4	-11.1	-7.6	-19.5			
Day 2	-6.62	-6.66	-10.3	-7.04	-13.4			
Day 3	-10.2	-12.2	-14.1	-11.2	-17.3			

Table 3.5: Zeta size analyzed for $Ag-Sn/SnO_2$ NPs at different pH of PBS and in the Saline solution

Time	Hydrodynamic diameter (in nm) Ag-Sn/SnO ₂ NPs in PBS and Saline Solution							
	PBS (pH 5)	PBS (pH 6.9)	PBS (pH 7.4)	PBS pH 8	Saline			
0 min	712.3	722.8	133.1	236.6	289.2			
15	749.3	620.2	159.7	345.1	656.8			
min								
30	763.2	749.3			292			
min								
45	718.4	676.4	152.8	1007	202			
min								
60	676.4	801.3	192.9	444	195.3			
min								
1.5 h	733.2	768.2	241	327	225			
2 h	833.6	683.8	161	376.2	453.3			
2.5 h	766.3	728.2	517	276	272.3			
3.5 h	714	792	180	400.1	481.2			
4.5 h	728	757	157.5	447.3	413			
6 h	777.1	803			321.5			
24 h	594.1	680	397.2	560.1	348.3			
Day 2	693.9	635.7	426.7	732.4	370.4			
Day 3	3843	1385	601	4716	5461			

Further, the rapid development of the newly synthesized nano materials to prevent microbial infection is helping in the management of the current global health care crisis against antimicrobial resistance. Therefore, $Ag-Sn/SnO_2$ nanocomposite system further

has been used as an anti-microbial agent against a few target microbes and has shown advantageous effects in treating microbial infections. The detailed study has been discussed in the subsequent sections.

All the bacterial strains showed almost similar effects against the zone of inhibition for the same nano composite material, however *C. albicans* behaved differently. Based on the average value, we chose *A. baumannii* for the MIC study. Whereas, for in silico study, we chose fungal strain due to their superior anti-fungal behaviour.

3.2.4.2 In-silico study

A widely used computational docking tool determines the binding mode and affinity of interactive ligand-protein interaction which helps in the understanding of the interaction mechanism. It has been predicted that single metal/metal-oxide has the potential application in the biomedical field. Active silver ion exhibits antimicrobial, bactericidal, and anti-biofilm activity. While SnO₂ nanomaterials have good optical and electronic properties there is still a tremendous need to analyze their biological properties. Therefore, we have performed docking predication using Ag, SnO₂, and Ag/Sn-SnO₂ as ligands for molecular docking on the different molecular target LpfD (PDBID-5AFO) of *E. Coli*, Bmfr (PDBID-5E3J) *A. baumannii*, FoxA (PDBID-5WEW) *K. pneumonia*, PqsR (PDBID-4JVI) *P. aeruginosa*, Als3 (PDBID-4LEB), Hsp90 (PDBID-6CJP) and Cyp51 (PDBID-5V5Z) of *C.albicans*. We observed the lowest binding affinity (kcal mol⁻¹) for Ag ions -1.5 to -2 (kcal mol⁻¹) when it binds to the target proteins of microorganisms while for SnO₂ the binding energy was observed in the range

Table 3.6 Shows the binding energy (kcal mol-1) and interaction parameters of Ag, SnO_2 , and $Ag-Sn/SnO_2$ NPs associated with different interacting molecular targets.

Sr. No.	Organism Name/ PDB-ID	Ligand	Binding energy(k	Inhibition Constant	Amino acid /hydrogen bond	Interacting residues
	molecular target		cal/mol)			
1	E. Coli (LpfD)	Ag	-1.48	82.04 mM		HIS322, SER275, ASP274, LEU239, SER238
	PDB-ID: 5AFO	SnO ₂	-3.58	2.37 mM		TYR95, LYS130, GLY128,
		Ag- Sn/SnO ₂	-5.71	65.78 μΜ		LYS109, PHE106, VAL102, GLN103
2	A. baumannii (RstA) PDB-ID: 5E3J	Ag	-1.73	53.94 mM		THR23, ALA20, ILE12, VAL56,VAL13,GLU14, ASP58, LEU84
		SnO_2	-3.90	1.39 mM		ILE12, VAL56
		Ag- Sn/SnO ₂	-7.01	7.29 µM	ALA106 (2.108 Å)	VAL109, ALA106, GLN93 , TYR104 , VAL105
3	K. pneumonia (FosA)	Ag	-1.48	82.78 mM		LEU114, ILE72, PHE70, SER71, MET28, CYS42
	PDB-ID :	SnO_2	-3.60	2.31mM	LYS111 (1.914 Å)	LYS111, THR66, HIS110
	5WEW	Ag- Sn/SnO ₂	-6.51	17.05μΜ	ARG55 (2.183 Å), HIS110 (1.746 Å)	ARG55, HIS110, THR58, LYS111, TYR66, SER63, THR66
4	P. aeruginosa	Ag	-1.64	63.28 mM		SER205, GLN203, HIS204,
	(PqsR) PDB-ID : 4JVI					LEU208 , ASP150, ASP131, SER199, SER201
		SnO ₂	-3.92	1.33 mM	ILE155 (1.766 Å)	LYS154, ILE155, GLN160, TYR270
		Ag- Sn/SnO ₂	-7.50	3.16 μΜ	LEU197 (2.073 Å)	TYR258, ALA168, ILE263, GLN194, VAL211, LEU197, LEU207, SER196
5	C. albicans (Als3)	Ag	-1.59	68.62 mM		TYR226, VAL119 , GLY120, GLY27 , PHE117, ARG171
	PDB-ID : 4LEB	SnO ₂	-4.04	1.1 mM		TYR255, GLN187
		Ag- Sn/SnO ₂	-6.13	32.02 μΜ	SER159 (2.094 Å) ASN225 (1.986	SER159, ASN225, TYR21, THR296
	C. albicans (Hsp90) PDB-ID: 6CJP	Ag	-1.63	63.89 mM	Å) 	LEU176, ASN40, THR174, ILE80, ASP82, ALA41, ARG81, ILE67
	TDD ID . OCSI	SnO ₂	-4.14	926.71 μM	ILE99 (2.024 Å)	ILE99
		Ag- Sn/SnO ₂	-7.47	3.35 μΜ	THR12 (1.811 Å)	THR160, PHE159 , TRP151, VAL161, THR12, HIS9 , VAL93, LYS89, THR8
	Candida albicans (Cyp51)	Ag	-1.74	53.47 mM		SER361, PRO424, THR365, PHE422, LEU323, LEU329, VAL332, ILE333
	PDB-ID: 5V5Z	SnO ₂	-4.09	1.01 mM	HIS468 (1.894 Å)	ARG467 , VAL112, HIS468, ALA114
		Ag- Sn/SnO ₂	-7.71	2.22 μΜ	ARG381 (2.189 Å)	LYS143, HIS468, TYR132, ARG381, PHE105, GLY465, GLY464, ILE471, ILE304

of -3 to -4 (kcal mol⁻¹). However when Ag/Sn-SnO₂ was evaluated through docking then the highest binding affinities achieved were -5.71, -7.50, -6.51, -7.50, -6.13, -7.47 and, -7.71 (kcal/mol) with the molecular targets of *E. Coli*, *A. baumannii*, *K. pneumonia*, *P. aeruginosa and C. albicans* (Als3, Hsp90 andCyp51), respectively as represented in Table 3.6. Similarly, the minimum required concentration for targeted inhibition also decreased from milli to micro molar concentrations (see Table 3.6). Further, we have scrutinized the binding energy affinity of Ag, SnO₂, and Ag/SnO₂ required active motif residues of various target proteins (Fig. 3.23 and 3.24). LpfD of *E. coli* consists of N-

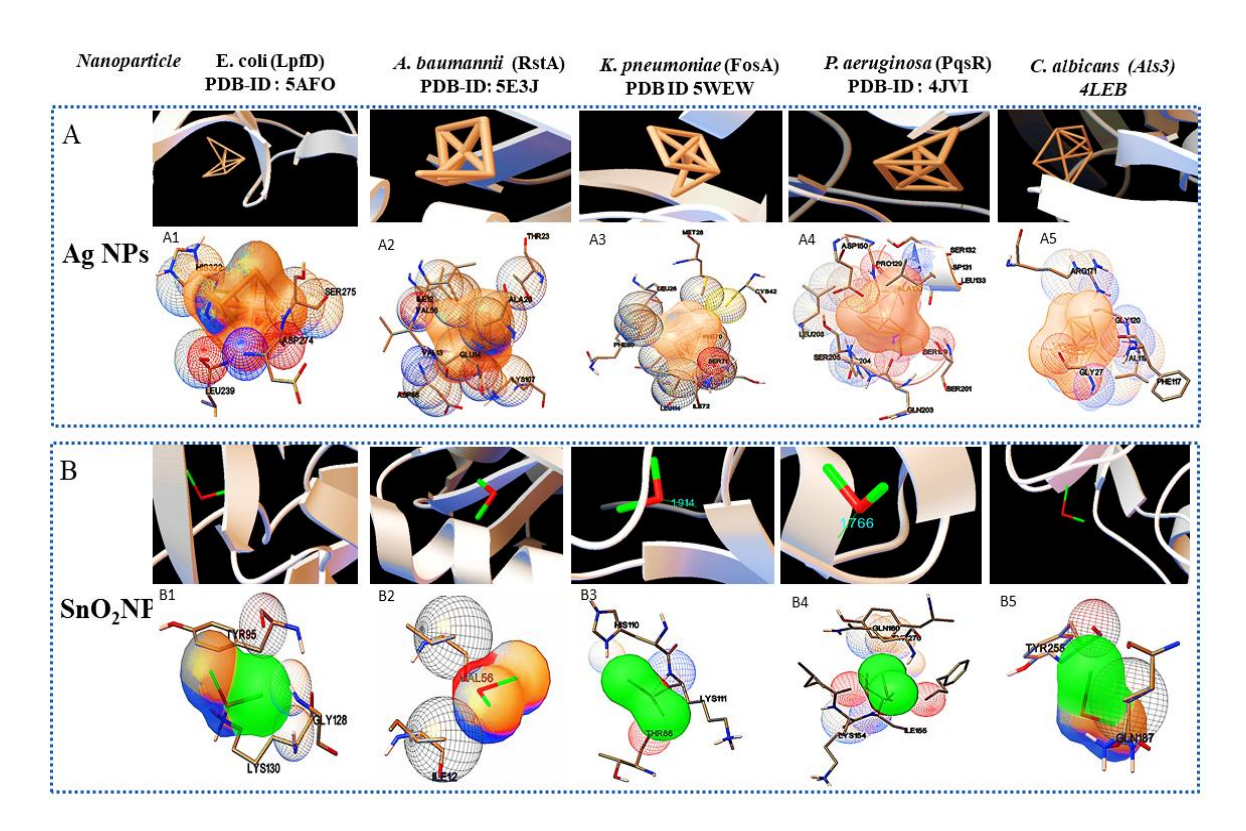


Figure 3.23: Show the nanoparticles-protein interactions. A): Ag nanoparticles-protein interactions, B): SnO₂ nanoparticle- protein interactions. 1, 2, 3, 4, and 5 are the different crystal structures of molecular protein targets Lpfd, RstA, FosA, PqsR, and Als3 of E.coli, A. baumannii, k. pneumoniae, P. aeruginosa, and C. albicans, respectively. (Ag-Coral), (Sn-lime green).

terminal adhesion and C-terminal pilin domain and amongst the residues of 1-183 found conserved with the *K. pneumoniae* MrkD or with the other *E. coli* species.²⁴⁴ It is revealed that the SnO₂ and Ag/Sn-SnO₂ nanoparticles interact at the N-terminal adhesion domain of LpfD through hydrophobic interactions with the Tyr95, Lys130, Gly128 and Lys109, Phe106, Val102, and Gln103 due to their higher binding affinity. While Ag interacts at the C-terminal domain (see Fig. 3.23 B1 and Fig. 3.24 C1). Involvement of RstA in biofilm initiation and resistance development of *A. baumannii* is considered a potential target. Active conformation of RstA contains two main residues such as Thr85 and Tyr104.^{190,245}

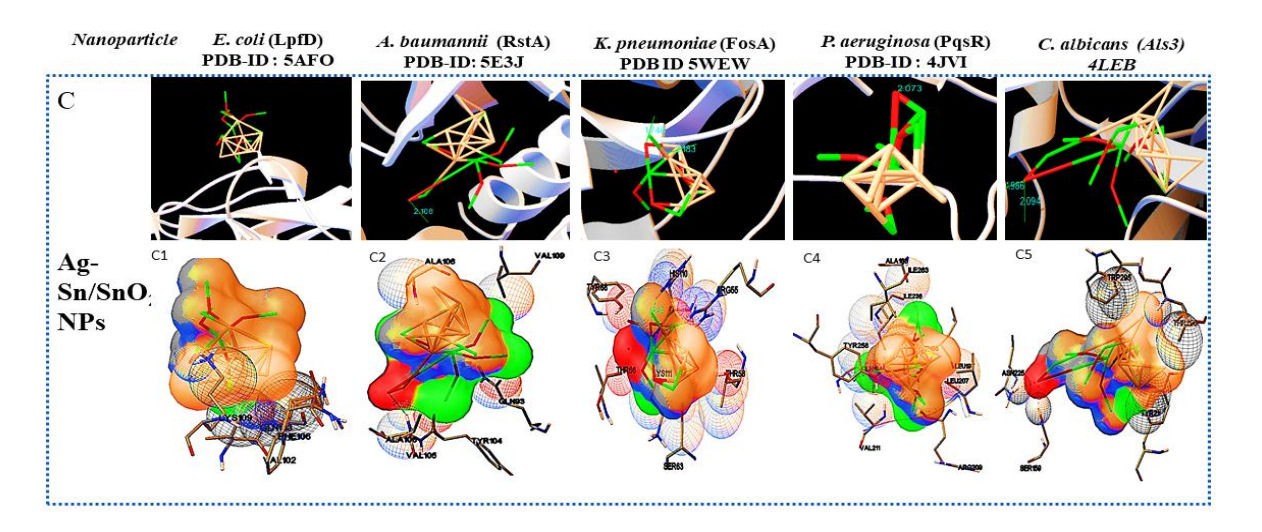


Figure 3.24: Shows the nanoparticle-protein interactions. C: Ag-Sn/SnO₂ nanoparticles-protein interactions, 1,2,3,4 and 5, are the crystal structures of molecular protein target Lpfd, RstA, FosA, PqsR, and Als3 of E.coli, A. baumannii, K. pneumoniae, P. aeruginosa, and C. albicans, respectively. (Ag-Coral), (Sn-lime green).

It is also found that only Ag/Sn-SnO₂ nano particles interact with the active residue TYR104 and with the other interacting residues such as Val109, Ala106, Gln93, and Val105 of the motif (Fig. 3.24 C2). It is noticed that the FosA protein is involved in

resistance development. It is further observed that the high binding energy affinity plays an important role in between Ag-Sn/SnO₂ and FosA and the value obtained to be -6.51 kcal mol⁻¹, which mainly plays with the interacting residues such as Arg55, His110, Thr58, Lys111, Tyr66, Ser63 and Thr66 (Fig. 3.24 C3). Further, the interaction results between Ag, SnO₂, Ag-Sn/SnO₂, and PqsR are revealed that the PqsR is involved in pathogenicity. It can be noted that the various inhibitors bound at the active motif residues of proteins through the polar and non-polar interactions, such as Stigmatellin y. interacted through Pro129, Ala187, Ala190, and Val211, 188 while the Asn206(H), Arg209(H), Leu197(H), Glu259(H), Phe221, Leu207(H) and Ser196 residues interact with the quinolone derivative. 187 Similarly, Leu208(H), Gln194(H) Met 224 Ile236 and Leu207, Val211, Pro210 Arg209, and Ser196 residues interact with the Zingerone. In the similar line, herein it is noticed that the Ag/Sn-SnO₂ NPs exhibited the highest inhibitory action via interacting with the residue Leu197 by the formation of hydrogen bonds and other nonpolar interactions with the Tyr258, Ala168, Ile263, Gln194, Val211, Leu207, and Ser196 residues as shown in Fig. 3.24 C4 that occurred with a highest binding affinity of -7.50 kcal mol⁻¹. A series of other possible interactions occurred with the Ag, Sn-SnO₂ and Ag/Sn-SnO₂ NPs, and the protein residues and their affinity values are highlighted in Table 3.6 and the nature of interactions associated are also shown in Fig. 3.23. However, due to the unavailability of P. aeruginosa (Gram-ve) bacterium strain the in vitro study has not been performed with P. aeruginosa strain in this work.

Similar to adhesion protein LpfD of *E. coli*, over expression of agglutinin-like sequence protein 3 of *C. albicans* plays an important role in adherence and invasion to host for the biofilm formation and iron acquisition (explained in the subsequent section).

Surface displayed enolase has an important role in candida pathogenicity and the over expression of Als3 is required for the surface display of enolase. The N-terminal domain of Als3 and central repeat domains have an important role in interaction with adhesin and enolase. Further, the Als3 binds to ferritin of the host cells and enables the *C. albicans* invasion and biofilm formation (Fig. 3.28) shown in the subsequent section). Thus Als3 is a potential molecular target for inhibition of *C. albicans species*. With this aim to find out the Ag, SnO₂, and Ag/Sn-SnO₂ NPs mediated inhibitory actions here in this work, the Als3-nanoparticle interaction studies through the molecular docking have been carried out. The obtained results revealed enhanced antifungal activities against the candida for Ag/Sn-SnO₂ compared to the Ag and SnO₂ NPs.

It is also found that the Ag/Sn-SnO₂ NPs interacted with the Als3 by forming 2 hydrogen bonds with Ser159 (2.094 Å) and Asn225 (1.986 Å) and interacted with the other residues such as Ser159, Asn225, Tyr21, and Thr296 (see Fig. 3.24C5). The details of the different interactions and their binding energy associated with the different interactions are listed in Table 3.6. Therefore, the in silico studies exhibit that the Ag/Sn-SnO₂ is useful for the prevention of the growth of the microorganism via adhesion even in the invasive nature of the strains.

3.2.4.3 In-vitro antimicrobial study and MIC

Further, the effective potential of composite nanoparticles for antimicrobial/antifungal effects is confirmed through the *in vitro* studies. The results of the Luria broth dilution technique for antibacterial activity are shown in Fig. 3.25 and Fig. 3.26. It is observed that the Ag-Sn/SnO₂ nanocomposite NPs show excellent

antibacterial activity compared to the SnO₂ and Ag NPs system alone. As an example, the low concentration of 250 μg/ml of Ag-Sn/SnO₂ is exhibiting excellent antimicrobial response at 6 hr. Further, the antimicrobial response of Ag-Sn/SnO₂ has been tested through the disk diffusion study as shown in Fig. 3.27 (a-d). It is seen that the zone of inhibition of Ag-Sn/SnO₂ NPs against the *C. albicans* is 18 mm, which is quite high compared to the results obtained for Ag NPs and SnO₂ NPs separately.

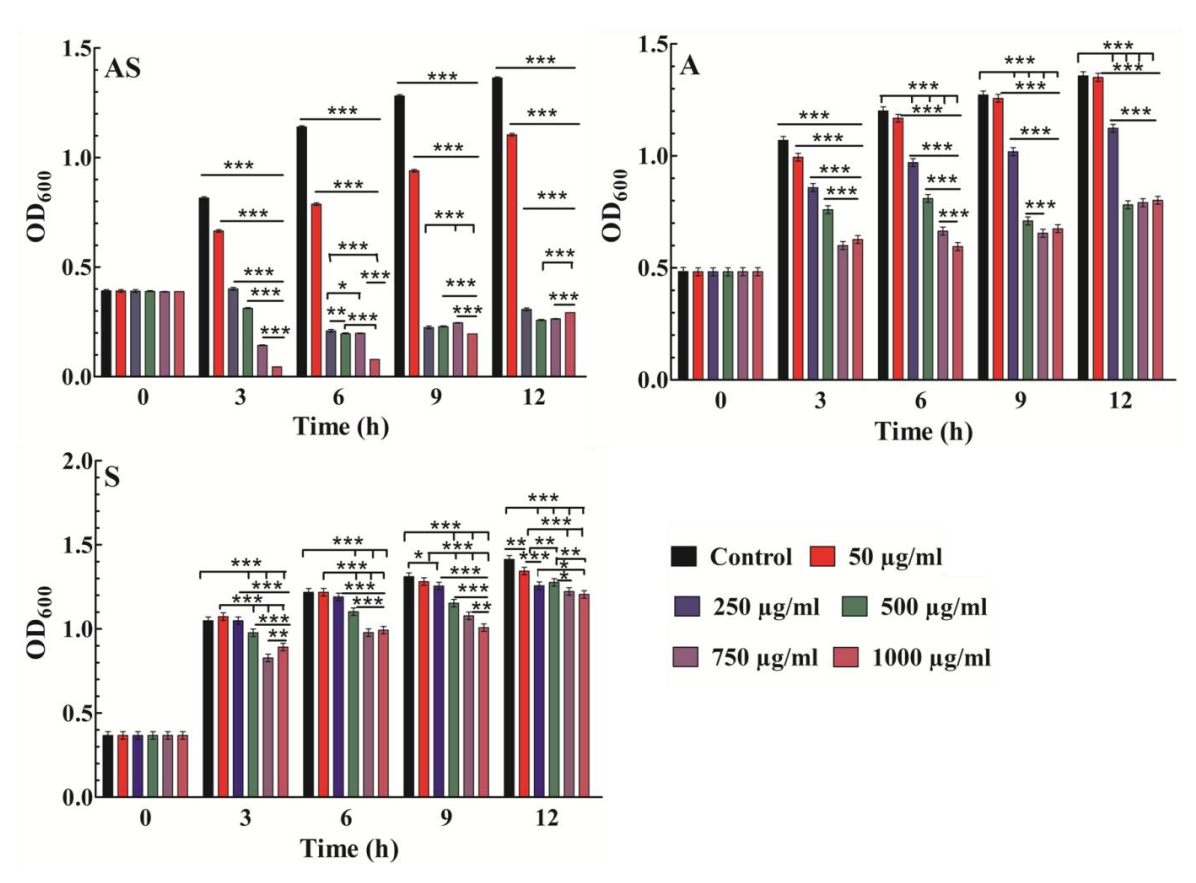


Figure 3.25: Results show the antibacterial activity of (a) $Ag/Sn-SnO_2$ composite NPs; (b) Sn/SnO_2 NPs alone and (c) AgNPs alone in E. coli bacterium obtained by Luria broth technique; (d) comparative antibacterial activity results calculated from the zone of inhibition study for Ag NPs, Sn/SnO_2 NPs and for the Ag $-Sn/SnO_2$ composite NPs in different strains. *P<0.05, **P<0.01, ***P<0.001

The zone of inhibitions is found to be 12 mm and 7 mm for Ag NPs and SnO₂ NPs, respectively (see Table 3.8). It can be noted that Ag NPs and SnO₂ NPs used here were synthesized through a similar approach From Table 3.8, we can further infer that the zone of inhibition is best obtained using Ag-Sn/SnO₂ NPs against the fungal strain *C. albicans*. This can also be seen from Fig. 3.27 (e).

To find out the effective minimum dose of Ag-Sn/SnO₂ composite NPs against the microbes, the MIC values for Ag, SnO₂ and Ag-Sn/SnO₂ NPs against microorganism

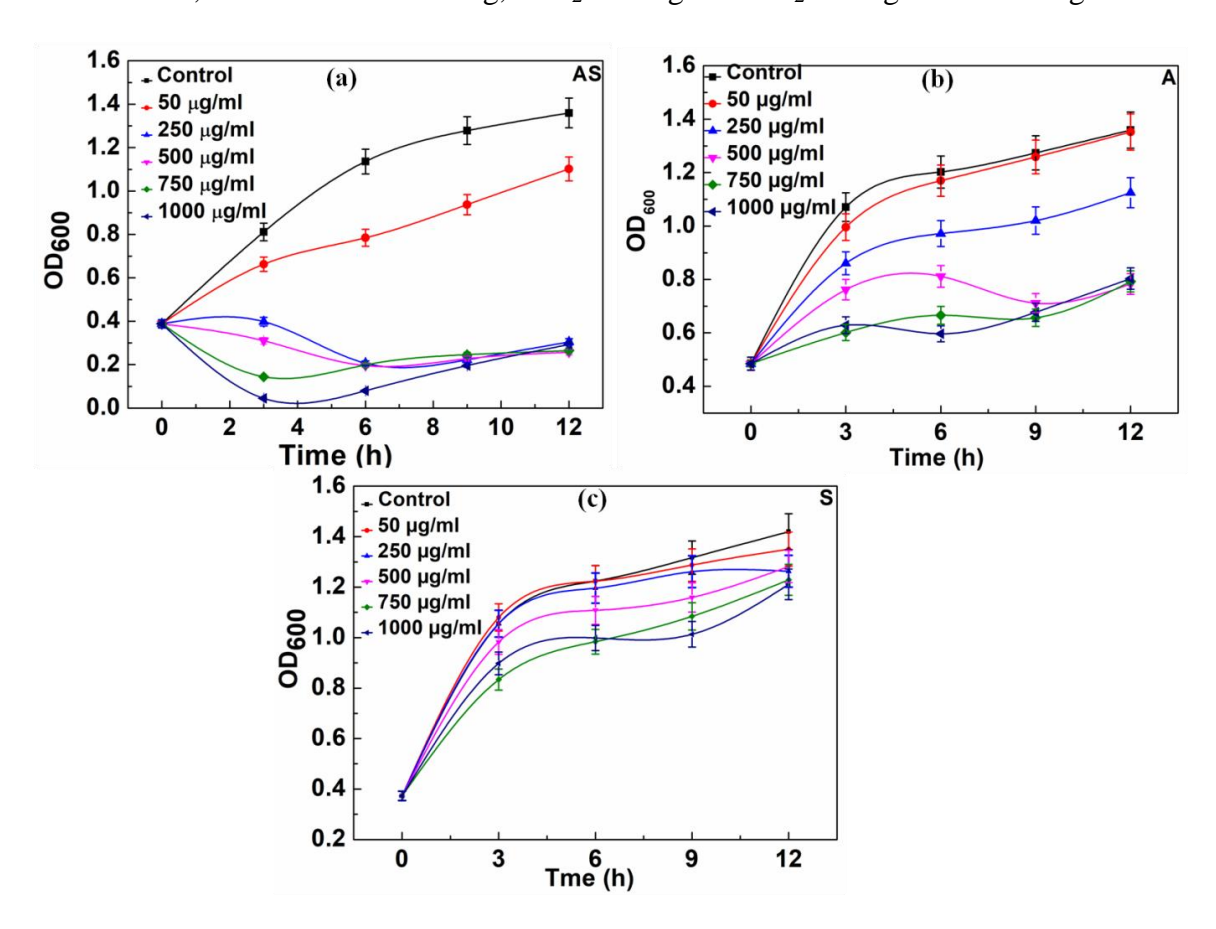


Figure 3.26: Results show the antibacterial activity for (a) Ag/Sn-SnO2 NPs composite system. (b) for Ag NPs alone and (c) for Sn/SnO2 NPs alone in E. coli bacterium by Luria broth technique.

(A. baumannii) have been calculated using twelve different concentrations such as 10 μg/mL, 5 μg/mL, 2.5 μg/mL, 1.25 μg/mL, 0.625 μg/mL, 0.312 μg/mL, 0.156 μg/mL, 0.07 μg/mL, 0.03 μg/mL, 0.019 μg/mL, 0.015 μg/mL, and 0.010 μg/mL of each material. The MIC values obtained in A. baumannii for Ag, SnO₂, and Ag-Sn/SnO₂ NPs have been shown in Table 3.7. These values show that Ag-Sn/SnO₂ NPs are two times more efficient than the Ag NPs and 41.67 times more efficient than Sn/SnO₂ NPs when they were used separately. Hence, all these results prove that the Ag-Sn/SnO₂ composite nanoparticles system is superior to the Ag or Sn/SnO₂ NPs as an antimicrobial agent.

Table 3.7: Show the minimum inhibitory concentration (MIC).

Sample	Composition	MIC Value	
AS	Ag-Sn/SnO ₂	0.015 (μg/mL)	
A	Ag	$0.03 \; (\mu g/mL)$	
S	Sn/SnO ₂	0.625 (µg/mL)	

Table 3.8: Zone of inhibition results obtained for the different microbes.

Sample	Sample	<i>E</i> .	<i>A</i> .	<i>C</i> .	К.
name	composition	Coli	baumannii	albicans	pneumonia
2b	Ag-Sn/SnO ₂	10mm	10 mm	18 mm	6 mm
A	Ag	9mm	10mm	12mm	7mm
S	Sn	8mm	11mm	7mm	Static effect

In an earlier study, mild effectiveness against the C. $albicans^{248}$ has been reported, where a core-shell $Ag@SnO_2$ was used. In another study²¹⁵ it has been reported that the

Ag/Sn-SnO₂ explored the possibility of the anti bactericidal activity, however, a detailed study has not been performed. In another study²³¹ the anti bactericidal activities of Ag NPs doped in SnO₂ against *E. coli* and *S. aureus* have also been demonstrated where the efficiency of killing these organisms was found to be very less compared to the Ag-Sn/SnO₂ NPs that is used in this work. In a recent study²⁴⁹ comprising of reduced graphene, oxide-metal oxide composite the ZOI for *C. albicans* was found to be between 16-19.5 mm for different composites i.e. RGO-NiO, RGO-AgO, and RGO-ZnO which is similar to the results obtained in this study. However, for the same compositions, the ZOI were higher for the bacterial strains yet the MIC values varied between 0.97 μg/mL-500 μg/mL for various microbes which are quite high than what we have obtained here in this study.

In another study, mixed metal oxide NPs of ZrO₂-Ag with various ratios of Ag were tested for different species of *Candida* including *C. albicans* and the ZOI was between 8 mm-19 mm which is quite good. However, in this study too, the MIC is higher which means that even though the ZOI is similar, the MIC is efficient in our case. In another study, ZrO₂-ZnO was explored for antifungal activity in which the ZOI was ca 3-6 mm for *C. albicans*. This study also found the composite material to be non-toxic towards human mononuclear cells. ¹¹⁹ Previously, the core-shell Ag-SnO₂²³¹ also had shown better antibacterial activity than the single Ag or SnO₂. Obeizi et. al²⁵⁰ also have synthesized Ag-SnO₂ nanocomposite by precipitation method and it is found to be effective against both gram-positive and gram-negative bacteria and the highest ZOI was an observer for *S. aureus* (~27 mm). The MIC values varied between 8-128 μ/mL. The authors also studied biofilm inhibition activity and found the synthesized material to be

around 73% for *S. aureus* which means that Ag-SnO₂ can also work as a biofilm inhibition material. Thus, we can safely say that Ag-Sn/SnO₂ composite NPs used in this work are very promising to prevent the growth of bacteria as well as fungi. Compared to previous and recent work in terms of simplicity and antimicrobial efficiency, these composite NPs are prepared in a single step without the use of surfactant and thus it is

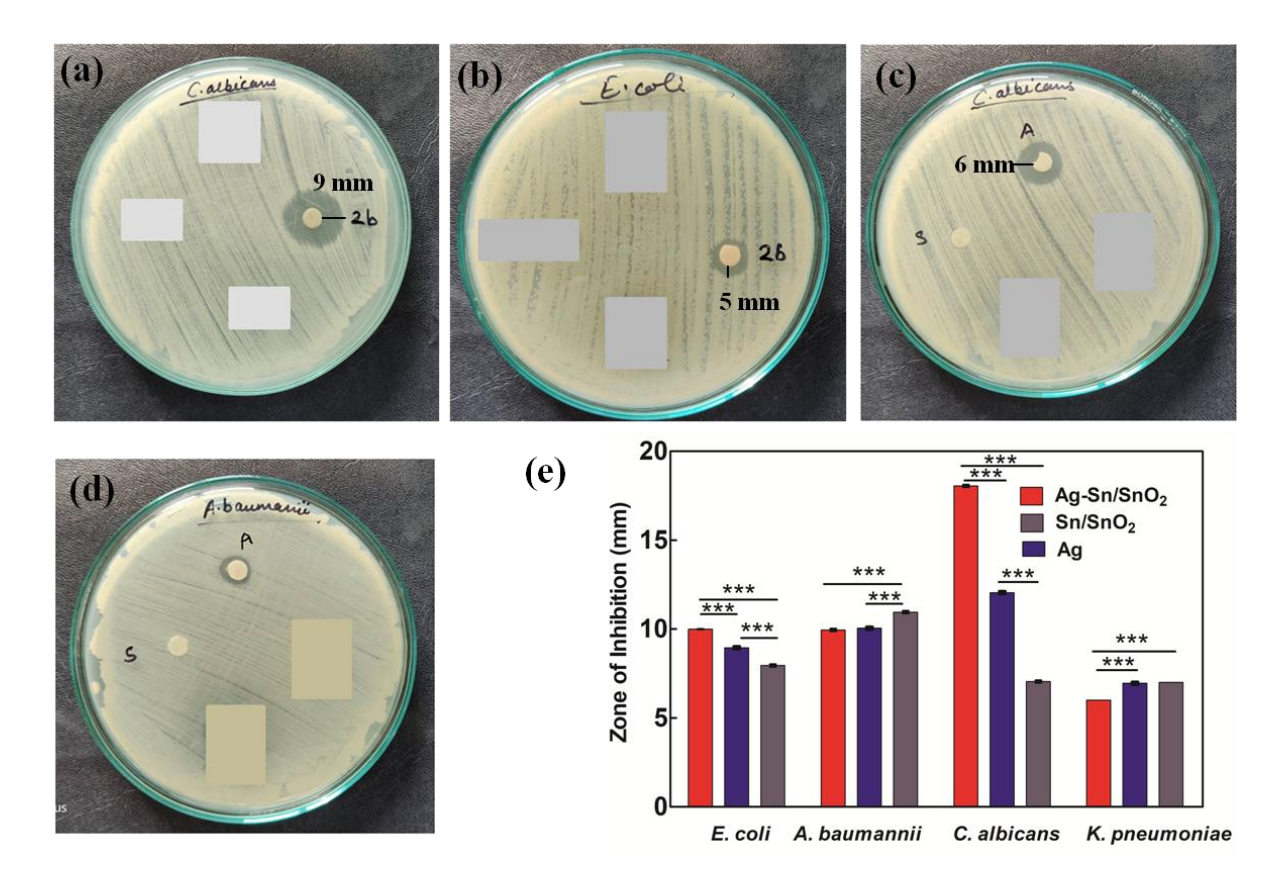


Figure 3.27: Results show the zone of inhibition for (a) Ag- Sn/SnO_2 composite NPs in C. albicans; (b) Ag- Sn/SnO_2NPs in E. coli; (c) Ag NPs alone (marked as "A") and Sn/SnO_2 NPs alone (marked as "S") in C. albicans; (d) Ag NPs alone (marked as "A") and Sn/SnO_2 (S) in A. baumannii; and (e) comparative zone of inhibition results obtained for different microbes against Ag NPs, Sn/SnO_2 NPs and for Ag $-Sn/SnO_2$ composite NPs. *P<0.05, **P<0.01, ***P<0.001

facile synthesis, cost-effective, and acts as both bacterial as well as fungal material. However, it acts as a better antifungal than antibacterial material. In the present study, the Ag-Sn/SnO₂ NPs exhibited a better inhibition which may be due to the presence of metallic Sn⁰ in the Ag-Sn/SnO₂ composite nanoparticle system and they are in the mixed-phase. The smaller the particle size, surface porous structure, and elemental composition are also the controlling factors for achieving promising results.

3.2.4.4 Probable Mechanism study

It can be noted that the antimicrobial effect is also controlled by the type and size of the nanoparticles. Different nanoparticles will have different efficiency of killing the microbes. The smaller the size of the NPs more will be the surface energy and it is easy to penetrate inside the cell wall of the microbes. Further, the concentration of the nanoparticles is also important in killing the microorganism. Once Ag nanoparticles come in contact with the bacterial wall it produces Ag+. Subsequently, when Ag/Ag+ enters inside the cell through diffusion or other methods such as phagocytosis/endocytosis, then it can damage the DNA. It is also evident that Ag nanoparticles can rupture the cell wall of the microorganism through the pit formation. Further, Ag NPs also can damage mitochondria besides generating reactive oxygen species (ROS)²¹⁶. Nanoparticles also interact with the important cellular components of the microorganism and kill them. 41,94,153 Additionally due to the high surface potential of Ag/Sn-SnO₂ there may be a possibility of creating electronic repulsions with the fungal or bacterial cell wall, which leads to the generation of H₂O₂ and very active ROS with high extent that subsequently killed the microorganism. ²¹³ To add to this the size of the Ag/Sn-SnO₂ NPs is quite small (below 10 nm in diameter) and the surface to volume ratio is high. Thus it accelerates the reaction with the cellular components^{217,214} and prevents the cellular functions of the microorganism and inhibit their growth by killing them.

Therefore, from these results, it can be concluded that the synergistic effects of the Ag/Sn-SnO₂ composite nanoparticles may be assembling all the pathways of the inhibiting bacterial and fungal growth and thus providing a better option compared to the earlier reported nanoparticles used for similar purposes. A schematic representation of the killing of microorganisms using Ag/Sn-SnO₂ NPs is shown in Fig. 3.28 which has been correlated with the band energy gap for the samples. We have observed nearly equivalent antibacterial and antifungal activity for Ag/Sn-SnO₂ NPs in all E. Coli, A. baumannii, K. pneumonia, P. aeruginosa, and C. albicans pathogen as per in silico study. However, the in vitro results exhibited higher activity against candida compared to the other organisms. To understand this difference we have scrutinized whether the Ag/Sn-SnO₂ NPs target the different molecular proteins of the candida or not. To do the same, chaperone Hsp90 which governs the key function of the morphogenesis, and Lanosterol 1 4α -demethylase which is a key enzyme for the ergosterol biosynthesis were selected. Candida albicans pathogenicity follows different mechanisms. Over expression of Asl3 increased the adhesion and interaction with invasion proteins (cadherin) induces endocytosis in the host cell. This yeast-host contact triggers the yeast to hypha-transition and raises the biofilm formation.²⁵¹ Similar to this, other factors influence the fungal pathogenicity like Hsp90, which is responsible for the biofilm formation and the drug efflux governs the key function of the morphogenesis. Most of the azole drugs target ergosterol biosynthesis, but the drug efflux increases the drug resistance. 252 The detailed mechanism for the Ag/SnSnO₂ NPs mediated killing of *Candida* has been shown in Fig. 3.28. Targeting to the Hsp90 may alter the virulence property of *Candida* and the ATPase domain of the Hsp90 is the active site for binding with the inhibitors. The nanoparticles used for this work have interacted with the ATPase domain. ^{192,253}

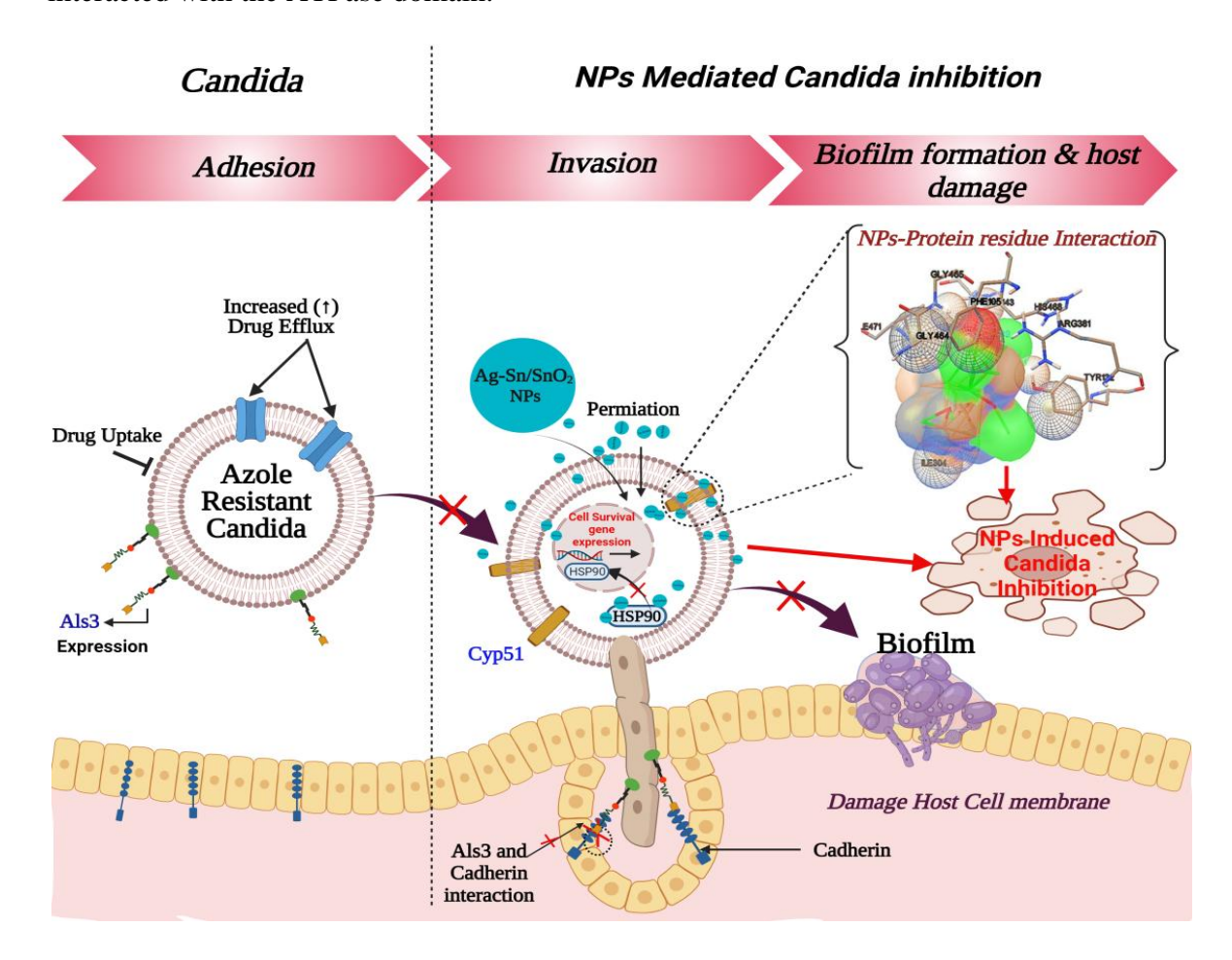


Figure 3.28: Schematic representation for the inhibition of Candida.

It should be mentioned that the Ag/Sn-SnO₂ NPs system has formed only one hydrogen bond with the THR12 residue and interacted with the active residues such as PHE159 and HIS9 as shown in Fig. 3.29 (b). For this interaction, the associated binding energy has been calculated to be -7.47, which is higher in value compared to the binding

energy required to associate with the Als3 protein. The detailed results have been enlisted in Table 3.6 for other interactions involved. Further, it can be noted that most of the antifungal agents have azole groups that can target the Lanosterol 1 4α -demethylase which is a conserved sequence of *C. albicans, C. krusei, C. tropicalls, and C. glabrata*. From our study, it is found that a higher binding affinity acts between the Ag/Sn-SnO₂ NPs and Lanosterol 1 4α -demethylase (-7.71 kcal/mol) (Table 1) as compared to the earlier reported results for the fluconazole (-4.44 kcal/mol) or ketoconazole (32.55 kcal/mol).

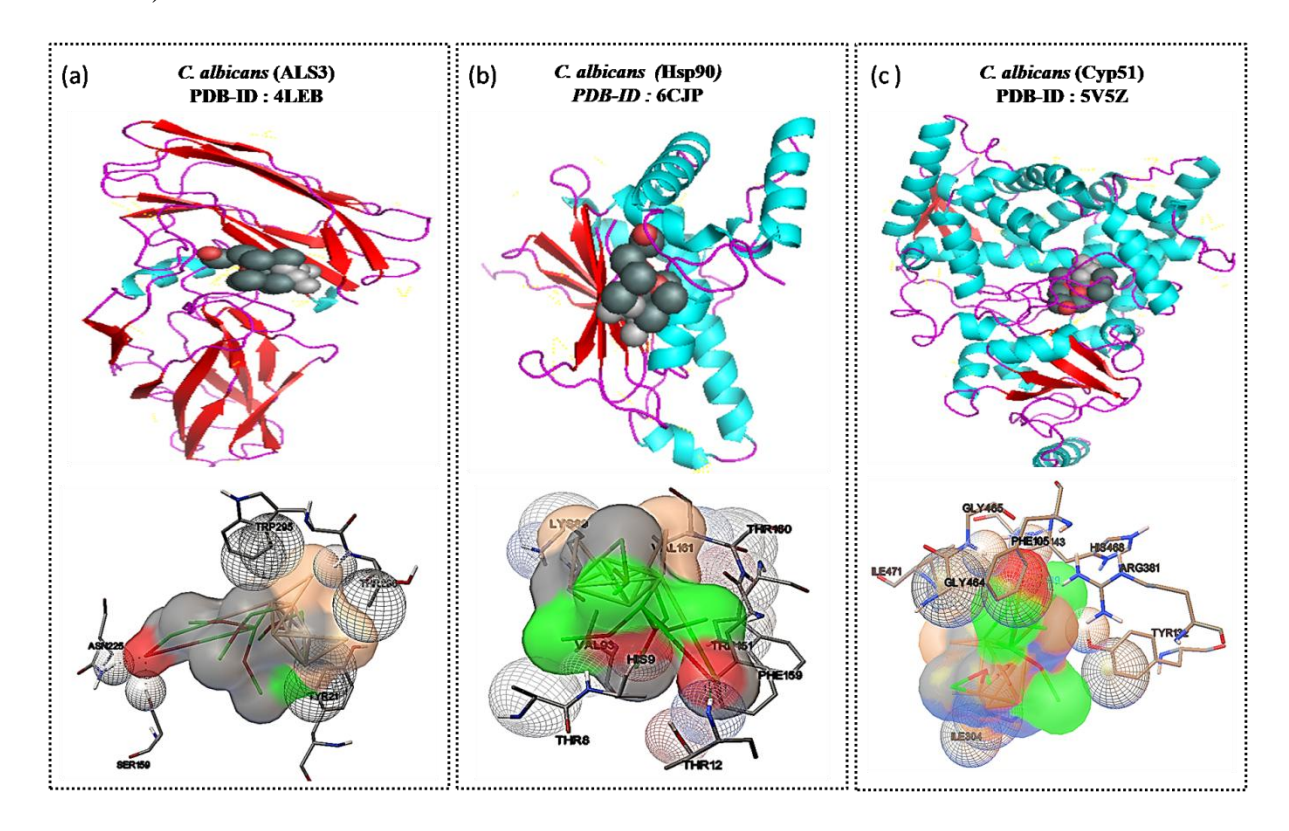


Figure 3.29: Shows the molecular interactions associated with molecular target proteins of C. albicans and Ag/Sn-SnO₂ NPs. (a), (b), and (c), represent the crystal structures of Als3, Hsp90, and Cyp51, respectively. The upper part of each panel represents the full ribbon structure of the protein interacted with nanoparticles while the lower panel shows the corresponding interaction with amino acid residues and Ag/Sn-SnO₂ nanoparticles.

Further from this study, it is evident that the binding of Ag/Sn-SnO₂ is possible with the active heme interacting pocket. It can be noted that the Lys143 of Lanosterol 1 4α -demethylase is involved in ionic interaction with the heme ring and it affects the beta bulge. Similarly, the Tyr132, Phe105, and G464 of Lanosterol 1 4α -demethylase are also involved in heme propionate since they are the active sites for the azole moiety. The mutation of the active sites of these protein residues further conforms to the development of the resistance against the azole group of the antifungal agents. Eurther, I304 and I471 are the main chains active components of beta carbon of the heme helix which increase the polarity of the heme helix. 255 From this study it is observed that the Ag/Sn-SnO₂ NPs exhibited interaction with the heme propionate residues such as Lys143, His468, Tyr132, Arg381, Phe105, Gly465, Gly464, Ile471, and Ile304 by forming the hydrogen bonds with the Arg 381 residue of Lanosterol 1 4α -demethylase (Fig.3.29.(c)) and increase the inhibition of the Candida strains. Further, the in silico results showed that the interactions of Ag/Sn-SnO₂ NPs with Als3, Hsp90, and Cyp51 which inhibit the growth of the Candida strains and also prevent the invasion and biofilm formation (Fig. 3.28). This inhibitory interaction of Ag/Sn-SnO₂ confirms that the Ag/Sn-SnO₂ nanoparticle can be a potential candidate against the *candida*. Additionally, the Ag/Sn-SnO₂ composite NPs can be used against *Candida* since it has a higher inhibitory activity to the different molecular targets.

3.2.5 Conclusions for this part:

The present work describes the cost-effective facile synthesis of mesoporous antimicrobial composite nanoparticles consisting of nano-silver (nano-Ag) and tin/tin oxide

(Sn/SnO₂) NPs in a defined ratio by chemical reduction method without using surfactants. The as-prepared nanocomposite is characterized by various techniques and is>10 nm, irregular shape, and shows the presence of Ag, Sn, and SnO₂ without any other impurity. The prepared nano-sized composite of Ag/Sn-SnO₂ has been tested on bacterial and fungal strains and it has been shown that the composite nanoparticles act as bactericidal as well as fungicidal components. It has a very low minimum inhibitory concentration (MIC) compared to the individual components of the composite nanoparticle system. The MIC values are also one of the lowest in currently available literature which makes this composite material a promising one for use in biological applications. Although the in-silico docking showed similar results for microbes but the ZOI values said otherwise which is why different proteins were targeted to understand its mechanisms. Thus, this study provides an insight towards understanding the mechanism which might be useful for future studies. Based on these results, it can be concluded that Ag/Sn-SnO₂ nanocomposite particles can be used in the broad prospective development of the health care technology and for preventing the bio-film formation to prevent the growth of infections caused due to the micro-organism. Further, with this component increased resistance to traditional antibiotics/ antifungal drugs led to the demand for other therapeutics that can be satisfied useful for preventive measures. However, more studies need to be conducted especially in gram-positive bacterial strains, and also tested for cytotoxicity to further understand the synthesized material which will improve its application domain.

CHAPTER 3: Part III

3.3 Preparation of CuO-Sn/SnO₂ and CuO-Ag/AgO nanocomposites and their comparative Antimicrobial activity

3.3.1 Abstract

Since Ag is one of the most widely used NPs for antimicrobial activity; its overuse has again become a concern. Few reports of bacteria gaining resistance to Ag nanoparticles are also seen. To address this issue, this part focuses on synthesizing CuO-Sn/SnO₂ nanocomposite was synthesized as an alternative to Ag nanoparticles, and the CuO-Ag/AgO was also synthesized to understand the comparative study in different strains. From the in-vitro studies in gram-positive strains, we could see similar results for CuO-Ag/AgO and CuO-SnO₂/Sn. However, in the LB broth technique, we saw some resistance after a certain time. These results motivate making Sn/SnO₂ an alternative to Ag if it is further studied upon.

3.3.2 Introduction:

Ag nanoparticles are considered one of the best forms of antimicrobial agents and it has been in use for a long time now. However, recently some form of Ag resistance is observed which is concerning. Further, infection due to microbial adhesion, bio-film, and colony formation on the sensitive surfaces and skins have become harmful to health due to severe infections and development of diseases and is one of the major concerns due to the developed resistance to antibiotics. Nanoparticles possess unique properties which make them suitable candidates for biological and biomedical applications

including the management of the major infection as discussed in previous chapters.³³ As an example, hospital-acquired infections (HAIs) and their transmission from one person to another person via metal surfaces have been a major worry especially during the pandemic, which could be managed through the formation of nanoparticles coatings on the regularly used materials in hospitals including the hospital beds and surgical tools.²⁵⁶ It is recently reported that nanocomposites consisting of transition metals have shown antibacterial and antifungal properties including copper.²⁵⁷ These nanoparticles are useful in making the anti-microbial membranes and consequently enhance the antifungal properties. Nanomaterials consisting of transition metals also act as photocatalysts, therefore surfaces made of these photocatalyst nanomaterials or surfaces coated with these photocatalyst nanomaterials have become a potential technology to reduce HAIs.²⁵⁷ Nanoparticles consist of high specific surface areas which allow higher interactions between the metal nanoparticles to microbes, leading to enhanced microbial activity.²⁵⁸

Cu and CuO NPs have been in use as antimicrobial drugs for a long time now. Lately, due to on rising of the covid-19 pandemic; it has been in use as a form of coating agent to prevent further transmissibility in hospitals setting. Copper also possesses a unique electronic structure with ionic conductivity and its electron mobility can be improved with a narrow bandgap for enhancement of antifungal effects. In this present study, we focused on the earth-abundant copper (Cu) based nanocomposites for obtaining easier and cost-effective nanocomposites for antimicrobial applications. This present work focuses on the synthesis and development of CuO- Ag/AgO and CuO-SnO₂ nanocomposites and their antimicrobial capabilities were investigated by which we are

also focusing on developing an alternative solution to Ag NPs. Previously, Nanocomposites using the above nanoparticles have been synthesized in various ways such as microwave-assisted method,²⁵⁹ electrical discharge methods,²⁶⁰ wire explosion method,²⁶¹ biosynthesis method,²⁵⁸ hydrothermal,²⁶² etc. were investigated and found to have a great impact on microbial studies in various strains such as *E. coli, S. aureus, P aeruginosa, B. subtilis, Aspergillusniger, C. albicans*, etc. Cu-SnO₂ also have been proposed for bilayer coating to reduce HAIs.²⁶³ These works although suggest good antimicrobial activities against both bacteria and fungus; have their challenges such as higher concentration, size, complex synthesis route, etc.

In the above line, in this work, we have tried to bridge the gap of antimicrobial efficiency by synthesizing CuO-Ag/AgO and CuO-Sn/SnO₂ NCs without using surfactant or any capping agents (anionic, cationic, and amphoteric surfactants) and a comparative study of morphological, chemical, structural properties were investigated using various characterization techniques. Further, the surface charge/zeta potential, the chemical functionalities and electronic environment and Surface Plasmon effects, stability, and the concentration of the components in the colloidal suspensions which also play a major role in their performances have been evaluated. Thus the synthesized composite nanoparticles have been qualified in these directions for their use in antimicrobial purposes. Considering these properties, the composites were tested against various strains and their antimicrobial activities were compared. Further, in this work, a fair balance among a potent antifungal, nontoxic, and cost-effectiveness of the material synthesis have been ensured and a novel cost-effective synthesis of composite nanoparticles consisting of

copper, silver, tin, and their oxide materials has been proposed as evaluated through their in-vitro studies and proposed mechanism.

3.3.3 Methodology:

3.3.3.1 Synthesis of CuO/Ag-AgO:

1.4 g of AgCl and 1.8 g CuCl₂.2H₂O were added in methanol under continuous stirring.

30 mmol of NaBH₄ solution in methanol was added dropwise until the colour changed from bluish-green to brown. It was centrifuged, washed, and dried overnight at 80°C and preserved for characterizations.

3.3.3.2 Synthesis of CuO/Sn-SnO₂:

As discussed above, 1.8 g of CuCl₂.2H₂O and 2 g of SnCl₂.2H₂O were added in methanol under continuous stirring. 30 mmol of NaBH₄ solution was added dropwise and left for stirring until color changed (from blue to brown) and brown persisted. This was then washed several times with DI water, centrifuged, and dried at 80° C.

3.3.3.3 In-vitro studies:

The antimicrobial activities were studied by the three techniques i.e. LB Broth, Disk Diffusion, and MIC values were conducted as mentioned in Chapter 2 (page 33 and 34) of the thesis.

3.3.4 Results and Discussions

3.3.4.1 Characterizations

Composite nanoparticles were synthesized as discussed in the experimental

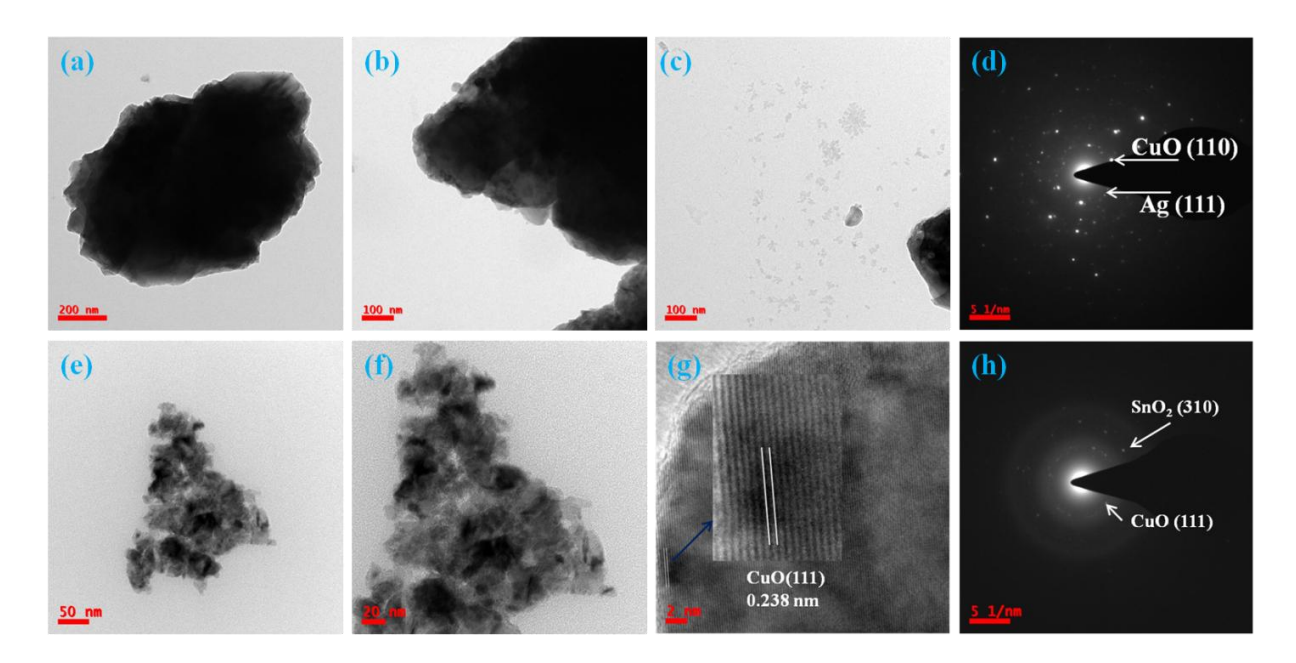


Figure 3.30: TEM images of (a-c) CuO/Ag-AgO nanocomposites; (d) SAED pattern of CuO/Ag-AgO composites nanoparticles; (e-f) TEM image of CuO/Sn-SnO₂ nanocomposites; (g) HRTEM image showing d-spacing of CuO in CuO/ Sn-SnO₂ composite nanoparticles and (h) SAED pattern of CuO/ Sn-SnO₂ nanocomposite.

section. The particle size and surface morphology have been confirmed through the TEM study. Fig. 3.30 (a-c) shows the bright-field TEM images of CuO-Ag/AgO composite nanoparticles and Fig. 3.27 d shows the SAED pattern of the obtained CuO-Ag/AgO nanoparticles. Fig 3.30 (a-c) shows a slight agglomeration of the nanoparticles. SAED diffraction pattern corresponding to the diffraction planes for CuO (110) and Ag (111). Fig. 3.30 (e-f) shows the bright-field TEM images of CuO-/Sn-SnO₂ composite nanoparticles, (c) shows the HRTEM image and Fig. 3.30 (h) shows the SAED pattern of the obtained CuO-SnO₂ nanoparticles. Nanoparticles are irregular-shaped. Concentric rings that represent the nature of nanoparticles were observed from the SAED pattern from Fig 1(h). Planes corresponding to CuO (111) and SnO₂ (310) were indexed from the

fringes of the SAED pattern of the CuO-SnO₂ nanocomposite. These results co-relate with the XRD patterns shown in Fig. 3.31 as well.

The as-synthesized nanocomposites were characterized through XRD and Fig. 3.31 (a) and (b) show the obtained XRD patterns. XRD was used to analyze the crystal structures of the synthesized copper oxide/silver (CuO/Ag) and copper oxide/tin oxide (CuO/SnO₂) nanocomposites. Sharp peaks indicate the crystalline nature of the nanocomposites. XRD pattern of CuO-Sn/SnO₂ nanocomposite is indexed to the following planes (002), (111) and ($\bar{1}13$) and the corresponding peaks of tin oxide were indexed to (210) and (310). All these peaks were indexed to JCPDS data (80-0076) of the

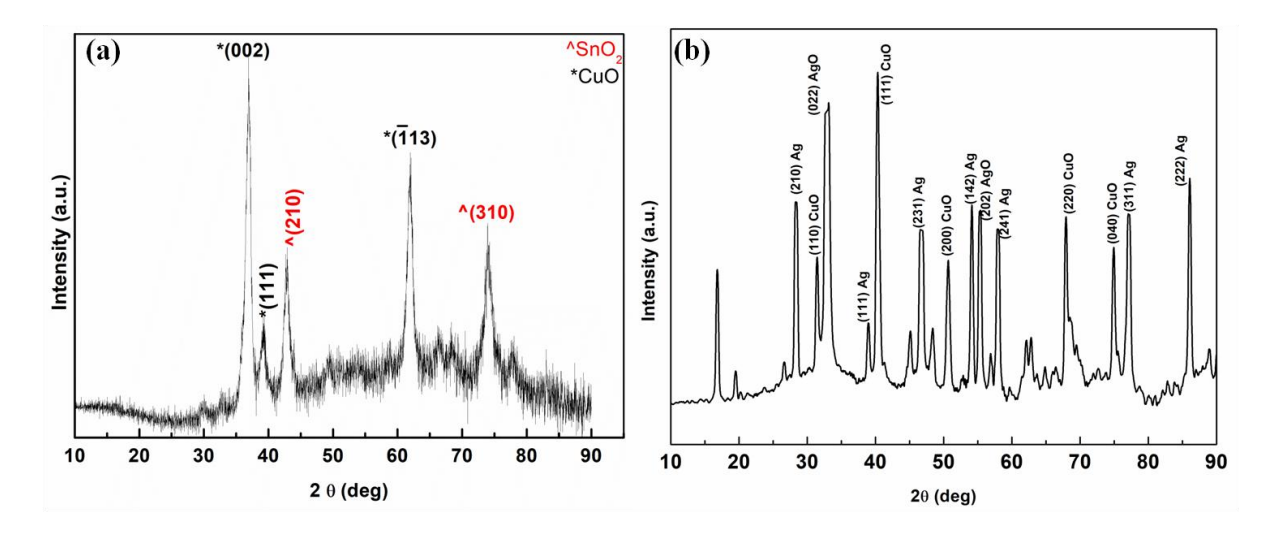


Figure 3.31: XRD patterns of (a) CuO/Sn-SnO₂ nanocomposite (b) CuO-Ag/AgO nanocomposite.

monoclinic phase of CuO nano particles²⁶⁴ and tetragonal rutile structure of SnO₂ NPs (JCPDS No. 41-1445).²⁶⁵ XRD pattern of synthesized CuO-Ag/AgO nanocomposite is presented in Fig. 3.28 b and the main planes of CuO are (110), (111), (200), (220), and (040) were indexed. Main planes corresponding to Ag are indexed to (210), (111), (142),

(241), (311), and (222), and planes of AgO are indexed to (022), (231), and (202). All the indexed peaks were in good agreement with the literature and JCPDS file No. 04-0783 for cubic Ag and AgO JCPDS file No. 84-1108.^{266–268} The results obtained from TEM and XRD are matching well both for CuO/SnO₂ and CuO/Ag-AgO composite nanoparticles.

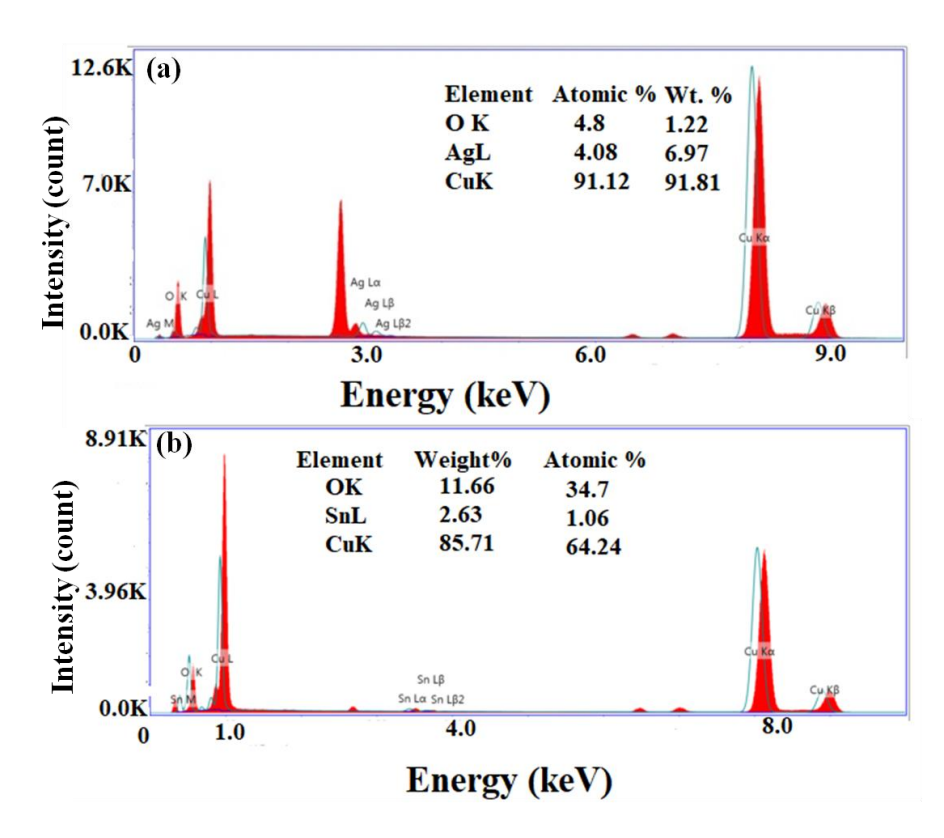


Figure 3.32: EDS spectra of (a) CuO-Ag/AgO nanocomposite and (b)CuO-Sn/SnO₂ nanocomposite

To understand the elemental composition further, EDS analysis was done which is shown in Fig. 3.32 (a) and (b). Fig. 3.32 (a) and Fig. 3.29 (b) show elemental composition analysis of CuO-Ag/AgO and CuO-Sn/SnO₂ nanoparticles, respectively. From this investigation, Fig 3.32 a shows the EDS spectrum of CuO-Ag/AgO

nanocomposite with CuO and Ag, AgO and no other impurities are present. The EDS spectra of CuO-SnO₂ nanoparticles contained tin oxide and copper elements as shown in Fig. 3.32 (b). From this investigation, it is evident that Copper is the major element or matrix element in both the nanocomposite materials. Tin and silver are present in less concentration in both the nanocomposites, respectively. The weight percentages of the characterized CuO-Ag/AgO and CuO-Sn/SnO₂ nanoparticles are shown in the EDS pattern itself. However, this result only gives us evidence for the presence of all the elements because we have used C coated copper grid and the percentage cannot be absolute as the grid also can give some intensity.

To further analyze the elemental composition, XPS was done. Fig. 3.33 and Fig. 3.34 show the XPS spectra of CuO-Ag/AgO and CuO-Sn/SnO₂ nanoparticles, respectively. The major matrix element copper in both the nanocomposites is observed at binding energy ~933 eV as shown in Fig. 3.33 (a-b) and Fig. 3.34 (a-b). Other overlapping copper bands appeared at 953eV (Cu 2p_{1/2}) and 76eV for CuO-SnO₂ nanoparticles. The Cu 2p_{3/2} and Cu 2p_{1/2} gap of 20 eV with the binding energy of 933 eV and 953 eV show the formation of CuO^{269,270} as shown in Fig. 3.33 (a). The remaining elements such as silver and tin were observed in Fig. 3.33 (c) and 3.34 (c), respectively. Silver occurred at 372 eV and 366 eV for the primary Ag 3d region with the splitting energy of 6 eV which is also shown in the inset of Fig. 3.30 a. Although the energy gap is the same, there is a negative shift in the peaks than the reported values for Ag.²⁷¹ This might be due to the presence of Copper which is more electronegative than Ag. Similarly, we can also see the presence of SnO₂ in CuO-SnO₂ in Fig. 3.33 c. The binding energy of 493.7 eV and 486 eV for Sn 3d_{3/2} and Sn 3d_{5/2}, respectively is shown in Fig 3.34 c, which

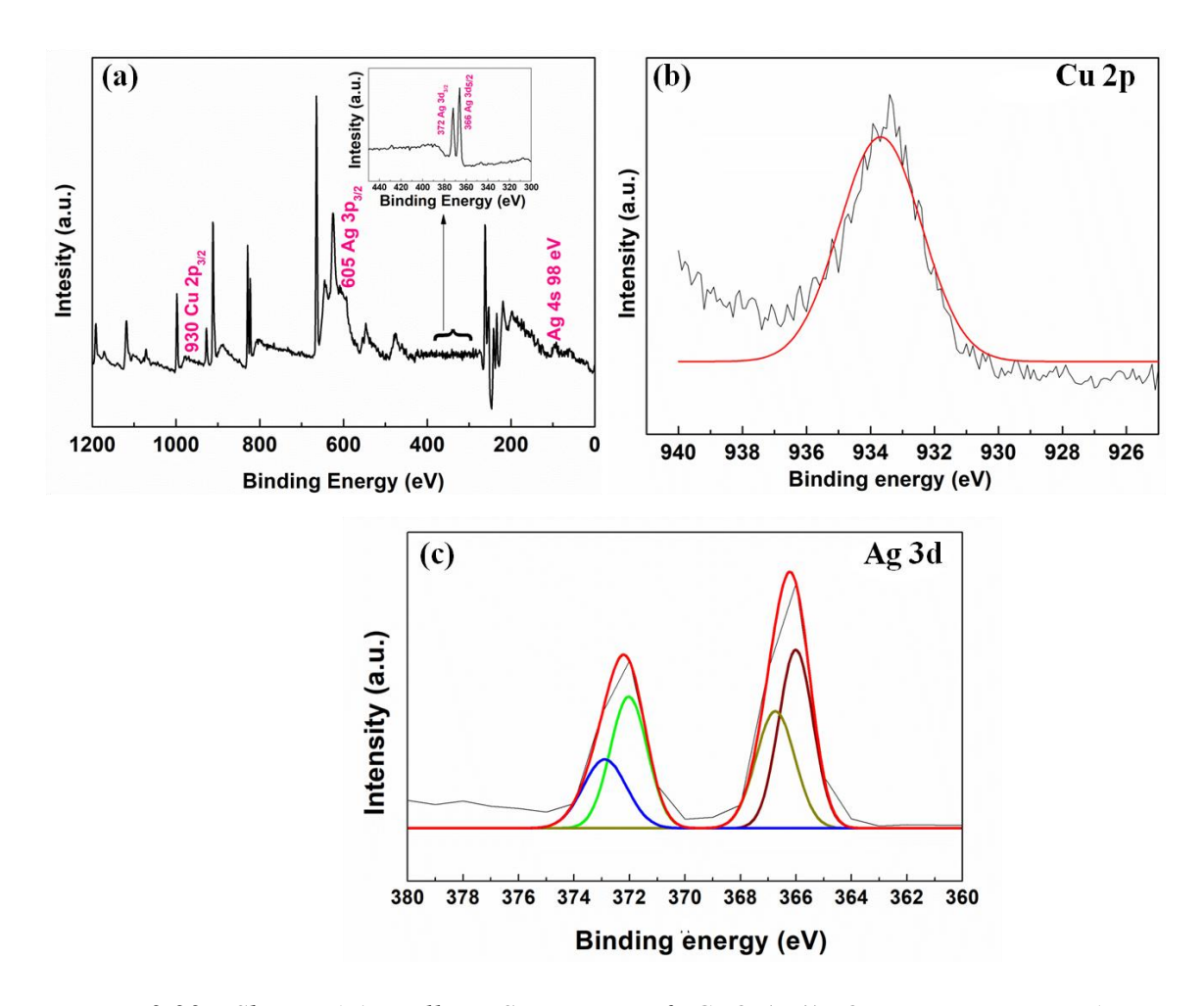


Figure 3.33: Shows (a) Full XPS spectra of CuO-Ag/AgO nanocomposite (inset: expanded form); (b) Cu 2p spectra of CuO-Ag/AgO nanocomposite and (c) Ag 3d spectra of CuO-Ag/AgO nanocomposite.

shows the presence of Sn^{+4} and is matching well with the literature.²⁷² It is also seen that Sn 3d can be fitted into two peaks and the other is Sn^0 which also matches with the literature. Thus, XPS shows the presence of CuO, Ag^0 , Ag^{+2} , Sn^{+4} , and Sn^0 . These results confirm the formation of CuO/Ag-AgO and CuO-Sn/SnO₂ along with XRD patterns as discussed above.

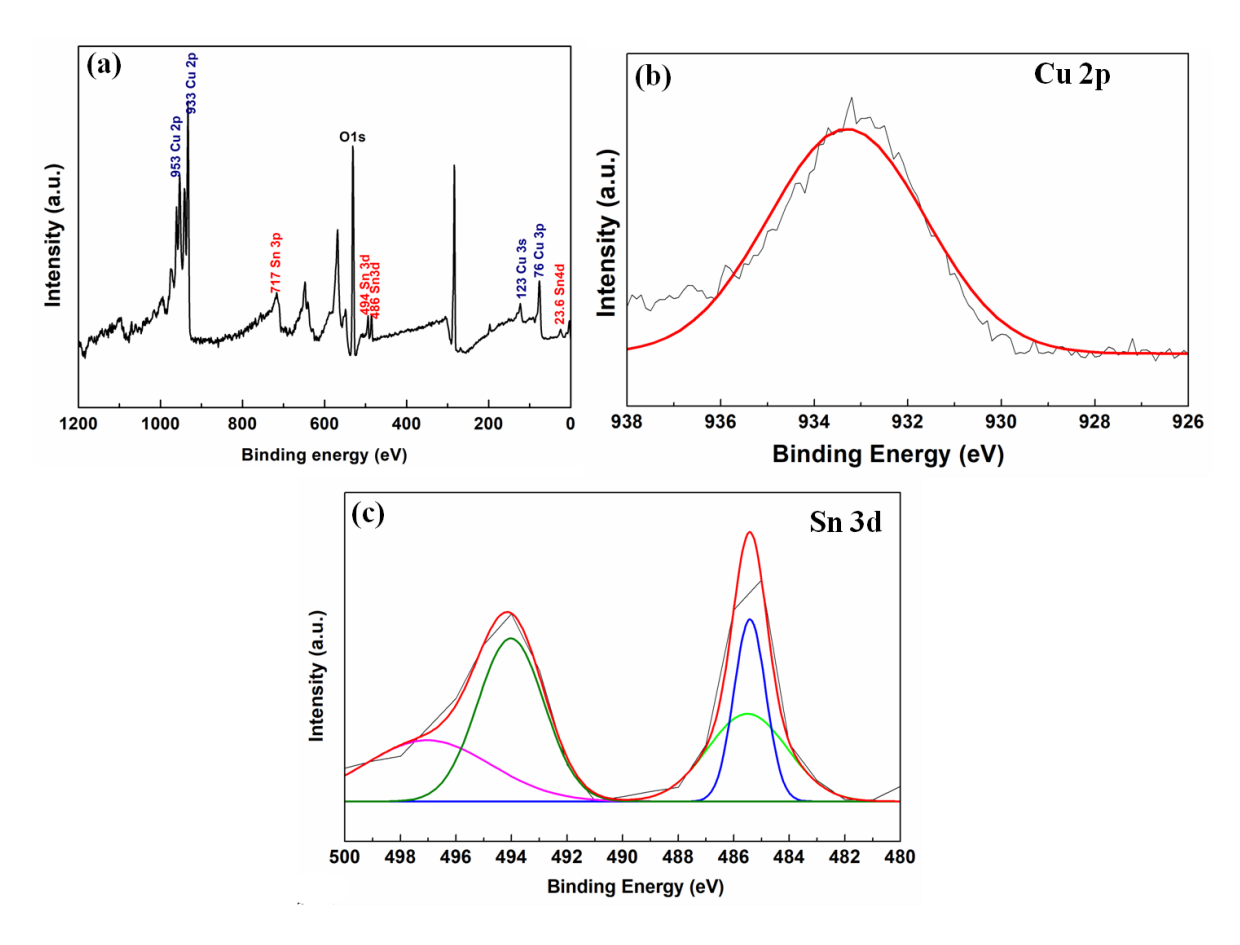


Figure 3.34: Shows (a) Full XPS spectra of CuO-Sn/SnO₂ nanocomposite; (b) Cu 2p spectra and (c) Sn 3d for CuO-Sn/SnO₂ nanocomposite.

Further, the as-synthesized nanocomposites were investigated with BET instrument to find out desorption, adsorption in the sample, and the surface areas of the nanoparticles were calculated from the obtained BET curves. Fig. 3.35 shows the BET Curves of (a) CuO-Ag/AgO nanocomposite and (b) CuO-SnO₂ nanocomposites. From these BET curves, the specific surface areas of CuO-Ag/AgO and CuO-SnO₂ nanoparticles were measured to be 1.96 m²/g and 15.0 m²/g respectively. The pore size distribution shows pore width between 2-4 nm as it is seen in the inset of Fig. 3.35 (a-b). The average particle size and morphologies of the matrix CuO nanoparticle were

confirmed by TEM bright-field images (in Fig 3.30). The TEM micrograph clearly showed the agglomeration of the nonstructural with homogeneities and with spherical morphologies of CuO nanoparticles which might affect the specific surface areas of the composite nanoparticles.

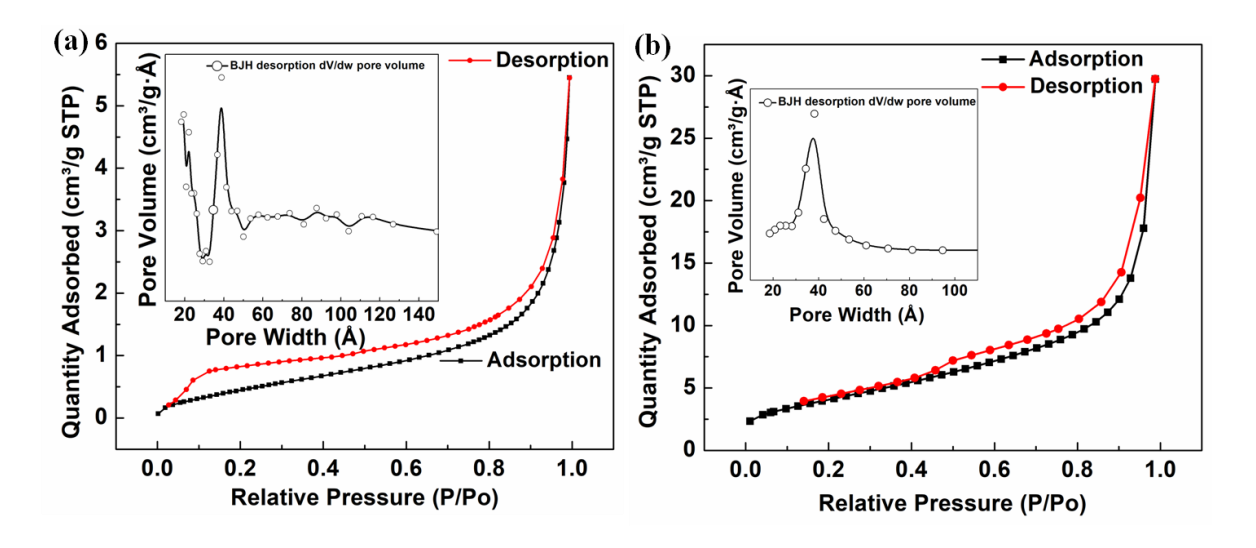


Figure 3.35: BET Curves of (a) CuO-Ag/AgO nanocomposite and (b) CuO-Sn/SnO₂ nanocomposite and inset pore size distribution curve.

The optical property of CuO-Ag/AgO and CuO-Sn/SnO₂ nanoparticles was measured using a UV-Visible absorption spectrometer. The absorption spectra of the CuO-Ag/AgO and CuO-SnO₂ nanoparticles are shown in Fig. 3.36 (a,c). The UV-Vis is seen to have a broad peak at around 275 nm for CuO-Ag/AgO NCs and 511 nm for CuO-Sn/SnO₂ which might be due to the presence of SPR of CuO. The optical band gap energy of (E_g) of the obtained CuO-Ag/AgO and CuO-Sn/SnO₂ nanoparticles were calculated from the Tauc's relation shown in equation 3.1:

where α is the absorption coefficient, ν is the frequency of the photon and h ν is the energy of the incident photon, 'n' is the exponent that determines the type of electronic transition causing the absorption and can take the values 1/2 and 2 for direct and indirect,

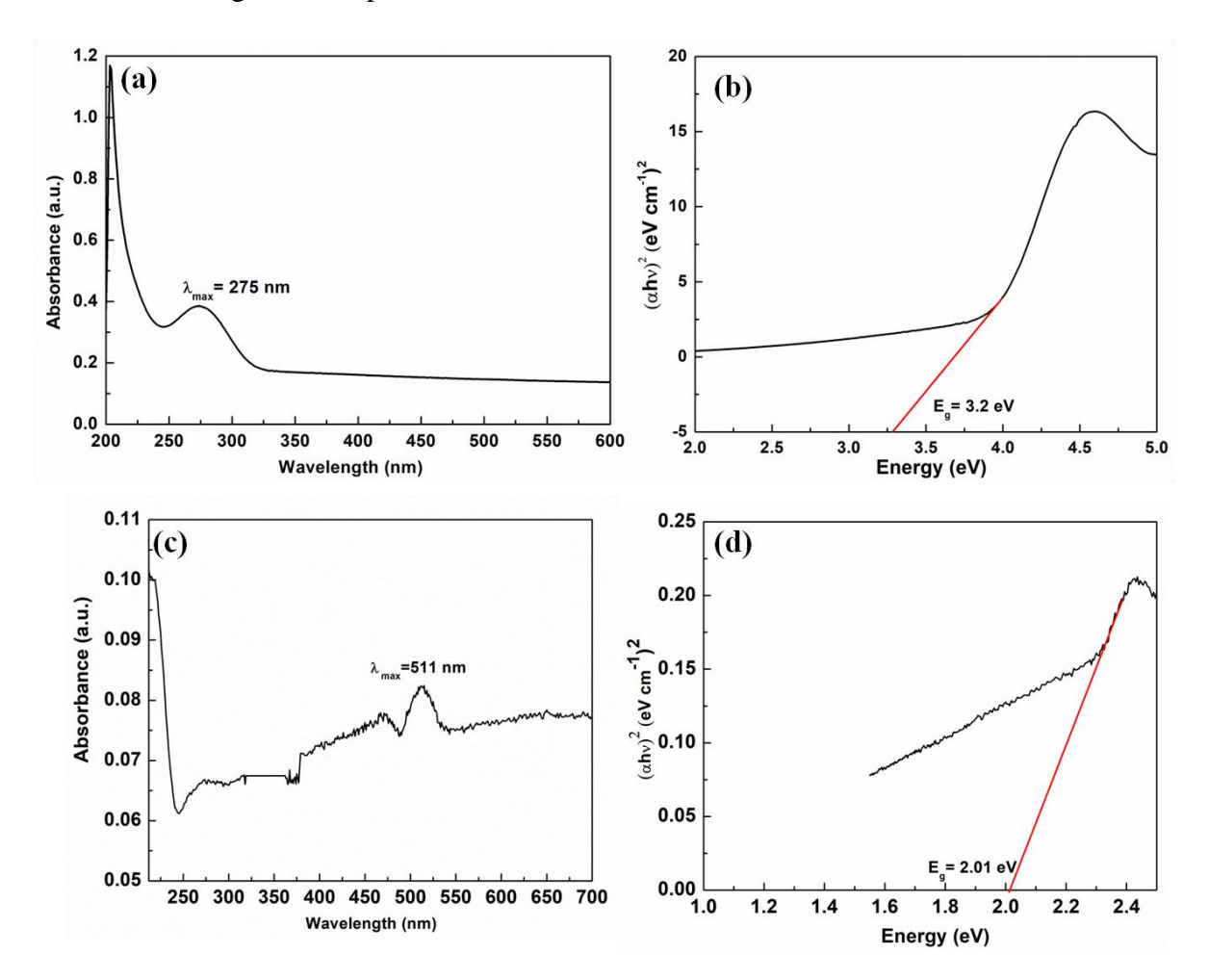


Figure 3.36: UV-Vis spectroscopy of: (a) CuO-Ag/AgO nanocomposites; (c) CuO-Sn/SnO₂ nanocomposites; Band gap energy of the (b) CuO-Ag/AgO composite nanoparticles; (d) CuO-Sn/SnO₂ nanocomposite.

respectively. The energy intercept of a plot of $(\alpha h \upsilon)^2$ vs h υ yields E_g for a direct transition as shown in Fig. 3.36 (b) and Fig. 3.36 (d) and the absorption spectrum of CuO-Ag/AgO and CuO-Sn/SnO₂ nanoparticles, respectively. The energy band gap of the CuO-Ag/AgO

NPs are estimated from the energy intercept of the extrapolation of the linear portion of the curve to 3.2 eV. It is much larger than that of the band gap of bulk CuO (1.54 eV). A strong blue shift is observed here due to the quantum confinement effects resulting from the decrease in the size of the bulk to nanoparticles. For CuO-Sn/SnO₂ the band gap is calculated as 2.01 eV which is higher than CuO and lower than bulk SnO₂ (~3.6 eV).

The TGA thermogram for the CuO-Ag/AgO and CuO-Sn/SnO₂ nanoparticles was shown in Fig. 3.37 (a) and (b) respectively. The results showed a similar weight loss

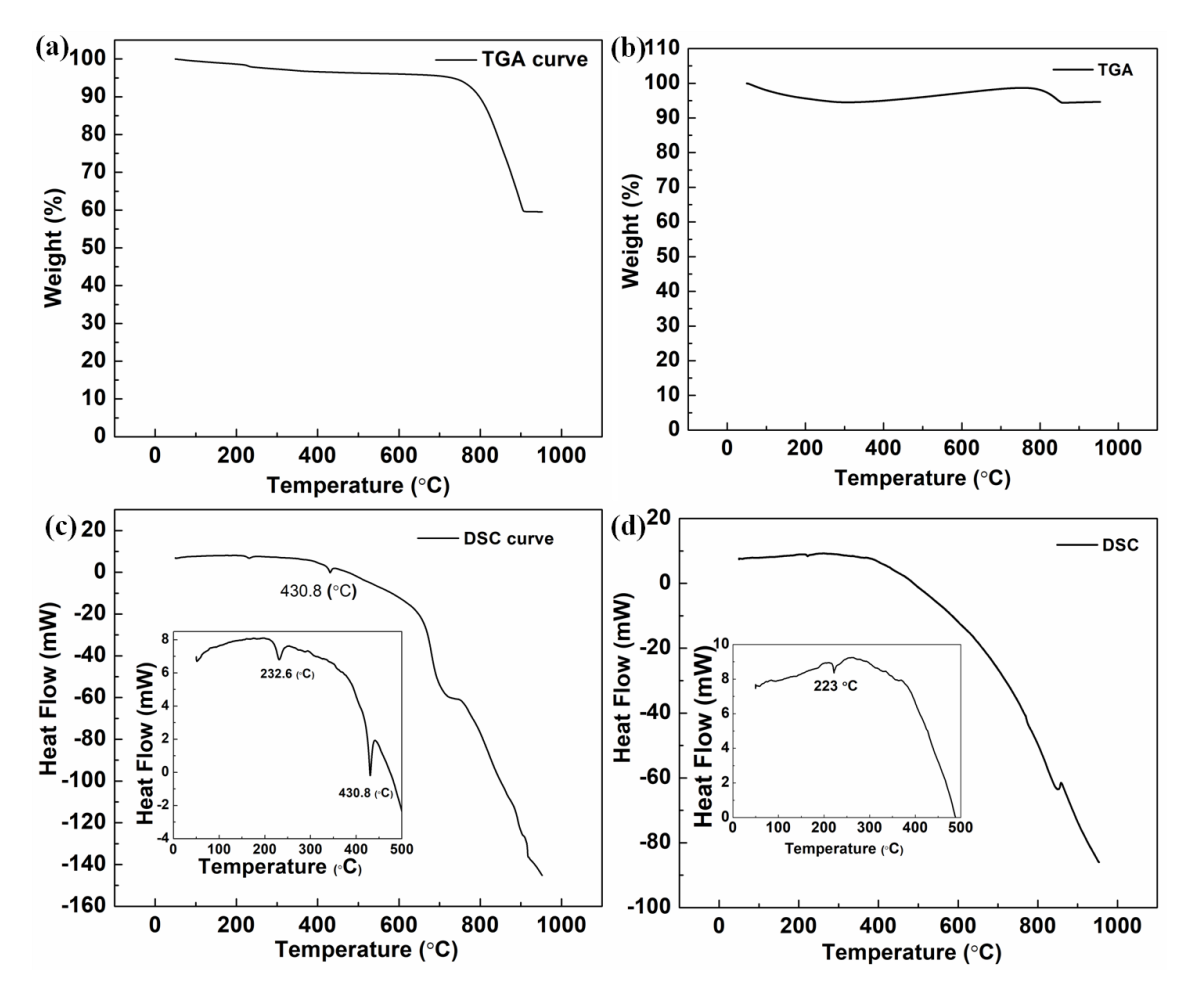


Figure 3.37: TGA Curves of (a) CuO-Ag/AgO nanocomposite (b)CuO/Sn-SnO₂ nanocomposite and DSC curve of (c) CuO-Ag/AgO nanocomposite; (d) CuO/Sn-SnO₂ nanocomposite.

below 200 ° C which is due to the loss of moisture from the surface of the materials. The weight loss of around 30% occurred in CuO-Ag/AgO and it becomes stable at 850° C. The TGA curve shows an increase in weight in CuO-Sn/SnO₂ NC from around 200° C till 800 ° C when it finally decreases and becomes stable from around 850° C. This increase in weight is due to the oxidation of Sn where it converts into SnO₂. The DSC curve is shown in Fig. 3.37 (c) and 3.37 (d). From both the figure we can see an endothermic peak ~232 ° C due to the melting of Sn (the melting temperature of Sn is 231.9 ° C). The endothermic peak at 430 ° C is either due to the tiny particles of Ag NPs or the phase change of AgO to Ag.

All of these above results support the formation of CuO-Ag/AgO NCs and CuO-Sn/SnO₂ NCs. Usually when CuO-Ag/AgO and CuO-SnO₂ nanoparticles are dispersed in water; they are inclined to agglomerate due to van der Waal's forces of interactions. However, if the particles obtain charge upon dispersion, the accumulation may be barred if the electrostatic repulsive forces overcome attractive van der Waal's forces. The zeta potential of CuO-Ag/AgO and CuO-Sn/SnO₂ nanoparticles dispersed in water was found to be -7.59 mV and -22.2 mV, respectively. The negative value of zeta potential may be accredited to the formation of hydroxyl groups on the particles' surface upon dispersion in water.

Hence, these results suggest that the NCs can be used as antimicrobial materials. Further, these were tested against bacterial and the results are discussed in subsequent sections.

3.3.4.2 Antimicrobial Results:

The results of the disk diffusion test are shown in Fig. 3.38 and the values are tabulated in Table 3.9. From Fig. 3.38, we can see a clear zone of inhibition and it can be said that these NCs can inhibit the growth. The Zone of inhibition (ZOI) of NCs and single CuO are between 8-11 mm. Further, the MIC values were calculated in *A. baumannii* which is also shown in Table 3.9.

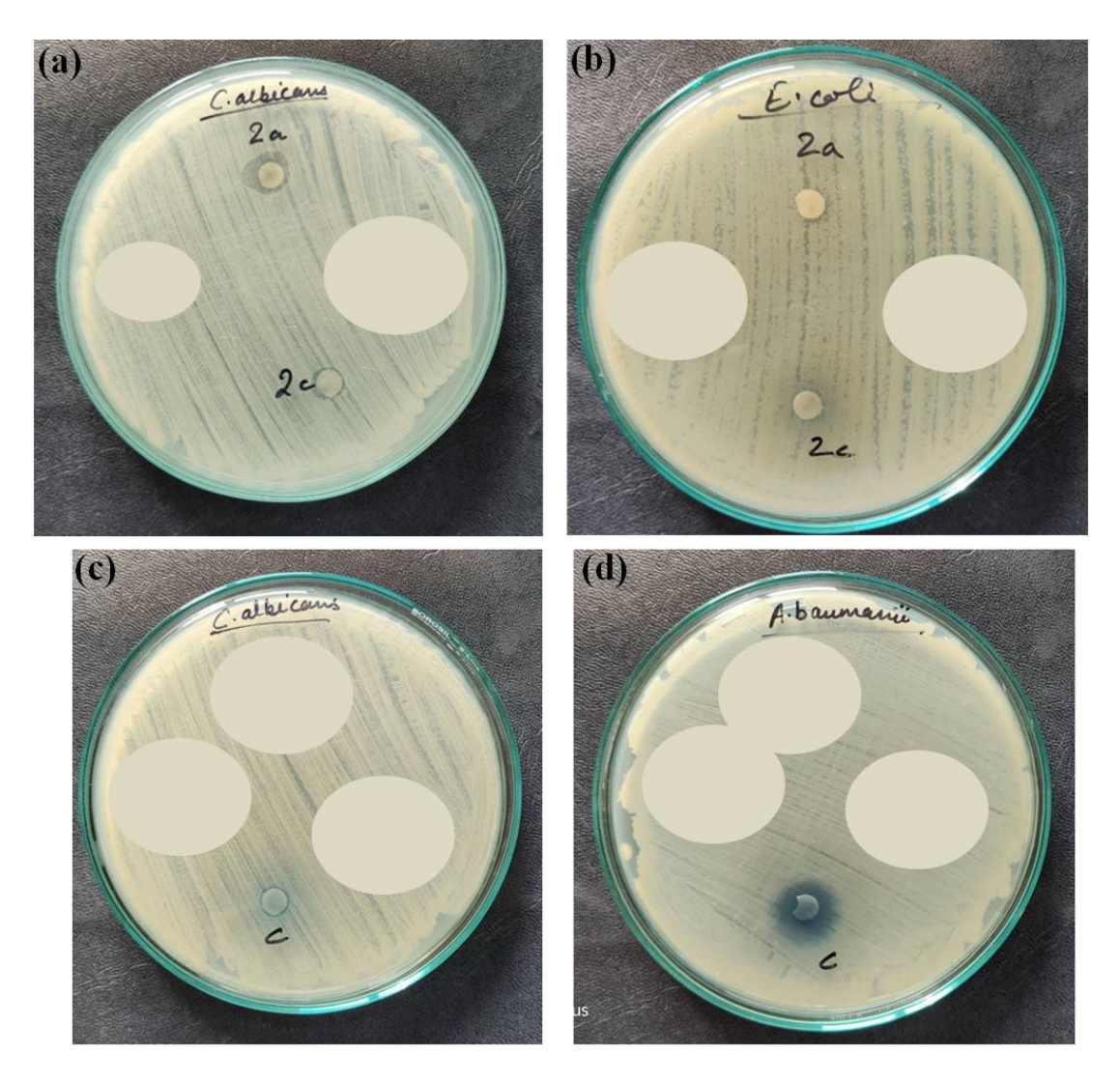


Figure 3.38: The Zone of Inhibition of (2a) CuO-Ag/AgO NCs; (2c) CuO-Sn/SnO₂ NCs and (c) CuO NPs.

Table 3.9: Zone of inhibition values for different NPs composite

Sample	E. Coli	<i>A</i> .	Candida	K. pneumonia	MIC
name		baumannii	albicans		(μg/mL
CA (2a)	8 mm	8 mm	10 mm	8 mm	0.156
CS (2c)	10 mm	7 mm	7 mm	6 mm	0.625
C (CuO)	-	11 mm	7 mm		1.25

From the values, we can see that the CuO-Ag/AgO NCs showed better MIC values compared to CuO-Sn/SnO₂. Single CuO however had greater MIC values than both the NCs. *A. baumannii*. Ag NPs act in multiple ways for inhibition of bacterial growth which is the release of Ag ions, generation of ROS, and the NPs themselves is efficient in killing bacteria by disrupting the transport system, rupturing the DNA, cell membrane, etc. which might have played the role to have lower MIC values.²⁷³ However, we also notice that the two composite materials have the zone of inhibition values quite close to each other which might mean that the two nanocomposites behave in similar ways. Previously, Sathishkumar et. al²⁵⁹ have conducted studies on Cu: SnO₂ NPs and found ZOI of between 5-19 mm in *P. aureginosa* and *S. aureus* depending on the doping % of Cu. They had observed higher concentration of Cu in SnO₂ improved the inhibition of bacteria. Similarly, Shahriyari et. al²⁶¹ have found that by increasing the current in Cu:Sn oxide nanocomposite, the bacterial growth is inhibited.

This result also showed that with the increase in the concentration of oxides, growth inhibition takes place. Further, they have found that the NPs showed better results against *B. subtilis* than *E. coli*. The study further states that the presence of oxide enhances ROS generation and the interaction of particles with the bacterial walls.

Nandhakumar et. al²⁶² in their study against *C. albicans* for Ag:CuO nanocomposite had found ZOI to be around 18 mm and they had mainly attributed this due to ROS generation which was generated due to the excited electrons from the metal oxides. However, all these studies have shown higher MIC values even if ZOI is higher whereas in the current study better MIC values are observed.

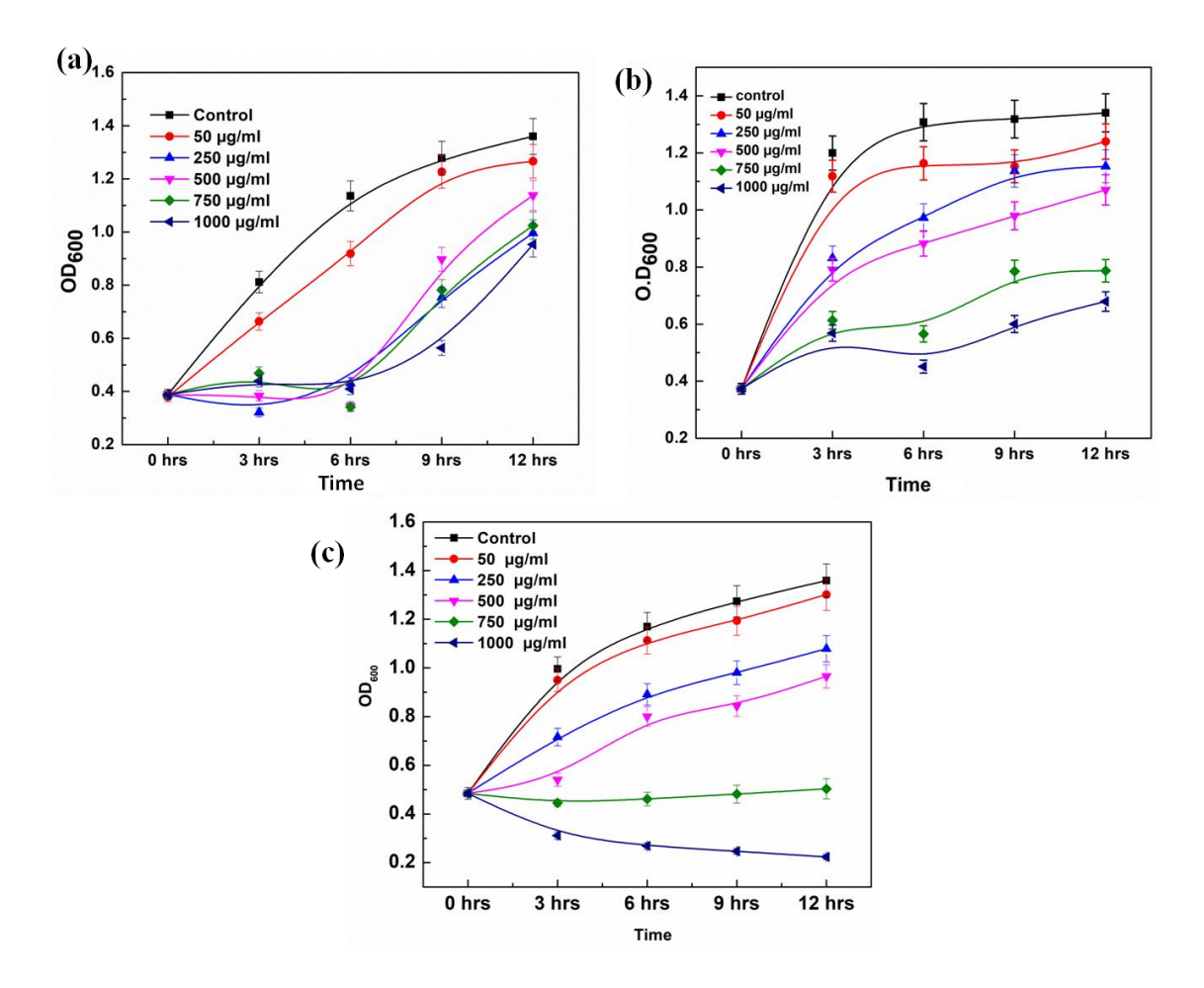


Figure 3.39: Growth Kinetics study in E. coli bacteria (a) CuO-Ag/AgO Nanocomposite; (b) CuO-Sn/SnO₂ Nanocomposite and (c) CuO Nanoparticles.

Further, a bacterial kinetics study of the nanocomposites was done in *E. coli* bacterium and compared it with single CuO which is shown in Fig. 3.36. From Fig. 3.39

(a), we can see that for CuO-Ag/AgO NC, there is a decrease in OD values up to 6 h at concentrations ≥250 μg/mL. After 6h, we see an increase in the OD values which means that the NCs no longer inhibit the growth but help in their growth even at higher concentrations. For CuO-Sn/SnO₂ NC, we see an overall growth pattern in Fig. 3.39 (b) which shows that the OD values have decreased and there is no sudden increase in the OD values like CuO-Ag/AgO NCs. From the single Cu we see that at concentration≥700 μg/mL, the OD values are quite low. From these results, we can say that CuO-Sn/SnO₂ is showing better results than the CuO-Ag/AgO NCs. This also might mean that at higher concentrations Ag and CuO are not resisting the growth, unlike CuO-SnO₂.

3.3.4.3 The mechanism for antimicrobial activity

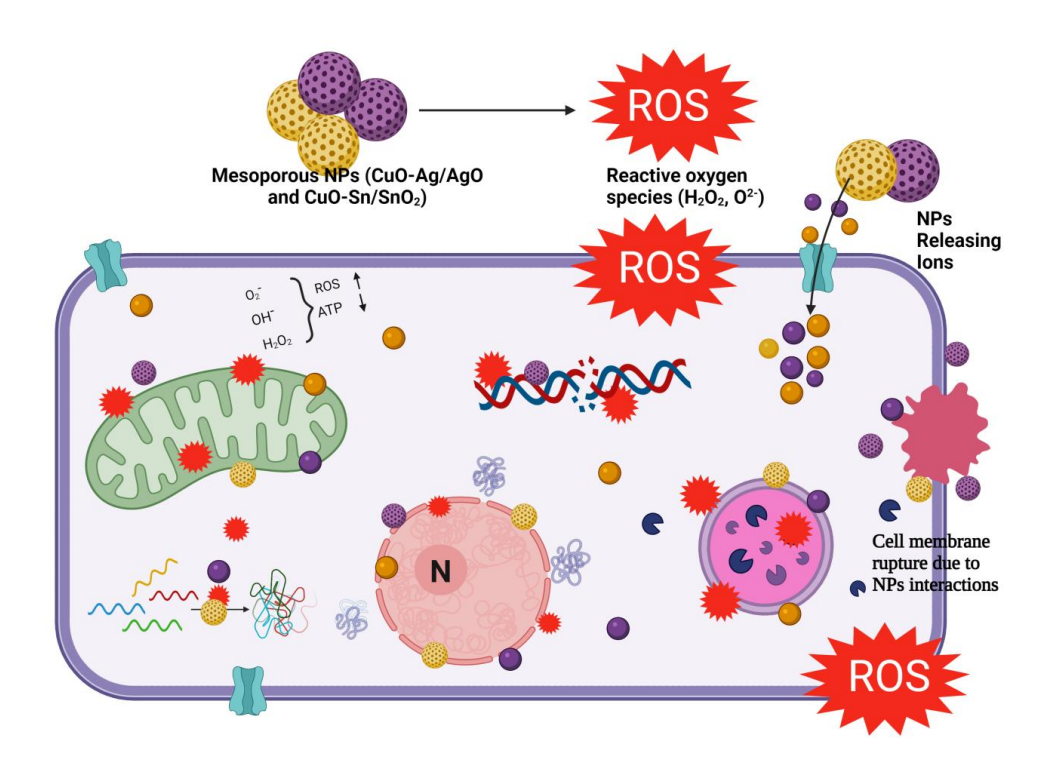


Figure 3.40: Probable mechanism of the composite system of CuO-Ag/AgO and CuO-Sn/SnO₂ for the killing of the microbes.

Further to understand the mechanism, the schematic diagram is shown in Fig 3.40. Ag Nps have multiple mechanisms like the release of Ag ions, disrupting the bacterial/fungal walls, ROS generation, etc. Similarly, CuO NPs and SnO₂ generate ROS and initiate the killing efficiency of the NC material. These composite material releases ions like Cu⁺², Sn⁺⁴, Ag⁰, which reacts with the carboxyl group of the bacterial membrane protein. Simultaneously, when the material penetrates the membrane, it also comes in contact with cellular components like RNA and this helps in the generation of ROS. The ions and ROS then disrupt the DNA, nuclei, membrane, etc. which will further kill the bacteria. Previously, Sathish et. al²⁵⁹ also have discussed similar results. Moreover, a higher amount of oxide improves ROS generation. So by combining all these processes we can predict the mechanism of these two nanocomposites to be similar.

3.3.5 Conclusions for this part:

In this current work, $CuO-Sn/SnO_2$ and CuO-Ag/AgO nanocomposites were successfully developed without using any capping agents. The composite nanoparticles were tested with bacterial pathogens like *E. Coli*, *A. baumannii*, *Candida albicans*, and *K. pneumonia*. Their structural, morphological, optical, and biological studies revealed that the synthesized CuO-Ag/AgO and $CuO-SnO_2$ nanocomposites show excellent antibacterial properties, particularly when Ag/AgO nano particles interacted with CuO it has shown MIC value of 0.156 and when SnO_2 nanoparticles were employed it has shown MIC value of $0.625~\mu g/mL$. These results are promising and the materials can be used as an alternate antimicrobial agent.

CHAPTER 3: Part IV

3.4 Synthesis and characterization of ternary metal oxide nanoparticles and their in-vitro antimicrobial studies

3.4.1 Abstract

In this part, ternary metal oxide nano composites of CuO-SnO₂-ZnO, Ag-CuO-SnO₂, SnO₂-Ag-ZnO, and Ag-CuO-ZnO were synthesized and their properties were studied by various characterization techniques. The specific surface area, pore width, etc. improved compared to the bi-metal oxide nanocomposites. Except for CuO-SnO₂-ZnO, all other three composite materials have particle sizes>10 nm. Further, the antimicrobial tests by various in-vitro techniques were carried out and the results show that these composite materials can be effective antimicrobial agents.

3.4.2 Introduction

Due to their improved stability and synergistic properties, ternary metal composites can be an alternative to single and bi-metallic nanocomposites for antimicrobial activity. They can provide an effective medium to act against various bacterial and fungal strains. The synthesis of ternary metal oxide nanoparticles and alloys is not a new concept. Alloys of Cu-Ag-Sn, Cu-Sn-Zn, and Sn-Ag-Zn have been synthesized before. ^{274–276} In recent years, some more ternary metal oxide nanocomposites have been synthesized for antimicrobial activities. ^{277–279} CdO-CuO-ZnO nanocomposite was synthesized by microwave-assisted techniques and tested against *S. aureus* and *S. typhi*. ²⁷⁷ Similarly, MgO-Cr₂O₃-ZrO₂ has been synthesized by the wet chemical method

and studied for its antibacterial activity.²⁷⁹ Transition metal complex due to their unique properties such as varying oxidation states, stability, etc. are being used for various applications like energy storage, antibacterial, catalytic, sensors, etc. 280,281 Transition metal oxides such as ZnO, SnO₂ and CuO have two-dimensional layered structures, similar to graphene. However, when used alone, they may not give the desired results. SnO₂ and ZnO have wide bang gap energy and thus absorb light in the UV region. Noble metals like Ag have surface plasmon resonance. When these materials are used in composite form, they can balance out each other's properties and give better results in various fields including biomedical. ^{282–284} Bi-metallic NPs have enhanced properties but single or monometallic have various disadvantages such as large band gap and faster recombination rate. Some other tri-metal for photocatalytic and antimicrobials have also been studied recently. For eg. ZnO-V₂O₅-WO₃ nanocomposite synthesized by the coprecipitation method has shown enhanced antibacterial activity compared to their bimetallic nanocomposites.²⁸⁵ Further, this nanocomposite material also had an excellent photocatalytic activity which could solve many environmental issues. With this motivation and a desire to develop ternary composite materials for antimicrobial activity, four different types of ternary metal composites were synthesized, characterized and their in-vitro bacterial and fungal studies were undertaken. The mixture of metal and semiconductor complex or various transition metals together was focused to study their size, compositions, and their effect on various bacterial and fungal strains.

3.4.3 Methodology

Synthesis of composite materials:

The synthesis work has also been filed for patents at Indian Patent Office with (i) *Application no.:* 202011017968, dated: April 27, 2020, (ii) Application No.: 202011031802, dated: July 24, 2020. Briefly, the synthesis is described below:

3.4.3.1 Synthesis of Ag/CuO/SnO₂ (ACS):

10 mmol of AgCl, CuCl₂.2H₂O, and SnCl₂.2H₂O were taken and stirred in a beaker for 30 minutes with methanol at RT (25 ° C). In another beaker, 90 mmol of NaBH₄ was left to disperse itself in methanol without any external stirring. This beaker was kept in the ice bath. After 30 mins, the NaBH₄ solution was added dropwise at the rate of one drop per two seconds in the solution mixture of the salt. The color changed from greenish to brownish/blackish. It was left under stirring for 2 hrs, centrifuged (12k rpm/20 min), washed several times with water and methanol (1:1), and dried overnight (12 h) at 80°C. It was then sent for characterization.

3.4.3.2 Synthesis of Ag/CuO/ZnO (ACZ):

A similar procedure as mentioned above was adopted with salts of AgCl, CuCl₂.2H₂O, and ZnCl₂. After 2 hrs of stirring, the color changed from greenish to light brown.

3.4.3.3 Synthesis of SnO₂/Ag/ZnO (SAZ):

The color changed from light brown to dark brown at the end of the reaction. The method and the quantity of the salts taken are the same as the ACS sample preparation. Here the salts used were AgCl, ZnCl₂ and SnCl₂.2H₂O.

3.4.3.4 Synthesis of CuO/SnO₂/ZnO (CSZ):

For this 10 mmol of SnCl₂.2H₂O, ZnCl₂ and CuCl₂.2H₂O were taken and the same

procedure was adopted. The color changed from greenish, then black while adding NaBH₄ solution and greenish after the reaction was completed.

Characterizations and In-vitro studies were conducted as per the description in Chapter 2.

3.4.4 Results and Discussions

3.4.4.1 Characterizations

For the morphology, crystal structure, and size distribution, TEM studies were done and are shown in Fig. 3.41. From Fig. 3.41 (a-b), we can see the TEM image of Ag-ZnO-SnO₂ nanocomposites which are of various sizes and somewhat look spherical. The HR-TEM image and the SAED pattern are shown in Fig. 3.41 (c) and (d) respectively. From the HR-TEM image we can see the presence of Ag (111), ZnO (101), and SnO₂ (101) with lattice fringe values of 0.23 nm, 0.27 nm, and 0.26 nm respectively. The SAED pattern also shows the presence of ZnO (102), SnO₂ (301), and Ag (111) with the d-spacing values of around 0.19 nm, 2.3 nm, and 1.42 nm respectively. The average size of the particles is calculated to be ~28 nm (Fig. 3.42 (c)). The particles in ACZ are slightly larger than the rest of the materials as seen in Fig. 3.41 (e-g) and these are closely linked with each other in a cross-linked way. The SAED pattern (Fig. 3.41 h) shows the presence of Ag (111), ZnO (101), and CuO (002) with d-spacing of ~0.23 nm, ~0.27 nm, and ~0.25 nm respectively. The average particle size of the Ag-ZnO-CuO nanocomposite is calculated as ~55.2 nm (Fig. 3.42 b). The TEM image of CSZ nanocomposite is shown in Fig. 3.37 (i-j). The lattice fringe can be seen in Fig. 3.41 (k) with planes (110) and (101) of ZnO and (200) of Cu₂O. The lattice distances of these are 0.28 nm, 0.27 nm, and

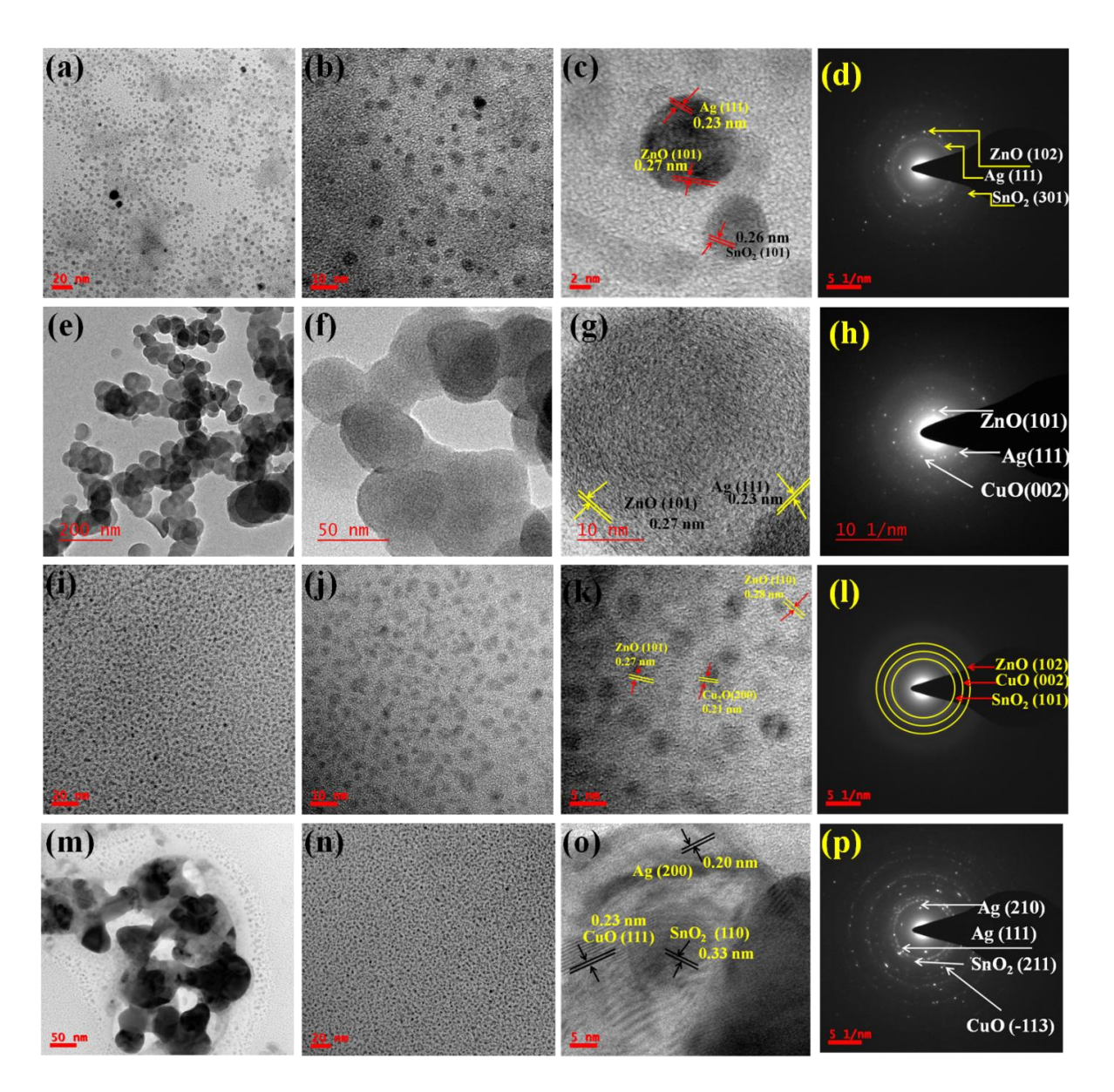


Figure 3.41: TEM image of: (a-b) SAZ, (e-f) ACZ, (i-j) CSZ and (m-n) ACS; HR-TEM image of: (c) ASZ, (g) ACZ, (k) SAZ and (o) ACS; SAED pattern of: (d) SAZ; (h) ACZ; (l) CSZ and (p) ACS

0.21 nm respectively. This also shows that CSZ has the presence of Cu_2O as opposed to other composites discussed in this article. The Cu_2O can be formed because of the

incomplete reduction and is a part of the formation of CuO. The particles are really small with some particles as small as 1 nm. The average particles size of the nanocomposite

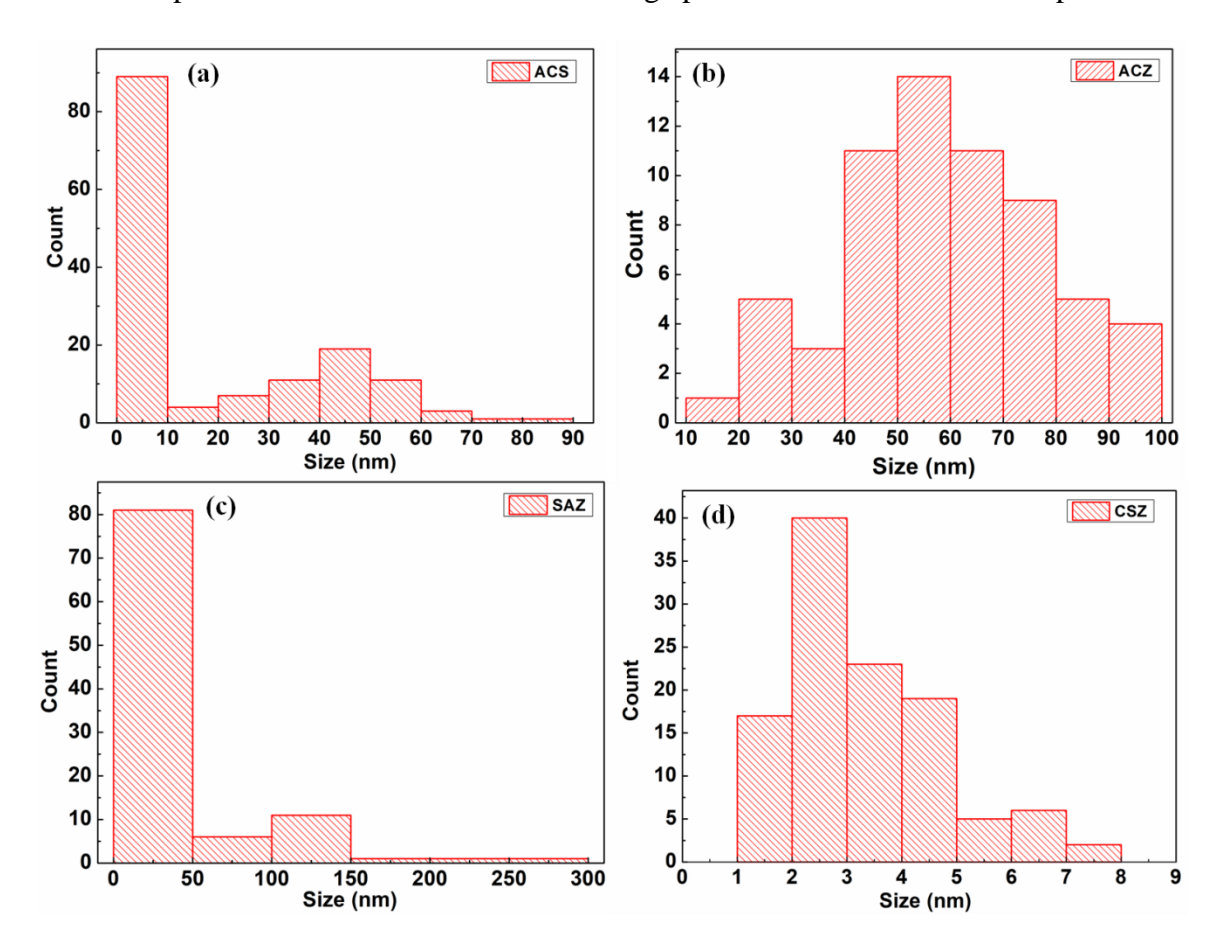


Figure 3.42: Particle size distribution of (a) ACS nanocomposite; (b) ACZ nanocomposite; (c) SAZ nanocomposite and (d) CSZ nanocomposite.

CSZ is 3.9 nm (Fig. 3.42 d). The SAED pattern shows that it has a distinct ring-type pattern. This also can be correlated with the XRD patterns in Fig. 3.43 (d). Similarly, the HR-TEM image of ACS nanocomposite in Fig. 3.41 (o) shows the lattice fringe of CuO (111) and SnO₂ (110) with the values of 0.23 nm and 0.34 nm respectively. The lattice fringe with the d-spacing values of 0.23 nm could also be for Ag (111). The SAED pattern is shown in Fig. 3.41 (p). It shows the presence of SnO₂ (211), CuO (-113), Ag

(210), and Ag (111) with d-spacing of 1.7 nm, 0.15 nm, 0.23 nm respectively. The TEM image of ACS nanoparticles as seen from Fig. 3.41 (m-n) consists of small particles (~5 nm) and larger particles (~45 nm) with an average particle size of ~21.4 nm (Fig. 3.42 a). It consists of a core-shell type of morphology as seen in Fig. 3.37 (m). The average particles size as calculated from the TEM image is CSZ<ACS<SAZ<ACZ (Fig. 3.42). The XRD pattern of the nanocomposite materials is shown in Fig. 3. The XRD image of Ag-CuO-ZnO nanocomposites, Ag-CuO-SnO₂, SnO₂-Ag-ZnO, and CuO-SnO₂-ZnO NCs are shown in Fig. 3.43 (a), (b), (c), and (d) respectively. From Fig. 3.43 (a) we can see the

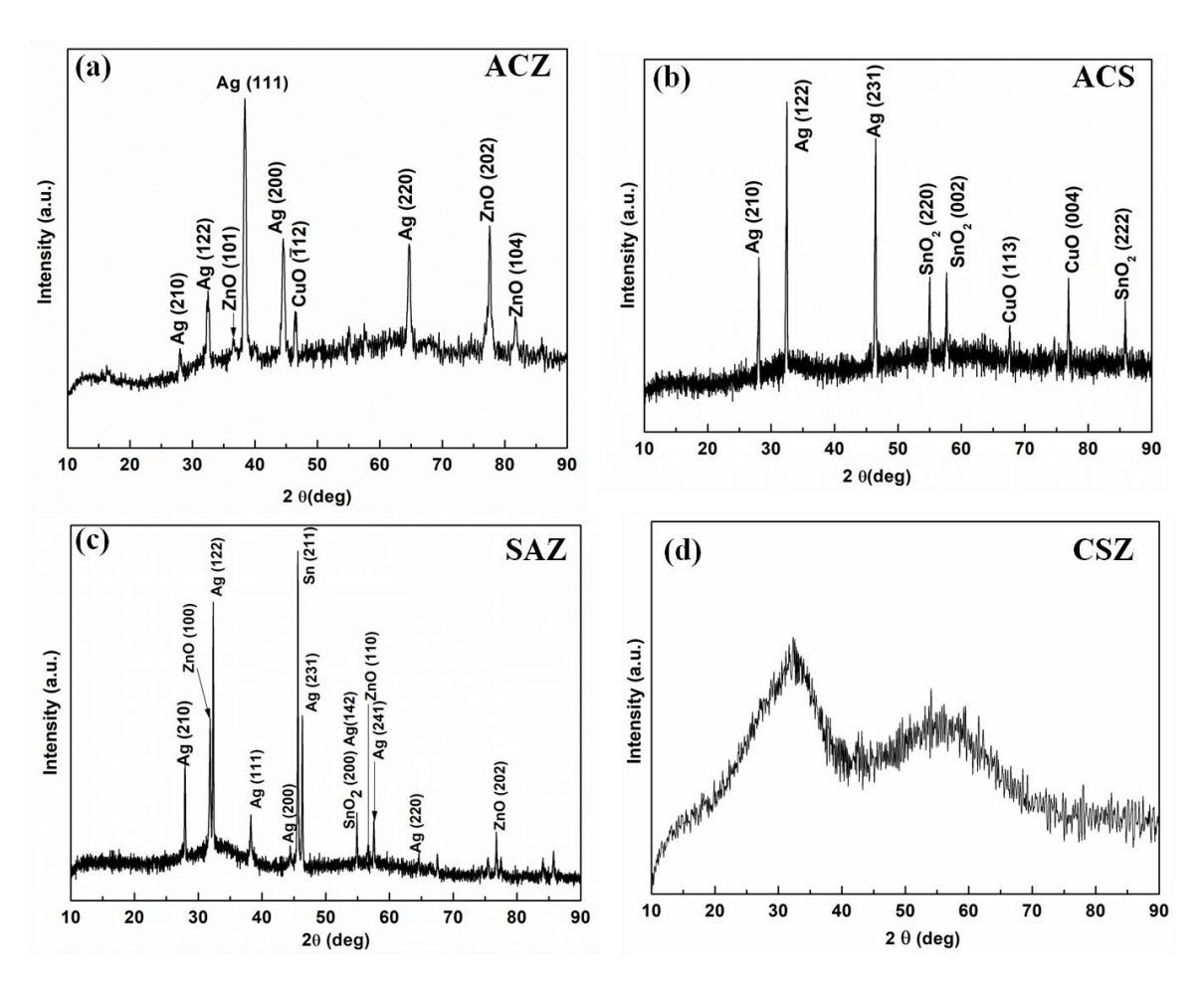


Figure 3.43: XRD patterns of (a) Ag-CuO-ZnO (ACZ), (b) Ag-CuO-SnO₂ (ACS), (c) SnO₂
-Ag-ZnO (SAZ) and (d) CuO- SnO₂-ZnO (CSZ) nanocomposites.

planes of cubic Ag (210). Ag (111), Ag (200), Ag (220) for $2\theta \sim 28^{\circ}$, ~ 38.1 , 44.2, and 64.3 respectively according to JCPDS file no. (04-0783). The planes of hexagonal ZnO (101) and (104) and cubic CuO (-112) are also seen which corresponds to JCPDS card numbers (36-1451) and (80-0076) respectively. Thus, this shows the formation of Ag/CuO/ZnO nanocomposite material. From Fig. 3.43 (b), we can see that the nanocomposites are crystalline in nature and shows the presence of Ag (210), Ag (122), Ag (231) corresponding to JCPDS card no. (04-0783); SnO₂ (222), SnO₂ (220) and SnO₂ (002) corresponding to the JCPDS card number (41-1445). This SnO₂ is tetragonal rutile phase. The nanocomposite ACS also has cubic CuO (113) and CuO (004) phases. This shows that Ag-CuO-SnO₂ nanocomposite is formed. From Fig. 3.43 (c), we can see the phases of SnO₂, Ag, ZnO, and also a few peaks corresponding to Sn. At around 2θ~54.8°, phases of Ag (142) and SnO₂ (200) coincide. The planes correspond to Sn (211) at 2θ~45° tetragonal Sn (JCPDS 86-2265). From Fig. 3.43 (d), we can see that the material is slightly amorphous in nature. The broad peaks indicate that several phases of different materials might be present together, for example- ZnO (101), SnO₂ (110), SnO₂ (101), and Ag (210) at $2\theta \sim 31^\circ$, 26.3° , 34.2° , and 28.1° respectively might have coincided to form broad peaks. All these results along with the TEM images, lattice fringes, and SAED pattern confirm the formation of Ag-CuO-ZnO (ACZ), Ag-CuO-SnO₂ (ACS), SnO₂-Ag-ZnO (SAZ), and CuO-SnO₂-ZnO (CSZ) nanocomposites.

The UV-Vis spectroscopy of the nanocomposite was conducted to find their optical property which is shown in Fig. 3.44 (b). In the ACZ nanocomposite, we see two absorption peaks at ~682 nm and ~371 nm. In ACS nanocomposite, we can see the absorption peaks at ~221 nm and ~269 nm whereas for SAZ we could see peaks at ~219

nm and ~424 nm. However, we could only see one peak at ~250 nm in the CSZ nanocomposite. The absorption peak at ~371 nm could be due to the presence of ZnO, at ~221 nm and ~219 nm it is probably due to the presence of SnO₂, at ~424 nm is due to the surface Plasmon resonance of Ag nanoparticles and at ~250 nm it could be due to the presence of CuO. At ~682 nm it could be due to the SPR of Ag nanoparticles as when there is a higher Ag concentration, the nanocomposite could show at a higher range as reported earlier.²⁸⁷ However a slightly red shift is observed which might be due to the presence of other oxides as it is a composite material.

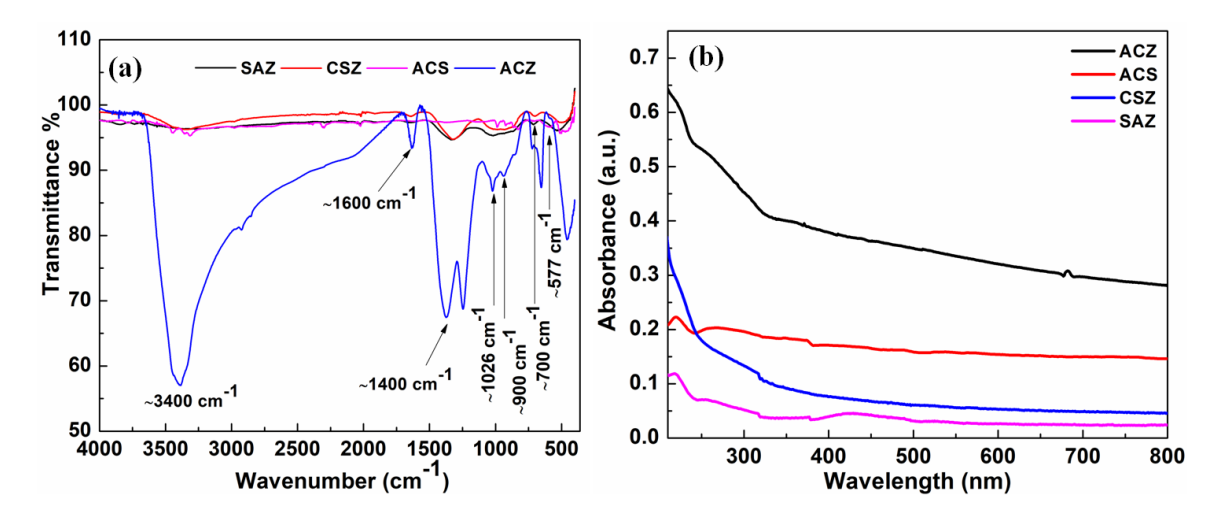


Figure 3.44: (a) FTIR of tri metal oxide nanocomposites: CuO/SnO₂/ZnO (CSZ); Ag/CuO/ZnO (ACZ); SnO₂/Ag/ZnO (SAZ) and Ag/CuO/SnO₂ (ACS); (b) UV-Vis of the different nanocomposites

To understand the constituents of the materials, FTIR analysis was done (Fig. 3.44 a). From Fig. 3.44 a, the band at $\sim 3400 \text{ cm}^{-1}$ is due to the presence of the O-H bond due to the surface hydroxyl. The band at $\sim 1600 \text{ cm}^{-1}$ might be due to the bending vibration of H₂O molecules. At around 900 cm⁻¹ and $\sim 1400 \text{ cm}^{-1}$ might be due to the various bending and stretching vibration of O₂ molecules. The oxide and metal bands

could be seen around 1000 cm⁻¹ in all the compositions. At ~700 cm⁻¹, we could see the vibration of Sn-O bands in the SAZ, CSZ, and ACS composite. At ~482 cm⁻¹ Ag-O bands could be seen. Bands that appeared at ~460 cm⁻¹, ~577 cm⁻¹, ~510 cm⁻¹, ~650 cm⁻¹, and ~1026 cm⁻¹ could be due to the presence of Zn-O or Cu-O, Cu-O, Zn-O, Cu-O, and Cu-O bonds respectively.

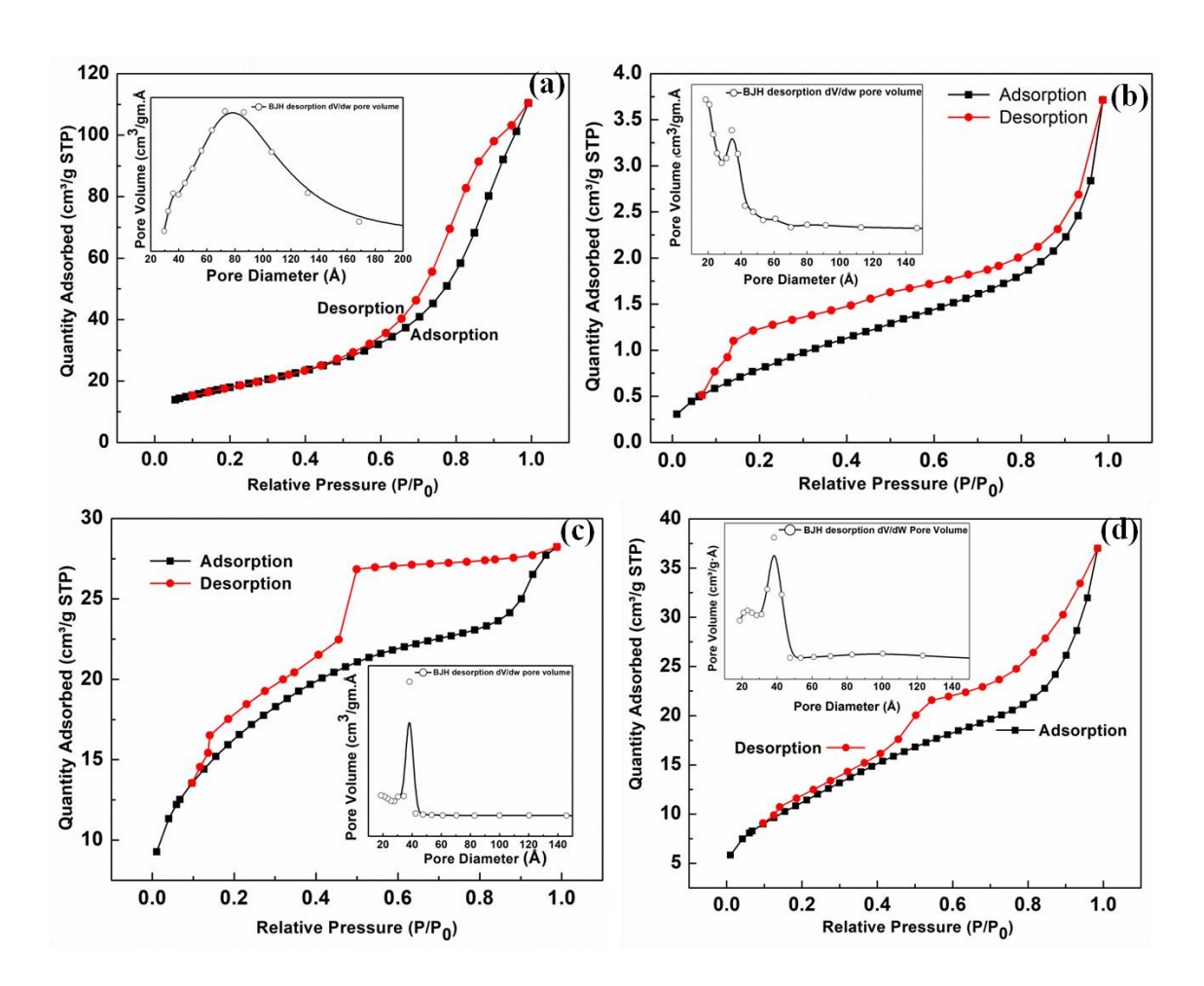


Figure 3.45:BET surface area results of :(a) ACZ, (b) SAZ, (c) ACS, (d) CSZ and inset pore size distribution curve.

To understand the nature of the nanocomposite materials, the BET experiment was conducted and the specific surface area and average pore size of the material are

shown in Table 3.10. From the table we can see that the specific surface area of the materials is in the order of ACZ>ACS>CSZ>SAZ and the average pore width is in the order of ACZ>ACS>CSZ>SAZ. This is also shown in Fig. 3.44. From the figure, we can see that the hysteresis loop is complete and is of type 4 adsorption spectrum for ACZ, SAZ, and ACS (Fig. 3.44 a, b, c respectively). All the materials are mesoporous in nature.

Table 3.10: BET surface area and pore size

Material	BET surface area	Average pore diameter
ACZ	63.78 m²/g	73.1 Å
SAZ	$3.24 \text{ m}^2/\text{g}$	34.4 Å
ACS	58.34 m ² /g	38.1 Å
CSZ	41.95 m ² /g	38.3 Å

From the TGA thermograph, in Fig. 3.46, we can see the weight loss of around 10% up to 100°C and further 10 % up to 200 °C -220 °C in ACS nanocomposite. In other samples, we can see some weight loss (7-10%) up to 220°C. All these weight losses can be termed as the loss of surface moisture. These losses are also sharp and rapid which occurred due to the surface moisture content of the samples, which are higher and rapidly decreasing. From 200 °C till 680 °C, we don't see any significant weight loss in SAZ, from 680°C to ~810°C, there is a significant loss of weight around 15% which might be due to phase changes of SnO₂. In CSZ and ACZ, we observe a similar trend till 780 °C and up to 760°C respectively with weight loss of up to 10%. This might be due to certain

changes in CuO phases. Further, we see weight loss ~20% and ~22% in ACZ and CSZ respectively until they become stable ~900 °C. In ACS, we observe a weight loss of 15% till 750 °C and another 15% till 900 °C before it becomes stable. The phase changes can be explained by the DSC curve in Fig. 3.47. After 900 °C, we do not observe any changes and can say that the ternary composites have undergone all the transformations by then. From Fig. 3.43, we can see an exothermic peak at ~420°C in SAZ, ACS, and CSZ which might be due to the slight melting of Ag. At around 923°C we can also observe some transition in ACS, CSZ, and ACS which might be due to some phase changes in CuO.

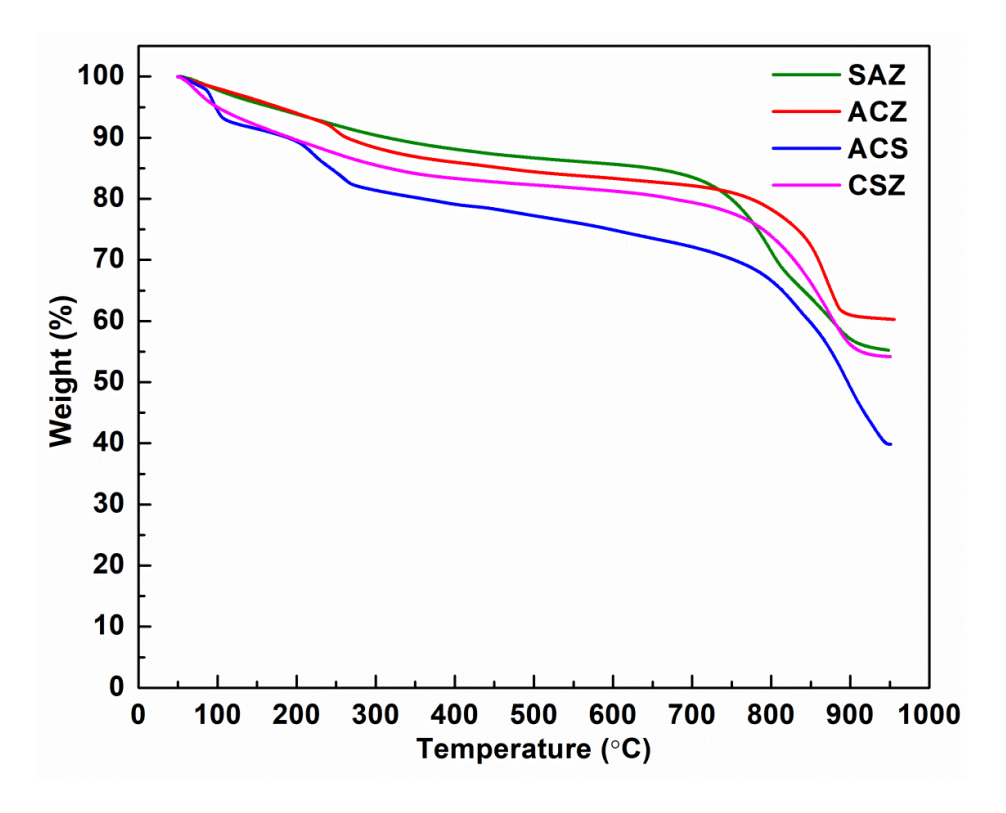


Figure 3.46: TGA of: (CSZ) CuO-SnO₂-ZnO; (ACZ) Ag-CuO-ZnO, (SAZ) SnO₂-Ag-ZnO, and (ACS) Ag-CuO-SnO₂ nanocomposites.

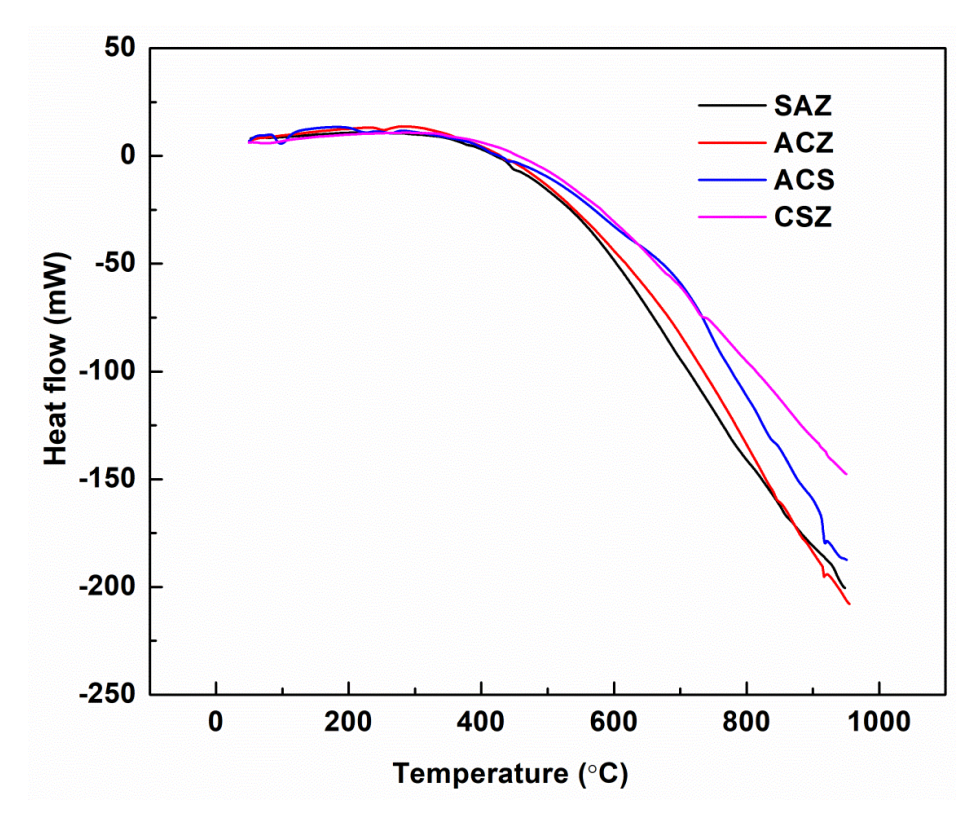
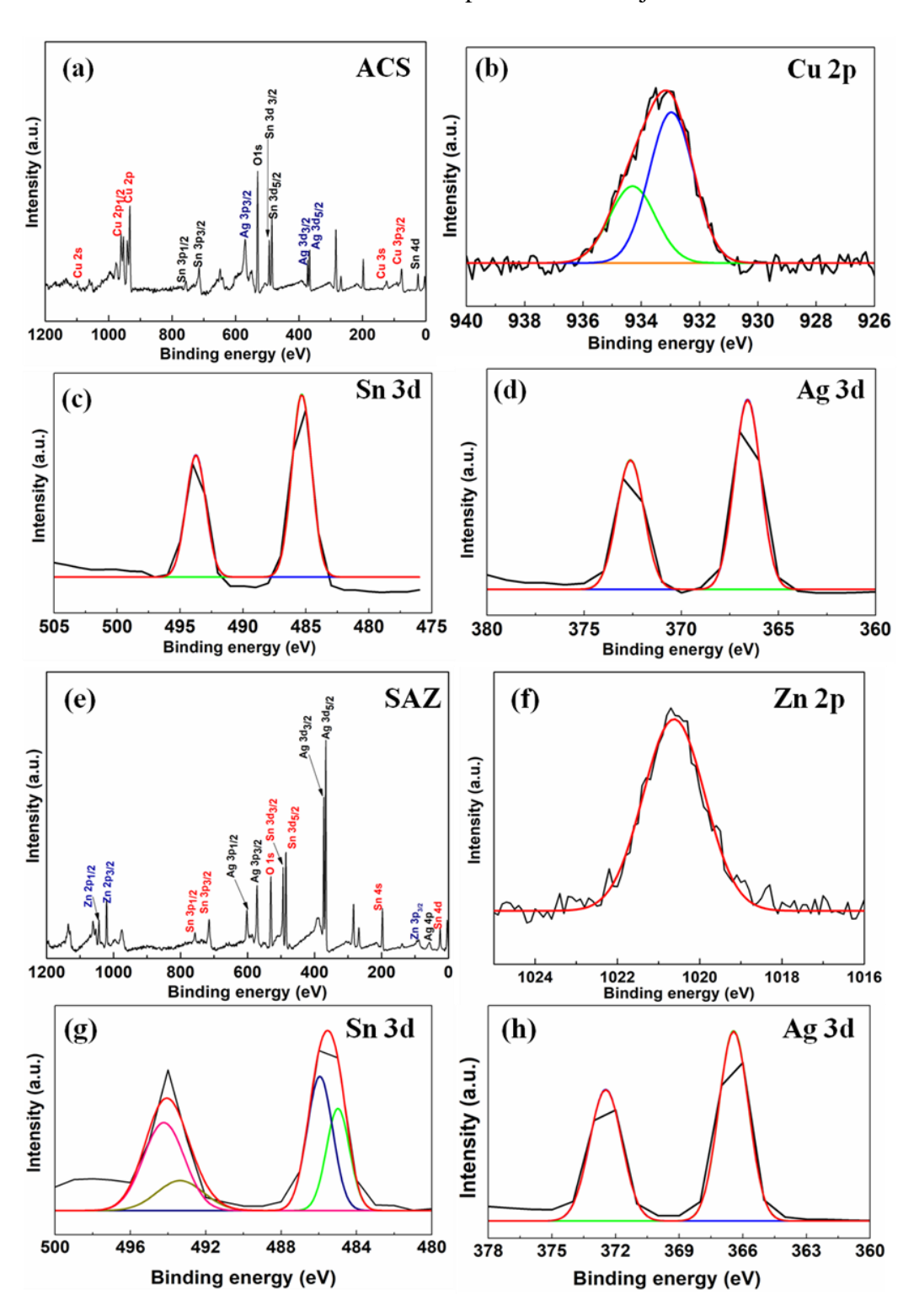


Figure 3.47: DSC profile of (a) CuO-SnO₂-ZnO (CSZ), (b) Ag-CuO-ZnO (ACZ), (c) SnO₂-Ag-ZnO (SAZ), (d) Ag-CuO- SnO₂ (ACS) nanocomposite.

To understand the elemental composition, XPS analysis was done which is shown in Fig. 3.48. Fig. 3.48 (a) (e) (i) and (m) shows the full spectra of: (a) Ag/CuO/SnO₂ (ACS) nanocomposite; (e) SnO₂/Ag/ZnO (SAZ) nanocomposite; (i) SnO₂/CuO/ZnO (CSZ) nanocomposite; (m) Ag/CuO/ZnO (ACZ) nanocomposite. From the figure, we can see the presence of Zn 2p_{1/2}, Zn 2p_{3/2} at Binding Energy (BE) of ~1045 eV and ~1022 eV respectively in ACZ, CSZ, and SAZ. We also see the presence of Zn 3p_{3/2} at ~75 eV in CSZ and SAZ. Typical characteristic peaks of Cu 2p_{1/2} and Cu 2p_{3/2} are observed in CSZ, ACZ, and ACS nanocomposites at ~953 eV and ~933 eV. Besides, we also get to see other peaks of Cu 3p_{3/2} and Cu 3s in ACS and CSZ at ~74 eV and ~124 eV, respectively.

Furthermore, a small peak of Cu 2s at ~1096.7 eV is seen in the ACS nanocomposite. Similarly, Sn $3d_{3/2}$, Sn $3d_{5/2}$, Sn $3p_{3/2}$, Sn $3p_{1/2}$ peaks at ~ 493.8 eV, ~484.9 eV, ~714.2 eV, ~756.8 eV respectively in SAZ, CSZ, and ACZ. At about 24.3 eV Sn 4d peaks are observed in ACS, ACZ, and SAZ. Besides these, at 136.3 eV, Sn 4s peak is seen in SAZ. Now coming to the Ag peaks, the characteristics peaks of Ag 3d_{5/2} and Ag 3d_{3/2} are observed in ACS, and SAZ nanocomposites at ~367.2 eV and ~373.2 eV, respectively. Ag 3p_{3/2} peak can be seen in ACS, ACZ, and SAZ at around ~572 eV. In SAZ nanocomposites, we also get to see the peaks for Ag 3p_{1/2} and Ag 4p at around ~603.8 eV and ~60.3 eV, respectively. The distinct C peak at ~280 eV is seen in all four tri-metallic nanocomposites. In ACS nanocomposite, Cu 2p_{3/2} peaks (Fig. 3.48 b) can be fitted into two peaks which show the presence of both Cu⁺¹ and Cu⁺² at ~933.6 eV and ~932.1 eV. This is contradictory to the XRD results above which clearly do not show the presence of Cu₂O. This means a trace amount of Cu₂O can be present in the ACS nanocomposites which might be due to the reaction step that reduces it to the CuO. However, Ag 3d (Fig. 3.44 d) and Sn 3d (Fig. 3.44 c) show the presence of only one type of composition i.e., Ag⁰ and Sn⁺⁴ oxidation states. In SAZ nanocomposites, Zn 2p (Fig. 3.44 f) and Ag 3d (Fig. 3.44 h) can be fitted into ZnO and Ag with Zn⁺² and Ag⁰ oxidation states. The Sn 3d (Fig. 3.44 g) shows two types of the state i.e. Sn^{+4} and Sn^{0} which match well with the XRD results shown in Fig. 3 c. From Fig. 3.48 (j-l), we could see the presence of Cu⁺² in Cu 2p, Sn⁺⁴ in Sn 3d, and Zn⁺² in Zn 2p of CSZ nanocomposites. In ACZ, we can see the presence of Zn⁺² in Zn 2p (Fig. 3.48 n), Ag⁰ in Ag 3d (Fig. 3.48 o), and Sn⁺⁴ in Sn 3d (Fig. 3.48 p). An extra peak in Ag 3d at the higher BE might be due to the loss of Ag or

the shake-up peaks. For all the composites, O 1s peaks were observed at ~531 eV which also indicates the formation of oxide complex rather than just the metals.



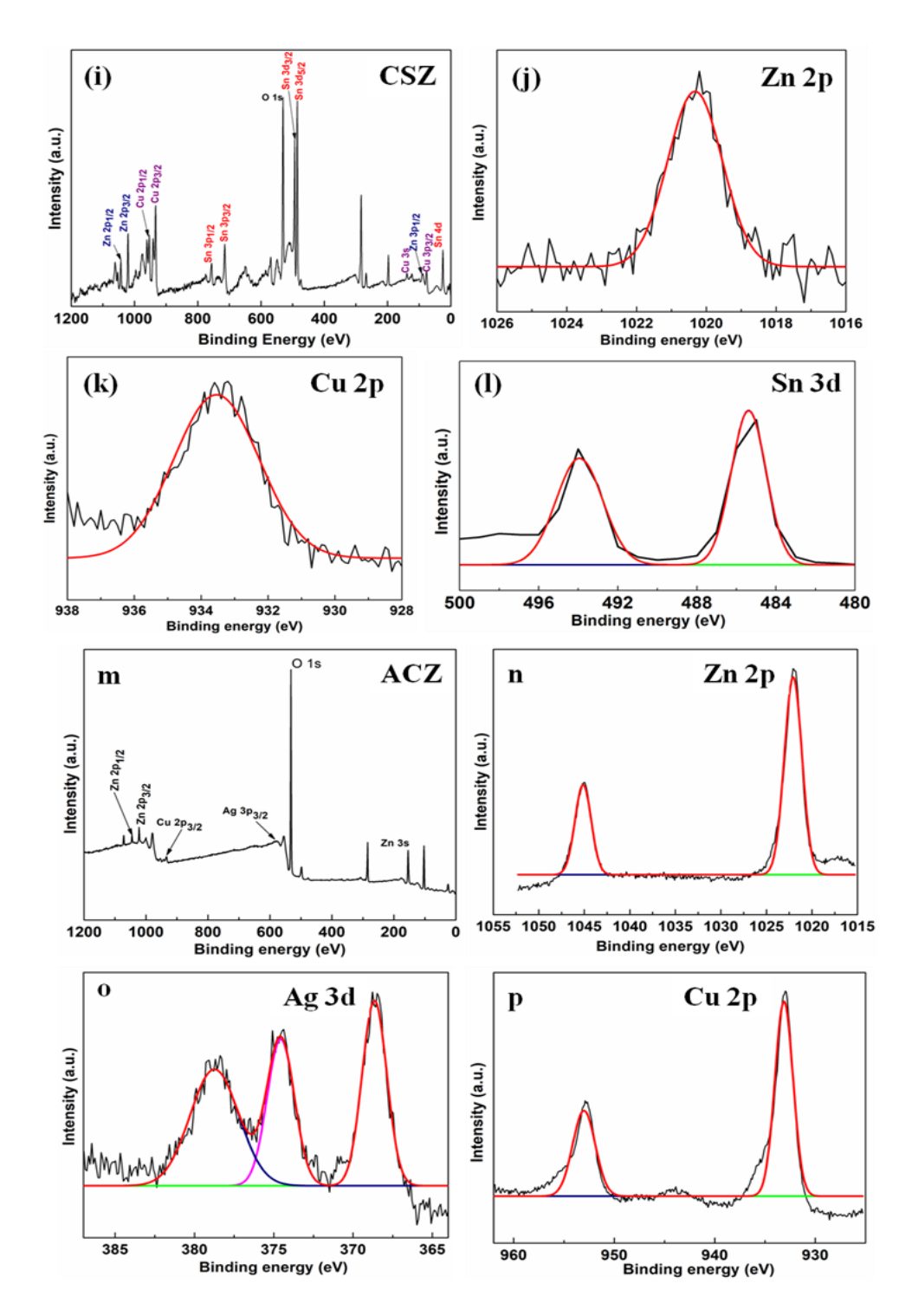


Figure 3.48: Full XPS spectra of (a) Ag-CuO-SnO₂ (ACS) nanocomposite; (e) SnO₂-Ag-ZnO (SAZ) nanocomposite; (i) SnO₂-CuO-ZnO (CSZ) nanocomposite; (m) Ag-CuO-ZnO (ACZ) nanocomposite; XPS spectra of: ACS (b) Cu 2p, (c) Sn 3d, (d) Ag 3d; SAZ (f) Zn 2p, (g) Ag 3d, (h) Sn 3d; CSZ (j)Zn 2p, (k)Cu 2p, (l) Sn 3d; ACZ (n) Zn 2p, (o) Ag 3d, and (p) Cu 2p.

Table 3.11: Zeta Potential values of the different composite materials

ıl (mV)

Zeta potential values were measured whose results are tabulated in Table 3.11 which shows that the values are in the order of CSZ>SAZ>ACZ>ACS. All these values depict that these nanocomposites can be used as biological materials. All these results thus make our nanocomposites suitable for various biological applications.

3.4.4.2 In-vitro studies

The results of growth kinetics of different ternary nanocomposites in different concentrations in *E. coli* bacterium are shown in Fig. 3.49 (a-d). From Fig., we can observe significant results in ACS (Fig. 3.45 d), some positive results in SAZ and ACZ (Fig. 3.49 a and b respectively), and minor effects in CSZ (Fig. 3.49 c). Since *E. coli* are made up of thin layers of lipopolysaccharides (1-3 µm) and which are also negative in charge, it is easy for NPs to penetrate through the cell membrane and cause cell death or membrane damage due to the release of ions. Now CSZ is not being able to perform as significantly as others might be due to the absence of Ag⁺. Although Cu²⁺ can release a much higher level of ions than the Ag⁺, 288 Ag still shows better efficiency than Cu because Cu is an essential element for maintaining homeostasis even though both Ag and

Cu have an affinity for thiols. Thus, Cu prevents toxicity while Ag can help in preventing the growth of energy cells. In short, it might be because Cu helps and support the growth and survival of the bacteria. Thus, it might be safe to say that mechanisms like Reactive Oxygen Species Generation, the charge of NPs, size of NPs, ions release, etc. contribute to the inhibition of bacterial growth.

The MIC shown in Table 3.12 reveals that the MIC values are in the order of ACZ>SAZ>ACS>CSZ. These MIC were also calculated in gram-negative *A. baumannii*. MIC ACZ shows better MIC which is 87.82% and 93.91% efficient than SAZ and ACS, respectively. Although, there have been reports of better antimicrobial efficiency of NPs this is the first time we have reported such low MIC values for tri-metal nanocomposites. This could be co-related with the UV-Vis in Fig. 3.45 (b). Since ACZ shows the presence of SPR Ag in the visible range and also ZnO, CuO which shows higher band gap energy and frequency in the UV range which might provide better efficiency as discussed earlier. ^{282,283}

Table 3.12: Minimum Inhibitory Constant (MIC) values for different composite NPs

Sample Name	Sample composition	MIC Value (μg/mL)
3a	ACZ	0.019
3b	SAZ	0.156
3c	CSZ	1.25
2d	ACS	0.312

The results of the disk diffusion method and zone of inhibition are shown in Fig. 3.50 and Table 3.13. From these two data, we could see that the tri-metal oxide nanocomposites show a positive bactericidal effect on both gram-negative strains as well as the fungal

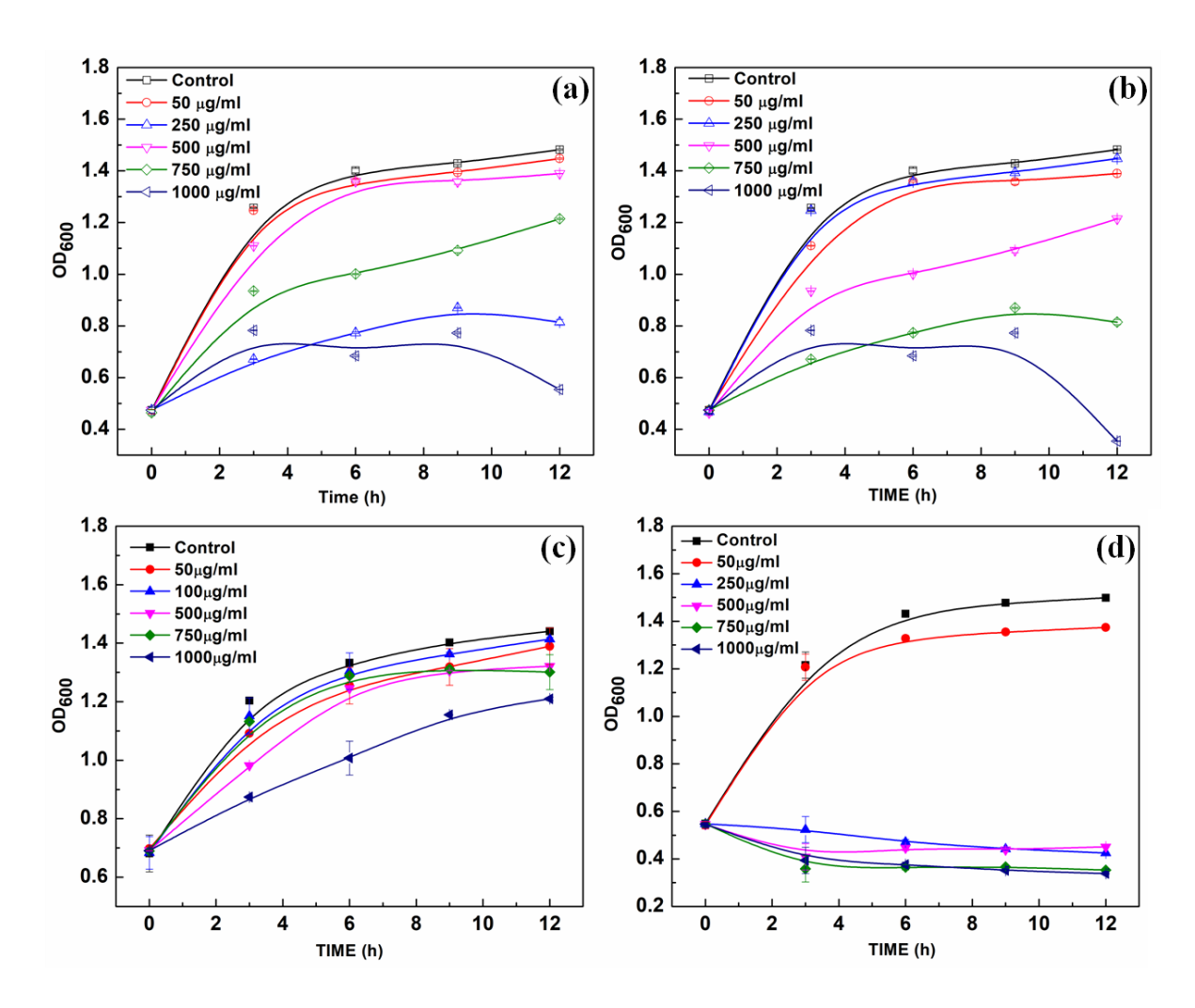


Figure 3.49: Growth kinetics of E. coli (DH5 α) in different concentrations of (a) Ag-CuO-ZnO nanocomposite; (b) SnO₂-Ag-ZnO nanocomposite; (c) CuO- SnO₂-ZnO nanocomposites and (d) Ag-CuO- SnO₂ nanocomposites. Values are represented as $mean\pm S.D$ (n=3)

strain (*C. albicans*). Here we can observe better antifungal properties than the gramnegative bacteria and SAZ shows quite a good efficiency against the fungal strain. Recently, ZrO₂-Ag₂O bimetallic have shown good antifungal activity against *C. albicans*¹¹⁸, and our materials show a good combination for SAZ (SnO₂-ZnO-Ag). Ag alone could trigger toxicity and hence, the synergistic effects of the ZnO and SnO₂ might

Table 3.13: Zone of inhibition (in mm) calculated via disk diffusion method

Sample name	Sample composition	E. Coli	A. baumannii	Candida albicans	K. pneumonia
3a	Ag-CuO-ZnO	8 mm	8 mm	7 mm	6 mm
3b	SnO ₂ -Ag-ZnO	9 mm	9 mm	16 mm	7 mm
3c	CuO-SnO ₂ -Zn	9 mm	9 mm	7 mm	7 mm
2d	Ag-CuO-SnO ₂	10 mm	9 mm	7 mm	6 mm

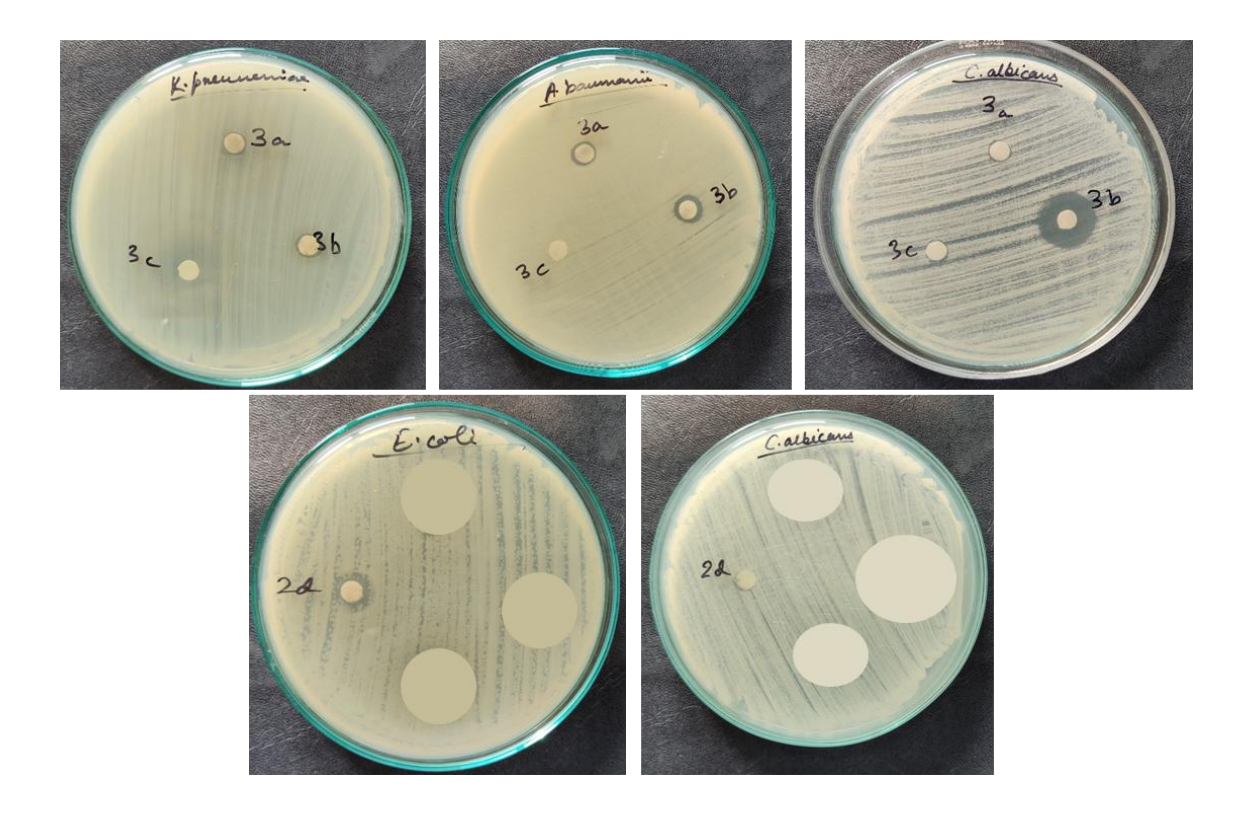


Figure 3.50: Disk Diffusion method of 3a: Ag-CuO-ZnO nanocomposite; 3b: SnO₂-Ag-ZnO nanocomposite; 3c: CuO-SnO₂-ZnO nanocomposites and 2d: Ag-CuO- SnO₂ nanocomposites

have helped. The mechanism of action for antifungal is similar to the bacterial one where ROS generation, cell wall rupture, etc are the primary reasons. However, Studies related to the SnO_2 mechanism of action still has some gap.

3.4.5 Conclusions for this part:

Like bimetallic, trimetallic composition could also be alternative antimicrobial nanoparticles. All nanocomposites have shown positive results as antimicrobial agents. However, we have tested only in gram-negative bacteria and to come to a broader perspective, we need to see it in gram-positive bacteria too. Since gram-positive have different cell thicknesses, they might act differently. Also, we haven't been able to establish exactly how the presence of SnO₂ affects the zone of inhibition. However, these results could pave the way towards better research and development of antimicrobial agents for clinical use.

CHAPTER 3

3.5 PART V: An attempt to synthesize quaternary metal oxide nanocomposite and study its antibacterial activity

3.5.1 Abstract

As the demand for antimicrobial drugs is continuous and bi and quaternary nanocomposites showed tremendous potential, in this part quaternary nanocomposite was synthesized similarly. The TEM results showed the average particle size was around 8 nm which is similar to the bi-metal oxide nanocomposite and lower than the tri-metal oxide composite. The specific surface area has increased (~80 m²/g). Further, the antimicrobial efficiency also improved, and in fact, for *A. baumannii* which is under critical priority risk it showed the highest zone of inhibition (24 mm) and this result does give some hope for the future of antibiotic materials. In the growth kinetics study, we could see inhibition percentage to be greater than 70% for concentrations≥500 μg/mL.

3.5.2 Introduction

Till the last chapter (Chapter 3- part IV), we have reported bi and tri metal oxide nanocomposites for their antimicrobial activity. We have so far understood the urgency to develop new nanomaterials for antimicrobial activities. Developing antimicrobial drugs has caught the attention of various stakeholders and thus now quaternary materials as antibacterial materials are also gaining momentum. The development of quaternary materials for dental application has started some time ago with the development of various forms of dental material especially with polymer and ammonium.²⁹³ Graphene

oxide based quaternary ammonium composite has been studied for their antibacterial effect before for wound healing.²⁹⁴ Graphene based quaternary nanocomposite (Graphene, Fe₃O₄@Fe core@shell, and ZnO) has also been synthesized and used for electromagnetic absorption properties. Recently, Govindhasamy et. al²⁹⁵ synthesized quaternary nanocomposite containing Zn-Pb-Cd-Cu oxide (ZnO-CdO-PbO-CuO) by one pot synthesis method and have found it effective against pathogens available in an aqueous medium. A quaternary composite material consisting of Ni, Cu, PANI/PVA (polyaniline-polyvinyl alcohol) has been synthesized by chemical oxidative polymerization of polyaniline and has been tested against various microbial strains. The results of the zone of inhibition were between 17-23 mm for different strains i.e. E. coli (23 mm), K. pneumoniae (23 mm), Proteus sp. (17 mm), and for S. aureus (18 mm). However, it was ineffective against A. niger. Despite these efforts, there is constant demand to develop antimicrobial drugs. Development of quaternary NCs material by chemical reduction method without the use of surfactant is new and thus may be effective to find out solutions of the antimicrobial resistance problems. Here in this chapter, we have tried to synthesize tetra metal (oxide) nanocomposites with the same elements discussed earlier i.e. Zn, Cu, Ag, and Sn. So in this chapter, we have synthesized the tetra metal oxide nanocomposite material. The Nanocomposite has been tested in gram negative bacteria and it has also been tested in C. albicans to check antifungal and antibacterial activities.

3.5.3 Methods

3.5.3.1 Synthesis:

Similar to previous methods, here 10 mmol of ZnCl₂, AgCl₂, SnCl₂, and CuCl₂ were taken in 100 mL methanol under continuous stirring. When the colour changed from milky white to green; a dropwise solution of 50 mmol of NaBH₄ and 50 mL methanol was added. The colour started changing instantaneously. After a few hrs (2-3h), the solution was removed, washed five times with distilled water, and dried overnight at 80° C. It was then characterized by XRD, TEM, BET, XPS, UV-Vis, FTIR, and TGA.

3.5.3.2 In-Vitro studies:

Antibacterial activity was observed by Luria broth dilution technique and Disk Diffusion method to calculate the zone of inhibition and MIC has been calculated to find out the minimum inhibitory concentration. The Optical Density (OD) value was observed for 12 h at an interval of every three hours. The ZOI was measured in mm.

3.5.3.3 Statistical Analysis:

All results were expressed as mean±SD for n=3. The zone of inhibition results was analyzed by one-way ANOVA and Bonferroni post-test analysis and P<0.001 is considered significant here. The percentages of inhibition are expressed as two-way ANOVA analysis and no post analysis was done. The p value of < 0.0001 is considered significant here.

3.5.4 Results and Discussions

3.5.4.1 Characterizations:

The TEM image of the nanocomposites is shown in Fig.3.51 TEM image (a-c) of Ag-CuO-ZnO-SnO₂ nanocomposite material; (g) SAED pattern of Ag-CuO-ZnO-SnO₂ nanocomposite; (h-i) HR-TEM image of Ag-CuO-ZnO-SnO2 nanocomposite and inset (c) particle size distribution of the nanocomposite. From the TEM image, we can see particles with nearly spherical shapes and in various sizes like 3 nm to some around 50 nm. The maximum numbers of particles are between 1-10 nm as seen and the average particle size is around 8.23 nm. The larger particles could be generated due to the close interaction of the various small particles as we can see from Fig. 3.51 (c) and (e) or also might be due to the presence of two oxides together as some form of dark and field image is seen in Fig. 3.51 (c) (circled). The HR-TEM images reveal the presence of CuO (110), SnO₂ (110), ZnO (102), and Ag (111) with d-spacing of 0.27 and 0.26 nm for CuO, 0.33 nm for SnO₂, 0.18 nm for ZnO, and 0.23 nm for Ag. These results match well with the available literature. Also, the SAED pattern of the nanocomposite material shown in Fig. 3.47 (g) shows the presence of Ag (222), SnO₂ (211), CuO (110), Ag (210), and ZnO (102). From the TEM image, we can see that there is the presence of Ag, CuO, ZnO, and SnO₂. The size and morphology are well in agreement with the nanosized particles. The IIFT image as shown in Fig. 3.51 (h inset) shows the position where two different phases have distinct IFFT fringes. From these results, we can conclude that two different oxides are formed.

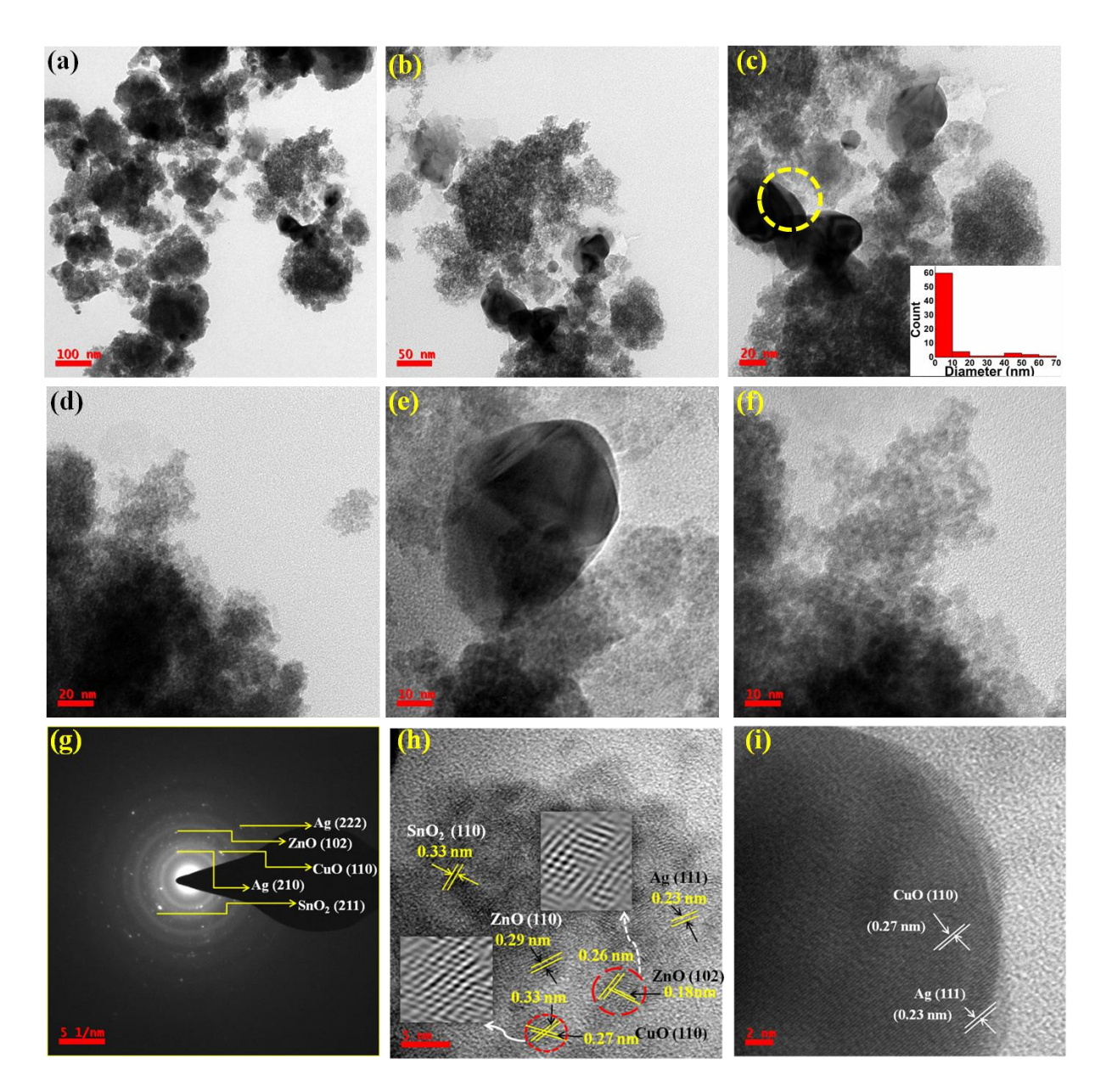


Figure 3.51:TEM image (a-c) of Ag-CuO-ZnO- SnO₂ nanocomposite material; (g) SAED pattern of Ag-CuO-ZnO- SnO₂ nanocomposite; (h-i) HR-TEM image of Ag-CuO-ZnO-SnO₂ nanocomposite and inset (c) particle size distribution of the nanocomposite.

The EDS analysis of the nanocomposite was done in TEM and it is shown in Fig. 3.54. From the figure, we see the presence of Zn, Cu, Ag, Sn, and O_2 as expected. From

both TEM and EDS, we can say that the results matched and the formation of the nanocomposites can be established.

To verify these, XRD analysis was done which is shown in Fig. 3.52. The diffraction pattern from the XRD shows the presence of ZnO, Ag, CuO, and SnO₂ as per the JCPDS data. The peaks clearly show the presence of all oxides as expected. The peaks indicate the presence of Ag (210), Ag (111), Ag (231), Ag (142), and Ag (241) at 2θ values of ~28°, ~38.1°, ~46.1°, ~54.8°, and ~57.3° respectively according to the JCPDS file no (04-0783) for FCC Ag. Based on the JCPDS file no (36-1451), the peaks at 2θ ~62.8° and ~67.9° show the presence of hexagonal wurtzite structure of ZnO (103) and ZnO (112) respectively. Similarly, the peaks at $2\theta \sim 54.8^{\circ}$, $\sim 58.2^{\circ}$, $\sim 71.4^{\circ}$, and $\sim 87.2^{\circ}$ show the presence of tetragonal SnO₂ according to the JCPDS file no. (41-1445). The planes representing these 20 values are SnO₂ (220), SnO₂ (002), SnO₂ (202), and SnO₂ (330) respectively. The XRD graph also shows the presence of cubic CuO (110) and CuO $(\bar{1}12)$ at 20 values of ~32.4° and ~46.2°, respectively according to the JCPDS file (80-0076). We also observe that some peaks coincide like at ~46°, ~55°, and ~57° where two phases of different components coincide. This can also be correlated with the TEM image as shown in Fig. 1 (c) and (h). The crystallite size was calculated by the Debye-Scherrer formula (Eqn 3.2).²⁹⁶

$$D = 0.9\lambda/\beta cos\theta \dots (3.2)$$

From the above formula (3.2), the crystallite size for CuO (111) is calculated as ~25 nm, and for Ag (111) is ~24 nm.

To understand the optical properties of the nanocomposite material, the UV-Vis experiment was run from 190 nm-800 nm shown in Fig. 3.53 (a). From the spectra, we

can see there is only one broad spectrum around ~274 nm which might be due to the dominant presence of SnO_2 . The broad spectrum is also possible because at a particular time and wavelength many molecules are undergoing transition. The band gap energy was calculated using the Tauc plot for indirect transition and calculated as $E_g = 3.41$ eV. Since there are multiple compositions; the band gap is affected similarly, i.e., it does not represent any particular match with the literature. For e.g., ZnO has E_g around 3.2 eV- 3.6 eV, CuO has a narrow E_g of 1.2-1.4 eV, Ag has $E_g \sim 2$ eV depending on their absorption bands and SnO_2 has around 3.6-3.8 eV. So we can say that the band gap is higher in value with respect to ZnO and SnO_2 influence.

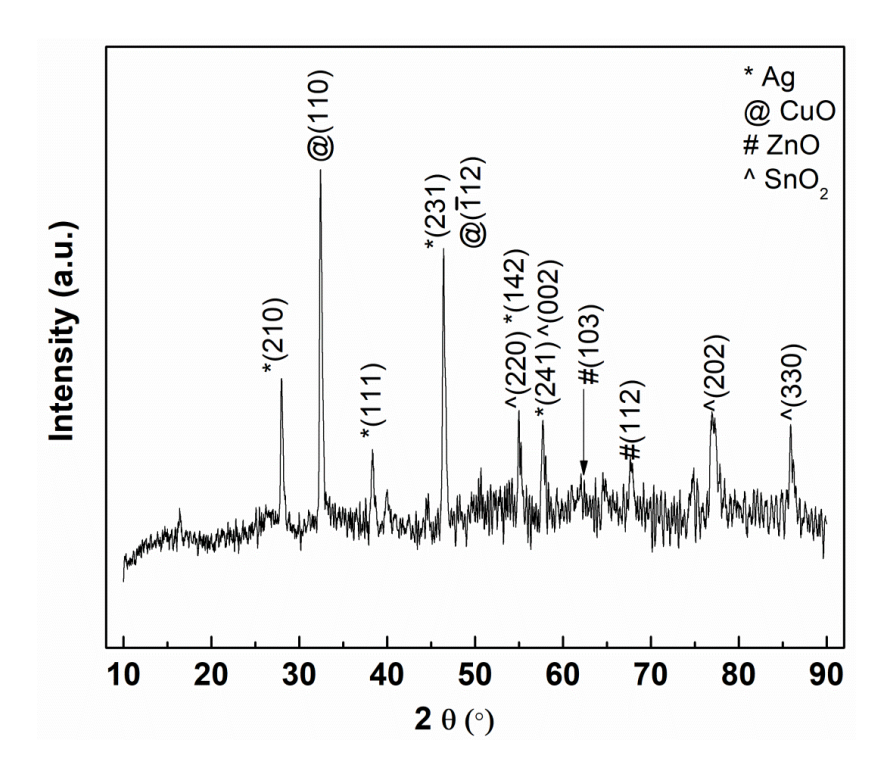


Figure 3.52: XRD pattern of Ag-CuO-ZnO-SnO₂ nanocomposite

The FTIR spectrum is shown in Fig. 3.53 (b) and from there; we can see the broad peak around 3500 cm⁻¹, which might be due to the O-H group present in surface water.

The bands at 512 cm⁻¹ and 724 cm⁻¹ might be due to the presence of stretching vibration of Ag-O and O-Sn-O respectively. The band at 924 cm⁻¹ appeared due to the symmetric stretching vibration of the O-H group.²⁹⁷ From the FTIR bands we could see the presence of other minor peaks too which are due to the fingerprint region. The broad band at ~1600 cm⁻¹ appeared due to the presence of surface water molecules.

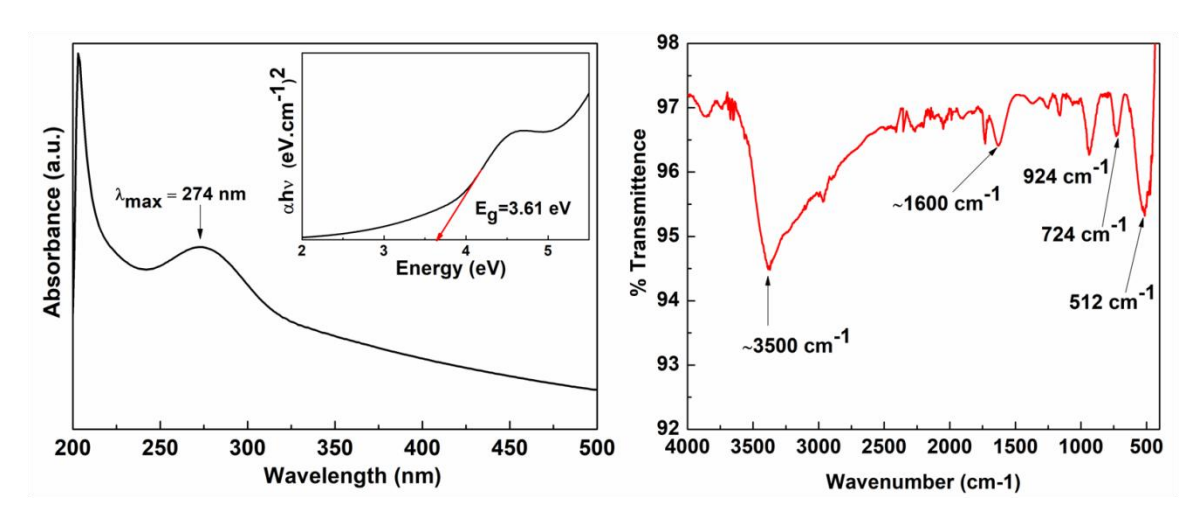


Figure 3.53:(a) UV-Vis spectra of Ag-CuO-SnO₂-ZnO nanocomposite and inset Tauc plot for band gap energy; (b) FTIR spectra of the nanocomposite.

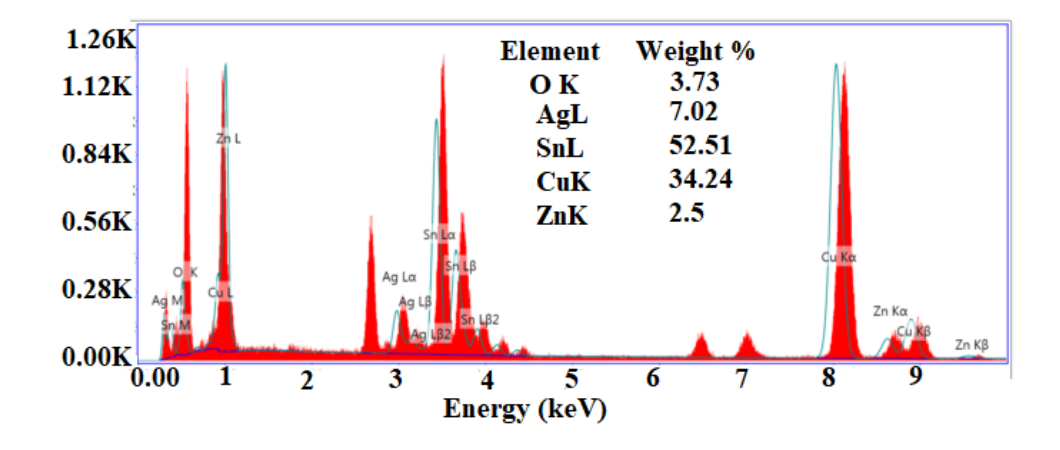


Figure 3.54: EDS spectroscopy of the nanocomposite representing the elemental composition.

The BET surface area of the nanocomposite material was calculated with N_2 adsorption-desorption and is calculated to be 81.41 m²/g and BJH Adsorption's average pore width is found to be 47.2 Å as shown by figure 3.55 (inset). The BET surface area shows the presence of mesoporous pores (2 nm-50 nm) and the isotherm is type IV. With the presence of more particles, the composite material might have a lesser specific surface area due to the closure of the pores, and in this case, the pores are wide and the surface to volume ratio has increased. This also means that the particles are not blocking each other and have high porosity. An improved specific surface area is a good property for biological applications.

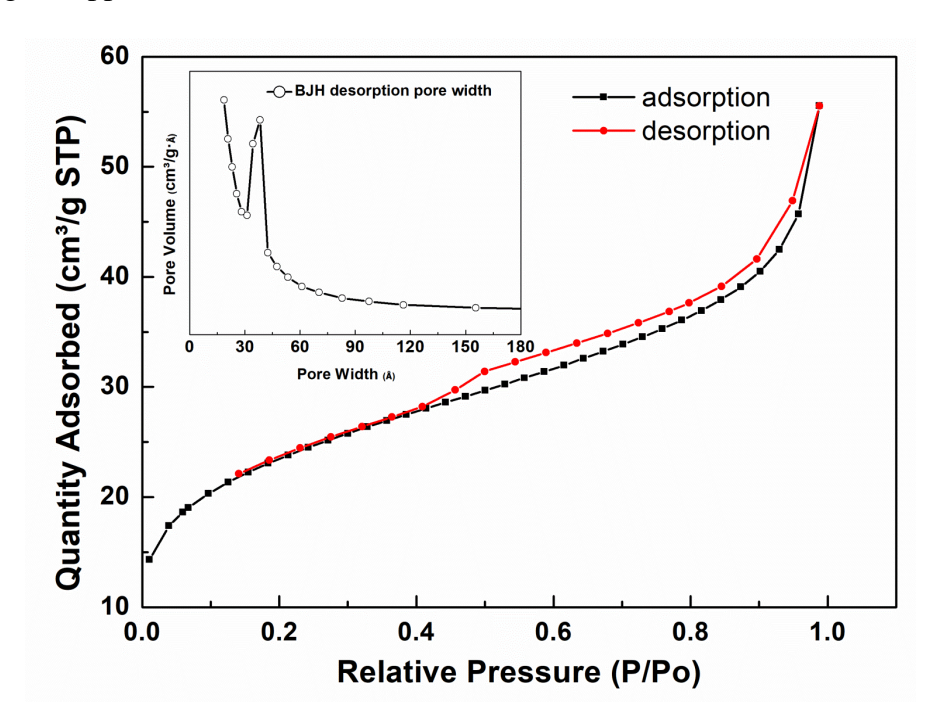


Figure 3.55: N₂ adsorption-desorption plot of the tetra oxide nanocomposite material.

The thermogravimetric analysis (TGA) profile is shown in Fig. 3.56 (a). There are three major weight losses occurred at ~194°C, ~350°C, ~597°C, and at ~892 °C. The

weight loss of around 15% initially at 194°C is due to the loss of moisture and water from the surface. The weight loss of around 0.5% at 350°C might be due to the decomposition of Ag and ZnO.²⁹⁸ The 0.5% weight loss at 597 °C might be due to the decomposition of SnO₂ and 25% at 892 °C might be due to the decomposition of CuO to CuO₂.²⁹⁹ The DSC thermogram shown in Fig. 3.56 (b) is in agreement with the TGA curve. There is a small endothermic peak at around 774°C and 928 °C which might be due to the transition of CuO.³⁰⁰

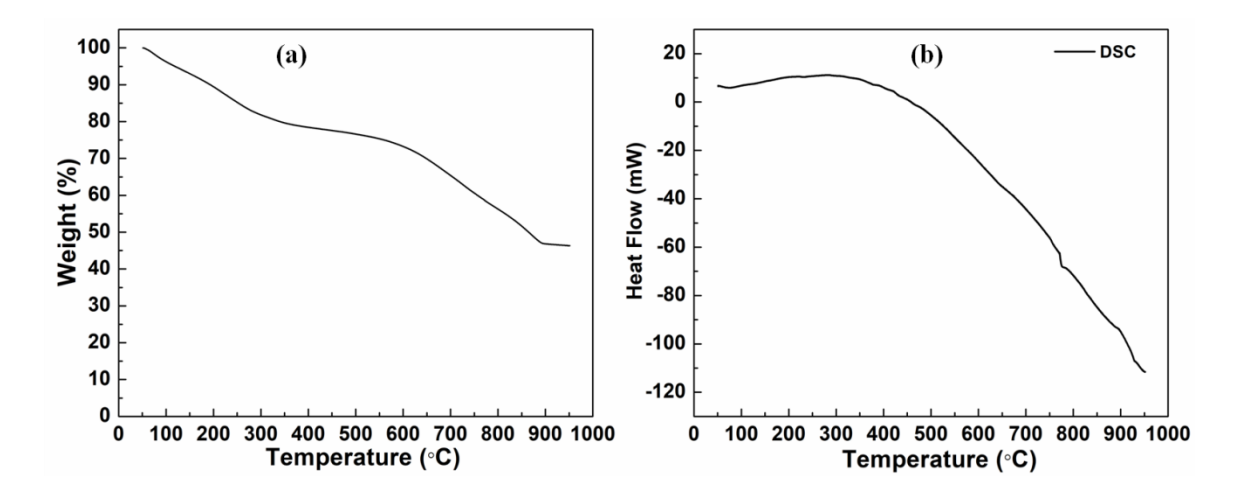


Figure 3.56: (a) TGA curve Ag-CuO-SnO₂-ZnO nanocomposite; (b) DSC curve of the Ag-CuO-SnO₂-ZnO nanocomposite.

The XPS spectra of the quaternary nanocomposite material show the presence of Zn $2p_{1/2}$, Zn $2p_{3/2}$, Cu $2p_{3/2}$, O1s, Sn $3d_{3/2}$, Sn $3d_{5/2}$, Ag $3d_{3/2}$, Ag $3d_{5/2}$, Zn $3p_{3/2}$, Cu $3p_{3/2}$ as seen in full XPS spectra in Fig. 3.57 (a) as per the NIST database. The peak fitting of Cu 2p peak reveals the presence of only one type of Binding energy i.e. for CuO at ~933.7 eV (Fig. 3.57 b). The binding energy of Sn 3d as seen in Fig. 3.57 (d) shows the presence of three curves at 485.4 eV, 493.8 eV, and 498.1 eV of the Ag-CuO-SnO₂-ZnO

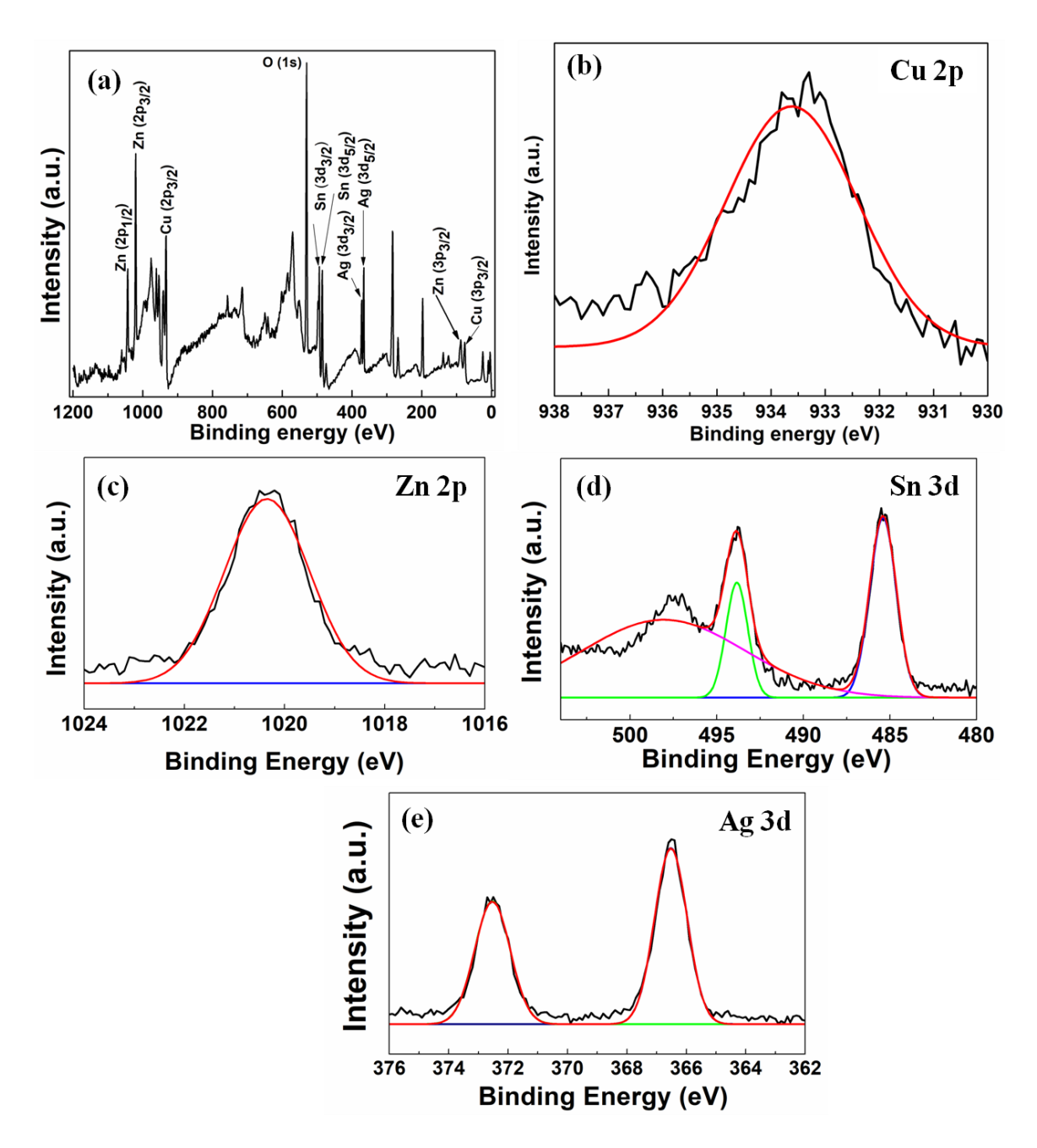


Figure 3.57: XPS spectra of: (a) Full spectra of CuO-Ag-ZnO-SnO₂ nanocomposite; (b) Cu 2p; (c) Zn 2p; (d) Sn 3d, and (e) Ag 3d.

NCs. The first two are the characteristic Binding energy bands of Sn 3d with the splitting energy of 8.4 eV, which matches well with the literature. 301,302 The extra peak is due to

the shakeup peak which occurs due to the energy transition. Zn 2p has binding energy at 1020.3 eV and has the presence of only one type of oxidation state i.e. Zn²⁺ (Fig. 3.57 c). From Fig. 3.57 (e), we can see two strong peaks of Ag 3d at 366.5 eV and 372.5 eV, which tells that the Ag has only one oxidation state and is Ag⁰. From these results, we can conclude that our composite material consists of CuO, ZnO, Ag, and SnO₂ which match well with the XRD and the TEM results.

3.5.4.2 In-vitro results:

Now coming to the antimicrobial results; a growth kinetics study of the bacteria is E. coli (DH5 α) has been done which is shown in Fig. 3.57 (a). From the figure, we can see that the effective concentration is as low as 250 µg/mL and the Optical Density value drastically decreases just after 6 h. We can also see that for 500 µg/mL, better results are obtained compared to other higher concentrations even though there isn't much difference. Since our nanocomposite has its own colour, it is also possible that there is some absorbance of its own due to which there is a higher OD value for higher concentration. From these results, the percentage of inhibition was calculated as shown in Eqn. 3.3:

% of Inhibition =
$$\frac{\text{OD}_{\text{control}} - \text{OD}_{\text{A}}}{\text{OD}_{\text{control}}} * 100 \dots (3.3)$$

Where,

A= different OD values with different concentrations at a different time interval. The Percentage of inhibition is expressed in Fig. 3.58 (b). From the figure, we can see that w.r.t the control values, all the concentrations above 50 μ g/mL show a positive result. From the same figure, we can also see that for concentrations \geq 500 μ g/ml, there

are similar results and shows inhibition between 70%-85% depending on the time interval (Table 3.14). Hence, we can safely say that 500 $\mu g/mL$ is equally suitable and we need not go up to 1000 $\mu g/mL$.

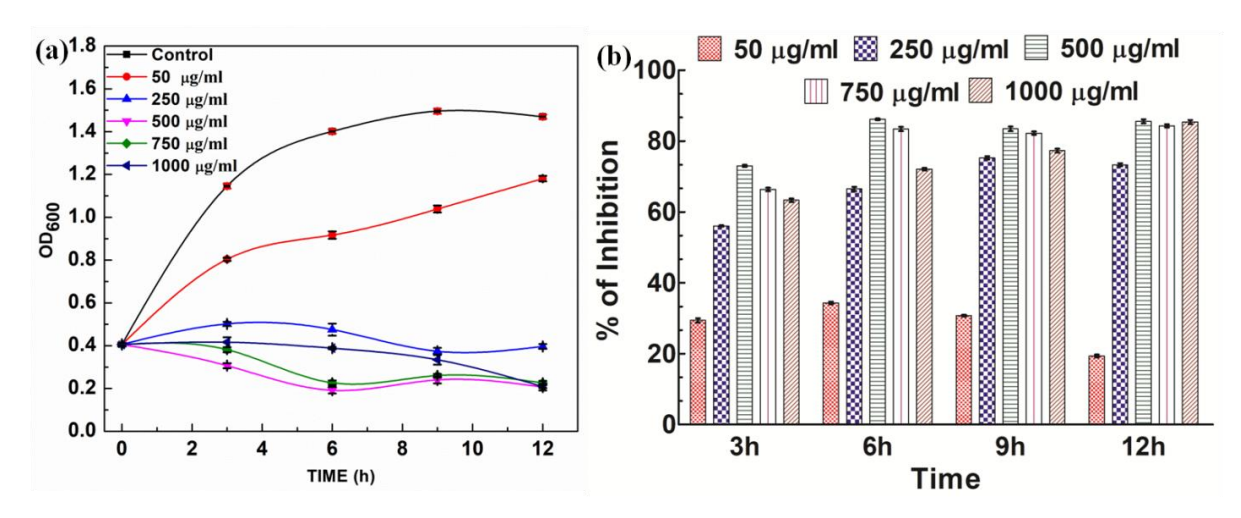


Figure 3.58: (a) Growth kinetics in E. coli bacteria by LB broth technique. The plot is expressed as a mean \pm SD (n=3); (b) Percentage of inhibition w.r.t. control at a different time interval. P<0.0001

Table 3.14: Percentage of inhibition at a different time interval with different concentrations w.r.t control at that particular time

Time (h)	Concentrations							
	50 μg/ml	250 μg/ml	500 μg/ml	750 μg/ml	1000 μg/ml			
3	29.8 %	56.2%	73.2 %	66.7%	63.6 %			
6	34.6 %	66.1 %	86.3 %	83.8 %	72.2%			
9	30.6 %	74.9 %	83.9 %	82.6 %	77.6 %			
12	19.6 %	73.0 %	85.9 %	84.6 %	85.7 %			

Although bacterial cell like *E. coli* cells is expected to not have uptake mechanisms to facilitate NPs for the cells damage, yet few reports talk about the opposite of this. It is

found that they also have a similar type of uptake mechanism to damage the cells. This is also promoted due to the internalization of NPs. 303–305 This means that even in E. coli the inhibition is promoted by ROS generation. Previous study on Ag also has shown that ROS generation depends on the bioavailability of the ions in dissolved form but at the same time also depends on the physiology of the respective NPs. 307

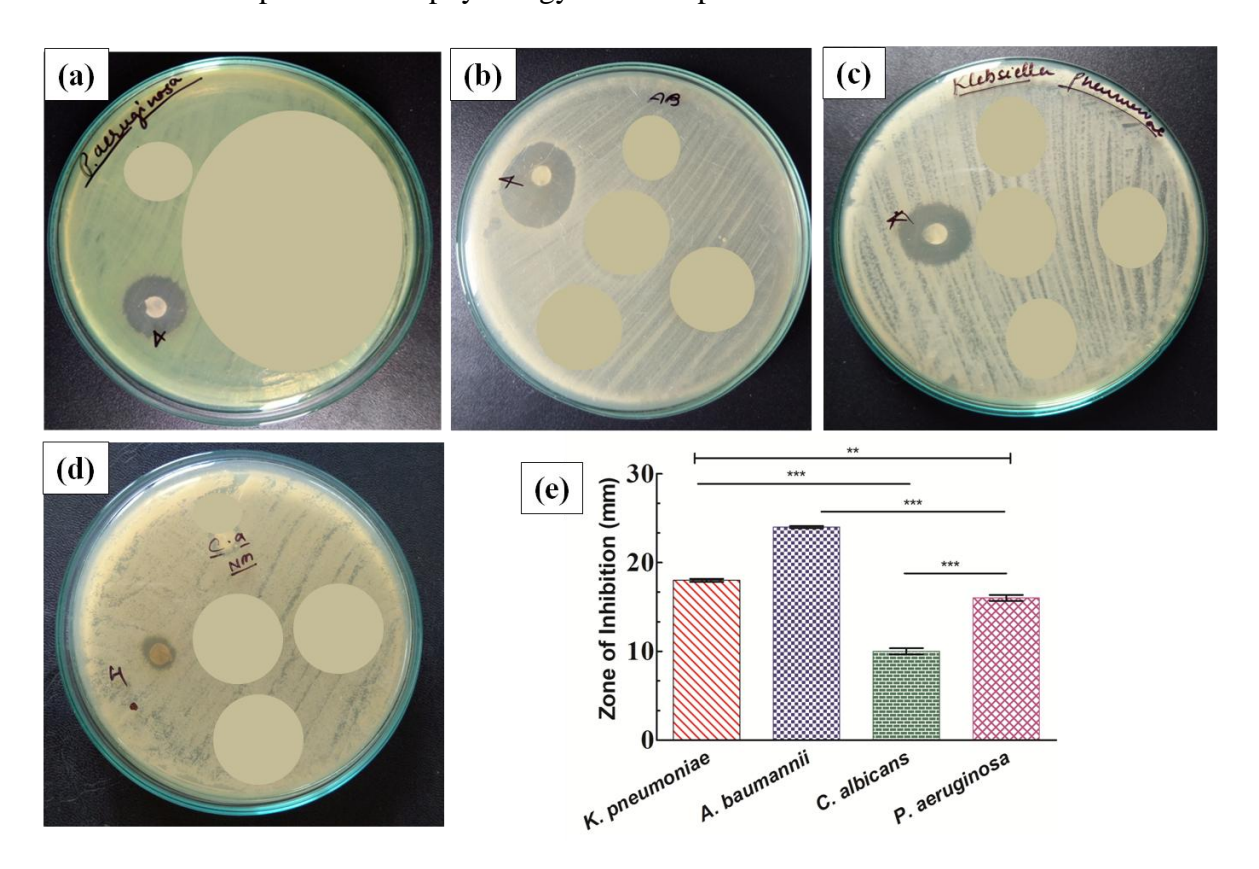


Figure 3.59: Disk Diffusion of (a) P. aeruginosa; (b) A. baumannii; (c) K. pneumoniae; (d) C. albicans and (e) graphical representation of the zone of inhibition. ***P<0.0001, **P<0.001

For the disk diffusion method, three gram negative bacterial strains and one fungal strain (*Candida albicans*) were chosen and the results are shown in Fig. 3.59 (a-d). From the figure and the graphical representation of the ZOI in Fig. 3.59 (e), we can see that the

nanocomposite material has positive results for all the strains (both bacterial and fungal) but for A. baumannii, it shows an exceptional result with ZOI value of 24 mm. For K. pneumonia, P. aeruginosa, and the C. albicans ZOI are 18 mm, 16 mm, and 10 mm respectively. The MIC value calculated in A. baumannii showed that the value was as low as 0.019 µg/mL. It is an opportunistic nosocomial bacteria that can cause infections ranging from pneumonia to sepsis. 308,309 In one of the recent studies during covid-19, it was also found that A. baumannii was the most resistant bacteria. 308 The same study also showed that in many cases, several infections may occur simultaneously. It is indeed a positive sign that our composite has shown effect against all these bacterial and fungal strains as we may not need multiple drugs to treat an infection. A. baumannii has developed a lot of resistance in the past decade against a lot of antibiotics and is also capable of multi drug resistance. 309,310 WHO has also developed a list of bacteria that are a global threat and A. baumannii are among the most threatening one which needs immediate attention.³¹¹ Recently, the mechanism of ZnO NPs with the present antibiotics (ceftazidime and ciprofloxacin) against A. baumannii was studied and they found ZOI of around 33 mm and 38 mm, respectively which is quite good. 312 However, in our case we have tested only for the NPs currently and this is one of the best results reported so far.

3.5.4.3 Probable Mechanism of the antimicrobial action

Coming to the mechanisms, Tewari et. al³¹³ concluded by their study that the chemical synthesis of ZnO is one of the best ways to combat *A. baumannii*. They also had shown that ROS generation is the way by which ZnO functions against bacterial walls. This in turn enhances the membrane lipid per-oxidation. These effects together then

cause the membrane of other parts like DNA, protein, etc. to leak. Similarly, several mechanisms such as physical damage,³¹⁴ membrane damage independent of ROS generation and solely based on particles,³¹⁵ ROS based on the crystallinity of the materials,³¹⁶ and ion release,³¹⁷ etc. Thus we cannot say that one method might have worked here. There might be a combination of one or more than one step which needs further analysis. The specific surface area is also high, the porosity, crystalline, ion release all might have come to work together to have such an effect. Also, sometimes band gap plays an important role in the antibacterial activity which we have reported in the previous chapter.

3.5.5 Conclusions for this part:

Tetra metal oxide nanocomposite was successfully synthesized and tested against various gram negative and fungal strains. The composite showed an excellent result for *A. baumannii* although it is effective against all the tested pathogenic strains. The nanocomposite has an average size of around 8 nm and has semi-crystalline in nature with a high specific surface area. Coming to the antimicrobial activity, the combined effect of all the oxides and Ag might have instigated the nanocomposite to follow multiple pathways for the action against the bacterial and the fungal strains which further needs investigation. The results obtained in this could be a breakthrough because *A. baumannii* is already on the critical priority list of WHO and needs immediate attention.

CHAPTER 4: Summary and Conclusions

4.1 Summary

This chapter mentions the overview of this Dissertation. In this dissertation, the composite materials of the metals and mixed metal oxide nanoparticles have been successfully synthesized by the chemical reduction method using NaBH₄ as the reducing agent without using a surfactant. These materials have been characterized by various techniques and then have been studied for antimicrobial activities.

Moreover, the inference of each chapter has been discussed in the following sections.

4.1.1 Chapter 1

This chapter initiates with a detailed introduction to nanotechnology, its applications, and its importance in the biological field. This is followed by the description of the existing problem of antimicrobial resistance and the application of metal-based nanoparticles for antimicrobial use. The chapter also draws various studies carried out in this field by citing various works of literature available. It also describes the choice of the reducing agent and the synthesis route adopted. This chapter finally states the significance and motivation behind this work and lays out the objectives of this dissertation.

4.1.2 **Chapter 2**

In this chapter, a detailed list of the precursor used for the synthesis of various composite NPs has been mentioned. The detailed experimental procedure to synthesize the materials has been mentioned in this chapter. Then the detailed procedure of all the antimicrobial

tests i.e. LB Borth dilution techniques, Disk Diffusion method, and MIC method has been elaborately described. The characterization methods used in this dissertation have been discussed in the chapter. This chapter also briefly describes the working principle of all the techniques used.

4.1.3 Chapter 3

This chapter discusses the results of this dissertation work. This work is inspired to find the antimicrobial drug to address the challenge that is present due to microbial resistance. Chapter -3 is divided into five parts. Each part has been summarized below.

4.1.3.1 Chapter 3- part I

ZnO NPs have been in use for a long time now in various applications including biomedical and antibacterial. Thus this part discusses the comparison of the bi-metallic nanocomposites with single ZnO. ZnO and bimetallic NCs of ZnO-Ag₂O/Ag, ZnO-CuO, ZnO-SnO₂ were successfully synthesized and all the NCs are below the size of 10 nm. Colloidal stability is an important parameter for biological applications of nanomaterials. Thus, the stability of the NCs was studied by taking PBS, Saline, and PB solutions, and the materials were found to be stable. Further, the docking technique was used to predict the antimicrobial activity of the nanocomposites, and ZnO- Ag₂O/Ag was found to have the least Binding energy. The Nanocomposite materials were evaluated for antimicrobial activities by in-vitro techniques and it correlated with the in-silico docking method. The bandgap energy calculated by the Tauc plot was also found to have some effect on the antimicrobial activity which was finally shown in the mechanism study.

4.1.3.2 Chapter **3-** part **II**

In continuation of the above part, this part also deals with the bimetallic composite system of Ag-Sn/SnO₂. Ag-Sn/SnO₂ nanocomposite was successfully synthesized and found to be around 8 nm in size by TEM. The pores were between 3-5 nm from the BJH desorption pore size distribution. Further, the in-silico studies showed that the binding energy for all the strains (*C. albicans, E. coli, A. baumannii, K. aeruginosa, K. pneumonia*) was the same. However, when the in-vitro studies were done, *C. albicans* showed the highest zone of inhibition, i.e. 17 mm. Further, a mechanism study by choosing different proteins (Hsp90) in *C. albicans* has been discussed in this chapter. Finally, the bimetallic nanocomposite of Ag-Sn/SnO₂ is an effective antibacterial and antifungal agent and more effective towards *C. albicans*.

4.1.3.3 Chapter 3-part III

This part deals with finding an alternative to Ag NPs by using CuO and SnO₂. In this chapter, CuO-SnO₂/Sn and CuO-Ag/AgO composite nanoparticles were synthesized successfully and studied for antimicrobial activity. The in-vitro antimicrobial studies from the disk diffusion assay showed that the two nanocomposites have a similar zone of inhibition i.e. around 7-11 mm. However, from the LB broth technique result study, CuO-Sn/SnO₂ nanocomposite had better efficiency than CuO-Ag/AgO which might be due to the resistance developed by the bacteria against this nanocomposite. And thus it can be said that the CuO-SnO₂ composite system can be used as an effective alternative to single Ag or CuO-Ag.

4.1.3.4 Chapter 3-part IV

In this part of the results and discussion chapter, trimetallic oxide nanocomposites of Ag-CuO-SnO₂ (ACS), CuO-SnO₂-ZnO (CSZ), ZnO-Ag-CuO (ACZ), and Ag-ZnO-SnO₂ (SAZ) were synthesized and studied for their antimicrobial activity in an in-vitro medium. The particle size of the synthesized nanoparticles was between 3-56 nm and in the order of CSZ<ACS<SAZ<ACZ. The Specific surface areas were between 3.4 m²/g-63.7 m²/g. The nanocomposites also showed an effective result against gram-negative bacteria and fungi (*C. albicans*). Further based on the disk diffusion method, Ag-CuO-SnO₂ showed the highest zone of inhibition in *K. pneumonia* compared to other oxides.

4.1.3.5 Chapter 3-part V

In this part, the quaternary nanocomposite of CuO-ZnO-SnO₂-Ag was synthesized and its properties were studied. Further, this was also studied for antibacterial activity. The major findings and summary from the chapter are appended below:

- ➤ The average particle size of the nanocomposite material was c.a. 8.23 nm and the optical band gap energy calculated from the Tauc plot was 3.61 eV.
- The disk diffusion experiment showed that the quaternary nanocomposite was effective against all the pathogens and showed the best results against *A. baumannii*.
- The LB broth technique also showed that the nanocomposite was efficient in inhibition of E. coli bacterium as early as 6 h and >75% effective for ≥500 μg/mL.

Finally, the results of the zone of inhibition and the MIC values of various composite materials in this dissertation are tabulated below:

Table 4.1: zone of inhibition and MIC values of all the materials synthesized in this dissertation

Materials	E.	<i>A</i> .	<i>C</i> .	<i>K</i> .	Р.	MIC
	coli	baumannii	albicans	pneumoniae	aeruginosa	μg/ mL
Ag/AgO	9 mm	10 mm	12 mm	Static effect	6 mm	0.039
Cu/CuO	8 mm	11 mm	7 mm	Static effect	6 mm	1.25
SnO ₂	8 mm	11 mm	7 mm	Static effect	4.2 mm	1.25
ZnO	8 mm	8 mm	9.5 mm	6.5 mm	8 mm	0.312
ZnO-CuO	8 mm	9.25 mm	9 mm	8 mm	8.3 mm	0.312
ZnO-SnO ₂	8 mm	9 mm	8.5 mm	6.25 mm	7.5 mm	0.019
ZnO-Ag ₂ O/Ag	8 mm	14 mm	10.5 mm	11.5 mm	17 mm	0.010
CuO-Ag/AgO	8 mm	8 mm	10 mm	10 mm	-	0.156
Ag-SnO ₂ /Sn	10	10 mm	18 mm	6 mm	-	0.015
	mm					
CuO-SnO ₂ /Sn	10	7 mm	7 mm	6 mm		0.625
	mm					
Ag-CuO-SnO ₂	10	9 mm	7 mm	16 mm		0.312
	mm					
ZnO-Ag-CuO	9 mm	8 mm	7 mm	6 mm		0.019
Ag-ZnO-SnO ₂	9 mm	9 mm	16 mm	7 mm		0.156
CuO-SnO ₂ -ZnO	9 mm	9 mm	7 mm	7 mm		1.25
Ag-CuO-SnO ₂ -	11	24 mm	10 mm	18 mm		0.019
ZnO	mm					

4.2 Conclusions and future aspects of this work

We have successfully synthesized the stable nanoparticles and composites containing bi, tri, and tetra metal oxide without using surfactant or capping agents for biological use i.e. antimicrobial activity. These were studied for their morphological, optical, thermal state, specific surface area, etc. by various characterization techniques. And finally, we also have used docking tools Auto-Doc 4.1 for in-silico studies to understand the mechanisms and protein interaction with the nanocomposites. Based on the in-vitro antimicrobial activity the following major conclusions can be drawn:

- > Tetra metal oxide looks promising for all the microbes and can open a new door to replace conventional organic antibiotics.
- Although quaternary composite material shows effective results in all the strains, bi-metallic is also showing effective results and it can be modified more instead of going to tetra-metal complex.
- ➤ However, for *A. baumannii* which is also in the critical priority risk of WHO, the quaternary nanocomposite could be a ray of hope.

Nano-toxicity is an emerging issue. The resistance developed against Ag nanoparticles has been discussed in previous chapters and thus this calls for all the more responsibility. Hence the nanocomposites need to be evaluated for various toxicity-related issues too. Moreover, the materials in this dissertation have been tested against gram-negative bacteria and to come to more conclusive terms we also need to study its behavior in gram-positive bacteria. This is underway currently and thus the following future scopes of the work are also proposed:

- Studying the behavior in various human cell lines to understand the toxicity of the nanocomposites
- ➤ In-vivo experiments can be undertaken to make these NCs suitable for use in wider areas.
- Another aspect of the suggested work is to study the properties of the materials and see if it changes upon calcination or not and how this affect the overall microbial results.
- These nanocomposite material properties have been studied by various characterization techniques and thus it could also be explored for photocatalytic activity.

All these aspects are also under consideration by our research group and fellow members have already started work in this line. We have a suitable metal oxide base antimicrobial component. It can be noted that many of the above compositions are already filed for patents.

5. Appendix

Table A 1: Zeta Potential analysis (ξ in mV) for Z (ZnO) and AZ (ZnO-AgO₂/Ag) in PBS in different pH.

Time	Ze	eta potentia	l of the sa	mples in (m)	-	Buffer S	aline (PB	S)
		Z (Z	nO)	(III)	*	Z (ZnO-A	AgO ₂ /Ag)	
	pH 5	pH 6.9	pH 7.4	pH 8	pH 5	pH 6.9	pH 7.4	pH 8
0 min	-11.0	-15.3mV	-15.5	-23.4	-10.9	-14.2	-14.2	-1.9
15 min	-11.5	-15.5 mV	-18.7	-23.8	-10.4	-15.5	-16.2	-1.9
30 min	-11.8	-15.9	-17.9	-22.6	-10.4	-19.5	-14.1	-1.9
45 min	-11.9	-17.1	-17.1	-22.6	-11.9	-20.3	-14.5	-1.8
60 min	-12.5	-17.41	-16.1	-21.3	-12.9	-20.3	-12.9	-1.9
1.5 h	-11	-18.6	-11.9	-20.4	-11.2	-19.3	-13.0	-2.0
2 h	-12.2	-18.5	-11.12	-13.2	-11.2	-20.8	-13.2	-2.2
3 h	-10.9	-19	10.18	-8.23	-12.3	-20.6	-12.4	-2.6
24 h	-11.9	-20.0	-22.4	-7.24	-10.5	-19.2	-12.8	-2.0
48 h	-9.8	-19.3	-20.7	-7.9	-7.321	-20.1	-11.9	-0.99
Day 3	-10.2	-13.1	-18.2	-2.10	-7.8	-14.6	-10.1	-4.1
Day 4	-8.1	-10	-13.2	-6.897	-6.32	-8.78	-8.6	-3.1
Day 5	-3.2	-3.8	-7.1	-6.1	-9.8	-7.2	-8.4	-0.9
Day 6	-2.881	2.213	-7.3	-7.87	-7.7	6.99	-8.81	-4.4
Day 7	-10.9	-1.842	-9.2	-11.2	-10.7	-10.2	-11.3	-1.5

Table A 2: Zeta Potential analysis (ξ in mV) for different samples in Saline.

Time	7	Zeta potential of t	the Samples in Sali	ne
		(1	mV)	
	Z(ZnO)	AZ (ZnO-	SZ (ZnO-SnO ₂)	CZ (ZnO-CuO)
		AgO ₂ /Ag)		
0 min	-15.8	-24.3	-13.7	-21.2
15 min	-15.4	-20.6	-13.9	-22.9
30 min	-17.2	-21.6	-14.8	-22.9
45 min	-11.7	-19.3	-13.9	-22.1
1 h	-14.5	-22.6	-13.4	-22.1
1.5 h	-15.7	-20.5	-13.7	-21.6
2 h	-15.5	-23.0	-14.1	-22.6
3 h	-16.6	-18.5	-13.5	-20.9
24 h	-13.5	-12.0	-19.5	-4.5
48 h	-8.2	-9.6	-16.4	-6.2
72 h	-14.5	-16.3	-13.5	-10.2
Day 4	-14.1	-3.2	-8.2	-6.2
Day 5	-12.8	-9.3	-4.3	-5.1
Day 6	-6.0	-7.9	-5.2	-4.98
Day 7	-6.25	-8.4	-8.8	-5.53
	1	1	1	1

Table A 3: Zeta potential analysis (ξ in mV) for Z(ZnO) and AZ (ZnO-AgO₂/Ag) in Phosphate Buffer Solution (PB).

	Z(ZnO)			AZ (ZnO-AgO ₂ /Ag)			
	pH 5	pH 6.9	pH 7.4	pH 8	pH 5	pH 6.9	pH 7.4	pH 8
Time								
0 min	-8.9	-22.2	-44.4	-36.3	-6.05	-26.8	-31.5	-33.5
15 min	-9.0	-23.4	-45.6	-36.5	-6.31	-27.3	-	-33.5
30 min	-9.1	-24.5	-47.2	-36.4	-6.52	-26.4	-	-36.9
45 min	-8.0	-25.4	-47.5	-35.8	-6.49	-28.2	-31.1	-35.0
1 h	-7.8	-26.1	-52.4	-36.0	-6.92	-28.7	-28.9	-35.8
1.5 h	-8.5	-24.8	-50.5	-34.0	-6.22	-29.3	-	-32.2
2 h	-8.8	-29.4	-50.1	-39.1	-6.89	-27.4	-29.2	-39.3
3 h	-8.6	-23.3	-51.4	-36.5	-6.73	-27.6	-29.7	-37.4
24 h	-8.7	-26.0	-	-37.0	-6.92	-20.7	-35.2/	-41.2
							-25.8	
48 h	-10.9	-22.3	-18.8	-10.591	-6.72	-25.6	-29.9	-22.6
72 h	-13.4	-21.0	-16.7	-11.5	-6.88	-19.7	-16.2	-34
Day 4	-12.3	-19.2	-21.7	-	-6.31	-17.4	-22.2	-
Day 5	-	-25.8	-23.1	-	-	-23.5	-26.1	-
Day 6	-	-11.2	-25.8	-	-	-25.2	-33.5	-
Day 7	-	-15.4	-23.4	-	-	-29.5	-32.3	-
			1		1			1

Table A 4: Zeta potential analysis (ξ in mV) for SZ (ZnO-SnO₂ and CZ (ZnO-CuO) in PB for SZ and CZ.

	SZ (ZnO-SnO ₂					CZ (Zn	O-CuO)	
	pH 7.4	pH 6.9	pH 5	pH 8	pH 6.9	pH 7.4	pH 5	pH 8
Time								
0 min	-28.5	-20.6	-8.4	-41.0	-28.4	-34.6	-7.8	-35.1
15 min	-25.6	-19.5	-8.4	-41.5	-22.1	-34.3	-8.3	-36.1
30 min	-29.9	-20.6	-8.2	-41.2	-21.2	-36.0	-7.9	-36.1
45 min	-25.4	-20.1	-7.1	-40.4	-21.2	-33.7	-7.4	-36.9
1 h	-26.1	-18.8	-7.8	-42.4	-20.2	-35.5	-8.1	-34.2
1.5 h	-28.2	-21.4	-8.6	-41.6	-21.0	-35.3	-7.5	-33.7
2 h	-29.4	-20.7	-8.4	-44.1	-20.1	-31.6	-7.9	-35.6
3 h	-29.0	-19.5	-8.4	-44.5	-20.6	-32.2	-6.2	-33.9
24 h	-23.1	-22.9	-8.3	-43.6	-21.1	-29.7	-7.4	-27.9
48 h	-24.2	-23.1	-7.2	-15.1	-24.8	-27.9	-8.3	-23.3
Day 3	-26.3	-26.5	-	-	-28.5	-28.2	-	-
Day 4	-24.4	-17.8	-	-	-21.4	-13.9	-	-
Day 5	-17.3	-25.8	-	-	-23.1	-29.3	-	-
Day 6	-35.5	-27.8	-	-	-20.8	-15.4	-	-
Day 7	-34.0	-32.0	-	-	-27.4	-26.9	-	-

DLS study: particle size in nm

Table A 5: Particle size analysis through DLS for Z (ZnO) in Phosphate Buffer Saline (PBS) (particle size in nm).

	pH 5	рН 6.9	pH 7.4	pH 8
Time	42.9	202.9		116.0
0 min	152.4	122.8	122.6	107.2
15 min	102.4	209.8	92.4	121.7
30 min	164.7	108.9	120.6	129.0
45 min	176.4	98.6	91.05	128.7
1 h	163.5	331.8	79.96	130.2
3 h	23.5	378.3	14.4	129.8
24 h	80.4	48.36	82.5	126.4
48 h	128.7	166.0	80.8	111.0
72 h	52.9	218.2	83.67	182.5
Day 4			76.67	171.6
Day 5		65.90	82.12	-
Day 6	55.24	202.9	92.1	198.2
Day 7	396.3	122.8	122.14	121.0

Table A 6: Particle size analysis through DLS in PBS for AZ (ZnO-AgO2/Ag), particle size in nm

	pH 5	рН 6.9	pH 7.4	pH 8
Time	70.9	-	79.17	63.5
0 min	158.8	65.0	61.8	104.5
15 min	82.5	78.9	78.5	104.9
30	100.1	94.4	62.0	92.3
45 min	234.1	76.3	71.5	99.3
1 h	139.7	160.8	66.4	89.4
1.5 h	132.4	92.3	75.7	98.8
2 h	67.28	170.0	77.8	78.9
2.5 h	18.6	27.0	68.9	75.9
3 h	39.3	45.8	65.7	98.4
4 h	28.4	94.0	79.4	116.7
5 h	517.4	73.3	62.2	91.3
6 h		101.2	58.9	99.9
24 h	40.8	22.2	187.8	121.8
48 h	32.8	94.6	39.6	119.8
Day 3	-	81.0	93.2	150.1
Day 4	176.1	135.3	79.9	102.1
Day 5	19.6	91.1	63.6	121.5
Day 6	70.9	415.3	70.5	63.5
Day 7	158.8	320.6	79.2	104.5

Table A 7: Particle size analysis through DLS in Saline solution, particle size in nm.

	ZnO	AZ (ZnO-	CZ(ZnO-CuO)	SZ(ZnO-SnO ₂)
		AgO ₂ /Ag)		
Time	43.6			49.8
0 min	418.8	32.7	29.5	59.2
15 min	61.9	22.2	37.4	64.7
45 min	73.7	30.6	41.7	49.4
1 h	46.0	33.4	29.2	58.4
3 h	45.5	44.8	45.3	60.02
4 h	72.8	13.8	43.0	46.2
5 h	67.9	26.3	50.9	69.8
6 h	46.3	30.3	58.0	53.6
24 h	54.4	14.0	73.9	56.2
48 h	49.4	39.3	63.4	67.5
72 h	30.8	44.8	40.8	77.7
Day 4	20.9	33.0	33.5	72.5
Day 5	19.5	41.8	436.9	34.8
Day 6	125.8	48.0	130.3	273.2
Day 7	100.8	57.5	136.2	65.3

Table A 8: Particle size analysis through in PB for ZnO, particle size in nm.

	pH5	pH 6.9	pH 7.4	pH8
Time	181	123		75.8
0 min	441	112	53.3	32.8
40 min	508	159	58.8	57.7
1 h	583	204	78.9	40.7
1.5 h	678	178	29.5	49.4
2 h	593	198	30.3	69.4
3 h	572	167	34.2	30.8
4 h	567	179		23.6
5 h	560	240		51.4
6 h	522	226		33.9
24 h	914	180	61.1	-
48 h	648	178	-	75.8
Day 3	181	231	-	-
Day 4	-	338	-	-
Day 5	-	274	-	-
Day 6	-	225	16.54	-
Day 7	-	195	-	-

Table A 9: Particle size analysis through DLS in Phosphate Buffer (PB) AZ (ZnO-Ag₂O/Ag), particle size in nm.

	pH 5	pH 6.9	pH 7.4	рН8
Time	70.9			63.5
0 min	158.8	188.1	84.9	104.5
15 min	82.5	121.5	88.8	104.9
45 min	100.1	180.5	30.6	92.3
1 h	234.1	65.9	27.4	99.3
2 h	139.7	152.3	76.9	89.4
2.5 h	132.4	138.7	38.5	98.8
3 h	67.3	129.3	10.8	78.9
4 h	185.7	164.2	16.4	75.9
24 h	393.3	153.7	10.6561	98.4
48 h	283.8	47.7	-	116.7
Day 3	517.4		-	91.3
Day 4	-		-	99.9
Day 5	407.6	14.2	-	121.8
Day 6	328.4	38.2	6.9	119.8
Day 7	-	1.8243	-	150.1

Table A 10: Particle size analysis through DLS in PB for CZ (ZnO-CuO), particle size in nm.

	pH 5	pH 6.9	pH 7.4	pH8
Time				-
0 min	156.9	187.2		-
20 min	154.2	67.8	204.1	25.6
40 min	148.4	-	227.0	15.421
1 h	152.3	-	237.6	5.75
2 h	152.9	133-3	238.8	-
2.5 h	193.4	-	233.1	-
3 h	178.4	-	249.8	-
4 h	195.5	-	200.7	-
5 h	196.7	79.4	230.4	2.67
6 h	268.6		232.4	
24 h	156.9		130.9	-
48 h	-	63.3	190.9	-
Day 3	-	140.4	153.3	-
Day 4	-	93.6	160.9	-
Day 5	-	94.8		-
Day 6	-	46.7	551.7	-
Day 7	-	12.2	248.9	-

Table A 11: Particle size analysis through DLS in PB for SZ ($ZnO\text{-}SnO_2$), particle size in nm

	pH5	pH 6.9	pH 7.4	pH 8
Time				
0 min	177.2	116.4	78.6	110.2
20 min	197.4	88.0	-	121.9
40 min	172.2	91-7	-	118.7
1 h	206.3	134.6	101.9	121.1
1.5 h	185.6	28.5	78.8	134.6
2 h	271.4	146.9	66.6	123.1
3 h	210.0	143.9	-	122.0
4 h	324.5	110.5	-	120.7
5 h	255.4	137.8	60.6	116.9
6 h	388.2	695	-	134.1
24 h	177.2	25.5	80.1	110.0
48 h	-	42.3	47.3	-
Day 3	-	34.2	81.6	-
Day 4	-	141.6	80.9	-
Day 5	-	467.3	495.9	-
Day 6	-	0.8838	-	-
Day 7	-	-	78.6	-

6. Bibliography

- 1 R. P. Feynman, *Eng. Sci.*, 1960, **23**, 22–36.
- L. A. Kolahalam, I. V Kasi Viswanath, B. S. Diwakar, B. Govindh, V. Reddy and Y. L. N. Murthy, *Mater. Today Proc.*, 2019, **18**, 2182–2190.
- D. Rawtani, M. Tharmavaram, G. Pandey and C. M. Hussain, *TrAC Trends Anal. Chem.*, 2019, **120**, 115661.
- 4 I. Khan, K. Saeed and I. Khan, *Arab. J. Chem.*, 2019, **12**, 908–931.
- J. Jampílek and K. Král'ová, in *Micro and Nano Technologies*, Elsevier, 2017, pp. 23–54.
- 6 M. S. Chavali and M. P. Nikolova, *SN Appl. Sci.*, 2019, **1**, 607.
- 7 N. Baig, I. Kammakakam and W. Falath, *Mater. Adv.*, 2021, **2**, 1821–1871.
- 8 Antimicrobial resistance, https://www.who.int/news-room/fact-sheets/detail/antimicrobial-resistance.
- 9 New report calls for urgent action to avert antimicrobial resistance crisis, https://www.who.int/news/item/29-04-2019-new-report-calls-for-urgent-action-to-avert-antimicrobial-resistance-crisis.
- M. E. A. de Kraker, A. J. Stewardson and S. Harbarth, *PLOS Med.*, 2016, 13, e1002184.
- E. Agnew, C. Dolecek, R. Hasan, M. Lahra, H. Merk, O. Perovic, D. Sievert, R. Smith, A. Taylor and P. Turner, *Global antimicrobial resistance and use surveillance system (GLASS) report*, 2021.
- 12 C. Dall, WHO reveals new global antibiotic resistance data, more concerns, https://www.cidrap.umn.edu/news-perspective/2021/06/who-reveals-new-global-antibiotic-resistance-data-more-concerns.
- N. K. Ganguly, Antimicrobial Resistance Is a Serious Threat To Public Health in India, https://science.thewire.in/health/antimicrobial-resistance-is-a-serious-threat-to-public-health-in-india/.
- 14 V. T. Avika; Dixit, Neeta; Kumar, Sanjiv; Kumar, Indian J Community Med, 2019,

- **44**, 4–8.
- S. R. Shrivastava, P. S. Shrivastava and J. Ramasamy, *JMS J. Med. Soc.*, 2018,
 32, 76–77.
- 16 V. V. Mogasale, P. Saldanha, V. Pai, P. D. Rekha and V. Mogasale, *Sci. Reports* 2021 111, 2021, **11**, 1–7.
- N. Thacker, N. Pereira, S. D. Banavali, G. Narula, T. Vora, G. Chinnaswamy, M. Prasad, R. Kelkar, S. Biswas and B. Arora, *Indian J. Cancer*, 2014, **51**, 438.
- B. Veeraraghavan, M. R. Jesudason, J. A. J. Prakasah, S. Anandan, R. D. Sahni, A. K. Pragasam, Y. D. Bakthavatchalam, R. J. Selvakumar, T. N. Dhole and C. Rodrigues, *Indian J. Med. Microbiol.*, 2018, 36, 32–36.
- V. Patwardhan, D. Kumar, V. Goel and S. Singh, *J. Lab. Physicians*, 2017, 9, 264–268.
- 20 P. R. Hsueh, *Int. J. Antimicrob. Agents*, 2012, **40**, S1-3.
- A. Ponce-de-Leon, E. Rodríguez-Noriega, R. Morfín-Otero, D. P. Cornejo-Juárez, J. C. Tinoco, A. Martínez-Gamboa, C. J. Gaona-Tapia, M. L. Guerrero-Almeida, A. Martin-Onraët, J. L. Vallejo Cervantes and J. Sifuentes-Osornio, *PLoS One*, 2018, 13, e0198621.
- 22 AMR surveillance Network, Indian Council of Medical Research, 2020.
- 23 S. G. Kurz, J. J. Furin and C. M. Bark, *Infect. Dis. Clin. North Am.*, 2016, **30**, 509–522.
- 24 R. Singh, S. P. Dwivedi, U. S. Gaharwar, R. Meena, P. Rajamani and T. Prasad, *J. Appl. Microbiol.*, 2020, **128**, 1547–1567.
- 25 J. Davies and D. Davies, *Microbiol. Mol. Biol. Rev.*, 2010, **74**, 417–433.
- N. Kumar, B. Das and S. Patra, in *Antimicrobial Nanoarchitectonics*, Elsevier, 2017, pp. 261–278.
- 27 C. J. Thomson, E. Power, H. Ruebsamen-Waigmann and H. Labischinski, *Curr. Opin. Microbiol.*, 2004, **7**, 445–450.
- 28 S. Andrei, G. Droc and G. Stefan, *Discoveries*.
- FDA approves new antibacterial drug to treat complicated urinary tract infections as part of ongoing efforts to address antimicrobial resistance | FDA,

- https://www.fda.gov/news-events/press-announcements/fda-approves-new-antibacterial-drug-treat-complicated-urinary-tract-infections-part-ongoing-efforts, (accessed 6 November 2021).
- 30 N. Savage, *Nature*, 2020, **586**, S55–S56.
- W. H. Organization, 2020 antibacterial agents in clinical and preclinical development: an overview and analysis, 2021.
- P. Beyer and S. Paulin, Bull. World Health Organ., 2020, 98, 151.
- B. Das and S. Patra, in *Nanostructures for Antimicrobial Therapy: Nanostructures in Therapeutic Medicine Series*, Elsevier, 2017, pp. 1–22.
- 34 J. N. Pendleton, S. P. Gorman and B. F. Gilmore, *Expert Rev. Anti. Infect. Ther.*, 2013, **11**, 297–308.
- A. León-Buitimea, C. R. Garza-Cárdenas, J. A. Garza-Cervantes, J. A. Lerma-Escalera and J. R. Morones-Ramírez, *Front. Microbiol.*, 2020, **11**, 1669.
- 36 M. Mahlapuu, J. Håkansson, L. Ringstad and C. Björn, *Front. Cell. Infect. Microbiol.*, 2016, **6**, 194.
- 37 C. G. Starr and W. C. Wimley, *Biochim. Biophys. Acta (BBA)-Biomembranes*, 2017, **1859**, 2319–2326.
- 38 A. J. Huh and Y. J. Kwon, *J. Control. release*, 2011, **156**, 128–145.
- M. J. Hajipour, K. M. Fromm, A. A. Ashkarran, D. J. de Aberasturi, I. R. de Larramendi, T. Rojo, V. Serpooshan, W. J. Parak and M. Mahmoudi, *Trends Biotechnol.*, 2012, 30, 499–511.
- 40 L. Miao, C. Wang, J. Hou, P. Wang, Y. Ao, Y. Li, N. Geng, Y. Yao, B. Lv and Y. Yang, *Bioresour. Technol.*, 2016, 216, 537–544.
- 41 L. Wang, C. Hu and L. Shao, *Int. J. Nanomedicine*, 2017, **12**, 1227–1249.
- 42 E. Weir, A. Lawlor, A. Whelan and F. Regan, *Analyst*, 2008, **133**, 835–845.
- A. S. Abd-El-Aziz, M. R. Benaaisha, A. A. Abdelghani, R. Bissessur, L. H. Abdel-Rahman, A. M. Fayez and D. A. El-ezz, *Biomolecules*, 2021, **11**, 1568.
- D. Cheng, M. Yu, F. Fu, W. Han, G. Li, J. Xie, Y. Song, M. T. Swihart and E. Song, *Anal. Chem.*, 2016, 88, 820–825.
- 45 X. Dai, Q. Guo, Y. Zhao, P. Zhang, T. Zhang, X. Zhang and C. Li, ACS Appl.

- Mater. Interfaces, 2016, 8, 25798–25807.
- 46 Y. Wang, X. Ding, Y. Chen, M. Guo, Y. Zhang, X. Guo and H. Gu, *Biomaterials*, 2016, **101**, 207–216.
- 47 S. Yun and J. J. Huang, *Retin. Pharmacother.*, 2016, **55**, 84–92.
- 48 K. M. Varier, M. Gudeppu, A. Chinnasamy, S. Thangarajan, J. Balasubramanian, Y. Li and B. Gajendran, eds. M. Naushad, S. Rajendran and F. Gracia, Springer International Publishing, Cham, 2019, pp. 321–355.
- 49 X. Hong, J. Wen, X. Xiong and Y. Hu, *Environ. Sci. Pollut. Res.*, 2016, **23**, 4489–4497.
- I. V Sukhorukova, A. N. Sheveyko, N. V Shvindina, E. A. Denisenko, S. G. Ignatov and D. V Shtansky, *ACS Appl. Mater. Interfaces*, 2017, **9**, 4259–4271.
- 51 J. Chen, L. Wu, M. Lu, S. Lu, Z. Li and W. Ding, *Front. Microbiol.*, 2020, **11**, 365.
- 52 R. Vijayaraghavan, *Mater. Sci. Eng. C*, 2017, **77**, 1027–1034.
- C. Karunakaran, V. Rajeswari and P. Gomathisankar, *Mater. Sci. Semicond. Process.*, 2011, **14**, 133–138.
- 54 V. Shanmugam and K. S. Jeyaperumal, *Appl. Surf. Sci.*, 2018, **449**, 617–630.
- 55 M. Nowak and W. Barańska-Rybak, Antibiot., 2021, 10.
- 56 M. G. Correa, F. B. Martínez, C. P. Vidal, C. Streitt, J. Escrig and C. L. de Dicastillo, *Beilstein J. Nanotechnol.*, 2020, **11**, 1450–1469.
- F. A. Khan, in *Applications of Nanomaterials in Human Health*, Springer, 2020, pp. 1–13.
- B. Devrim and A. Bozkır, in *Nanostructures for Antimicrobial Therapy*, Elsevier, 2017, pp. 169–202.
- A. A. Yaqoob, H. Ahmad, T. Parveen, A. Ahmad, M. Oves, I. M. I. Ismail, H. A. Qari, K. Umar and M. N. Mohamad Ibrahim, *Front. Chem.*, 2020, 8, 341.
- 60 G. Borkow and J. Gabbay, *Curr. Chem. Biol.*, 2009, **3**, 272–278.
- 61 K. Gold, B. Slay, M. Knackstedt and A. K. Gaharwar, *Adv. Ther.*, 2018, **1**, 1700033.
- 62 M. B. Galib, M. Mashru, C. Jagtap, B. J. Patgiri and P. K. Prajapati, J. Ayurveda

- Integr. Med., 2011, 2, 55.
- N. Castro Alarcon, J. L. Herrera Arizmendi, M. C. Luis Alberto, I. P. Guzman Guzman, A. Perez Centeno and M. A. Santana Aranda, *Microbiol. Res. Int.*, 2016, **4**, 55–62.
- 64 M. R. Bindhu, M. Umadevi, M. K. Micheal, M. V. Arasu and N. A. Al-Dhabi, Mater. Lett., 2016, 166, 19–22.
- Z. S. Rezaei, A. Javed, M. J. Ghani, S. Soufian, F. F. Barzegari, M. A. M. Bayandori and S. H. Mirjalili, *Iran. J. Pathol.*, 2010, 5, 83–89.
- T. Xia, M. Kovochich, J. Brant, M. Hotze, J. Sempf, T. Oberley, C. Sioutas, J. I. Yeh, M. R. Wiesner and A. E. Nel, *Nano Lett.*, 2006, **6**, 1794–1807.
- 67 T. C. Long, N. Saleh, R. D. Tilton, G. V Lowry and B. Veronesi, *Environ. Sci. Technol.*, 2006, **40**, 4346–4352.
- 68 J. Lovrić, S. J. Cho, F. M. Winnik and D. Maysinger, *Chem. Biol.*, 2005, **12**, 1227–1234.
- 69 C. Rodríguez-Serrano, J. Guzmán-Moreno, C. Ángeles-Chávez, V. Rodríguez-González, J. J. Ortega-Sigala, R. M. Ramírez-Santoyo and L. E. Vidales-Rodríguez, *PLoS One*, 2020, 15, e0230275.
- M. E. Terlizzi, G. Gribaudo and M. E. Maffei, Front. Microbiol., 2017, 8, 1566.
- 71 C. B. Ong, L. Y. Ng and A. W. Mohammad, *Renew. Sustain. Energy Rev.*, 2018, 81, 536–551.
- B. Abebe, E. A. Zereffa, A. Tadesse and H. C. A. Murthy, *Nanoscale Res. Lett.*, 2020, **15**, 190.
- M. Rosenberg, K. Ilić, K. Juganson, A. Ivask, M. Ahonen, I. V. Vrček and A. Kahru, *PeerJ*, 2019, **7**, e6315.
- 74 J. J. Hostynek and H. I. Maibach, *Copper and the Skin*, CRC Press, 2006.
- V. B. P. Sudha, S. Ganesan, G. P. Pazhani, T. Ramamurthy, G. B. Nair and P. Venkatasubramanian, *J. Health. Popul. Nutr.*, 2012, **30**, 17.
- 76 J. J. Hostynek and H. I. Maibach, *Dermatol. Ther.*, 2004, **17**, 328–333.
- 77 J. J. Hostynek and H. I. Maibach, *Copp. Ski.*, 2006, 115–148.
- P. A. O'Brien, R. Kulier, F. M. Helmerhorst, M. Usher-Patel and C. d'Arcangues,

- Contraception, 2008, **77**, 318–327.
- 79 D. Mitra, E.-T. Kang and K. G. Neoh, *ACS Appl. Mater. Interfaces*, 2020, **12**, 21159–21182.
- J. J. Castellano, S. M. Shafii, F. Ko, G. Donate, T. E. Wright, R. J. Mannari, W. G. Payne, D. J. Smith and M. C. Robson, *Int. Wound J.*, 2007, **4**, 114–122.
- 81 S. H. Lee and B.-H. Jun, *Int. J. Mol. Sci.*, 2019, **20**, 865.
- A. D. Bhagwat, S. S. Sawant, B. G. Ankamwar and C. M. Mahajan, *J. Nano-Electron. Phys.*, 2015, **7**, 7–10.
- 83 Z. Ying, Q. Wan, Z. T. Song and S. L. Feng, *Nanotechnology*, 2004, **15**, 1682.
- 84 H. A. Hemeg, *Int. J. Nanomedicine*, 2017, **12**, 8211.
- Y. N. Slavin, J. Asnis, U. O. Häfeli and H. Bach, J. Nanobiotechnol., 2017, 15, 65.
- 86 S. Mahira, A. Jain, W. Khan and A. J. Domb, 2019, pp. 1–37.
- T. C. Dakal, A. Kumar, R. S. Majumdar and V. Yadav, Front. Microbiol., 2016, 7, 1831.
- P. V Baptista, M. P. McCusker, A. Carvalho, D. A. Ferreira, N. M. Mohan, M. Martins and A. R. Fernandes, *Front. Microbiol.*, 2018, **9**, 1441.
- 89 S. M. Dizaj, F. Lotfipour, M. Barzegar-Jalali, M. H. Zarrintan and K. Adibkia, *Mater. Sci. Eng. C.*, 2014, **44**, 278–284.
- 90 N. Beyth, Y. Houri-Haddad, A. Domb, W. Khan and R. Hazan, *J. Evidence-Based Complement. Altern. Med.*, 2015, **2015**, 246012.
- 91 B. L. Guo, P. Han, L. C. Guo, Y. Q. Cao, A. D. Li, J. Z. Kong, H. F. Zhai and D. Wu, *Nanoscale Res. Lett.*, 2015, **10**, 336.
- 92 Y. Liu, L. He, A. Mustapha, H. Li, Z. Q. Hu and M. Lin, *J. Appl. Microbiol.*, 2009, **107**, 1193–1201.
- 93 L. S. Reddy, M. M. Nisha, M. Joice and P. N. Shilpa, *Pharm. Biol.*, 2014, **52**, 1388–1397.
- 94 S. Amininezhad, A. Rezvani, M. Amouheidari, S. Amininejad and S. Rakhshani, *Zahedan J. Res. Med. Sci.*, 2015, **17**, e1053.
- 95 S. Rehman, S. M. Asiri, F. A. Khan, B. R. Jermy, H. Khan, S. Akhtar, R. Al Jindan, K. M. Khan and A. Qurashi, *ChemistrySelect*, 2019, **4**, 4013–4017.

- 96 M. Zarei, A. Jamnejad and E. Khajehali, *Jundishapur J. Microbiol.*, 2014, **7**, e8720.
- 97 I. Sondi and B. Salopek-Sondi, J. Colloid Interface Sci., 2004, 275, 177–182.
- 98 O. Mahapatra, M. Bhagat, C. Gopalakrishnan and K. D. Arunachalam, *J. Exp. Nanosci.*, 2008, **3**, 185–193.
- 99 M. Ahamed, H. A. Alhadlaq, M. A. M. Khan, P. Karuppiah and N. A. Al-Dhabi, *J. Nanomater.*, 2014, **2014**, 637858.
- 100 A. Azam, A. S. Ahmed, M. Oves, M. S. Khan, S. S. Habib and A. Memic, *Int. J. Nanomed.*, 2012, **7**, 6003–6009.
- 101 G. Grass, C. Rensing and M. Solioz, Appl. Environ. Microbiol., 2011, 77, 1541– 1547.
- J. L. Graves, M. Tajkarimi, Q. Cunningham, A. Campbell, H. Nonga, S. H. Harrison and J. E. Barrick, *Front. Genet.*, 2015, 6, 42.
- 103 C. Gunawan, C. P. Marquis, R. Amal, G. A. Sotiriou, S. A. Rice and E. J. Harry, ACS Nano, 2017, 11, 3438–3445.
- A. Panáček, L. Kvítek, M. Smékalová, R. Večeřová, M. Kolář, M. Röderová, F. Dyčka, M. Šebela, R. Prucek, O. Tomanec and R. Zbořil, *Nat. Nanotechnol.*, 2018, 13, 65–71.
- 105 L. Ren, D. Chen, Z. Hu, Z. Gao, Z. Luo, Z. Chen, Y. Jiang, B. Zhao, C. M. L. Wu and C.-H. Shek, *RSC Adv.*, 2016, **6**, 82096–82102.
- N. Zhang, Y. Gao, H. Zhang, X. Feng, H. Cai and Y. Liu, *Colloids Surf. B.*, 2010, 81, 537–543.
- 107 M. Sharma, S. Hazra and S. Basu, *Adv. Powder Technol.*, 2017, **28**, 3085–3094.
- A. Perdikaki, A. Galeou, G. Pilatos, I. Karatasios, N. K. Kanellopoulos, A. Prombona and G. N. Karanikolos, ACS Appl. Mater. Interfaces, 2016, 8, 27498–27510.
- J. Alimunnisa, K. Ravichandran and K. S. Meena, J. Mol. Liq., 2017, 231, 281–287.
- 110 S. Kumar, R. Nigam, V. Kundu and N. Jaggi, *J. Mater. Sci. Mater. Electron.*, 2015, **26**, 3268–3274.

- 111 G. Giusti, V. Consonni, E. Puyoo and D. Bellet, *ACS Appl. Mater. Interfaces*, 2014, **6**, 14096–14107.
- 112 S. Stankic, S. Suman, F. Haque and J. Vidic, J. Nanobiotechnol., 2016, 14, 1–20.
- 113 N. Basavegowda and K.-H. Baek, *Molecules*, 2021, **26**, 912.
- 114 N. Arora, K. Thangavelu and G. N. Karanikolos, Front. Chem., 2020, 8, 412.
- 115 O. Yamamoto, T. Ohira, K. Alvarez and M. Fukuda, *Mater. Sci. Eng. B*, 2010, **173**, 208–212.
- J. Vidic, S. Stankic, F. Haque, D. Ciric, R. Le Goffic, A. Vidy, J. Jupille and B. Delmas, *J. Nanoparticle Res.*, 2013, **15**, 1595.
- 117 M. Paszkiewicz, A. Gołąbiewska, Ł. Rajski, E. Kowal, A. Sajdak and A. Zaleska-Medynska, *J. Nanomater.*, 2016, **2016**, 2187940.
- A. P. Ayanwale, B. L. Estrada-Capetillo and S. Y. Reyes-López, *Processes*, 2021,9, 773.
- 119 A. P. Ayanwale, B. L. Estrada-Capetillo and S. Y. Reyes-López, *Inorg. Chem. Commun.*, 2021, **134**, 108954.
- 120 R. Vittal and J. Bai Aswathanarayan, *Sci. Against Microb. Pathog. Commun. Curr. Res. Technol. Adv.*, 2011, 197–209.
- 121 G. R. Tortella, J. C. Pieretti, O. Rubilar, M. Fernández-Baldo, A. Benavides-Mendoza, M. C. Diez and A. B. Seabra, *Crit. Rev. Biotechnol.*, 2021, 1–19.
- 122 P. Merkl, S. Long, G. M. McInerney and G. A. Sotiriou, *Nanomater.*, 2021, 11.
- I. Das Jana, P. Kumbhakar, S. Banerjee, C. C. Gowda, N. Kedia, S. K. Kuila, S. Banerjee, N. C. Das, A. K. Das and I. Manna, ACS Appl. Nano Mater., 2020, 4, 352–362.
- 124 S. M. El-Megharbel, M. Alsawat, F. A. Al-Salmi and R. Z. Hamza, *Coatings*, 2021, 11, 388.
- M. Abinaya, B. Vaseeharan, M. Divya, A. Sharmili, M. Govindarajan, N. S. Alharbi, S. Kadaikunnan, J. M. Khaled and G. Benelli, J. trace Elem. Med. Biol. organ Soc. Miner. Trace Elem., 2018, 45, 93–103.
- 126 J. Saranya, B. S. Sreeja, M. Arivanandan, K. Bhuvaneswari, S. Sherin, K. S. Shivani, G. SaradhaPreetha and K. K. Saroja, *J. Inorg. Organomet. Polym. Mater.*,

- , DOI:10.1007/s10904-021-02128-5.
- A. A. A. Ahmed, A. A. Al-Mushki, B. A. Al-Asbahi, A. M. Abdulwahab, J. M. A. Abduljalil, F. A. A. Saad, S. M. H. Qaid, H. M. Ghaithan, W. A. Farooq and A.-E. H. Omar, J. Phys. Chem. Solids, 2021, 155, 110113.
- 128 J. Jang, J.-M. Lee, S.-B. Oh, Y. Choi, H.-S. Jung and J. Choi, ACS Appl. Mater. Interfaces, 2020, 12, 35826–35834.
- 129 K. Sivaranjan, O. Padmaraj, J. Santhanalakshmi, M. Sathuvan, A. Sathiyaseelan and S. Sagadevan, *Sci. Rep.*, 2020, **10**, 2586.
- 130 S. Akhtar, S. Rehman, S. M. Asiri, F. A. Khan, U. Baig, A. S. Hakeem and M. A. Gondal, *Mater. Sci. Eng. C*, 2020, **116**, 111156.
- Mahfooz-ur-Rehman, W. Rehman, M. Waseem, B. A. Shah, M. Shakeel, S. Haq,U. Zaman, I. Bibi and H. D. Khan, *J. Chem. Eng. Data*, 2019, 64, 2436–2444.
- J. A. Garza-Cervantes, A. Chávez-Reyes, E. C. Castillo, G. García-Rivas, O. A. Ortega-Rivera, E. Salinas, M. Ortiz-Martínez, S. L. Gómez-Flores, J. A. Peña-Martínez and A. Pepi-Molina, Sci. Rep., 2017, 7, 1–16.
- 133 S. Iravani, H. Korbekandi, S. V. Mirmohammadi and B. Zolfaghari, *Res. Pharm. Sci.*, 2014, **9**, 385.
- 134 P. K. Dikshit, J. Kumar, A. K. Das, S. Sadhu, S. Sharma, S. Singh, P. K. Gupta and B. S. Kim, *Catalysts*, 2021, **11**, 902.
- 135 M. G. Guzmán, J. Dille and S. Godet, *Int J Chem Biomol Eng*, 2009, **2**, 104–111.
- 136 M. A. Ahmad, S. Aslam, F. Mustafa and U. Arshad, *Sci. Rep.*, 2021, **11**, 1–9.
- 137 K. Rajendran and S. Sen, *Der Pharm. Lett.*, 2015, **7**, 37–42.
- 138 R. Javed, M. Zia, S. Naz, S. O. Aisida, N. ul Ain and Q. Ao, J. Nanobiotechnology, 2020, 18, 1–15.
- 139 R. Zhao, W. Kong, M. Sun, Y. Yang, W. Liu, M. Lv, S. Song, L. Wang, H. Song and R. Hao, *ACS Appl. Mater. Interfaces*, 2018, **10**, 17617–17629.
- 140 S. Gautam, N. Shrestha, S. Mahato, T. P. A. Nguyen, S. R. Mishra and G. Berg-Beckhoff, *Sci. Rep.*, 2021, **11**, 1–12.
- 141 L. Singhi, K. D. Sagili, B. N. Sharath, K. Bhandari, P. K. Dadul, M. Gautam, C. Ravichandra, S. Chadha and S. Satyanarayana, *Public Heal. action*, 2018, 8, 162–

168.

- 142 Health & Family Welfare Department | State Portal-Sikkim, https://sikkim.gov.in/DepartmentsMenu/health-family-welfare-department/National Health Mission/state-tb-control-society-rntcp, (accessed 14 November 2021).
- 143 K. R. Devi, J. Pradhan, R. Bhutia, P. Dadul, A. Sarkar, N. Gohain and K. Narain, *Sci. Rep.*, 2021, **11**, 1–16.
- 144 D. Van Soolingen, J. Intern. Med., 2001, **249**, 1–26.
- N. T. N. Lan, H. T. K. Lien, L. B. Tung, M. W. Borgdorff, K. Kremer and D. Van Soolingen, *Emerg. Infect. Dis.*, 2003, **9**, 1633.
- 146 K. Kremer, M. J. van der Werf, B. K. Y. Au, D. D. Anh, K. M. Kam, H. R. Van Doorn, M. W. Borgdorff and D. van Soolingen, *Emerg. Infect. Dis.*, 2009, **15**, 335.
- 147 S. T. Swati A.; Sachdeva, Suicide in Sikkim: A Socio-Psycho Assessment, 2016.
- 148 R. Joshi, S. K. Yadav, H. Mishra, N. Pandey, R. Tilak and S. Pokharia, *Heteroat. Chem.*, 2018, **29**, 1–14.
- M. D. R. N. Zulfikar, A.H.M.D.; Siddiqua, M. Nahar, L.; Habib and M. D. S. Uddin, Nizam; Hassan N.; Rana, *Int. J. Pharm. Pharm. Sci.*, 2011, **3**, 198–203.
- 150 A. Raghunath and E. Perumal, *Int. J. Antimicrob. Agents*, 2017, **49**, 137–152.
- A. Sirelkhatim, S. Mahmud, A. Seeni, N. H. M. Kaus, L. C. Ann, S. K. M. Bakhori, H. Hasan and D. Mohamad, *Nano-Micro Lett.*, 2015, **7**, 219–242.
- 152 S. Prabhu and E. K. Poulose, *Int. Nano Lett.*, 2012, **2**, 32.
- 153 Y. H. Hsueh, P. H. Tsai and K. S. Lin, *Int. J. Mol. Sci.*, 2017, **18**, 793.
- 154 L. Wang, C. Hu and L. Shao, *Int. J. Nanomed.*, 2017, **12**, 1227–1249.
- 155 A. Azam, A. S. Ahmed, M. Oves, M. S. Khan and A. Memic, *Int. J. Nanomed.*, 2012, **7**, 3527–3535.
- A. Fakhri, S. Behrouz and M. Pourmand, *J. Photochem. Photobiol. B.*, 2015, **149**, 45–50.
- M. A. Radzig, V. A. Nadtochenko, O. A. Koksharova, J. Kiwi, V. A. Lipasova and I. A. Khmel, *Colloids surfaces. B.*, 2013, 102, 300–306.
- 158 K. Zheng, M. I. Setyawati, D. T. Leong and J. Xie, Coord. Chem. Rev., 2018, 357,

- 1-17.
- 159 A. Perdikaki, A. Galeou, G. Pilatos, A. Prombona and G. N. Karanikolos, *Langmuir*, 2018, **34**, 11156–11166.
- 160 I. Sondi and B. Salopek-Sondi, *J. Colloid Interface Sci.*, 2004, **275**, 177–182.
- N. Zhang, Y. Gao, H. Zhang, X. Feng, H. Cai and Y. Liu, *Colloids Surf.*, B., 2010, 81, 537–543.
- 162 M. Sharma, S. Hazra and S. Basu, *Adv. Powder Technol.*, 2017, **28**, 3085–3094.
- 163 E. Ó. Muimhneacháin, F. J. Reen, F. O'Gara and G. P. McGlacken, *Org. Biomol. Chem.*, 2018, **16**, 169–179.
- 164 J. M. Farrow III, G. Wells and E. C. Pesci, *PLoS One*, 2018, **13**, e0205638.
- 165 G. Nabiel, Y., & Barakat, *Microbiol. Res. J. Int.*, 2021, **31**, 58–68.
- A. D. Tomich, E. H. Klontz, D. Deredge, J. P. Barnard, C. L. McElheny, M. L. Eshbach, O. A. Weisz, P. Wintrode, Y. Doi, E. J. Sundberg and N. Sluis-Cremer, *Antimicrob. Agents Chemother.*, 2019, **63**, e01524-18.
- 167 C. J. Raorane, J.-H. Lee, Y.-G. Kim, S. K. Rajasekharan, R. García-Contreras and J. Lee, *Front. Microbiol.*, 2019, **10**, 990.
- 168 Y. Gong, T. Li, C. Yu and S. Sun, Front. Cell. Infect. Microbiol., 2017, 7, 520.
- P. Paik, M. Pandey, S. Patra, M. Singh, K. Wasnik, P.S. Gupta, Indian Patent Application Number 202011031802.
- 170 P. Paik, M. Pandey, M. Singh, R. Tilak, Indian Patent Application Number 202011017968.
- 171 K. Momma and F. Izumi, *J. Appl. Crystallogr.*, 2011, **44**, 1272–1276.
- 172 K. Bankura, D. Maity, M. M. R. Mollick, D. Mondal, B. Bhowmick, I. Roy, T. Midya, J. Sarkar, D. Rana, K. Acharya and D. Chattopadhyay, *Carbohydr. Polym.*, 2014, 107, 151–157.
- 173 A. S. Ethiraj and D. J. Kang, *Nanoscale Res. Lett.*, 2012, **7**, 70.
- 174 I. Das, S. Sagadevan, Z. Z. Chowdhury and M. E. Hoque, *J. Mater. Sci. Mater. Electron.*, 2018, **29**, 4128–4135.
- 175 P. Bazant, T. Sedlacek, I. Kuritka, D. Podlipny and P. Holcapkova, *Materials* (*Basel*)., 2018, **11**, 363.

- 176 Z. Cai, K.K. Kim and S. Park, *J. Mater. Res. Technol.*, 2020, **9**, 16289–16302.
- 177 M. A. Majeed Khan, S. Kumar, M. Ahamed, S. A. Alrokayan and M. S. AlSalhi, *Nanoscale Res. Lett.*, 2011, **6**, 434.
- 178 S. Honary and F. Zahir, *Trop. J. Pharm. Res.*, 2013, **12**, 255–264.
- 179 I. Cherniakov, A. J. Domb and A. Hoffman, Expert Opin. Drug Deliv., 2015, 12, 1121–1133.
- 180 L. Xu, B. Wei, W. Liu, H. Zhang, C. Su and J. Che, *Nanoscale Res. Lett.*, 2013, **8**, 536.
- 181 C. Zhou, L. Xu, J. Song, R. Xing, S. Xu, D. Liu and H. Song, *Sci. Rep.*, 2014, **4**, 1–9.
- 182 G. B. Hoflund, Z. F. Hazos and G. N. Salaita, *Phys. Rev. B*, 2000, **62**, 11126–11133.
- J. Rashid, M. A. Barakat, N. Salah and S. S. Habib, RSC Adv., 2014, 4, 56892–56899.
- 184 Z. Li, Y. Zhou, J. Zhang, W. Tu, Q. Liu, T. Yu and Z. Zou, *Cryst. Growth Des.*, 2012, **12**, 1476–1481.
- 185 M. Li, Y. Hu, S. Xie, Y. Huang, Y. Tong and X. Lu, Chem. Commun., 2014, 50, 4341–4343.
- 186 J. Ren, W. Wang, S. Sun, L. Zhang, L. Wang and J. Chang, *Ind. Eng. Chem. Res.*, 2011, **50**, 10366–10369.
- 187 I. Aleksic, J. Jeremic, D. Milivojevic, T. Ilic-Tomic, S. Šegan, M. Zlatović, D. M. Opsenica and L. Senerovic, ACS Chem. Biol., 2019, 14, 2800–2809.
- 188 S. Boopathi, R. Vashisth, P. Manoharan, R. Kandasamy and N. Sivakumar, *Bioorg. Med. Chem. Lett.*, 2017, **27**, 2113–2118.
- 189 L. Kumar, S. Chhibber, R. Kumar, M. Kumar and K. Harjai, *Fitoterapia*, 2015, 102, 84–95.
- 190 G. L. Draughn, M. E. Milton, E. A. Feldmann, B. G. Bobay, B. M. Roth, A. L. Olson, R. J. Thompson, L. A. Actis, C. Davies and J. Cavanagh, *J. Mol. Biol.*, 2018, 430, 806–821.
- 191 T. C. Russo, T.A.; Manohar, A.; Beanan, J.M.; Olson, R.; MacDonald, U.;

- Graham, J. Umland, *mSphere*, 2016, **1**, e00082-16.
- L. Whitesell, N. Robbins, D. S. Huang, C. A. McLellan, T. Shekhar-Guturja, E. V LeBlanc, C. S. Nation, R. Hui, A. Hutchinson, C. Collins, S. Chatterjee, R. Trilles, J. L. Xie, D. J. Krysan, S. Lindquist, J. A. Porco, U. Tatu, L. E. Brown, J. Pizarro and L. E. Cowen, *Nat. Commun.*, 2019, 10, 1–17.
- 193 R. Yuan, J. Tu, C. Sheng, X. Chen and N. Liu, Front. Microbiol., 2021, 12, 1280.
- 194 T. Xia, M. Kovochich, M. Liong, L. Mädler, B. Gilbert, H. Shi, J. I. Yeh, J. I. Zink and A. E. Nel, *ACS Nano*, 2008, **2**, 2121–2134.
- 195 K. R. Raghupathi, R. T. Koodali and A. C. Manna, *Langmuir*, 2011, 27, 4020–4028.
- 196 A. Baranwal, A. Srivastava, P. Kumar, V. K. Bajpai, P. K. Maurya and P. Chandra, *Front. Microbiol.*, 2018, **9**, 422.
- 197 R. K. Matharu, L. Ciric and M. Edirisinghe, *Nanotechnology*, 2018, **29**, 282001.
- 198 H. D. Beyene and T. G. Ambaye, Sustain. Polym. Compos. Nanocomposites, 2019, 387–412.
- 199 J. Sarfraz, T. Gulin-Sarfraz, J. Nilsen-Nygaard and M. K. Pettersen, *Nanomaterials*, 2021, **11**, 10.
- 200 P. J. Rivero, A. Urrutia, J. Goicoechea and F. J. Arregui, *Nanoscale Res. Lett.*, 2015, **10**, 1–22.
- 201 N. Savage, *Nature*, 2020, **586**, S55–S56.
- 202 M. P. Nikolova and M. S. Chavali, *Biomimetics*, 2020, 5, 27.
- 203 S. S. Hosseini, E. Ghaemi, A. Noroozi and F. Niknejad, *Mycopathologia*, 2019, **184**, 261–271.
- A. Raghunath and E. Perumal, Int. J. Antimicrob. Agents, 2017, 49, 137–152.
- E. Hoseinzadeh, P. Makhdoumi, P. Taha, H. Hossini, J. Stelling, M. Amjad Kamal and G. Md. Ashraf, *Curr. Drug Metab.*, 2016, **18**, 120–128.
- A. Hamad, K. S. Khashan and A. Hadi, J. Inorg. Organomet. Polym. Mater., 2020,
 30, 4811–4828.
- 207 L. P. Silva, A. P. Silveira, C. C. Bonatto, I. G. Reis and P. V. Milreu, *Nanostructures Antimicrob. Ther. Nanostructures Ther. Med. Ser.*, 2017, **10**, 577–

- 596.
- 208 J. W. Alexander, Surg. Infect. (Larchmt)., 2009, 10, 289–292.
- 209 S. Das and V. Jayaraman, *Prog. Mater. Sci.*, 2014, **66**, 112–255.
- 210 Z. Chen, D. Pan, Z. Li, Z. Jiao, M. Wu, C.-H. Shek, C. M. L. Wu and J. K. L. Lai, Chem. Rev., 2014, 114, 7442–7486.
- 211 D. Khan, A. Rehman, M. Z. Rafiq, A. M. Khan and M. Ali, *Curr. Res. Green Sustain. Chem.*, 2021, 4, 100079.
- M. Karmaoui, A. B. Jorge, P. F. McMillan, A. E. Aliev, R. C. Pullar, J. A. Labrincha and D. M. Tobaldi, *ACS Omega*, 2018, **3**, 13227–13238.
- 213 K. Kumar Nair, P. Kumar, V. Kumar, R. A. Harris, R. E. Kroon, B. Viljoen, P. M. Shumbula, M. Mlambo and H. C. Swart, *Phys. B Condens. Matter*, 2018, **535**, 338–343.
- A. Chávez-Calderón, F. Paraguay-Delgado, E. Orrantia-Borunda and A. Luna-Velasco, *Chemosphere*, 2016, **165**, 33–40.
- 215 T. Sinha, M. Ahmaruzzaman, P. P. Adhikari and R. Bora, *ACS Sustain. Chem. Eng.*, 2017, **5**, 4645–4655.
- 216 Y. Li, S. Gao, B. Zhang, H. Mao and X. Tang, *Electron. Mater. Lett.*, 2020, **16**, 195–206.
- E. B. Tibayan, M. A. Muflikhun, V. Kumar, C. Fisher, A. R. C. Villagracia and G. N. C. Santos, *Ain Shams Eng. J.*, 2020, **11**, 767–776.
- X. Wang, W. Xiao, J. Zhang, Z. Wang and X. Jin, *Electrochem. commun.*, 2019, 102, 52–56.
- 219 Y. E. Miao, S. He, Y. Zhong, Z. Yang, W. W. Tjiu and T. Liu, *Electrochim. Acta*, 2013, **99**, 117–123.
- D. Liu, J. Pan, J. Tang, W. Liu, S. Bai and R. Luo, J. Phys. Chem. Solids, 2019, 124, 36–43.
- O. Choi, K. K. Deng, N. J. Kim, L. J. Ross, R. Y. Surampalli and Z. Hu, Water Res., 2008, 42, 3066–3074.
- 222 F. Ayaal and K. Chehri, *Plant Arch.*, 2019, **19**, 33–44.
- B. Das, M. I. Khan, R. Jayabalan, S. K. Behera, S.-I. Yun, S. K. Tripathy and A.

- Mishra, Sci. Rep., 2016, 6, 1–12.
- 224 S. A. Mousavi, R. Ghotaslou, A. Khorramdel, A. Akbarzadeh and A. Aeinfar, *Ir. J. Med. Sci.*, 2020, **189**, 1343–1350.
- 225 J. M. 3rd Farrow, G. Wells and E. C. Pesci, *PLoS One*, 2018, **13**, e0205638.
- M. Sasaki, S. V Sitaraman, B. A. Babbin, P. Gerner-Smidt, E. M. Ribot, N. Garrett, J. A. Alpern, A. Akyildiz, A. L. Theiss, A. Nusrat and J.-M. A. Klapproth, Lab. Invest., 2007, 87, 1042–1054.
- V. Tak, P. Mathur, P. Varghese, J. Gunjiyal, I. Xess and M. C. Misra, *J. Lab. Physicians*, 2014, **6**, 96–101.
- 228 S. Ahmed, M. Shahid, N. Fatima, F. Khan and U. Tayyaba, *CHRISMED J. Heal. Res.*, 2020, **7**, 167–172.
- F. Coppens, J. Iyyathurai, S. Ruer, A. Fioravanti, J. Taganna, L. Vereecke, H. De Greve and H. Remaut, *Acta Crystallogr. D. Biol. Crystallogr.*, 2015, **71**, 1615–1626.
- 230 J. Lin, S.H. Oh, R. Jones, J. A. Garnett, P. S. Salgado, S. Rusnakova, S. J. Matthews, L. L. Hoyer and E. Cota, *J. Biol. Chem.*, 2014, 289, 18401–18412.
- 231 M. Parthibavarman, S. Sathishkumar, M. Jayashree and R. BoopathiRaja, *J. Clust. Sci.*, 2019, **30**, 351–363.
- 232 R. I. Priyadharshini, G. Prasannaraj, N. Geetha and P. Venkatachalam, *Appl. Biochem. Biotechnol.*, 2014, **174**, 2777–2790.
- G. Selvaraj and V. Rajendran, *Dig. J. Nanomater. Biostructures*, 2010, **5**, 925–930.
- Y. Porte, R. Maller, H. Faber, H. N. AlShareef, T. D. Anthopoulos and M. A. McLachlan, *J. Mater. Chem. C*, 2016, **4**, 758–765.
- 235 M. Rafique, M. Rafique, U. Kalsoom, A. Afzal, S. Hassan Butt and A. Usman, *Opt. Quantum Electron.*, 2019, **51**, 1–11.
- 236 T. Abdul kareem and A. Anu kaliani, *Arab. J. Chem.*, 2011, **4**, 325–331.
- 237 K. K. Nanda, S. N. Sahu and S. N. Behera, *Phys. Rev. A*, 2002, **66**, 13208.
- T. Siva Vijayakumar, S. Karthikeyeni, S. Vasanth, A. Ganesh, G. Bupesh, R. Ramesh, M. Manimegalai and P. Subramanian, *J. Nanosci.*, 2013, **2013**, 7.

- P. Manjula, S. Arunkumar and S. V Manorama, Sensors Actuators B Chem., 2011,152, 168–175.
- D. Amalric-Popescu and F. Bozon-Verduraz, Catal. Today, 2001, 70, 139–154.
- 241 C. V. Reddy, B. Babu and J. Shim, *Mater. Sci. Eng. B*, 2017, **223**, 131–142.
- 242 H. Letifi, Y. Litaiem, D. Dridi, S. Ammar and R. Chtourou, *Adv. Condens. Matter Phys.*, 2019, **2019**, 2157428.
- 243 I. Nurdin, in *MATEC Web of Conferences*, EDP Sciences, 2016, vol. 39, p. 1001.
- F. Coppens, J. Iyyathurai, S. Ruer, A. Fioravanti, J. Taganna, L. Vereecke, H. De Greve and H. Remaut, *Acta Crystallogr. D. Biol. Crystallogr.*, 2015, **71**, 1615–1626.
- T. A. Russo, A. Manohar, J. M. Beanan, R. Olson, U. MacDonald, J. Graham and T. C. Umland, *mSphere*, 2016, **1**, e00082-16.
- J. Karkowska-Kuleta, E. Wronowska, D. Satala, M. Zawrotniak, G. Bras, A. Kozik, A. H. Nobbs and M. Rapala-Kozik, *Cell. Microbiol.*, 2021, 23, e13297.
- E. S. Kioshima, C. S. Shinobu-Mesquita, A. K. R. Abadio, M. S. S. Felipe, T. I. E. Svidzinski and B. Maigret, *Biotechnol. Lett.*, 2019, **41**, 1391–1401.
- 248 R. V. Vijayalakshmi, R. Kuppan and P. P. Kumar, *J. Mol. Liq.*, 2020, **307**, 112951.
- S. Elbasuney, G. S. El-Sayyad, H. Tantawy and A. H. Hashem, *RSC Adv.*, 2021,
 11, 25961–25975.
- Z. Obeizi, H. Benbouzid, T. Bouarroudj, C. Benzaid and A. Djahoudi, *J. New Technol. Mater*, 2021, **10**, 10–17.
- 251 F. L. Mayer, D. Wilson and B. Hube, *Virulence*, 2013, **4**, 119–128.
- 252 M. Gulati and C. J. Nobile, *Microbes Infect.*, 2016, **18**, 310–321.
- 253 R. Yuan, J. Tu, C. Sheng, X. Chen and N. Liu, *Front. Microbiol.*, 2021, **0**, 1280.
- O. Gómez-García, D. Andrade-Pavón, E. Campos-Aldrete, R. Ballinas-Indilí, A. Méndez-Tenorio, L. Villa-Tanaca and C. Álvarez-Toledano, *Molecules*, 2018, **23**, 599.
- 255 M. V Keniya, M. Sabherwal, R. K. Wilson, M. A. Woods, A. A. Sagatova, J. D. A. Tyndall and B. C. Monk, *Antimicrob. Agents Chemother.*, 2018, **62**, e01134.
- 256 K. Page, M. Wilson and I. P. Parkin, *J. Mater. Chem.*, 2009, **19**, 3819–3831.

- 257 S. N. Sovari and F. Zobi, *Chem. 2020, Vol. 2, Pages 418-452*, 2020, **2**, 418–452.
- 258 N. Ghasemi, F. Jamali-Sheini and R. Zekavati, *Mater. Lett.*, 2017, **196**, 78–82.
- 259 M. Sathishkumar and S. Geethalakshmi, *Mater. Today Proc.*, 2020, **20**, 54–63.
- 260 D. Yarali, R. Ahmadi and R. Hosseini, UPB Sci. Bull. Ser. B Chem. Mater. Sci., 2020, 82, 79–94.
- F. Shahriyari, D. Yaarali, R. Ahmadi, S. Hassan and W. Wei, *Adv. Powder Technol.*, 2020, **31**, 2337–2347.
- E. Nandhakumar, P. Priya, P. Selvakumar, E. Vaishnavi, A. Sasikumar and N. Senthilkumar, *Mater. Res. Express*, 2019, **6**, 095036.
- T. Fukumura, E. Sambandan and H. Yamashita, J. Coatings Technol. Res., 2018, 15, 437–443.
- 264 P. C. Nagajyothi, P. Muthuraman, T. V. M. Sreekanth, D. H. Kim and J. Shim, Arab. J. Chem., 2017, 10, 215–225.
- 265 B. Babu, A. N. Kadam, R. V. S. S. N. Ravikumar and C. Byon, *J. Alloys Compd.*, 2017, **703**, 330–336.
- 266 O. Pawar, N. Deshpande, S. Dagade, S. Waghmode and P. N. Joshi, *J. Exp. Nanosci.*, 2015, **11**, 28–37.
- 267 N. K. Abdalameer, K. A. Khalaph and E. M. Ali, *Mater. Today Proc.*, 2021, **45**, 5788–5792.
- 268 B. Gauri, K. Vidya, S. Gadale -Dagade and S. Waghmode, *Res. J. Chem. Environ.*, 2016, **20**, 1–5.
- 269 R. P. Vasquez, Surf. Sci. Spectra, 1999, **5**, 262.
- 270 H. Li, Y. Zou and J. Jiang, *Dalt. Trans.*, 2020, **49**, 9274–9281.
- 271 X-ray Photoelectron Spectroscopy (XPS) Reference Pages: Silver, http://www.xpsfitting.com/2013/04/silver.html, (accessed 26 July 2021).
- 272 W. Xia, H. Wang, X. Zeng, J. Han, J. Zhu, M. Zhou and S. Wu, *CrystEngComm*, 2014, **16**, 6841–6847.
- 273 I. X. Yin, J. Zhang, I. S. Zhao, M. L. Mei, Q. Li and C. H. Chu, *Int. J. Nanomedicine*, 2020, **15**, 2555–2562.
- 274 A. Roshanghias, A.Yakymovych, J. Bernardi and H. Ipser, *Nanoscale*, 2015, 7,

- 5843-5851.
- 275 C. Y. Lin, U. S. Mohanty and J. H. Chou, *J. Alloys Compd.*, 2010, **501**, 204–210.
- 276 A. Roshanghias, J. Bernardi and H. Ipser, *Mater. Lett.*, 2016, **178**, 10–14.
- K. Kannan, D. Radhika, D. Gnanasangeetha, S. K. Lakkaboyana, K. K. Sadasivuni, K. Gurushankar and M. M. Hanafiah, *Inorg. Chem. Commun.*, 2021, 125, 108429.
- Y. Zhan, J. Lan, J. Shang, L. Yang, X. Guan, W. Li, S. Chen, Y. Qi and S. Lin, J. Alloys Compd., 2020, 822, 153579.
- 279 S. A. David, D. P. Jeba and J. Ashli, *SPAST Abstr.*, 2021, **1**.
- T. Munawar, M. N. ur Rehman, M. S. Nadeem, F. Mukhtar, S. Manzoor, M. N. Ashiq and F. Iqbal, *J. Alloys Compd.*, 2021, **885**, 160885.
- 281 C. Yuan, H. Bin Wu, Y. Xie and X. W. Lou, *Angew. Chemie Int. Ed.*, 2014, 53, 1488–1504.
- 282 M. Wang, M. Ye, J. Iocozzia, C. Lin and Z. Lin, *Adv. Sci.*, 2015, **3**, 1600024.
- E. E. Elemike, D. C. Onwudiwe, L. Wei, L. Chaogang and Z. Zhiwei, *Sol. Energy Mater. Sol. Cells*, 2019, **201**, 110106.
- 284 H. Liu, Y. Feng, H. Cao and J. Yang, *Nano-Micro Lett.*, 2014, **6**, 252–257.
- 285 F. Mukhtar, T. Munawar, M. S. Nadeem, M. N. ur Rehman, M. Riaz and F. Iqbal, *Mater. Chem. Phys.*, 2021, **263**, 124372.
- 286 Z. Li, X. Tao, Y. Cheng, Z. Wu, Z. Zhang and H. Dang, *Ultrason. Sonochem.*, 2007, **14**, 89–92.
- 287 S. R. Chalana, V. Ganesan and V. P. Mahadevan Pillai, AIP Adv., 2015, 5, 107207.
- 288 L. A. Tamayo, P. A. Zapata, N. D. Vejar, M. I. Azócar, M. A. Gulppi, X. Zhou, G. E. Thompson, F. M. Rabagliati and M. A. Páez, *Mater. Sci. Eng. C*, 2014, 40, 24–31.
- A. Rigo, A. Corazza, M. L. di Paolo, M. Rossetto, R. Ugolini and M. Scarpa, *J. Inorg. Biochem.*, 2004, **98**, 1495–1501.
- 290 M. C. Linder and M. Hazegh-Azam, Am. J. Clin. Nutr., 1996, 63, 797S-811S.
- 291 M. Kumari, V. P. Giri, S. Pandey, M. Kumar, R. Katiyar, C. S. Nautiyal and A. Mishra, *Pestic. Biochem. Physiol.*, 2019, **157**, 45–52.

- 292 K.-J. Kim, W. S. Sung, B. K. Suh, S.-K. Moon, J.-S. Choi, J. G. Kim and D. G. Lee, *BioMetals*, 2009, **22**, 235–242.
- H. Zhou, M. D. Weir, J. M. Antonucci, G. E. Schumacher, X.-D. Zhou and H. H.
 K. Xu, *Int. J. Oral Sci.*, 2014, 6, 77–86.
- 294 T. Liu, Y. Liu, M. Liu, Y. Wang, W. He, G. Shi, X. Hu, R. Zhan, G. Luo, M. Xing and J. Wu, *Burn. Trauma*, 2018, **6**, DOI:10.1186/s41038-018-0115-2.
- G. Murugadoss, K. Thiruppathi, N. Venkatesh, S. Hazra, A. Mohankumar, G. Thiruppathi, M. R. Kumar, P. Sundararaj, J. R. Rajabathar and P. Sakthivel, J. Environ. Chem. Eng., 2022, 10, 106961.
- 296 B. D. Cullity, *Elements of X-ray diffraction*, Addison-Wesley Pub. Co., Reading, Mass., 1956.
- 297 P. Raul, S. Senapati, A. Sahoo, I. Umlong, R. Devi, A. J. Thakur and V. Veer, *RSC Adv.*, 2014, 4, 40580–40587.
- 298 M. M. Abutalib and A. Rajeh, *Phys. B Condens. Matter*, 2020, **578**, 411796.
- 299 A. Lupu, J. Therm. Anal., 1970, 2, 445–458.
- 300 M. Biswas, H. An, S. M. Choi, J.-W. Son, J.-H. Lee, B.-K. Kim, H.-W. Lee and K. J. Yoon, *Ceram. Int.*, 2016, 42, 10476–10481.
- 301 J. F. Moulder, W. F. Stickle, P. E. Sobol and K. D. Bomben, *Perkin-Elmer Corp.*, *Eden Prairie*, *MN*.
- 302 Q. Ni, D. W. Kirk and S. J. Thorpe, *J. Electrochem. Soc.*, 2014, **162**, H40.
- 303 A. Kumar, A. K. Pandey, S. S. Singh, R. Shanker and A. Dhawan, *Chemosphere*, 2011, **83**, 1124–1132.
- 304 H. S. N. Jayawardena, K. W. Jayawardana, X. Chen and M. Yan, *Chem. Commun.*, 2013, 49, 3034–3036.
- 305 Y. Li, W. Zhang, J. Niu and Y. Chen, *ACS Nano*, 2012, **6**, 5164–5173.
- 306 L. M. Gilbertson, E. M. Albalghiti, Z. S. Fishman, F. Perreault, C. Corredor, J. D. Posner, M. Elimelech, L. D. Pfefferle and J. B. Zimmerman, *Environ. Sci. Technol.*, 2016, 50, 3975–3984.
- 307 A. Ivask, A. ElBadawy, C. Kaweeteerawat, D. Boren, H. Fischer, Z. Ji, C. H. Chang, R. Liu, T. Tolaymat, D. Telesca, J. I. Zink, Y. Cohen, P. A. Holden and H.

- A. Godwin, ACS Nano, 2014, 8, 374–386.
- 308 N. Chen, M. Zhou, X. Dong, J. Qu, F. Gong, Y. Han, Y. Qiu, J. Wang, Y. Liu and Y. Wei, *Lancet*, 2020, **395**, 507–513.
- 309 N. M. Clark, G. G. Zhanel and J. P. Lynch III, Curr. Opin. Crit. Care, 2016, 22, 491–499.
- 310 C. Ayoub Moubareck and D. Hammoudi Halat, *Antibiotics*, 2020, **9**, 119.
- WHO publishes list of bacteria for which new antibiotics are urgently needed, https://www.who.int/news/item/27-02-2017-who-publishes-list-of-bacteria-for-which-new-antibiotics-are-urgently-needed.
- 312 F. Ghasemi and R. Jalal, *J. Glob. Antimicrob. Resist.*, 2016, **6**, 118–122.
- V. Tiwari, N. Mishra, K. Gadani, P. S. Solanki, N. A. Shah and M. Tiwari, *Front. Microbiol.*, 2018, **9**, 1218.
- 314 O. Akhavan and E. Ghaderi, *ACS Nano*, 2010, **4**, 5731–5736.
- 315 T. Parandhaman, A. Das, B. Ramalingam, D. Samanta, T. P. Sastry, A. B. Mandal and S. K. Das, *J. Hazard. Mater.*, 2015, **290**, 117–126.
- 316 I. Perelshtein, A. Lipovsky, N. Perkas, A. Gedanken, E. Moschini and P. Mantecca, *Nano Res.*, 2015, **8**, 695–707.
- 317 C. Gunawan, W. Y. Teoh, C. P. Marquis and R. Amal, *ACS Nano*, 2011, **5**, 7214–7225.

Metal-Metal Oxide Nanocomposites: Synthesis, Characterization and Antimicrobial Activities

by Monica Pandey

Submission date: 19-Jan-2022 06:21PM (UTC+0530)

Submission ID: 1744100913

File name: Monica_Pandey.pdf (12.53M)

Word count: 40970

Character count: 201887

Metal-Metal Oxide Nanocomposites: Synthesis, Characterization and Antimicrobial Activities

ORIGINALITY REPORT

SIMILARITY INDEX

INTERNET SOURCES

PUBLICATIONS

STUDENT PAPERS

PRIMARY SOURCES

Monica Pandey, Kirti Wasnik, Shubhra Gupta, Monika Singh et al. "Targeted specific inhibition of bacterial and species by mesoporous Ag/Sn-SnO composite nanoparticles: and investigation ", RSC Advances, 2022

Publication

This is from the Student's own publication and forms part of the

Centre for Advanced Studies in Electronics Science & Technology

Monica Pandey, Monika Singh, Kirti Washop of Physics, University of Hyderabad HYDERABAD-500 048. Telanggna, India. Shubhra Gupta et al. "Targeted and Enhanced Antimicrobial Inhibition of Mesoporous ZnO-Ag O/Ag, ZnO-CuO, and ZnO-SnO Composite Nanoparticles ",

Omega, 2021 Publication

This is from the student's own publication and forms part of the thesis

Prof. M. GHANASHYAN KRISHHAM Centre for Advanced Studies in Electronics Science & Technology School of Physics, University of Hyderabad

www.ncbi.nlm.nih.gov Internet Source

This is from the Student's own publicahan and forms part of the thesis

Prof. M. GHANASHWAM KRISHNING am

Centre for Advanced Studies in

Electronics Science & Technology
School of Physics, University of Hyderabad
Internet Source

Publication and forms part of the thesis.

aip.scitation.org Internet Source

M. Thanashyam Prof. M. GHANASHYAM KRISHNA Centre for Advanced Studies in Electronics Science & Technology School of Physics, University of Hyderabad

HYDERABAD-500 046. Telangana, India.



13	Submitted to Chulalongkorn University Student Paper	<1%
14	es.scribd.com Internet Source	<1%
15	tudr.thapar.edu:8080 Internet Source	<1%
16	rinnert.1kcloud.com Internet Source	<1%
17	meliseptalenia1c415040site.wordpress.com Internet Source	<1%
18	Shiv Shankar, Jong-Whan Rhim. "Facile approach for large-scale production of metal and metal oxide nanoparticles and preparation of antibacterial cotton pads", Carbohydrate Polymers, 2017 Publication	<1%
19	A. Sankaran, K. Kumaraguru, B. Balraj. "Structural and Optical Behavior of CuO/Ag and CuO/Ag/Au Nanocatalysts Synthesized Via a Novel Two Step Synthesis Approach for Enhancement of Catalytic Activity", Journal of Inorganic and Organometallic Polymers and Materials, 2020 Publication	<1%
20	www.tandfonline.com Internet Source	<1%

21	J. Alimunnisa, K. Ravichandran, K.S. Meena. "Synthesis and characterization of Ag@SiO 2 core-shell nanoparticles for antibacterial and environmental applications", Journal of Molecular Liquids, 2017 Publication	<1%
22	upcommons.upc.edu Internet Source	<1%
23	www.haupa.com Internet Source	<1%
24	research.sabanciuniv.edu Internet Source	<1 %
25	tel.archives-ouvertes.fr Internet Source	<1%
26	Submitted to University of Sheffield Student Paper	<1%
27	apps.dtic.mil Internet Source	<1%
28	iopscience.iop.org Internet Source	<1%
29	Mufsir Kuniyil, J.V. Shanmukha Kumar, Syed Farooq Adil, Mohamed E. Assal et al. "Production of biodiesel from waste cooking oil using ZnCuO/N-doped graphene	<1%

nanocomposite as an efficient heterogeneous catalyst", Arabian Journal of Chemistry, 2021

Publication

30	eprints.qut.edu.au Internet Source	<1%
31	hdl.handle.net Internet Source	<1%
32	www.mdpi.com Internet Source	<1%
33	Qingxin Guan, Chanchan Xia, Wei Li. "Bio- friendly controllable synthesis of silver nanoparticles and their enhanced antibacterial property", Catalysis Today, 2019 Publication	<1%
34	Elizabeth M. Duselis, Maria C. Panepinto, John E.P. Syka, Christopher Mullen et al. "Improved Sequence Analysis of Intact Proteins by Parallel Ion Parking during Electron Transfer Dissociation", Analytical Chemistry, 2021	<1%
35	link.springer.com Internet Source	<1%
36	muroran-it.repo.nii.ac.jp Internet Source	<1%
37	dc.uwm.edu Internet Source	<1%

38	dspace.ncl.res.in:8080 Internet Source	<1%
39	Submitted to Indian School of Mines Student Paper	<1%
40	documents.mx Internet Source	<1%
41	worldwidescience.org Internet Source	<1%
42	Submitted to Higher Education Commission Pakistan Student Paper	<1%
43	Submitted to Hong Kong Baptist University Student Paper	<1 %
44	Tanur Sinha, Md. Ahmaruzzaman, Partha Pradip Adhikari, Rekha Bora. " Green and Environmentally Sustainable Fabrication of Ag-SnO Nanocomposite and Its Multifunctional Efficacy As Photocatalyst and Antibacterial and Antioxidant Agent ", ACS Sustainable Chemistry & Engineering, 2017 Publication	<1%
45	Zhengchun Wang, Tong Wu, Lan Xiao, Pingli Qin et al. "Multifunctional potassium hexafluorophosphate passivate interface defects for high efficiency perovskite solar cells", Journal of Power Sources, 2021	<1%

46	dokumen.pub Internet Source	<1%
47	hypothes.is Internet Source	<1%
48	repository.ntu.edu.sg Internet Source	<1 %
49	Submitted to IIT Delhi Student Paper	<1%
50	Submitted to Institute of Graduate Studies, UITM Student Paper	<1 %
51	Md. Rakibuddin, Subrata Mandal, Rajakumar Ananthakrishnan. " A novel ternary CuO decorated Ag AsO /GO hybrid as a Z-scheme photocatalyst for enhanced degradation of phenol under visible light ", New Journal of Chemistry, 2017 Publication	<1%
52	Narender Kumar Joon, Ning He, Michal Wagner, Marité Cárdenas, Johan Bobacka, Grzegorz Lisak. "Influence of phosphate buffer and proteins on the potentiometric response of a polymeric membrane-based solid-contact Pb(II) ion-selective electrode", Electrochimica Acta, 2017 Publication	<1 %

<19

Exclude quotes On Exclude bibliography On

Exclude matches

< 14 words

Curriculum Vitae

Monica Pandey

Research Scholar, School of Engineering Sciences and Technology, University of Hyderabad, Telangana, India-500046

Academic Qualifications

Ph.D. in Materials Engineering (Thesis Submitted)

School of Engineering Sciences and Technology, University of Hyderabad, Telangana-500046

B. Tech in Chemical Engineering (2010-2014)

Beant College of Engineering and Technology, Gurdaspur (Punjab Technical University) 143521

Division: first division with distinction (81%)

AISSSCE in 2010 (Physics, Chemistry, Biology, Mathematics, and English) Holy Cross School, Tadong, Gangtok, East Sikkim-737102 (Affiliated to CBSE) Division: first (75.6%)

AISSCE in 2008

Holy Cross School, Tadong, Gangtok, East Sikkim-737102 (Affiliated to CBSE) Division: First (88.6%)

Research Experience

- Presently working as Research Scholar (Materials Engineering) in School of Engineering Sciences and Technology at University of Hyderabad in the project: "Metal-Metal Oxide nanocomposites"
- Worked as JRF in Sikkim State Council for Science and Technology in the project: "Scientific Evaluation of Water Purification System" (August 2014-July, 2015)
- Six-month project in CSIR-INDIAN INSTITUTE OF PETROLEUM, Dehradun (18th Dec 2013- 26th June 2014) on Methane Activation via Tri Reforming using Nano-Structured Catalyst.

Technical Skills

- Synthesize nanomaterials by various top-down approaches including sol-gel, coprecipitation, solvothermal, chemical reduction, etc.
- Experience in handling various instruments- XRD, UV-Vis Spectrometer, BET instrument, and Zetasizer.

Patent Applications Filed:

- 1. A mesoporous anti-microbial nanocomposite and a method of preparation thereof. Pradip Paik;, **Monica Pandey**, Sukanya Patra, Monika Singh, Kirti Wasnik, Premshankar Gupta. (**Indian Patent Application No. 202011031802, 2020**)
- 2. A nanomaterial-based antimicrobial composition and a method of preparation thereof. Pradip Paik, **Monica Pandey**, Ragini Tilak, Monika Singh (**Indian Patent Application no.: 202011017968, 2020**)

Publications in journal:

- Monica Pandey, Monika Singh, Kirti Wasnik, Shubhra Gupta, Sukanya Patra, Prem Shankar Gupta, Divya Pareek, Somedutta Maity, N. Chaitanya, BMR Reddy, Ragini Tilak, and Pradip Paik "Targeted and Enhanced Antimicrobial Inhibition of Mesoporous ZnO–Ag₂O/Ag, ZnO–CuO, and ZnO–SnO₂ Composite Nanoparticles." ACS Omega 6, no. 47 (2021): 31615-31631.
- 2. **Monica Pandey**, Kirti Wasnik, Shubhra Gupta, Monika Singh, Sukanya Patra, Premshankar Gupta, Divya Pareek, Somedutta Maity, Ragini Tilak, and Pradip Paik. "Targeted specific inhibition of bacterial and Candida species by mesoporous Ag/Sn–SnO₂ composite nanoparticles: in silico and in vitro investigation." *RSC Advances* 12, no. 2 (2022): 1105-1120.
- 3. Prem S. Gupta, Kirti Wasnik, Sukanya Patra, DIvya Pareek, Monika Singh, Somedutta Maity, **Monica Pandey**, and Pradip Paik. "A review on Biodegradable Polymeric Materials for Bone Tissue Engineering (BTE) Applications." (2021)
- 4. Rajib K. Singha, Subhasis Das, **Monica Pandey**, Sachin Kumar, Rajaram Bal, and Ankur Bordoloi. "Ni nanocluster on modified CeO₂-ZrO₂ nanoporous composite for tri-reforming of methane." *Catalysis Science & Technology* 6, no. 19 (2016); 7122-7136.
- 5. Reena Goyal, Deepa Dumbre, LN Sivakumar Konathala, **Monica Pandey** and Ankur Bordoloi. "Oxidative coupling of aniline and desulfurization over nitrogen

rich mesoporous carbon." Catalysis Science & Technology 5, no. 7 (2015); 3632-3638.

Presentation in conferences:

- 1. **Monica Pandey,** Presented (Poster) in "NanoSciTech", November 8-10, 2017, Chandigarh, India.
- 2. **Monica Pandey,** Presented (Poster) in "ICN- 2019", April 12-14, 2019, Kottayam, India. (Best Poster Award)
- 3. Monica Pandey, Presented (Poster) in "ICAFNM- 2020", Kharagpur, India.
- 4. **Monica Pandey,** Presented (Poster) in "(Icbr-2020)", February 27-29, 2020, Varanasi, India.

Awards and Honors

- Gold Medal in Chemical Engineering Course at the University.
- Awarded CSIR-SRF Fellowship in 2020.
- Best Poster (3rd) at International Conference on Nanotechnology (ICN-2019), Kottayam, Kerala.
- Scholarships for meritorious students, Sikkim (2010).
- All Rounder Girl Child in School.

Other Significant Roles and Responsibilities

- Worked as an intern in Indian Oil Corporation Limited (IOCL) for six weeks project (May 14-22 June 2012) on the Economy of the plant and Motor Spirit Quality Unit.
- Worked in leadership positions at various stages:
 - ➤ President of Chemical Engineering Society in college
 - ➤ Vice President of Literary Society in college
 - ➤ Discipline Captain in School

Permanent Address

Lower Samdur, Near Shiv Mandir, PO/PS Ranipool, East Sikkim-737135

Declaration

I hereby declare that the information provided by me is true to the best of my knowledge.

Monica Pandey